Politecnico
di Torino
1859

ScuDo
Scuola di Dottorato ~ Doctoral School
WHAT YOU ARE, TAKES YOU FAR

Doctoral Dissertation
Doctoral Program in Chemical Engineering (35thcycle)

Multiscale Modeling of Food Emulsion Production Process

From Molecules to Mixing Equipment

By

Marco Ferrari

******

Supervisor(s):
Prof. Antonio Buffo, Supervisor
Prof. Gianluca Boccardo, Co-Supervisor
Prof. Marco Vanni, Co-Supervisor

Doctoral Examination Committee:
Prof. Ing. Martin Lísal, Referee, Institute of Chemical Process Fundamentals
Dr. Nida Sheibat-Othman, Referee, Université Claude Bernard Lyon 1
Prof. Matteo Fasano, Politecnico di Torino
Dr. Nicodemo Di Pasquale, Brunel University London
Prof. Daniele Marchisio, Politecnico di Torino

Politecnico di Torino
2023

Declaration

I hereby declare that, the contents and organization of this dissertation constitute my own original work and does not compromise in any way the rights of third parties, including those relating to the security of personal data.

Marco Ferrari
2023

* This dissertation is presented in partial fulfillment of the requirements for **Ph.D. degree** in the Graduate School of Politecnico di Torino (ScuDo).

I would like to dedicate this thesis to my loving parents

Acknowledgements

This work was carried out in the context of the VIMMP project (www.vimmp.eu), where the entire workflow will contribute to populate a marketplace for generic multiscale and multiphysics simulations. The VIMMP project has received funding from the European Union's Horizon 2020 Research Innovation Programme under Grant Agreement n. 760907. We thank Jan-Willem Handgraaf (Siemens Industry Software Netherlands B.V., Galileiweg 8, 2333 BD, Leiden, The Netherlands) for providing us with the CULGI software employed here and for his collaboration in conducting this research.

We acknowledge the CINECA award under the ISCRA initiative, for the availability of high performance computing resources and support. Computational resources were also provided by HPC@POLITO, a project of Academic Computing within the Department of Control and Computer Engineering at the Politecnico di Torino (www.hpc.polito.it).

At the end of my PhD, I warmly thank my supervisor, Prof. Antonio Buffo, and co-supervisors, Prof. Gianluca Boccardo and Prof. Marco Vanni, for their constant support and help in all the goals and difficulties faced during this long period. Special thanks go to Prof. Daniele Marchisio and all the members of my research group MuSyChEn. I am so glad to be part of this team and contribute to our shared mission.

I would like to thank Prof. Alexandra Komrakova and Yash Kothari from University of Alberta for their invaluable effort and availability during my research period in Edmonton, Canada.

Ringrazio adesso tutti i colleghi, in particulare, i miei compagni di ufficio, con i quali ho condiviso sia le gioie che le difficoltà incontrate durante gli anni del dottorato.

Vorrei ringraziare ancora tutti i miei amici, in particulare, Papo, Mino, Alberto, Alex, Cristiana e Francesco. Anche se ci vediamo poco, mi hanno sempre ascoltato e sostenuto e per questo ne sono immensamente grato.

Ringrazio anche tutti gli amici conosciuti ad Edmonton provenienti da tutto il mondo, i quali mi hanno fatto sentire come a casa anche se a migliaia di chilometri. Un ringraziamento speciale va in particolare ad Anna e Michela, le quali hanno reso l'esperienza in Canada indimenticabile e uno dei periodi più belli della mia vita.

Ringrazio immensamente Miriam per il suo instancabile sostegno e supporto. Ha condiviso con me i traguardi e le difficoltà di questo percorso ed è sempre stata al mio fianco nonostante i momenti di sconforto. Ma soprattutto ha contribuito a fare di me una persona migliore e se mi sento così oggi è sicuramente grazie a lei.

Il più caloroso ringraziamento va alla mia famiglia che mi ha sempre voluto bene e mi ha accompagnato in tutte le mie scelte di vita. Un pensiero speciale però lo dedico a papà, il quale è sempre stato un punto di riferimento e un grande esempio per me.

Abstract

Most of the well-known food emulsions, such as mayonnaise, are made of a continuous water phase, a dispersed phase with high oil content, and surfactants that stabilize the oil drops. The Droplet Size Distribution (DSD) is the most important property of the emulsion since the structure, stability, taste, and color of the final product depend on the DSD. The DSD in turn depends on the emulsion composition, the type of process, and the operating conditions in which the production process operates. The production of emulsions is based on mixing the ingredients and applying enough mechanical energy to the emulsion to reach the desired DSD. During the emulsification process, the interfacial properties between dispersed and continuous phases play an essential role in the formation and stabilization of the oil droplets. Many food emulsions are stabilized by surface-active biopolymers that adsorb to droplet surfaces and form protective coatings. Some of these functional molecules are integral components of more complex ingredients used in food products (e.g., egg yolk). Although the egg yolk is recognized as one of the most widely employed emulsifiers for both industrial and home-made food emulsion preparation, many issues need to be addressed, especially the adsorption mechanism of egg yolk proteins at the oil-water interface and their emulsifier behavior. Experimental research concerning the emulsifying properties of egg yolk proteins has been hindered by the difficulties in extracting individual components from the complex matrix. Hence, within the multiscale framework, different time- and space- scales were investigated to describe the modeling approach from the molecular scale (oil-water interface) to the macro-scale (production device). The oil-water interfacial system, where the emulsifier is one of the most surface-active proteins from the egg yolk, so-called Apovitellenin I, was investigated using different molecular modeling techniques. The protein adsorption behavior at the interface and the interactions with other co-surfactants were described with the help of an atomistic model and statistical analysis. Then, a coarse-grained model based on the Dissipative Particle Dynamics (DPD) was employed to consider

both the complex composition of the emulsion and the equilibration time required by macro-molecules to re-arrange at interfaces. Therefore, by combining the molecular methods with a thermodynamic model of protein adsorption, a complete description of the interfacial system stabilized by protein surfactants was achieved. The approach employed eventually showed how these techniques can be linked together to predict equilibrium properties that are difficult to obtain experimentally for the system investigated. In addition, a scaling scheme for DPD simulations was applied to oil-water interfacial systems to study different coarse-graining levels, highlighting the advantages and limits of the proposed method for conserving the equilibrium properties of such systems. Another modeling method was also investigated, namely the Lattice Boltzmann Model (LBM). Although both DPD and LBM are successfully employed in modeling mesoscopic systems, they are conceptually different. Therefore, the two techniques were compared when dealing with immiscible fluids in presence of surfactants, with the aim of finding a possible link between the molecular and the continuum modeling approaches. Finally, at the macroscale level of description of the production device, Computational Fluid Dynamics (CFD) simulations were employed to properly describe the non-Newtonian dynamics of the emulsion and clarify the influence of the type of flow on the DSD, namely pure shear versus elongational. To describe the evolution of the DSD, the Population Balance Modeling (PBM) was employed, in which coalescence and breakage of oil droplets were taken into account by appropriate kernels, which depend on local flow conditions.

Contents

List of Figures

List of Tables

Nomenclature

Roman Symbols

$\boldsymbol{F}$	force [N]
$\boldsymbol{s}$	collective variable
$\boldsymbol{x}$	position vector
$\hat{x}$	normalized x coordinate
$\hat{\mathbf{r}}_{ij}$	direction between beads i and j at positions $\mathbf{r}_i$ and $\mathbf{r}_j$
$\mathbf{E}$	symmetric rate-of-strain tensor
$\mathbf{F}$	component of DPD force
$\mathbf{f}$	summation of DPD force components
$\mathbf{M}$	transformation matrix
$\mathbf{r}$	position [DPD unit]
$\mathbf{S}$	relaxation matrix
$\mathbf{U}$	emulsion velocity [m/s]
$\mathbf{v}$	velocity [DPD unit]
$\mathscr{F}$	free energy density functional
$\vec{r}$	vector position
a	DPD interaction parameter defined for each bead pair ij

a	Frumkin-type intermolecular interaction parameter
A, B	numerical parameters related to the bulk free energy density
A_H	Hamaker constant [J]
b	adsorption equilibrium constant [m^3/mol]
b_j	adsorption equilibrium constant for the protein in the j-state [m^3/mol]
C	concentration
C	strength of the self-interaction between surfactants
c	percent interface coverage of surfactant $= d_s/d_s^\infty$
c	protein bulk concentration [mol/m^3]
c^*	critical protein bulk concentration [mol/m^3]
c_i	protein interface concentration [mg/m^2]
c_i	protein surface number density [#/A]
c_p	surfactant molecule number density [#/V]
c_s	speed of sound [lu]
c_α	discrete velocity [lu]
D	parameter related to the surface free energy density due to surfactant molecules
D	protein diffusion coefficient [m^2/s]
d	gap between rotor and stator [mm]
d_s	surfactant number density at interface
d_{32}	mean Sauter diameter [μm]
$D_{W,\mathrm{DPD}}$	simulated water self-diffusion coefficient at ambient conditions via DPD

$D_{W,Exp}$	experimental water self-diffusion coefficient at ambient conditions [m^2/s]
E	difference between the interaction strength of bulk phases with the surfactant
E	energy [J]
e	electric charge [C]
Ex	bulk surfactant solubility parameter $= \frac{D}{W\xi^2}$
f, g, and h	particle populations
f_1, f_2, and f_3	phase angles
F_{total}	total free energy functional
h	DPD base unit of length [Å]
K	fitting parameter in emulsion rheology model
k	constant parameter in interfacial tension relation
K_1	free adjustable model parameter in coalescence kernel
K_2	free adjustable model parameter in coalescence kernel
K_3	free adjustable model parameter in breakage kernel
K_4	free adjustable model parameter in breakage kernel
K_θ	elastic constant for angular vibration
k_A	stiffness of the angular bond constraint
k_b	Boltzmann constant [J/K]
K_r	elastic constant for bond vibration
k_S	stiffness of the length bond constraint
L	DPD box size
L	droplet diameter [μm]

L_α	quadrature abscissa
l_H	equilibrium length in harmonic spring quadratic potential
M	distribution moment
M	mobility
M	protein molecular mass [Da]
m	fitting parameter in emulsion rheology model
m	mass [DPD unit]
m	mass [kg]
N	number of molecules
N	number of point particles
N	quadrature approximation order
n	moles
n	number of DPD beads representing the protein molecule
n	total number of possible states of protein molecule
N_G	total number of steps
N_{phys}	number of physical molecules represented in DPD simulation
p	probability
p	thermodynamic pressure
p^*_{N}	normal component of the pressure tensor profile [DPD unit]
p^*_{T}	tangential component of the pressure tensor profile [DPD unit]
q	point charge
R	ideal gas constant [J/(K mol)]
R	radius

r	distance between point atomistic particles
r_c	DPD cutoff radius
R_g	radius of gyration [Å]
R_{eq}	equivalent radius of colliding drops of diameter L and L' [μm]
r_{eq}	equilibrium distance
r_{ij}	distance between beads i and j at positions $\mathbf{r}_i$ and $\mathbf{r}_j$
R_{max}	maximum rotor radius [mm]
S	scaling factor [m^2/s]
S	scoring function
S_e	standard deviation
T	temperature [K]
t	time [lu]
t	time [s]
U	harmonic spring quadratic potential
u_α	macroscopic velocity [lu]
V	total volume of the system [lu]
V	volume of the fragment in AFP [Å^3]
V_0	reference volume of a cluster of three water molecules in its lowest energy conformation [Å^3]
V_1, V_2, and V_3	Fourier coefficients in torsional energy term
v_i	scaled molecular volume of fragment i
W	height of the Gaussian function $G(\boldsymbol{s}, \boldsymbol{s'})$
W	parameter related to the excess free energy density

w	weighting coefficient
w_α	quadrature weight
X	box dimension [nm]
x	Cartesian coordinate normal to the interface [lu]
Y	box dimension [nm]
y_a, y_b	y coordinates defining the adsorption region
y_c, y_d	y coordinates defining the bulk region
Z	box dimension [nm]
Z	summation over all the states i
$\mathrm{Ca}_{\mathrm{cr}}$	critical capillary number
Ca	capillary number
Re	Reynolds number

Greek Symbols

α	Manas-Zloczower mixing index
α	proportionality coefficient
α_{EV}	global adjustable parameter in AFP
α_{res}	global adjustable parameter in AFP
β	$= 1/k_b T$
$\mathbf{\Omega}$	skew-symmetric rate-of-rotation tensor
χ	mass fraction
$\dot{\gamma}$	local shear rate [1/s]
ε	DPD base energy unit [J]
ε and σ	Lennard-Jones potential parameters

η	dynamic viscosity $[\mathrm{mPa} \cdot \mathrm{s}]$
η	solvent viscosity [cP]
η_c	continuous water phase viscosity $[\mathrm{mPa} \cdot \mathrm{s}]$
η_r	dimensionless relative viscosity
$\eta_{r,\infty}$	relative plateau viscosity for high shear rate
Γ	coefficient of mobility
Γ	interfacial tension [DPD unit]
Γ	interfacial tension of the free interface [DPD unit]
Γ	total adsorption of protein in all n states $[\mathrm{mol/m^2}]$
γ	DPD friction coefficient
γ	bias factor
Γ^*	critical total adsorption of protein in all n states $[\mathrm{mol/m^2}]$
κ_{int}	positive constant related to the interfacial tension
λ	ratio between oil viscosity η_{oil} and apparent emulsion viscosity η_{emul}
μ	chemical potential
μ_c and μ_d	dynamic viscosity of continuous and dispersed phases [lu]
ν	kinematic viscosity [lu]
ν	kinematic viscosity $[\mathrm{m^2/s}]$
ν	number of physical particles into one DPD bead
Ω	collision operator
ω	average molecular area of adsorbed proteins $[\mathrm{m^2/mol}]$
ω	rotor angular velocity [1/s]

ω_0	molar area of the solvent molecule [m^2/mol]
ω_{max}	maximum partial molar area of protein molecule [m^2/mol]
ω_{min}	minimum partial molar area of protein molecule [m^2/mol]
ϕ	coarse-graining level ratio (scaling ratio)
ϕ	oil fraction
ϕ	order parameter representing bulk phases
ϕ	torsional angle
π	surface pressure [mN/m]
π^*	critical surface pressure [mN/m]
ψ	order parameter representing the surfactant
ψ_c	auxiliary term in ψ profile
ρ	DPD number density
ρ	density [kg/m^3]
ρ	density [lu]
ρ	molar concentration of solvent [mol/l]
σ	DPD sigma parameter
σ	interfacial tension [lu]
σ	interfacial tension [mN/m]
σ	interfacial tension of the interface covered by protein surfactants [mN/m]
σ_0	interfacial tension of the free interface [mN/m]
σ_0	interfacial tension of a clean interface
σ_{calc}	interfacial tension computed via DPD [mN/m]

σ_{DPD}	DPD interfacial tension
τ	DPD base time unit [ps]
τ	relaxation time [lu]
θ	angle between point atomistic particles
θ	total surface coverage
θ_H	equilibrium angle in harmonic spring quadratic potential
θ_{eq}	equilibrium angle
θ_{ijk}	angle between DPD beads i, j, and k
ε	adjustable parameter in thermodynamic model of protein adsorption
$\mathit{\Omega}$	grand potential
ξ	thickness of the diffuse interface [lu]

Superscripts

$\bar{}$	volume-averaged
∞	maximum amount
C	conservative component of DPD force
D	dissipative component of DPD force
R	stochastic (random) component of DPD force
$'$	DPD system with different coarse-grained level with respect to the reference one
$\tilde{}$	reduced unit DPD system
A	angular bond spring potential between adjacent DPD beads ijk
eq	equilibrium
Exp	experimental value

$Model$	model prediction
r	repulsive component of DPD force
S	length bond spring potential between adjacent DPD beads ij

Subscripts

0	contribution from the adsorption of surfactant on the liquid-liquid interface
0	interface position
01	interface label
02	interface label
α and β	spatial coordinates x, y, and z in the Einstein notation
a	interval limit defining the interface region
ab	long-range energy term
$angles$	vibrational term
b	bulk
b	interval limit defining the interface region
BL	binary liquids
$bonds$	bonding term
$emul$	emulsion apparent property
ex	excess contribution in free energy density functional
Exp	experimental value
H	DPD protein bead type (two bonded beads model)
i	DPD bead
id	ideal

j	DPD bead $\neq i$
k	DPD bead $\neq i \neq j$
k	moment order $\in 0,...,2N-1$
n	number of iteration
O	DPD oil type bead
oil	oil property
P	DPD protein bead type (single bead model)
q	stencil
S	surfactant
T	DPD protein bead type (two bonded beads model)
$torsion$	torsional term
V	biased ensemble
v	volume
w	weight
w or W	DPD water type bead
x	x direction
xs	surface excess quantity
y	y direction
z	z direction
1	interface label
2	interface label
c	critical

Other Symbols

ΔG_{ads}	Gibbs free energy of adsorption [kJ/mol]
$\Delta G_{res,ij}$	residual Gibbs energy of mixing of a *hypothetical* equimolar mixture of fragments i and j in AFP [J]
Δt	time step [DPD unit]
Δt	time step [fs]
Δx and Δt	mesh and time steps [lu]
$\hat{\delta}(x)$	approximated Dirac delta function
$\langle O(\boldsymbol{r})\rangle$	value of the property depending on spatial coordinates in the unbiased ensemble
$\langle R_{g,Protein}\rangle$	protein mean radius of gyration [Å]
$\|\|\boldsymbol{s}-\boldsymbol{s'}\|\|$	distance between $\boldsymbol{s}$ and $\boldsymbol{s'}$ in the CVs space
$C(L,L')$	coalescence kernel [m^3/s]
$F(\boldsymbol{s})$	free energy surface obtained from a classical molecular dynamics simulation
$F_y(y)$	Helmholtz free energy obtained from metadynamics simulations along the y direction [kJ/mol]
$G(\boldsymbol{s},\boldsymbol{s'})$	small repulsive Gaussian function centered in the CVs space at the current value $\boldsymbol{s'}$
$g(L)$	breakage kernel [1/s]
$II_{\mathbf{\Omega}}$	second invariant of the skew-symmetric rate-of-rotation tensor $\mathbf{\Omega}$
$II_{\mathbf{E}}$	second invariant of the symmetric rate-of-strain tensor $\mathbf{E}$
$n(L)$	droplet size distribution
$P^{chem}_{\alpha\beta}$	‘chemical’ pressure tensor
$P^{th}_{\alpha\beta}$	‘thermodynamic’ pressure tensor
$V(\boldsymbol{s})$	added potential form in MetaD

Acronyms / Abbreviations

AFP	Automated Fragmentation and Parametrization method
BFS	Binary Fluid-Surfactant
BGK	Bhatnagar-Gross-Crook
CFD	Computational Fluid Dynamics
CG	Coarse-Grained
CV	Collective Variable
DPD	Dissipative Particle Dynamics
DSD	Droplet Size Distribution
IFT	Interfacial Tension
L	Lipids
LBM	Lattice Boltzmann Model
lDDT	Local Distance Difference Test
LDL	Low-Density Lipoprotein
lu	lattice units
MD	Molecular Dynamics
MetaD	Metadynamics
MRT	Multiple Time Relaxation
MSD	Mean-Squared Displacement
P	Protein
PBC	Periodic Boundary Conditions
PBE	Population Balance Equation
PBM	Population Balance Modeling

PC	Phosphatidylcholines
PL	Phospholipids
PME	Particle Mesh Ewald summation
POPC	1-palmitoyl-2-oleoyl-sn-glycero-3-phosphocholine
QMOM	Quadrature Method of Moments
RDF	Radial Distribution Function
RMSE	Root Mean Squared Error
SPME	Smooth Particle Mesh Ewald summation method
SRT	Single Relaxation Time
WTMetaD	Well-Tempered Metadynamics

Chapter 1

Introduction

In the food field, emulsions are frequently used and one of the most known is mayonnaise. Emulsions are formed starting from two or more immiscible fluids, usually, water and oil. In the case of mayonnaise, small oil droplets have been dispersed into a continuous water phase due to vigorous agitation [8]. Food emulsions are typically thermodynamically unstable and they are included in the class of macroemulsions, because they are characterized by a dimension of the oil droplets among 0.2÷50 μm [9, 10]. Due to the instability, after the emulsion is formed, the microdroplets of oil begin to approach each other until they come together by coalescence to form a larger droplet. When a drop is large enough, it separates from the aqueous phase and emerges at the surface. This occurs until a phase separation is reached [11]. The speed of this process can be influenced by several physical-chemical factors such as the type of the two fluids, droplet dimension, presence of molecules that could prevent phase separation, or the method of mixing [8]. In the case of more stable emulsions, called microemulsions, the size of the droplets, among 10÷100 nm, is as small as to prevent coalescence [9].

Many food emulsions are stabilized by surface-active biopolymers that adsorb on the droplet surface and form protective coatings [12]. Some of these functional molecules are integral components of more complex food ingredients used in food products (e.g., egg yolk, milk, and flour) [12, 13]. Although the egg yolk is recognized as one of the most widely employed emulsifiers for both industrial and home-made food emulsion preparation [12], many issues need to be addressed, especially the adsorption mechanism of egg yolk proteins at the oil-water interface and their emulsifier behavior [1]. Indeed, the egg yolk is a complex system with different structural levels consisting of non-soluble protein aggregates (granules) in suspension in a clear yellow fluid (plasma) that contains low-density lipoproteins (LDLs) and soluble proteins [1]. Experimental research concerning the emulsifying properties of egg yolk proteins has been hindered by the difficulties in extracting individual components from the complex matrix, therefore, they are less amenable to a detailed study by being less readily available in the pure form [14–16].

The mayonnaise is composed of mixing egg yolk, oil, water, salt, vinegar, and lemon juice [6, 7]. The two immiscible phases are oil and water, while vinegar and lemon juice are added to give flavor to mayonnaise and reduce the pH, which improves the stability of emulsions [17]. Egg yolk is the key ingredient as it contains biomolecules that can act as surfactants at the water-oil interface: phospholipids and surfactant proteins [8]. These molecules consist of a polar and apolar part which can interact with the water and oil phase, respectively; so these molecules position themselves at the interface and limit droplet coalescence that would lead to phase separation [18]. Among proteins of the egg yolk, one of the most surface active having the greatest emulsifying properties is the so-called Apovitellenin I [19, 20]. This is a homo-dimer of 82 amino acids per chain (approx 9 kDa), linked by a disulfide bond between the only two cysteines that are present in the structure [19, 20]. There is little information concerning this protein because it is unstable in water and it is difficult to isolate it [21]. In fact, its spatial conformation has not been experimentally determined yet. In the egg yolk, Apovitellenin I is found in the LDLs with other proteins, phospholipids, triglycerides, and cholesterol. When the LDLs reach the water-oil interface, they break and release the surfactant molecules. Therefore, proteins and phospholipids are free to diffuse at the interface, leading to a decrease in the interfacial tension stabilizing the emulsion (Figure 1.1) [1, 22].

During the emulsification process, the interfacial properties between dispersed and continuous phases of food emulsions play an essential role in the formation and stabilization of the oil droplets [12, 13]. Therefore, it is important to have a fundamental understanding of the factors that influence the type, concentration, interactions, and arrangement of surface-active molecules at interfaces [12, 13]. Computer modeling techniques can greatly enhance the comprehension of the way the molecules organize themselves in a liquid [23–26]. Molecular simulations can provide valuable insight into the relationship between molecular properties and structural organization that are relevant for a better understanding of the behavior

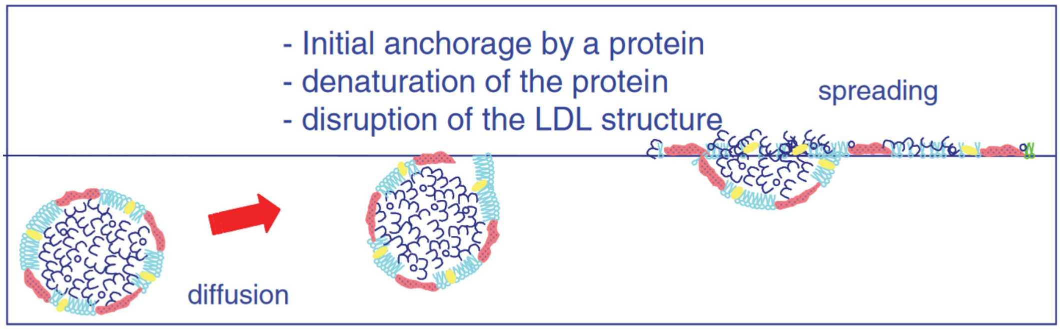

Fig. 1.1 Schematic representation of the adsorption mechanism of LDL extracted from hen egg yolk (image taken from Ref. [1]).

of food emulsions, including the miscibility/immiscibility of liquids, the formation of surfactant micelles, the adsorption and displacement of emulsifiers at interfaces, the transport of nonpolar molecules through aqueous phases, the conformation and flexibility of biopolymers in solution, polymer interactions, and the formation of gels [27–36].

In order to study the protein behavior at the interface, Molecular Dynamics (MD) simulations have been largely employed. This technique is widely used to study events that cannot be observed experimentally [37]. The first step in a molecular simulation is to define the characteristics of the molecules involved (e.g., size, shape, flexibility, and polarity) and the nature of the intermolecular pair potentials that act between them, making a number of simplifying assumptions as a compromise between the model reliability and a reasonable computational time [38]. A collection of these molecules is arbitrarily distributed within a box that represents a certain region of space, and the change in the conformation and/or organization of the molecules is then monitored as they are allowed to interact with each other. Depending on the simulation technique used, one can obtain information about the evolution of the structure with time and/or about the equilibrium structure of the molecular ensemble. The most commonly used computer simulation techniques in this context are the Monte Carlo approach and Molecular Dynamics. In these models the involved molecules can be described with all their atomistic details or some of them can be coarse-grained, as in Dissipative Particle Dynamics (DPD) [31, 39–43]. Many molecular modeling studies of food structures were carried out employing the aforementioned approaches [31]. The adsorption of flexible proteins (β-casein [44] and a proteinlike heteropolymer [45]) at an oil-water interface was studied by means of Monte Carlo simulations. On the other hand, the majority of MD studies on protein adsorption at fluid interfaces have been on globular proteins using both all-atom and coarse-grained models, with few studies on unstructured intrinsically disordered proteins [46–53]. Another molecular modeling technique is the so-called Metadynamics (MetaD) which is based on the MD but has the advantage of performing a probabilistic study to explore rare or transitional events [54].

Few works have been carried out on protein models via a coarse-grained technique, although this approach allows the simulation of large systems over relatively long-time scales with respect to full-atomistic studies [41, 42, 55]. Dissipative Particle Dynamics (DPD) uses simplified soft potentials and coarse-grained representations of modeled structures [40–42]. In contrast to MD, in DPD systems the intended physical properties are determined by means of parameter calibration. One of the most popular methods of calibration is based on mapping onto Flory–Huggins theory [42]. Another approach is to couple DPD with MD simulations to calibrate models by matching the structural data from the atomistic simulations [56–58]. Previous DPD studies investigated the adsorption of semi-flexible rod-like objects [59], conformation changes [60] or the folding of small proteins [61]. However, all computer molecular techniques have been successfully employed in the modeling of interfacial systems and in the calculation of the surface tension when an amphiphilic non-protein molecule acts as a surfactant [62–65]. Moreover, DPD is well-suited for modeling multi-component systems such as emulsions, and it has been used in a number of studies to look at the effect of adsorbed molecules on the stability of oil or water droplets in emulsions [31, 66–68]. These have mainly been carried out on hydrocarbon oil emulsions with synthetic copolymers as the adsorbing molecules, but the methodology and the general results are relevant also for food emulsions.

The adsorption mechanism of proteins at fluid interfaces is significantly different from that of common surfactants, such as non-ionic single-chained amphiphilic molecules with a hydrophilic head and a hydrophobic tail [69–76]. In particular, a common feature of all protein surfactants is the typical S-shaped trend of the surface pressure at increasing protein surface concentration [71–73]. Among other purposes, the thermodynamic model of protein adsorption was successfully employed to evaluate the protein adsorption energy at fluid interfaces from experimental data [69, 74].

Among molecular techniques, Dissipative Particle Dynamics (DPD) is a well-established method for simulating soft matter systems at the mesoscale level of description [40–42]. DPD is a coarse-graining technique designed for modeling various fluid systems. For example, this method has been used to simulate particulate suspensions [77–79], microfluidic systems [80], polymer solutions [81, 82], and interfacial systems [62–65, 83–85]. These last systems have been largely investigated by means of DPD due to its remarkable applications to industrial cases, such as for food engineering research [31, 66–68, 83]. Indeed, DPD has been successfully employed to analyze both static (most notably phase diagrams and interfacial tension calculations) [62, 82, 83, 86] and dynamic properties (such as transport processes) [43], even with amphiphilic and protein molecules acting as surfactants [62–65, 83, 84].

Initially, DPD was developed to be a truly mesoscopic method, in which both hydrodynamics and thermal fluctuations have a role. In fact, it was considered capable to bridge the whole gap between the atomistic scale, which is accessible by Molecular Dynamics (MD) simulations, and the macroscopic scale, investigated by the continuum modeling approach [42]. Recent works have seen this ambition of DPD being deeply discussed and developed [87]. It was shown that by using a top-bottom approach, i.e., starting from continuum description going to the mesoscale, it is possible to obtain a thermo-fluid dynamic consistent method, which includes both hydrodynamics and thermal fluctuations at lower scales. This method is referred to as Smoothed Dissipative Particle Dynamics (SDPD) [88, 89] since it combines Smoothed Particle Hydrodynamics (SPH) and DPD in a way that respects the fluctuation-dissipation theorem through the so-called GENERIC formalism [88, 89]. The main features of this method are the prescription of bead volume and transport properties, which are now input parameters of the simulation, rather than undefined or output values as in classical DPD. Moreover, a lot of effort has been put into addressing many issues of classical DPD, like the resulting unrealistic Equation of State with Many-Body Dissipative Particle Dynamics (MDPD) [90], the influence of temperature with Energy-Conserving Dissipative Particle Dynamics (EDPD) [91], and the lack of all possible friction forces between beads with Fluid Particle Method [92]. Speaking instead of the bottom-up approach to mesoscale, the theoretical framework to link the atomistic description and DPD has been recently established through the Mori-Zwanzig projection theory (MZ-DPD), which works very well for bonded atoms-molecules but not so well for unbonded interactions, which are very important in fluid systems to describe transport phenomena like diffusion [87]. Mainly due to this reason, together with the complexity of the newer DPD methods, classical DPD is still used nowadays by the scientific community, as it is a simpler and computationally cheaper method compared to more rigorous ones, with the caveat that all the parameters must be tuned every time a new system and the corresponding properties of interest are investigated.

In classical DPD the governing equations are usually expressed in reduced units, which means that the same equations represent a whole family of physical systems [42]. In the works Refs. [93, 94], Füchslin *et al.* and Arienti *et al.* showed that physical properties such as the mass density and the compressibility of a system can be invariant with respect to a specific choice for model parameters, that one can associate to the level of coarse-graining. In the work Ref. [95], it is applied a similar reasoning also for the viscosity and the Schmidt number.

When applying the appropriate scaling procedure, it was established that a single set of parameters expressed in reduced units represents systems at arbitrary length scales [92–94], even for bonded interactions [96, 97]. Such scale independence reported for bulk fluid interactions can hold because the energy associated with an individual particle is made proportional to the number of molecules it represents [93]. On the other hand, surface-dependent interaction parameters may be expected to vary with the level of coarse-graining. In fact, assuming a system that exhibits domain formation, it is physically plausible that those interaction parameters effectively shrink with an increase in the level of coarse-graining. However, if a DPD calculation can be performed at a small scale, then calculations at larger scales will also be feasible, at least with respect to the scaling of parameters [93].

At intermediate (mesoscopic) length scales, another approach can be used to describe fluid properties, and it utilizes the Lattice-Boltzmann equation [98]. This equation can be thought of as a reduced form of the Boltzmann equation, where the motion of the particles is discretized so that they are confined to a lattice and are only able to move in a limited number of possible directions, thus restricting the number of degrees of freedom. Since the particles are represented as probability distribution functions, the individual lattice points should not be thought of as being populated by individual particles, but by distributions of particles. Therefore, the Lattice-Boltzmann model (LBM) describes the fluid as being composed of particles that move according to two terms, one of which describes the streaming (movement) of particles and the second takes account of the changes to the probability distribution function that occur when particles collide. The LBM is in effect a way of solving the Navier–Stokes equation in a simplified fashion. Since the LBM considers particles, it is suitable for studying multi-component systems such as oil-water-surfactant ones where interfacial effects are critical [31]. It is in this particular area of multiphase flow and structural properties that LBM is likely to be of particular use in the modeling of food systems. Indeed, LBM has been applied to emulsion systems that have relevance to food. It was used to investigate the transition from a bijel (bicontinuous interfacially jammed emulsion gel) to a Pickering stabilized emulsion, by varying the particle concentration, contact angle, and the ratio of the oil and aqueous phases [99].

The phase field model has been implemented in the LBM framework [100–102]. This method can resolve the interface structure via an appropriate free energy functional, showing great potential to simulate the multiphase flow problems [100, 103, 104]. In the phase field model, the free energy not only determines the equilibrium properties but also strongly influences the dynamics of the multiphase system. Moreover, this model has shown promising results for the computation of binary mixture with surfactants [100–102, 105]. Although both DPD and LBM have been successfully employed in modeling mesoscopic systems, they are conceptually different. Therefore, a comparison between a generalized phase-field model in the LBM framework and DPD can provide valuable insight for simulating realistic oil-water-surfactant systems.

Mayonnaise, the food emulsion investigated in this work, is made of a continuous aqueous phase and a dispersed phase with high content of oil. The stability of the dispersion is provided by molecules present in the egg yolk that act as surfactants and accumulate at the oil-water interface preventing the coalescence of the oil droplets [6, 7, 12, 13, 106]. The droplet size distribution (DSD) is the most important property of the emulsion since the structure, stability, taste, and color of the final product depend on the DSD [6, 7, 12, 13, 106]. The DSD in turn depends on the emulsion composition, the type of process, and the operating conditions under which the production process operates [107]. In general, the production of emulsions is based on mixing the ingredients and applying suitable mechanical energy to the emulsion for promoting droplet formation and breakage, in order to reach the desired DSD. A typical mixing process is composed of two steps: first, the ingredients (mainly egg yolk, vinegar, oil, water, and salt) are mixed together in large stirred vessels at moderate rotational speed; then, this premixed emulsion is fluxed into a high-shear device [6, 7]. Several high-shear devices are used in the process industry [108–110], and for emulsions, a popular option is the cone mill mixer, where the oil droplets undergo breakage until the final DSD is reached [6, 7, 106]. This last step is crucial to fine-tune the DSD, in order to determine the properties of the final product.

A typical cone mill mixer is constituted of a solid conical frustum rotor inside a slightly larger stator of the same shape, forming a small gap in which the emulsion flows and experiences high shear stresses, due to the high rotational speed of the rotor. The emulsion, before transiting through the high-shear region, flows into a pre-mixing chamber, followed by a post-mixing chamber [6, 7].

Over time several attempts to model the DSD of mayonnaise have been made [6, 7, 106, 111, 112], but there are still many issues that need to be completely understood. For example, in the range of shear stresses developed inside the cone mill, highly concentrated emulsions show non-Newtonian dynamics, depending on both the oil content and the DSD, that need to be accounted for [6, 113]. In addition, when processing very viscous liquids the cone mill operates in the laminar regime; however, a simple Poiseuille-Couette flow field can undergo a transition to the Taylor-Couette regime above a critical operating condition [114–118], where counter-rotating toroidal vortices (also known as Taylor vortices) appear. Since the transition to Taylor vortices depends strongly on the geometry of the system [114] and the contribution of the axial flow component that has a stabilizing effect on the formation of these instabilities [119], a detailed flow field analysis must be carried out in order to predict the occurrence of these peculiar flow patterns. Previous modeling efforts focused on the high-shear zone in the cone mill [6, 7, 106], while the role of the pre- and post-mixing zones, before and after the high-shear region, was not investigated in details. Moreover, the influence of the local type of flow on drop breakage, namely pure-shear versus elongational, is not completely clear.

1.1 Aim and structure of the thesis

Within the multiscale framework, different time- and space- scales are here investigated to describe the modeling approach from the molecular scale (oil-water interface) to the macro-scale (production device), as shown in Figure 1.2. As already mentioned, several physical-chemical aspects are involved in the food emulsion

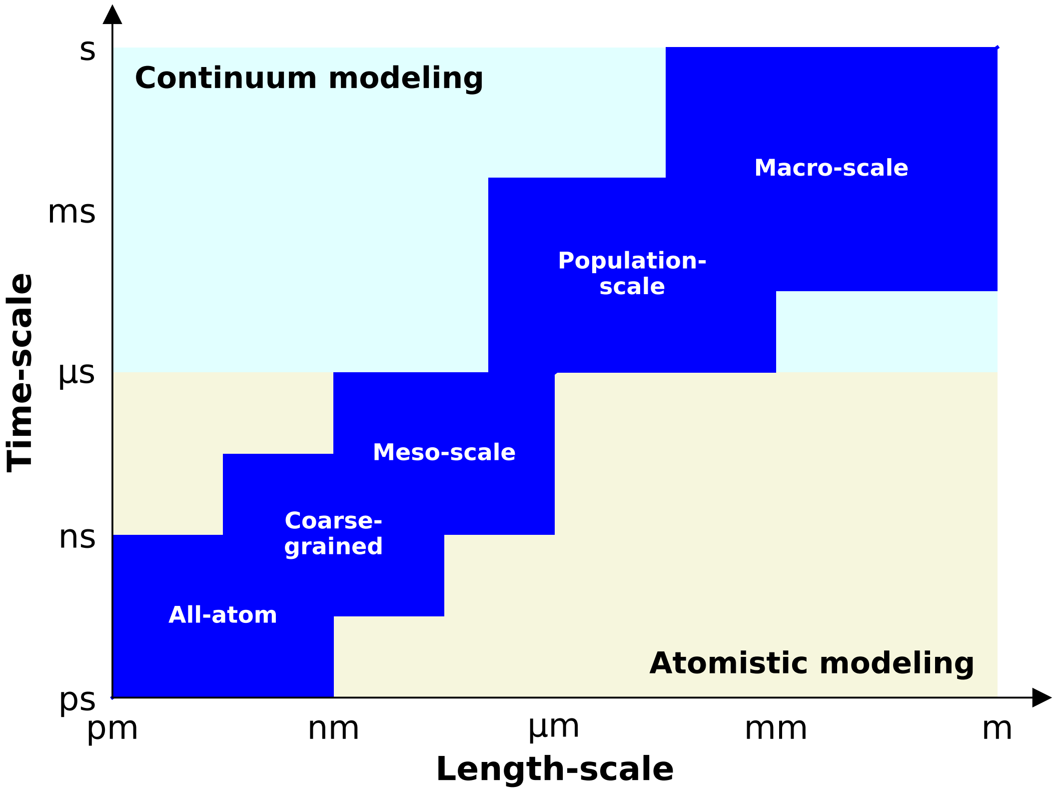

Fig. 1.2 Schematic representation of the different scales investigated in this work.

production process. Each of them can be studied by means of a specific modeling technique based on the scale investigated. Therefore, in this work, we aim to develop a computational model to simulate the production process with a multiscale approach in order to achieve a general and complete description of a food emulsion.

According to the multiscale nature of this work, each chapter of the thesis is dedicated to a particular scale. Hence, the scope, methods, and aspects investigated at each scale are summarized in the following.

Chapter 2 focuses on assessing the emulsifying properties of one of the most surface-active egg yolk proteins, the so-called Apovitellenin I, and any potential cooperative or competitive behavior in presence of co-surfactants (phospholipids). To do so, molecular simulations were carried out in a liquid-liquid interfacial system, consisting of water and soybean oil, with varying concentrations of phospholipids and for different spatial configurations. To evaluate the conformational stability of the protein at the water-oil interface, the Gibbs free energy was computed from metadynamics simulations as a function of the distance from the interface and of the radius of gyration. Moreover, a detailed analysis was also performed to determine which peptide residues were responsible for the protein adsorption at the oil-water interface, as well as the lowering of the surface tension.

Chapter 3 presents a molecular model of an oil/water interfacial system where the emulsifier is the egg yolk protein Apovitellenin I. Dissipative Particle Dynamics (DPD) was here adopted in order to simulate large systems over long time scales when compared with full-atom molecular dynamics (MD). Instead of a manual assignment of the DPD simulation parameters, a fully-automated coarse-graining procedure was employed. The molecular interactions used in the DPD system were determined by means of a parameter calibration based on matching structural data from atomistic Molecular Dynamics (MD) simulations. Despite the little availability of experimental data, the model was designed to test the most relevant physical properties of the protein investigated. Protein structural and dynamics properties obtained via MD and DPD were compared highlighting the advantages and limits of each molecular technique. Promising results were achieved from DPD simulations of the oil/water interface. The proposed model was able to properly describe the protein surfactant behavior in terms of interfacial tension decrease at increasing protein surface concentration. Lastly, we combined the above-mentioned results into a thermodynamic model to predict the interfacial tension behavior at increasing protein bulk concentration, which cannot be measured experimentally.

Chapter 4 focuses on the applications of a scaling scheme to interfacial systems as being one of the most successful uses of the classical DPD method. In particular, equilibrium properties such as the interfacial tension were analyzed at different levels of coarse-graining for planar oil-water interfaces with and without surfactant. A scaling factor for the interfacial tension was found due to the combined effect of the scaling scheme and the coarse-graining parameterization. Although the level of molecular description was largely decreased, promising results showed that it is possible to conserve the interfacial tension trend at increasing surfactant concentration, remarkably reducing modeling complexity. The same approach was also employed to simulate a droplet configuration. Both planar and droplet conformations were maintained, showing that typical domain formations of multi-component systems can be performed in DPD by means of the scaling procedure. Therefore, we explored the possibility to describe oil-water and oil-water-surfactant systems in standard DPD using a scaling scheme with the aim to highlight its advantages and limits.

Chapter 5 focuses on numerical simulations of two immiscible fluids in the presence of soluble surfactants via mesoscopic approaches, namely Lattice Boltzmann Model (LBM) and Dissipative Particle Dynamics (DPD). In this case, the surfactant was modeled as a typical non-ionic single-chained amphiphilic molecule with a hydrophilic head and a hydrophobic tail. Within the LBM framework, both the thermodynamic and hydrodynamic description of a realistic ternary system consisting of oil, water, and surfactants is represented by the phase-field model. Based on a DPD study, LBM simulations were performed to compare the two mesoscopic models in terms of reducing the interfacial tension at increasing surfactant concentration. Hence, the equilibrium properties were analyzed to check if the LBM approach can describe the same outcome of DPD simulations with the aim of finding a possible link between the molecular and continuum modeling approaches.

Chapter 6 is dedicated to modeling the last step of the food emulsion production process via computational fluid dynamics (CFD) and population balance modeling (PBM), to properly describe both the non-Newtonian dynamics of the emulsion and the evolution of the droplet size distribution (DSD). 2D and 3D CFD simulations showed that attention should be paid to the grid resolution to properly describe recognizable patterns observed in experiments. Moreover, CFD and PBM simulations clarified the role of the pre- and post-mixing zones in the high-shear mixer, as well as the effect of the type of flow, pure shear vs elongational, on droplet breakage.

Finally, in chapter 7 the main conclusions of this thesis are drawn, together with the final remarks.

Chapter 2

Atomistic model

2.1 Introduction

The main objective of this chapter is to study the interaction of Apovitellenin I at the water-oil interface, in the presence and absence of phospholipids using Molecular Dynamics and Metadynamics techniques. Therefore, with the help of an atomistic model and a statistical analysis, the main novelty is to provide a better understanding of the adsorption behavior at the oil-water interface of an egg yolk protein and its interactions with other co-surfactants. Moreover, the adsorption energy of the Apovitellenin I at the oil/water interface was here obtained from Metadynamics simulations. This information will be then transferred to a thermodynamic model of protein adsorption, in which the parameter calibration will be based on results obtained by means of coarse-grained molecular simulations. Thus, a link between the two scales can be achieved (see chapter 3 for more details).

This chapter is structured as follows: in section 2.2, the molecular description of the investigated system is presented; the molecular techniques here used are briefly introduced in section 2.3; simulation details are explained in section 2.4, together with all the approximations and hypothesis; section 2.5 shows the results of this chapter, and, finally, the main conclusions are drawn in section 2.6.

2.2 Molecular description of the macroscopic system

The first step in the development of the molecular model for an egg yolk protein-based emulsion is to identify the chemical species to be simulated and to define the characteristics of the molecules involved at the interface. In this section, a general description of the macroscopic system to be modeled is provided, together with the adopted simplifications.

As already mentioned, an example of a food emulsion where the egg yolk is widely used as an emulsifier is mayonnaise. This is a stable liquid-liquid emulsion with a high content of the dispersed oil phase. Although the general composition consists of oil, water, surfactants, and other additives, in the food industry there are several types of mayonnaise according to the nature of each component [12]. In this work, a regular mayonnaise with around 70% of fat content [12] is considered and the experimental work Ref. [7] is used as a reference to identify the ingredients of the mayonnaise, especially the molecules to play a primary role at the oil/water interface. It is important to highlight that also in this work the dispersed phase consists of soybean oil, while the chemical species that act as surfactants are derived from the egg yolk. These two components characterize the specific type of mayonnaise studied, therefore a further description of the vegetable oil and the egg yolk used in the production of the food emulsion is presented in order to correctly select the molecules to be modeled.

Regarding the dispersed phase, a fully refined soybean oil is employed in which the triglyceride molecules are present with a concentration larger than 99%, and all of the free fatty acids and other non-oil material has been removed by chemical means, and physical or mechanical separation [3]. Triglycerides are tri-esters consisting of glycerol bound to three fatty acid molecules. Based on the number of double bonds and the chain length, the fatty acids occurring in triglycerides of soybean oil are reported in Table 2.1. As can be seen, they are saturated, monounsaturated, and polyunsaturated with 16 or 18 carbon atoms according to the internal distribution [3]. For the sake of simplicity, here homo-triglycerides are taken into account where the three fatty acids are identical (without an internal distribution). Therefore, the triglyceride composition reported in Table 2.1 will be modeled as representative of the oil phase, instead of hydrocarbons as it was done in previous works on similar emulsions [66–68]. It should be noted that the protein adsorption to different hydrophobic materials may cause differences in the conformation of the adsorbed

Table 2.1 Experimental fatty acid distribution of soybean oil [3].

Fatty acid	***chain length : n. double bonds***	**Experimental weight fraction, %**
Palmitic acid	16:0	10.75 ± 2.75
Stearic acid	18:0	3.7 ± 1.7
Oleic acid	18:1	23.5 ± 6.5
Linoleic acid	18:2	53.5 ± 5.5
Linolenic acid	18:3	7.75 ± 3.25

molecule; in this sense, this simplification may have an impact that is difficult to quantify. That being said, it is known that modeling a simpler hydrocarbon–water system instead of a triglyceride–water system might not necessarily lead to realistic results [120], therefore a triglyceride–water system was modeled in this work.

The second fundamental component in mayonnaise production is the hen egg yolk. It is unquestionably an efficient ingredient in many food products as it combines nutritional, organoleptic and functional properties (emulsifying, coagulating, and gelling properties). Consequentially, egg yolk is widely used as an ingredient in many food emulsions [12, 121]. Hen egg yolk is an ideal example of natural supramolecular assemblies of lipids and proteins with different organization levels. It is mainly composed of two fractions – plasma and granules – which are natural nano- and micro-assemblies [1]. These two fractions possess different compositions, structures, and functionalities. Plasma contains a large number of lipids structured as low-density lipoproteins (LDLs), whereas granules are mainly composed of proteins aggregated in micrometric assemblies [1]. If plasma is responsible for the important emulsifying properties of yolk, granules bring interesting emulsifying properties when assemblies are in the form of micelles in presence of salts [122]. Assuming a pH equal to 3.8 for the mayonnaise [123], plasma proteins represent about 2/3 of the oil/water interface in acidic conditions (at all ionic strengths) [1]. Although plasma exhibits better emulsifying activity than granules, the latter may play a role in the mayonnaise stabilization providing a physical barrier to coalescence by microparticles of egg yolk granules adsorbed at the emulsion droplet interface [13, 124]. Indeed, in the work Ref. [125], it was concluded that the interfacial film in mayonnaise is composed of coalesced low-density lipoproteins and microparticles of granules. Previous works have shown that LDLs are likely to play primary roles in the formation and stabilization of egg yolk-based emulsions [1, 122, 126–128]. Consequentially, LDLs are considered to contribute mainly to yolk emulsifying properties [1]. LDLs are spherical nanoparticles (17–60 nm) with a lipid core of triglycerides and cholesterol esters in a liquid state surrounded by a monofilm of phospholipids and apoproteins [1, 19, 20, 121, 129–131]. The LDL adsorption mechanism at the oil-water interface was investigated by several works [1, 19, 22, 132–134]. LDL particles break down when they come into contact with the oil/water interface. Neutral lipids, phospholipids, and apoproteins are then released from the LDL core and can spread at the interface. Liberated triglycerides merge with the oil phase whereas phospholipids and apoproteins compete to adsorb at the oil-water interface. The liberated apoproteins are supposed to be totally insoluble and the adsorption process is almost irreversible. Therefore, LDLs serve as vectors of surfactant constituents (proteins and phospholipids) that could not be soluble in water until they reach the interface. Moreover, apoproteins situated on the LDL surface initiate the LDL disruption mechanism by their initial anchorage. This anchorage causes an unfolding of the LDL particle, leading to the destabilization of the external layer of the lipoprotein. The adsorption of apoproteins and phospholipids at the interface leads to the formation of a film that stabilizes the emulsion [132]. Therefore, both apoproteins and phospholipids are essential to understand the interfacial properties of egg yolk LDLs. The protein identified as Apovitellenin I is considered to be the most surface-active, among the apoproteins contained in LDL [19, 20]. Due to its structure and composition, which combines amphipathic character and flexibility, Apovitellenin I shows a great capacity to adsorb at the oil–water interface in emulsions [19]. In LDL, Apovitellenin I is mostly present as a homo-dimer, thus containing two identical polypeptide chains of 82 amino acid residues which are linked by a single disulfide bond at the cysteine residue [19, 20]. The sequence of the mature protein is available in the UniProtKB database [135] under the accession number P02659 (www.uniprot.org/uniprot/P02659). However, the detailed 3D structure and other physico-chemical information of Apovitellenin I are not available in the literature, increasing the complexity of its modeling approach.

2.3 Theoretical Background

In this section, the theoretical basis of the two main techniques adopted will be explained, giving more space for the discussion on MetaD since the theoretical concepts behind MD are well known. Regarding MetaD, more emphasis will be given to the Well-Tempered Metadynamics (WTMetaD) which is the specific technique adopted in this chapter.

2.3.1 Molecular Dynamics

Molecular Dynamics (MD) is a well-known computer simulation technique to mimic the motion of atoms, particles or molecules from which physicochemical properties (thermodynamic and structural) can be derived. Here only the main basic concepts are presented and a further detailed description can be found in the literature [38, 136].

All classic MD simulation methods rely on so-called force fields [137–140] to calculate interactions and evaluate the potential energy of the system as a function of pointlike atomic coordinates. A force field consists of both the set of equations used to calculate the potential energy and forces from particle coordinates, as well as a collection of parameters used in the equations. All common force fields subdivide potential functions into two classes. Bonded interactions cover covalent bond-stretching, angle-bending, and torsion potentials when rotating around bonds, all of which are normally fixed throughout a simulation. The remaining non-bonded interactions consist of Lennard-Jones repulsion and dispersion as well as Coulomb electrostatics. Given the potential and force (negative gradient of potential) for all atoms, MD is performed by integrating Newton's equation of motion. Therefore, this technique is deterministic. Indeed, by calculating the forces on each atom in a system, a prediction of the displacement of the atoms during a given time interval can be made and a trajectory of the system followed over time. In MD simulations, displacement of atoms is carried out over small time steps, typically 1 to 2 fs. Compared to the average time between molecular collisions, the size of the time step is extremely small because it is necessary to ensure that the magnitude of the force on the moving particle does not change significantly when the particle moves. The main limitation of this technique is that a huge number of computations have to be carried out to model events on timescales relevant to pertinent physicochemical phenomena using a sufficiently high number of molecules to accurately represent these phenomena. Consequentially, powerful computers and relatively long computation times are required to model even relatively simple molecular processes.

Hence, MD is a computational technique to study the evolution in time of a system made of point atomistic particles. There are basically two foundations on which MD rests: the ergodic theorem and Newton's equation for a system of fully atomistic molecules [141]. The system is therefore treated at the atomistic level, considering the interactions between each atom and the ones surrounding it. This presents a limitation since quantum mechanics correctly describes the physical behavior of a microscopic system and not classical mechanics. Until now, there are few computational tools powerful enough to solve the Schrödinger equations for a system containing a large number of molecules (order of thousands). In any case, solving Newton's equations turns out to be a good compromise between the computational cost and the prediction of system properties. Therefore, the main equation is Newton's equation of motion (Eq. (2.1)), solved during the MD simulation by means of Verlet's algorithm, a time integration that guarantees good numerical stability and time reversibility [142, 143].

$$\boldsymbol{F} = m\frac{d^2\boldsymbol{x}}{dt^2} = -\nabla E \ . \tag{2.1}$$

The energetic term E is the sum of four different contributions, as shown in Eq. (2.2): bonding (Eq. (2.3)), torsional (Eq. (2.5)), vibrational (Eq. (2.4)), and long-range energy (Eq. (2.6)) [143], in turn, formed by Coulomb and van der Waals interactions [144, 145]:

$$E = E_{ab} + E_{torsion} + E_{angles} + E_{bonds} \ , \tag{2.2}$$

$$E_{bonds} = \sum_{bonds} K_r\left(r - r_{eq}\right)^2 \ , \tag{2.3}$$

$$E_{angles} = \sum_{angles} K_\theta\left(\theta - \theta_{eq}\right)^2 \ , \tag{2.4}$$

$$\begin{aligned} E_{torsion} = \sum_i \frac{V_1^i}{2}\left[1 + \cos\left(\phi_i + f_1^i\right)\right] + \frac{V_2^i}{2}\left[1 + \cos\left(2\phi_i + f_2^i\right)\right] + \\ + \frac{V_3^i}{2}\left[1 + \cos\left(3\phi_i + f_3^i\right)\right] \ , \end{aligned} \tag{2.5}$$

$$E_{ab} = \sum_i^{on\ a}\sum_j^{on\ b}\left[\frac{q_i q_j e^2}{r_{ij}} + 4\varepsilon_{ij}\left(\left(\frac{\sigma_{ij}}{r_{ij}}\right)^{12} - \left(\frac{\sigma_{ij}}{r_{ij}}\right)^{6}\right)\right] f_{ij} \ , \tag{2.6}$$

where K_r and K_θ of Eqs. (2.3) and (2.4) are the elastic constants for bond and angular vibration, respectively, and $\left(r - r_{eq}\right)$ and $\left(\theta - \theta_{eq}\right)$, referring to the same equations, are the spatial and angular displacements with respect to the equilibrium condition, respectively. In Eq. (2.5), the terms V_1, V_2, and V_3, correspond to the Fourier coefficients of the series while ϕ represents the torsional angle and f_1, f_2, and f_3 represent the phase angles. Finally, the energy term for the non-bonding interactions of Eq. (2.6) is given by the Coulomb contribution added to the Lennard-Jones potential. It should be kept in mind that the Eq. (2.6) is also applied to atoms that are part of the same molecule but that are separated by three or more bonds. Also, $f_{ij} = 1$ in Eq. (2.6), except in the case where there is an intramolecular bond of type 1,4 where $f_{ij} = 0.5$.

The parameters to calculate these four contributions are contained in the force field and the choice of a specific force field with respect to another can profoundly influence the result of an MD simulation [38]. Other important and necessary approximations of MD are the Periodic Boundary Conditions (PBC) and the cut-off distance. Both of them have an influence on box construction. Applying PBC means that when a particle crosses a box face, with a certain velocity in modulus and direction, it reappears from the opposite face with the same velocity properties [146]. Instead, the cut-off is the maximum distance within which the interaction between two particles is considered [147]. The cut-off distance is also important in the Particle Mesh Ewald summation (PME) for the long-distance particle interaction [148–150]. More information regarding Molecular Dynamics can be found in the literature [37, 141, 143, 149, 151, 152].

2.3.2 Metadynamics

Unlike MD, MetaD is a technique used to force the system to explore states that would normally be energetically disadvantaged and that would require extremely long MD simulations. A Metadynamics simulation consists of a choice of one or more variables, depending on the spatial coordinates and called collective variables (CVs), which are forced to take on different values by the addition of a potential [153]. A possible form for the potential $V(\boldsymbol{s})$ can be expressed as [153]:

$$V(\boldsymbol{s}) = -\left(1 - \frac{1}{\gamma}\right) F(\boldsymbol{s}) \,, \tag{2.7}$$

where $F(\boldsymbol{s})$ is the free energy surface obtained from a classical MD simulation and $\boldsymbol{s}$ is the collective variable. The parameter γ is a constant, greater than 1, called bias factor. If γ tends to 1 the bias potential tends to 0 ($V(\boldsymbol{s}) = 0$), then, the MetaD simulation becomes equivalent to a classical MD simulation; in the limit case in which γ tends to $+\infty$ it is obtained that $V(\boldsymbol{s})$ tends to $-F(\boldsymbol{s})$ and each state is equally probable. At the end of the simulation, knowing the added potential for each collective variable, it is possible to perform a reweighting procedure to move the system from the biased to the unbiased ensemble. Therefore, it is possible to estimate the value of properties that depend on the spatial coordinates ($\langle O(\boldsymbol{r})\rangle$) of the unbiased ensemble by weighting each configuration obtained in the biased ensemble by the value of the bias acting on it [153–155]:

$$\langle O(\boldsymbol{r})\rangle = \frac{\langle O(\boldsymbol{r})e^{\beta V(\boldsymbol{s}(\boldsymbol{r}))}\rangle_V}{\langle e^{\beta V(\boldsymbol{s}(\boldsymbol{r}))}\rangle_V} \,. \tag{2.8}$$

In the previous equation, the term on the left without a subscript represents the value of the properties $\langle O(\boldsymbol{r})\rangle$ in the unbiased ensemble. Instead, all the terms on the right denoted by a subscript V are considered in the biased ensemble.

Well-Tempered Metadynamics

In a Well-Tempered Metadynamics simulation, it is performed the iterative builds of the bias $V(\boldsymbol{s})$. This one, iteration after iteration, will asymptotically take the form given by Eq. (2.7). This is made by the successive addition of small repulsive functions ($G(\boldsymbol{s},\boldsymbol{s'})$) that are deposited periodically in the CVs space. These have the form of a Gaussian centered in the CVs space at the current value $\boldsymbol{s'}$, as it is reported in Eq. (2.9) [153, 156, 157].

$$G(\boldsymbol{s},\boldsymbol{s'}) = We^{\|\boldsymbol{s}-\boldsymbol{s'}\|^2} \,, \tag{2.9}$$

where W is the height of the Gaussian and the term $\|\boldsymbol{s}-\boldsymbol{s'}\|$ represent the distance between $\boldsymbol{s}$ and $\boldsymbol{s'}$ in the CVs space. In this way, it is possible to calculate the bias potential as follows:

$$V_n(\boldsymbol{s}) = V_{n-1}(\boldsymbol{s}) + G(\boldsymbol{s},\boldsymbol{s}_n)e^{-\frac{1}{\gamma-1}\beta V_{n-1}(\boldsymbol{s}_n)} \,, \tag{2.10}$$

in which $V_0(\boldsymbol{s}) = 0$, β is the inverse temperature multiplied by the Boltzmann constant and the corrective term $G(\boldsymbol{s},\boldsymbol{s}_n)e^{-\frac{1}{\gamma-1}\beta V_{n-1}(\boldsymbol{s}_n)}$ decreases because the argument of the exponential goes to 0 like $1/n$, where n is the number of iteration. Each Gaussian is summed after a certain number of iterations N_G from the previous one. In this way, it is possible to explore some regions of the CVs space that normally are improbable in a classical MD simulation. At the end of a MetaD simulation, it is necessary to perform a reweighting procedure to obtain an energy function of one or more CVs in the unbiased system by applying Eqs. (2.11) and (2.12) [154, 155]:

$$\langle O(\boldsymbol{r})\rangle = \langle O(\boldsymbol{r})e^{-\beta[V(\boldsymbol{s}(\boldsymbol{r},t))-c(t)]}\rangle_V \ , \tag{2.11}$$

with:

$$c(t) = \frac{1}{\beta}\log\frac{\int e^{-\beta F(\boldsymbol{s})}d\boldsymbol{s}}{\int e^{-\beta(F(\boldsymbol{s})+V(\boldsymbol{s},t))}d\boldsymbol{s}} \ , \tag{2.12}$$

where β is the inverse temperature multiplied by the Boltzmann constant, $O(\boldsymbol{r})$ is a generic property depending on the spatial coordinates, $V(\boldsymbol{s}(\boldsymbol{r},t))$ is the deposited bias function of the collective variables, and $F(\boldsymbol{s})$ is the free energy surface obtained from an unbiased simulation. Further information about MetaD and other similar methods and variants can be found in the literature [54, 153, 156–159]. Once the value of the potential energy for each state explored by the MetaD simulation was obtained, it is possible to turn this information into a probability to find the system in a certain state with respect to others. According to statistical mechanics, the probability $p(E_i)$ is a function of energy and reads as follows:

$$p(E_i) = \frac{e^{-\beta E_i}}{\sum_i e^{-\beta E_i}} = \frac{e^{-\beta E_i}}{Z} \ , \tag{2.13}$$

where Z (*Zustandssumme*, "sum over states") represents the summation over all the states i explored by the system [160].

2.4 Model details

2.4.1 Approximations and hypothesis

In this section, all necessary hypotheses and approximations are presented and discussed, especially details of the chemical species involved in this work: protein, oil, water, and phospholipids. First, let us introduce some information about the protein under investigation: Apovitellenin I. As already stated, Apovitellenin I is a homo-dimer containing two identical polypeptide chains of 82 amino acid residues linked by a single disulfide bond at the cysteine residue in position 75 [161]. For further analyses, two applications were used: AlphaFold [162, 163] and H++ (http://biophysics.cs.vt.edu/H++) [164–166]. AlphaFold predicts different spatial structures for the protein, starting from its amino acid sequence. Each structure is associated with an index of prediction, called lDDT (Local Distance Difference Test), a superposition-free score that evaluates local distance differences of all atoms in a model. It varies between 0 and 100, indicating the accuracy of the prediction [167]. For this chapter, it was used the structure with the highest value of the index of prediction as shown in Figure 2.1. Moreover, it can be noticed that the region with the disulfide bond is correctly represented and predicted with the highest index than that of the rest of the molecule. The second application was used to predict the protonation state of each amino acid residue. By providing the primary structure and the pH value (here considered equal to 3.8), H++ returns the pKa for each amino acid in the protein. If the pH is less than the pKa then the functional group of the residue will be protonated, else it is deprotonated otherwise. This leads to a total charge for the protein equal to $+14\ e^{-}$.

For the oil phase, it was also necessary to assume some simplifications. In particular, the non-aqueous phase consists of soybean oil, and the fatty acid composition was already reported in Table 2.1. For the sake of simplicity, it was assumed that all the triglycerides contain only one type of fatty acid, namely without an internal distribution. In this way, the composition reported in Table 2.1 is considered as the weight fraction of triglycerides in the soybean oil. Hence, the number of molecules that composes the oil phase in the simulation box reflects such composition. All the information about structural conformation and topology for the triglycerides was obtained by using LigParGen (http://zarbi.chem.yale.edu/ligpargen/) [168–170].

As regards water, the TIP3P model was used. This model is characterized by a low computational cost, but it can not simulate the correct behavior of water at temperatures near 0 °C [171, 172]. A 50/50 volume ratio was assumed for the oil and water phases.

About the phospholipids, only POPC (1-palmitoyl-2-oleoyl-sn- glycero -3-phosphocholine) is taken into account in this work since it is identified as the

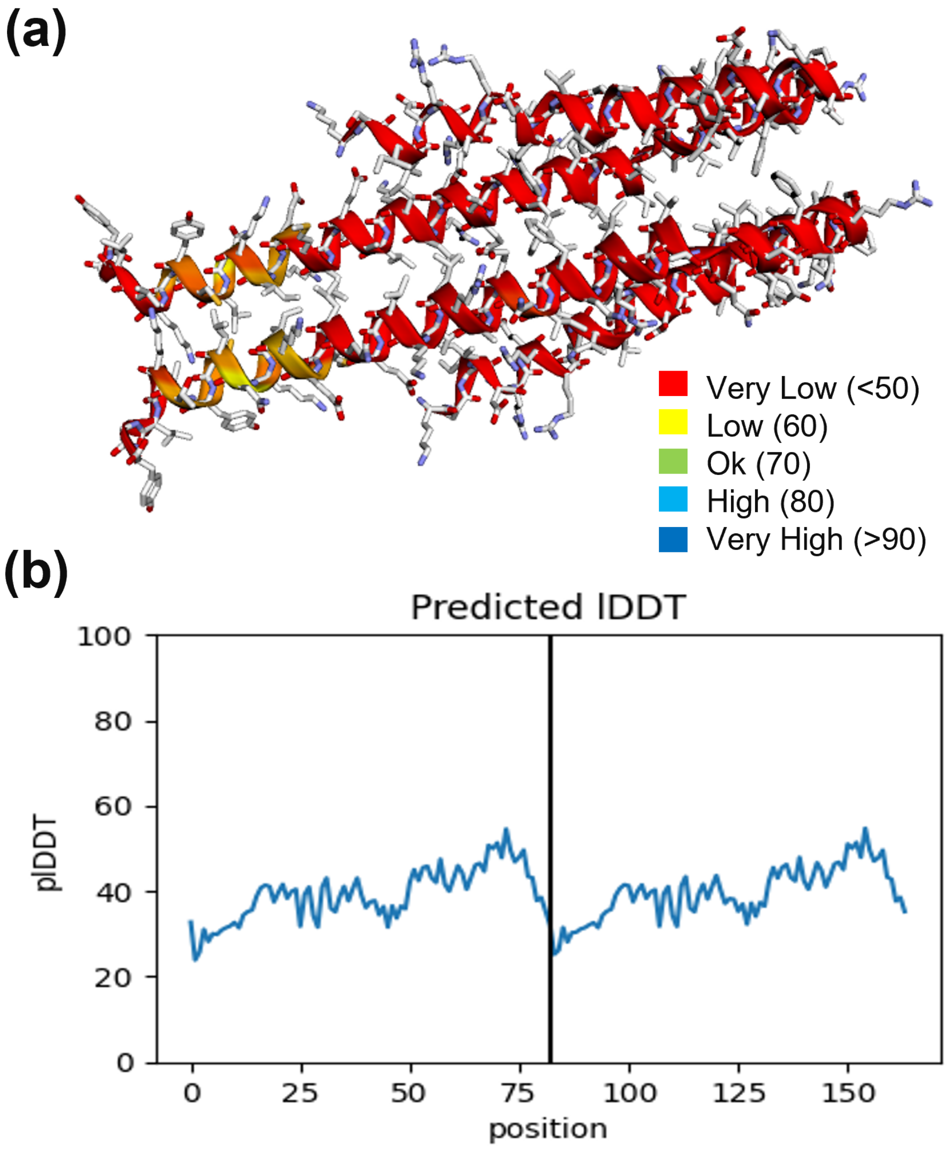

Fig. 2.1 Structure of the protein Apovitellenin I extracted from AlphaFold (a). Index of prediction for each amino acid residue (b).

Table 2.2 Details of systems investigated in this chapter together with box sizes.

Case	**Phospholipids**	**Dimension [nm]**		
		X	***Y***	***Z***
1	No phospholipids	12.15	24.30	12.15
2	Phospholipids in the water bulk, concentration equal to that found in egg yolk	12.15	24.30	12.15
3	Phospholipids at the interface, concentration equal to half of the saturation	11.70	23.40	11.70
4	Phospholipids at the interface, concentration equal to saturation	11.70	23.40	11.70

most abundant in the egg yolk [4, 5, 173]. The structural information regarding phospholipids can be obtained from the website Slipids (http://www.fos.su.se/~sasha/SLipids/) [173, 174].

2.4.2 Details of simulations

All the simulations were performed using GROMACS 20.6 [175–177] patched with Plumed 2.7.2 [178, 179]. All the systems were simulated using the Verlet list for the neighbor atoms with a cutoff of 1.0 nm and the PME [149, 150] for the electrostatic calculation. PBC were considered in all three directions. Since the protein has a non-zero net-total charge, an appropriate number of Cl^- ions was added to the system to assure electroneutrality. The MD simulations were performed as follows: the energy minimization of the system was first carried out, then, the equilibration step was divided into two stages: 100 ps in NVT (Isothermal–Isovolumetric ensemble) and 1 ns in NPT (Isothermal-Isobaric ensemble). The pressure was set equal to 1 bar by means of the Parrinello-Rhaman barostat [180], while the temperature was kept equal to 298 K through the Berendsen thermostat [181]. Finally, the MD production step was carried out with a time step equal to $\Delta t = 2$ fs for a total number of steps $N_G = 5 \times 10^7$. The OPLS-AA force field [145] was here employed to calculate the interactions between all the atoms in the system. Four cases were analyzed in this chapter as reported in Table 2.2, together with the corresponding box dimensions. To create the first system of Table 2.2, the oil phase was initially set up. Starting from a box with dimensions $X = Y = Z = 25.00$ nm, the five types of triglyceride molecules were randomly inserted in a number corresponding to the proportions of

Table 2.3 Mass fraction of proteins and phospholipids in the egg yolk [4, 5].

Fraction of LDL in the dried egg yolk (χ_{LDL})	0.66
Fraction of protein in LDL (χ_{P})	0.10
Fraction of lipids in the dried egg yolk (χ_{L})	0.63
Fraction of phospholipids in lipids (χ_{PL})	0.33
Fraction of phosphatidylcholines in phospholipids (χ_{PC})	0.76
Fraction of POPC in phosphatidylcholine (χ_{POPC})	0.154

Table 2.1. After the energy minimization and the equilibration steps, the box reached the dimensions $X = Y = Z = 12.15$ nm. Then, it was extended in the Y-dimension and a single protein molecule was placed in the center of the void phase. The remaining space was then solvated with water, thus creating the interfaces between oil and water. After that, fourteen molecules of water were replaced with an equal number of Cl^- ions. This system was used as the basis for the other three cases. For the second case, a sufficient number of water molecules were replaced with ten molecules of POPC. This choice was made by the calculation of the number of POPC molecules per protein ($N_{\mathrm{POPC}}/N_{\mathrm{P}}$), knowing the mass of each molecule [19, 20] (m_{P} is the protein mass and m_{POPC} is the POPC mass) and the mass fraction in the egg yolk (Table 2.3 and Eq. (2.14)) [4, 5].

$$\frac{N_{\mathrm{POPC}}}{N_{\mathrm{P}}} = \frac{\chi_{\mathrm{L}} \times \chi_{\mathrm{PL}} \times \chi_{\mathrm{PC}} \times \chi_{\mathrm{POPC}}}{\chi_{\mathrm{LDL}} \times \chi_{\mathrm{P}}} \times \frac{m_{\mathrm{P}}}{m_{\mathrm{POPC}}} = 9.05 \approx 10\ . \tag{2.14}$$

The value of $N_{\mathrm{POPC}}/N_{\mathrm{P}}$ was rounded up to compensate for possible approximation errors. In fact, the exact concentration of the Apovitellenin I is not known [19–21], so it was necessary to assume that all LDL proteins are molecules of Apovitellenin I. For the remaining two systems (Cases 3 and 4 of Table 2.2), the starting box was again the one used in Case 1 but with a smaller volume. This is due to the fact that, after the substitution of part of water and oil molecules with some POPC molecules, a void part remained in the box. Therefore, it was necessary to perform another equilibration step in an NPT ensemble in which the box volume was reduced to fill the void space with other molecules. The saturation concentration of POPC phospholipids at the water-oil interface is 0.635 nm^2/lipid [173]. Therefore, by knowing the superficial area of the interface, it is possible to calculate the number of phospholipid molecules to insert into the simulation box in order to have a concentration equal to half of the saturation (Case 3) and equal to the saturation (Case 4). It is important to remind here that there are two interfaces in each system due to the periodic boundary conditions in the three dimensions. Hence, the phospholipids were placed at each interface removing an equal volume of water and oil in order to keep a 50/50 volume ratio constant between the two phases. The phospholipids were already positioned in the correct orientation, with the polar part near the water phase and the apolar part near the oil phase. In summary, Figure 2.2 shows the snapshots of the four cases studied here.

About MetaD, the collective variables chosen for all the simulations are the protein radius of gyration, used as an index of the denaturation of the protein, and the distance between the protein center of mass and the oil phase. To reduce the computational cost, a further simplification was adopted: for computing the distance of the protein center of mass from the oil-water interface, each molecule of the oil phase was identified with a single atom of carbon. It was verified that the chosen carbon atom type was only present in oil molecules, not in phospholipids or protein molecules. In this way, the numerical density along the y-direction normal to the interfaces was compared for all the atoms of the oil phase and for the carbon atom chosen to represent the oil in order to guarantee the accuracy of this approximation, as shown in Figure 2.3. Thus, the oil phase was identified by a single atom belonging to each triglyceride molecule type, specifically the carbon of the carboxylic group of the central fatty acid residue. As shown in Figure 2.3, the two curves are coincident at the corresponding position of the two interfaces.

2.4.3 Model validation

In addition to the cases already described, another simulation study was conducted to validate the approach used in this chapter. As mentioned before, there is no experimental data in the literature concerning the isolated Apovitellenin I to compare the results obtained from our simulations. Therefore, the same approach was tested for a similar system whose details are available. In particular, the system described in the work Ref. [69] was reproduced and modeled with the same simulation parameters used for the case of Apovitellenin I. Therefore, for the sake of the comparison, the system consists of β-casein adsorbing at the air-water interface. The air phase is treated as a vacuum and the TIP3P model is used again for water [182]. The structure of β-casein was obtained from UniProtKB (code P02666, www.uniprot.org/uniprot/P02666). After checking the protonation state of the amino

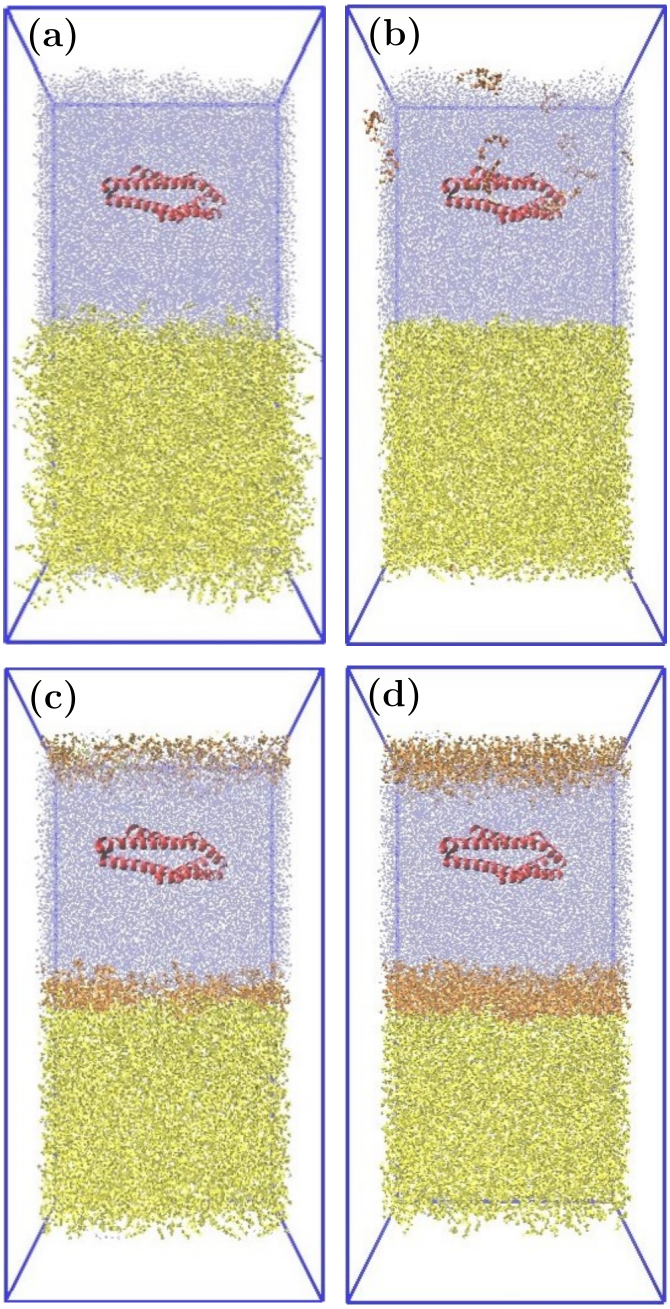

Fig. 2.2 Snapshots of the simulation boxes of the oil-water interfacial systems investigated here. For sake of better visualization, part of the solvent molecules was not shown (oil in yellow, water in blue, protein in red, and phospholipids in orange). (a) Case 1: no phospholipids; (b) Case 2: phospholipids in the water bulk at a concentration calculated from Eq. (2.14); (c) Case 3: phospholipids at the water-oil interface at a concentration equal to half of the saturation; (d) Case 4: phospholipids at the water-oil interface at a concentration equal to saturation.

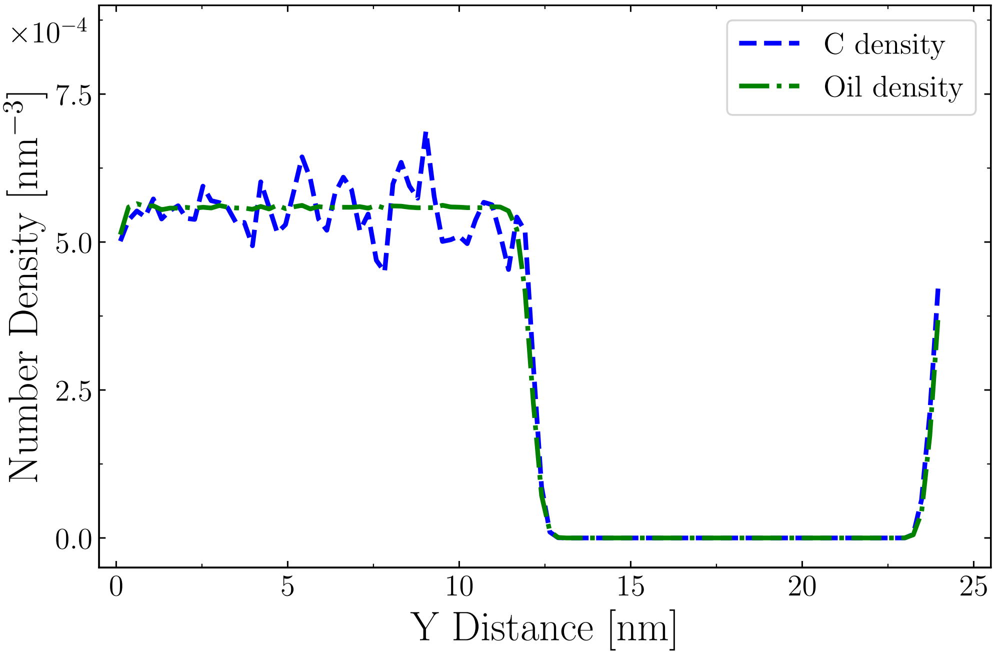

Fig. 2.3 Numerical density profiles of the single C atom (blue dashed line) and all atoms belonging to the oil phase (green dash-dotted line) along the *y*-direction normal to the interfaces.

acid residues with H++ at a pH equal to 7.4, the protein was placed at the center of the water bulk. The box construction was similar to the previous case of Apovitellenin I. Next, charge neutralization, energy minimization, and equilibration (1 ns in NVT ensemble) were conducted. The OPLS-AA force field was used again here. To maintain the water-air interface, instead of NPT, it was necessary to perform the simulation in the NVT ensemble by fixing the temperature equal to 23°C with the Berendsen thermostat. Regarding the metadynamics setup, the same parameters of the simulation of Apovitellenin I were used. Indeed, the two collective variables are the protein radius of gyration and the distance of the protein center of mass from the water-air interface. Since in this case the simulation was conducted in the NVT ensemble, the energy obtained from metadynamics is the Helmholtz free energy. One can switch to the Gibbs free energy ΔG_{ads} by applying the following expression [183]:

$$\Delta G_{ads} = \Delta F_{\text{MetaD}} = \left[-\frac{1}{\beta} \int_{y_a}^{y_b} e^{-\beta F_y(y)} dy \right] - \left[-\frac{1}{\beta} \int_{y_c}^{y_d} e^{-\beta F_y(y)} dy \right] , \tag{2.15}$$

where β is the inverse of the temperature multiplied by the Boltzmann constant, $F_y(y)$ is the Helmholtz free energy obtained from the metadynamics simulations along the y direction, and (y_a, y_b) and (y_c, y_d) are the adsorption and bulk region, respectively, which are arbitrarily chosen.

The convergence of the MetaD simulations for all the cases analyzed here is shown in Figure 2.4, where the variation of one of the CVs, namely the distance of the protein from the water-oil interface, is reported in the last 10% of the simulation time. Notably, it can be seen that the variation is quite modest, so all the simulations reached convergence. The meaning of the curves shown will be clarified in the next section.

2.5 Results and discussion

From the metadynamics simulations, the surface free energy was obtained for the four cases as varying the two collective variables: the protein radius of gyration and the distance between the center of mass of the protein and the oil-water interface, as shown in Figure 2.5. As can be seen, it is possible to have an overview of the collective variable space explored by each system during the simulations. The energy

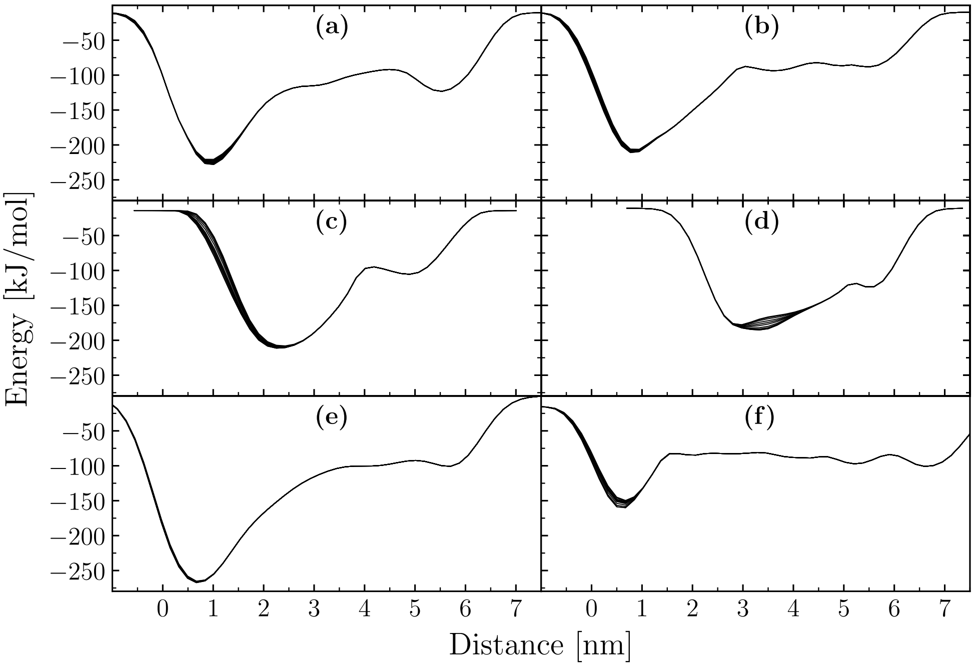

Fig. 2.4 Convergence of MetaD simulations: (a) system with only protein (bidimensional bias: distance from interface and radius of gyration); (b) system with protein and phospholipids in the bulk; (c) system with protein and phospholipids at the interface with a concentration equal to half of the saturation; (d) system with protein and phospholipids at the interface with a concentration equal to the saturation; (e) system with only protein (monodimensional bias: distance from the interface); and (f) β-casein simulation.

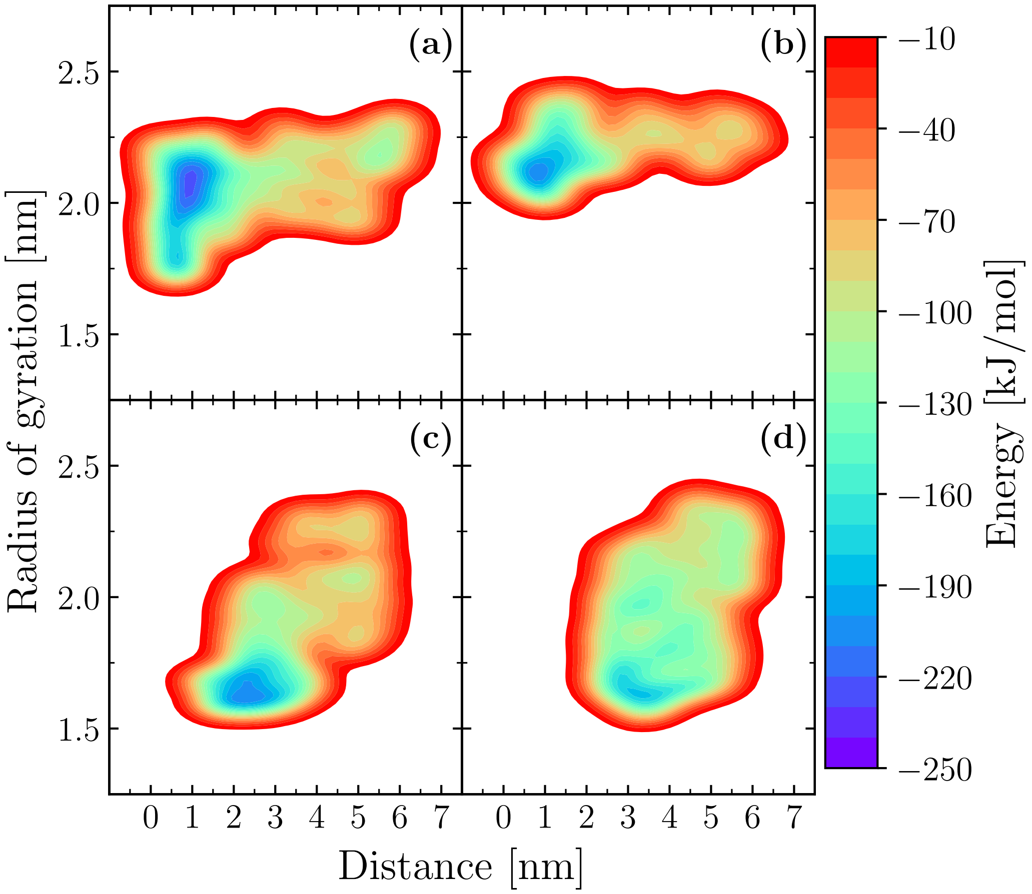

Fig. 2.5 Free energy surface for the four cases studied: (a) Case 1: no phospholipids; (b) Case 2: phospholipids in the water bulk at a concentration calculated from Eq. (2.14); (c) Case 3: phospholipids at the water-oil interface at a concentration equal to half of the saturation; (d) Case 4: phospholipids at the water-oil interface at a concentration equal to saturation.

in the Figure is Gibbs free energy because all the simulations have been conducted in the NPT ensemble. In order to have a clearer visualization, the probabilities associated with the various states were calculated as varying the distance (Figure 2.6) and the protein radius of gyration (Figure 2.7), according to the formula given in Eq. (2.13). As shown in Figure 2.6, it can be seen that the protein is fully adsorbed only in Cases 1 and 2. In fact, the highest peaks represent the most probable states of the system. It is important to underline here that the minimum distance is calculated considering the protein center of mass and not the closest atom to the oil-water interface. For this reason, the highest peak of probability is slightly shifted to values of the distance a bit larger than 0. In Cases 3 and 4, the highest probability peak is

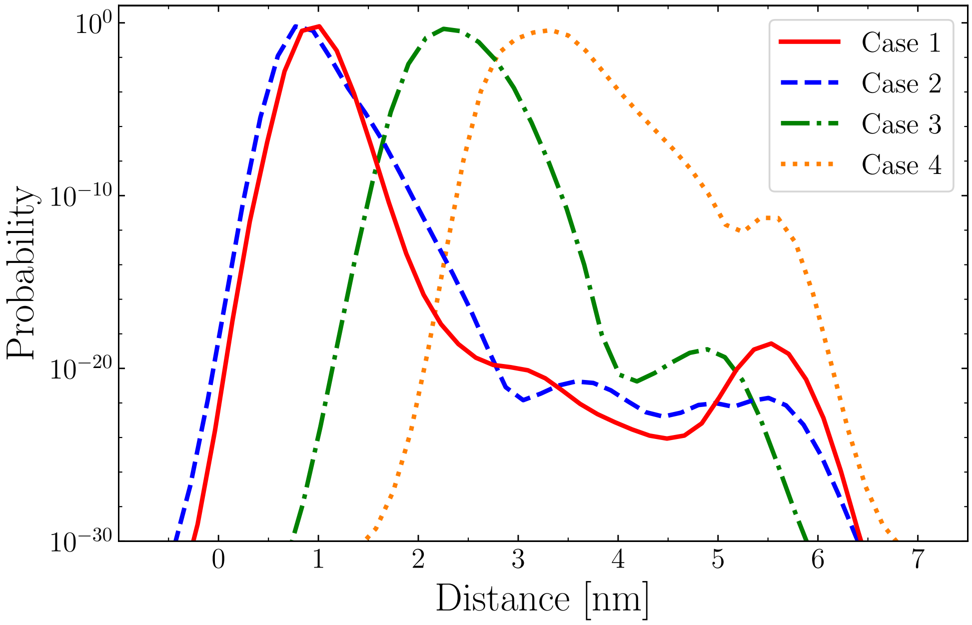

Fig. 2.6 Probability (logarithmic) at the variation of the distance from the oil-water interface: Case 1: no phospholipids (red continuous line); Case 2: phospholipids in the water bulk at a concentration calculated from Eq. (2.14) (blue dashed line); Case 3: phospholipids at the water-oil interface at a concentration equal to half of the saturation (green dash-dotted line); Case 4: phospholipids at the water-oil interface at a concentration equal to saturation (orange dotted line).

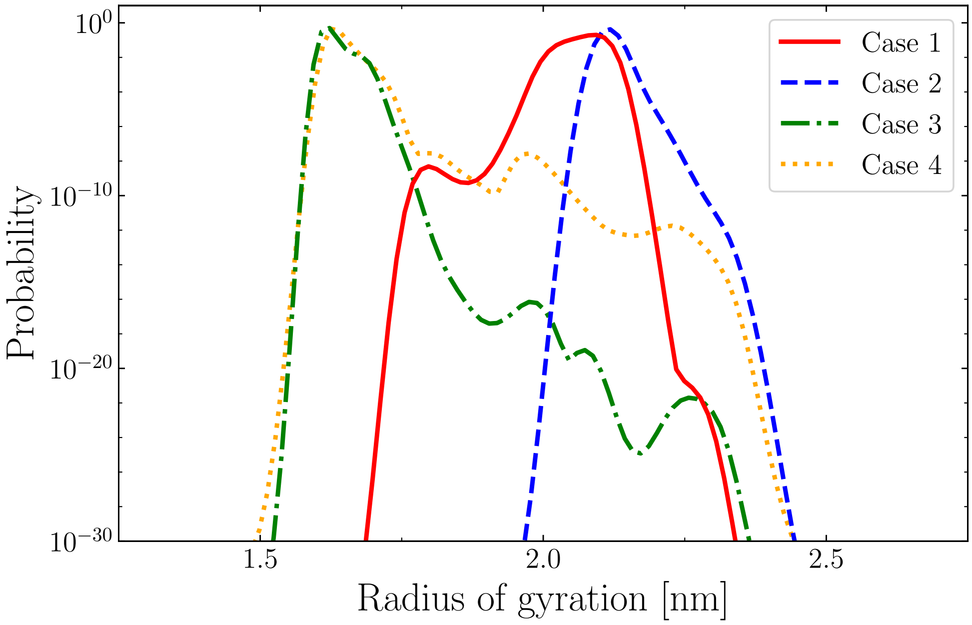

Fig. 2.7 Probability (logarithmic) at the variation of the protein radius of gyration: Case 1: no phospholipids (red continuous line); Case 2: phospholipids in the water bulk at a concentration calculated from Eq. (2.14) (blue dashed line); Case 3: phospholipids at the water-oil interface at a concentration equal to half of the saturation (green dash-dotted line); Case 4: phospholipids at the water-oil interface at a concentration equal to saturation (orange dotted line).

shifted to larger distances from the oil-water interface due to the steric hindrance given by the presence of phospholipids at the interface. Therefore, the protein positions itself near the oil-water interface without being able to completely adsorb. In fact, as can be noticed, the distance from the interface in Case 4 is larger than in Case 3. This is due to the fact that, in Case 4, there is a higher concentration of phospholipids at the interface, which hinders the adsorption of the protein even more than in Case 3. In addition, in Case 4 there is a higher probability to find the protein in the water bulk compared to Case 3 as indicated by the second-highest peak. The influence of the presence of free phospholipids in Case 2 is also compared to Case 1. By looking at Figure 2.6, the red continuous line (Case 1) and the blue dashed line (Case 2) have approximately the same trend for distances smaller than 3 nm. On the other hand, in Case 2 the presence of phospholipids makes the energy and probability profiles smoother, thus the peak in the water bulk at a distance from the interface of 5.5 nm is not present as in Case 1. This is shown in detail in Figure 2.8, where the protein energy profiles of Cases 1 and 2 are represented as a function of the distance from the interface. From these profiles, the protein Gibbs free energy of adsorption ΔG_{ads} at the oil-water interface can be estimated as the difference in the values of the energy associated with the protein at a distance close and far from the interface as reported in Figure 2.8. Therefore, the presence of free phospholipids affects the absolute value of ΔG_{ads}. In fact, for Case 1 $\Delta G_{ads} = -108.18$ kJ/mol, while ΔG_{ads} becomes equal to -122.71 kJ/mol for Case 2, meaning that the presence of free phospholipids in water bulk makes the protein adsorption even more likely to occur in Case 2 rather than in Case 1. However, these values of ΔG_{ads} seem to be reasonable for protein surfactants [184]. The presence of phospholipids in the water bulk has also an effect on the protein radius of gyration as shown in Figure 2.7 (red continuous line and blue dashed line). Both cases have the same highest probability peak at the value of the radius of gyration equal to 2.125 nm, but, when the phospholipids are not present (Case 1) the protein can explore a wider range of values for the radius of gyration. As regards the phospholipids at the interface (Cases 3 and 4), it can be seen that the protein which cannot fully adsorb at the interface has a most probable value of the radius of gyration smaller than that of Cases 1 and 2. This is most likely related to the fact that the protein molecule becomes smaller trying to penetrate the phospholipid layer. In Case 4 (Figure 2.7, orange dotted line) with phospholipids at the interface with the concentration of saturation, the protein

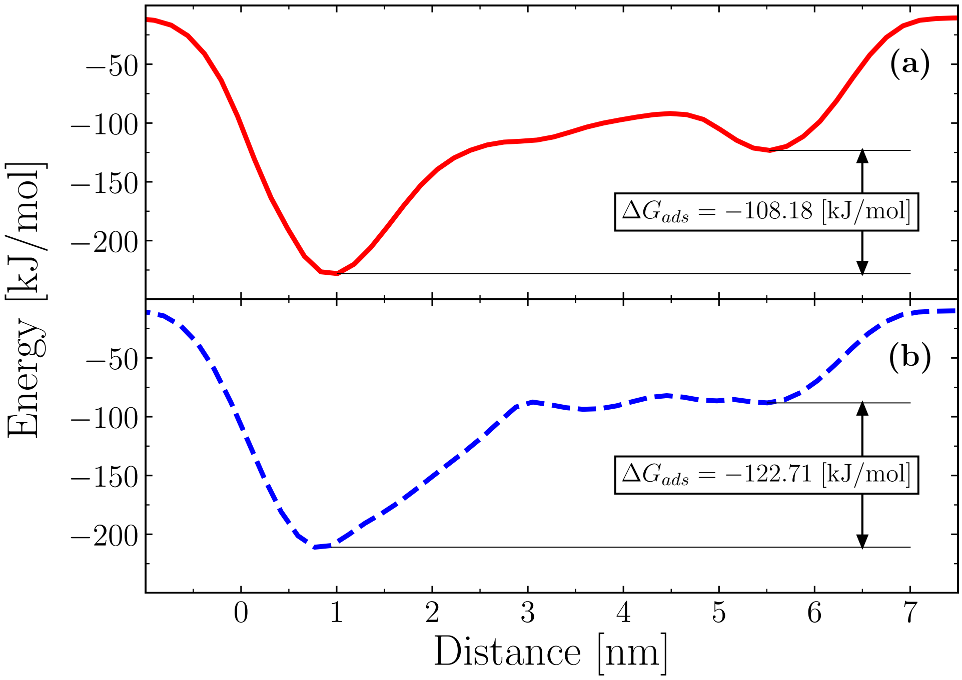

Fig. 2.8 Protein energy profiles and determination of the Gibbs free energy of adsorption at the oil-water interface: (a) Case 1: no phospholipids; (b) Case 2: phospholipids in the water bulk at a concentration calculated from Eq. (2.14).

can explore approximately the same region of the radius of gyration values as in Case 3 (Figure 2.7, green dash-dotted line) but with a higher probability of occurrence.

Moreover, for Case 1, it is conducted a more detailed analysis to investigate which are the amino acid residues involved in the adsorption process. Figure 2.9 shows the probability to find each amino acid residue distant from the interface as a function of its position in the chains. As can be seen, the portion of the protein mostly involved in the adsorption is the second half of one of the two chains of the protein. This region of the protein is strongly hydrophobic because it is mainly formed of such types of amino acid residues, thus they tend to adsorb onto the apolar oil interface. For the sake of better visualization, points with a probability higher than 0.9 are highlighted by red dots. It is also important to mention that, apart from the portion of the protein adsorbed (the red dots in Figure 2.9), the remaining part of the amino acid residues is free to move in the region close to the interface. For this reason, the other probability values are lower than 0.3. For a closer look at this behavior, Figure 2.10 shows the division of the amino acid residues of Apovitellenin

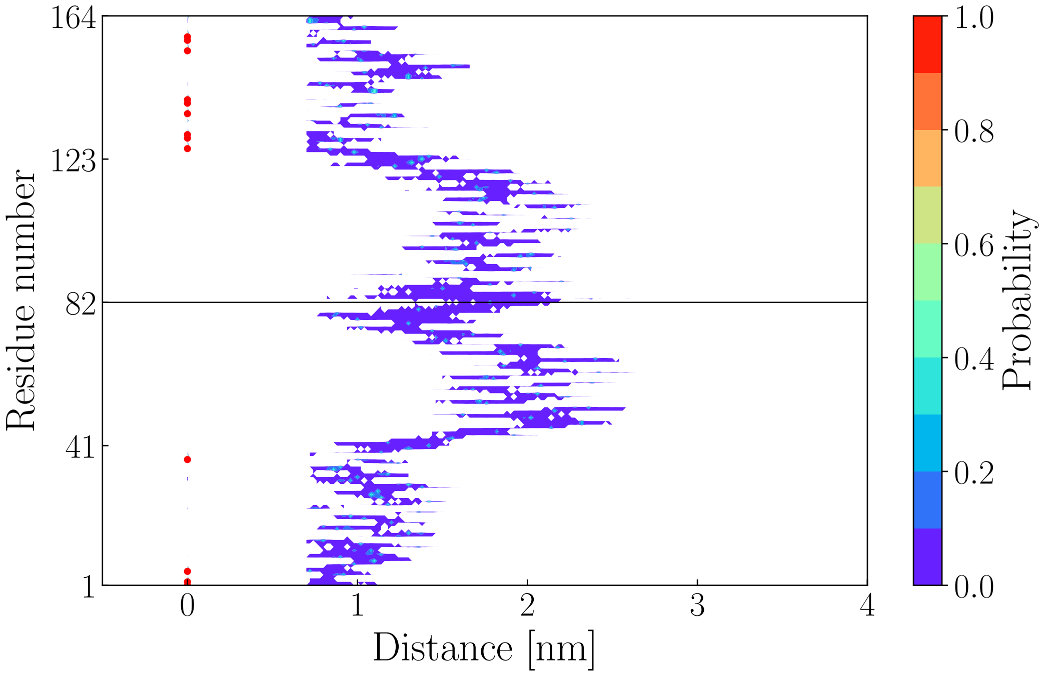

Fig. 2.9 Probability contour plot as a function of the distance from the oil-water interface for each amino acid residue. The black line shows the division between the two chains of Apovitellenin I; the red dots highlight the amino acid residues mostly involved in the protein adsorption with a probability higher than 0.9.

I into four groups: apolar, polar, positively charged, and negatively charged (aromatic amino acid residues were not considered). A large part of the amino acids are apolar (42.68%), followed by polar (23.17%), positively charged (14.64%), and negatively charged (10.96%). Aromatic amino acids account for only 8.53%. By looking at the probability values as a function of the distance from the interface in Figure 2.10, the amino acid residues that adsorb at the water-oil interface are almost all apolar; some polar and positively charged amino acid residues adsorb because they are close to the apolar region of the protein adsorbing at the interface.

In the last case studied here, the experiment with the β-casein from the work Ref. [69] is reproduced by the MD and MetaD approach with the same setup adopted for the Apovitellenin I simulations. The most important result here is the value of the Gibbs free energy of adsorption $\Delta G_{\beta-Cas,\mathrm{MetaD}} = -52.11$ kJ/mol, calculated by applying Eq. (2.15) to the Helmholtz free energy profile of Figure 2.11. This value is very similar to the one found in the literature which is $\Delta G_{\beta-Cas,Exp} = -59.4$ kJ/mol [69, 74].

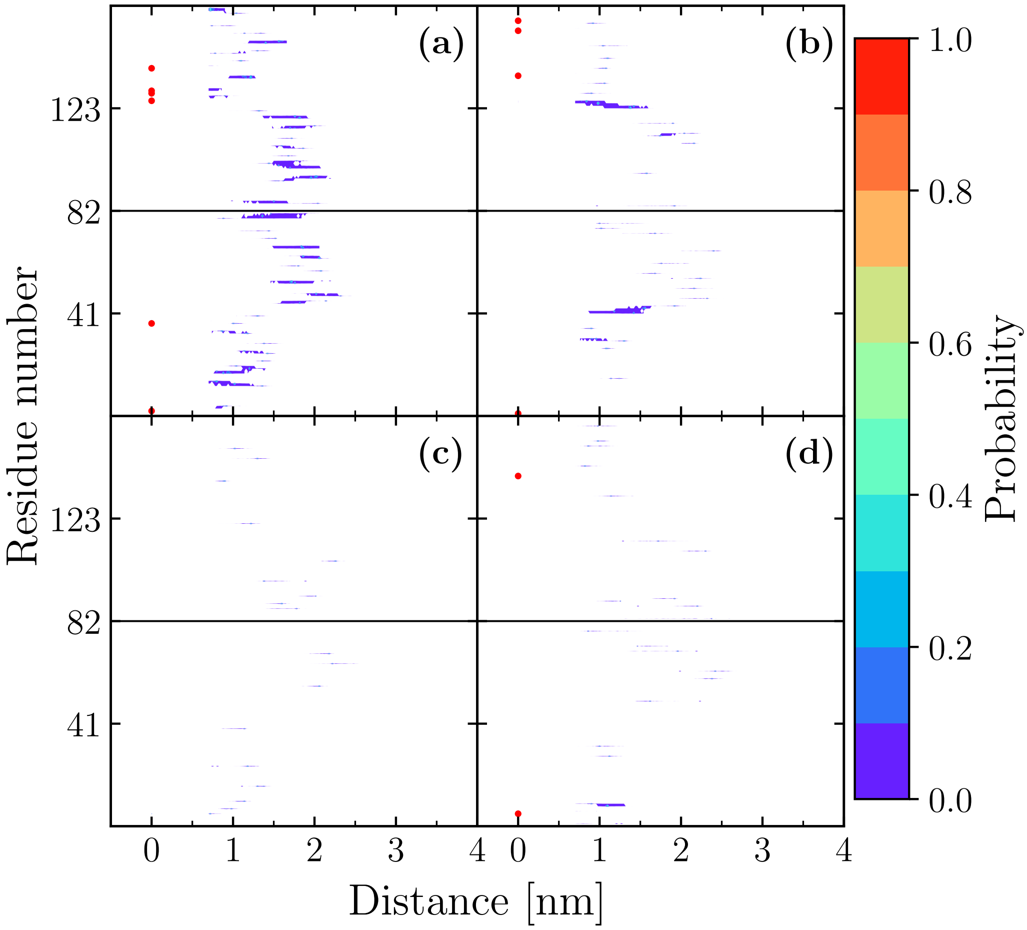

Fig. 2.10 Probability contour plot of each type of amino acid residues versus the distance from the interface: (a) non-polar, (b) polar, (c) negatively charged, (d) positively charged. The black line shows the division between the two chains of Apovitellenin I; the red dots highlight the amino acid residues mostly involved in the protein adsorption with a probability higher than 0.9.

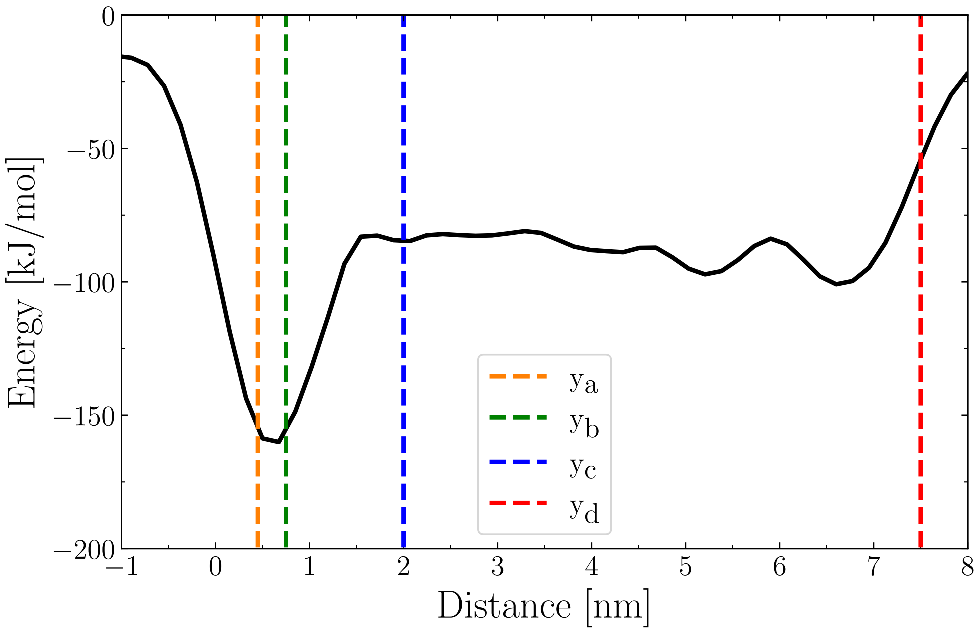

Fig. 2.11 Helmoltz free energy as a function of the distance of the β-casein from the air-water interface (black continuous line). The dashed lines represent the limits used in Eq. (2.15).

2.6 Conclusions

The adsorption of one of the proteins responsible for the stability of food emulsions like mayonnaise was studied using a modeling approach with Molecular Dynamics and Metadynamics. This protein, so-called Apovitellenin I, is not stable in aqueous solvents and is difficult to separate from the other particles of the egg yolk. Therefore, an attempt was made to study its behavior on a water-oil interface at different phospholipids concentrations. First of all, the adsorbed configuration of the protein has lower energy in comparison to the configuration in bulk, verifying that the protein under investigation can actually act as a surfactant. Therefore, the difference between the energy values in the two states is the energy of adsorption of the protein. It was also shown how phospholipids can influence adsorption. At low concentrations similar to those found in the egg yolk, phospholipids promote protein adsorption by going further to reduce the stability of the protein in water. At higher concentrations, when the water-oil interface is covered with phospholipids, it was pointed out how they go on to sterically inhibit the adsorption of the protein at concentrations equal to saturation and to half of the saturation. Phospholipids have an influence also on the protein radius of gyration. This was observed especially in the cases with the phospholipids at the interface. In fact, since the protein cannot completely adsorb, it tries to penetrate the phospholipid layer by reducing its radius of gyration. Moreover, the amino acid residues responsible for protein adsorption were identified. To validate the approach proposed, the value of the Gibbs free energy for the β-casein predicted from metadynamics simulations was computed and it is very similar to the one obtained experimentally.

Hence, the modeling approach here employed presents a deeper insight into the adsorption behavior of an egg yolk protein at the oil-water interface and its interaction with other co-surfactants. This method provides a notable advantage to estimate properties that are difficult to obtain experimentally. This is particularly true especially when research concerning the emulsifying properties of egg yolk proteins has been hindered by the difficulties in extracting individual components from the complex matrix. Therefore, these results are very promising and will be used in the next section to predict a macroscopic property of the protein investigated by applying a thermodynamic model of protein adsorption. In such a way, a link between two different molecular modeling techniques can be made with the remarkable purpose to transfer information to a larger scale.

Chapter 3

Coarse-grained molecular model

3.1 Introduction

The aim of this chapter is to model an oil/water interfacial system where the emulsifier is one of the most surface-active proteins from the egg yolk LDL, in order to provide new insights into the physics of the food emulsion production process. Despite the little availability of experimental data, the model was designed to test the most relevant physical properties of such a protein by means of the DPD approach in which the parameter calibration is based on MD simulations. Instead of a manual assignment, a fully *automated* coarse-graining procedure was employed for the molecules involved in the ternary system, assuming a flexible, disordered structure for the protein. Promising results were obtained in terms of both equilibrium and dynamic properties of the egg-yolk protein. The adsorption mechanism of an LDL-like particle is also qualitatively reproduced. Finally, the adsorption energy of the egg yolk protein at the oil/water interface obtained from metadynamics simulations (chapter 2) was then transferred to the thermodynamic model of protein adsorption, in which the parameter calibration is based on the results obtained by means of DPD simulations. Thus, it is possible to predict a macroscopic behavior of the protein investigated, namely the surface pressure curve at increasing protein bulk concentration. Therefore, by combining the results of the two molecular techniques (DPD and metadynamics), it is shown how these methods can be eventually used to predict equilibrium properties that are difficult to obtain experimentally.

This chapter is structured as follows: the molecular techniques here used are briefly introduced in section 3.2, together with the thermodynamic description of protein adsorption; the model development and calibration are explained in section 3.3, together with all the simulation details; section 3.4 shows the relevant results of systems investigated and, finally, in section 3.5 the main conclusions are reported.

3.2 Theoretical background

3.2.1 Dissipative Particle Dynamics

An extensive overview of the standard Dissipative Particle Dynamics (DPD) technique can be found elsewhere [40–42, 185]. Therefore, in this section only its main concepts are presented, while further details on the MD method are presented in section 2.3.1 and in the literature [38, 136].

DPD is a stochastic mesoscale particle model that has been devised to allow the simulation of the dynamics of mesoscopic particles, such as colloidal particles and/or groups of molecules that would require extremely long simulations and very large systems to be studied with MD. Unlike classic Molecular Dynamics, each DPD particle i, called bead, represents a molecular cluster (a molecule fragment or a group of solvent molecules) rather than an individual atom. The DPD system consists of N point particles of mass m_i, position $\mathbf{r}_i$ and velocity $\mathbf{v}_i$, whose time evolution is determined by Newton's second law of motion, usually integrated using the modified velocity Verlet algorithm [42, 142]. The major difference between MD and DPD, apart from the coarse-grained nature of the molecules, is the nature of the forces between them. The force $\mathbf{f}_i$ acting on each bead i contains three parts, each of which is pairwise additive:

$$\mathbf{f}_i = \sum_{j \neq i} (\mathbf{F}_{ij}^{\mathrm{C}} + \mathbf{F}_{ij}^{\mathrm{D}} + \mathbf{F}_{ij}^{\mathrm{R}}) \ , \tag{3.1}$$

where $\mathbf{F}_{ij}^{\mathrm{C}}$, $\mathbf{F}_{ij}^{\mathrm{D}}$, and $\mathbf{F}_{ij}^{\mathrm{R}}$ represent the conservative, dissipative, and stochastic (random) forces, respectively and the sum runs over all other particles within a certain cutoff radius r_c. The dissipative force $\mathbf{F}_{ij}^{\mathrm{D}}$ is a friction term that acts to push particles apart if they are approaching each other and to pull them back together if they are moving apart. It is represented as a pair potential between the particles that conserves both angular and linear momentum. This frictional term leads to a gradual loss of kinetic energy in the system, which is compensated for by the stochastic force $\mathbf{F}_{ij}^{\mathrm{R}}$ to ensure the conservation of energy. The dissipation-fluctuation theorem [41] leads to a relation between the friction coefficient γ and the DPD-sigma parameter σ, namely the amplitudes of the dissipative and random force, respectively. These two forces effectively act as a thermostat in DPD and their mathematical description is investigated in detail elsewhere [40–42, 185] and will not be discussed further. Here the conservative force $\mathbf{F}_{ij}^{\mathrm{C}}$ felt by bead i includes: 1) contributions from repulsive interactions with surrounding beads; 2) contributions due to the springs connecting bead i to other beads in the same molecule; and 3) contributions due to angle bending interactions.

The repulsive force $\mathbf{F}_{ij}^{r}$, which is modeled as a soft repulsion between beads i and j, is defined as follows:

$$\mathbf{F}_{ij}^{r} = \begin{cases} a_{ij}(1 - r_{ij}/r_c)\hat{\mathbf{r}}_{ij} & \text{if } r_{ij} \leq r_c \\ 0 & \text{if } r_{ij} > r_c \end{cases} , \tag{3.2}$$

where $r_{ij} = |\mathbf{r}_i - \mathbf{r}_j|$ is the distance between beads i and j at positions $\mathbf{r}_i$ and $\mathbf{r}_j$, respectively, and $\hat{\mathbf{r}}_{ij} = (\mathbf{r}_i - \mathbf{r}_j)/r_{ij}$ is the direction between the two beads. The parameters a_{ij} are the DPD interaction parameters defined for each bead pair, while r_c stands for the cutoff distance. For the system investigated in this work, their definition will be given in section 3.3.2 and they will be here used as fitting parameters for the calibration of the DPD model.

When dealing with chain molecules, two additional conservative terms are here considered to maintain bonds between neighbor beads. The adjacent beads are constrained with permanent lengths and angular bonds. In this study, the bonds were modeled using harmonic spring quadratic potentials given as:

$$U_{ij}^{S} = k_S(r_{ij} - l_H)^2 , \tag{3.3}$$

$$U_{ijk}^{A} = k_A(\theta_{ijk} - \theta_H)^2 , \tag{3.4}$$

where l_H and θ_H are the equilibrium lengths and angles for beads i, j, and k. The stiffness of the length and angular bond constraints is defined by the values of k_S and k_A.

As it is customary in DPD, the quantities here reported have to be considered reduced (dimensionless) and the scaling factors for the main properties (mass, length, time, energy) will be explained in section 3.3.3. Finally, it is important to point out that the coarse-graining of the molecular structures and the soft interactions allow larger systems to be modeled over significantly longer times than with (atomistic scale) molecular modeling [55, 185], thus allowing the dynamics of mesoscopic systems to be followed over relevant time scales as well as length scales.

3.2.2 Thermodynamic model of protein adsorption

The theory of protein adsorption, which is described in detail in the work Ref. [73], is based on the idea that multiple states of the protein molecule can exist in the interfacial layer. The large area and the large number of conformations of an adsorbed protein molecule can be modeled as a significant increase in the non-ideality of the surface entropy. This is the reason why the most simple isotherm models (e.g. Henry, Langmuir, Frumkin) cannot describe protein adsorption [73]. In contrast, this thermodynamic model of protein adsorption assumes that the partial molar area of the protein molecules can vary between a maximum (ω_{max}) at very low surface coverage to a minimum (ω_{min}) value at high surface coverage. The molar areas of two 'neighboring' conformations differ from each other by the value ω_0 corresponding to the molar area of the solvent and, therefore, it is assumed to be much smaller than the protein molar area in any state. Finally, the total number of possible states of the protein molecule, n, is defined by the above-mentioned parameters so that $\omega_0 = \Delta\omega = (\omega_{max} - \omega_{min})/(n-1)$. Then, the following equation of state was derived:

$$-\frac{\pi\omega_0}{RT} = \ln(1-\omega\Gamma) + \Gamma(\omega-\omega_0) + a(\omega\Gamma)^2 \,, \tag{3.5}$$

where $\pi = \sigma_0 - \sigma$ is the surface pressure, σ_0 and σ the interfacial tension of the free interface and that covered by protein surfactants respectively, R is the ideal gas constant, T the temperature, and a is a Frumkin-type intermolecular interaction parameter. $\Gamma = \sum_{i=1}^{n} \Gamma_i$ is the total adsorption of protein in all n states, $\theta = \omega\Gamma = \sum_{i=1}^{n} \omega_i \Gamma_i$ is the total surface coverage, and ω is the average molecular area of adsorbed proteins. The equation of the adsorption isotherm for each state (j) of the protein is given by:

$$b_j c = \frac{\omega\Gamma_j}{(1-\omega\Gamma)^{\frac{\omega_j}{\omega}}} \exp\left(-2a\left(\frac{\omega_j}{\omega}\right)\omega\Gamma\right) , \tag{3.6}$$

where c is the protein bulk concentration and b_j is the adsorption equilibrium constant for the protein in the j-state. Moreover, it can be assumed that all constants b_j have one and the same value for all states j from $i = 1$ to $i = n$, and therefore the adsorption constant for the protein molecule is given by $b = \sum_j b_j = nb_j$. This assumption allows defining each of the individual Γ_i in terms of the total adsorption, thus providing the distribution function of adsorptions over various states of the protein molecule:

$$\Gamma_j = \Gamma \frac{(1-\omega\Gamma)^{\frac{\omega_j-\omega_{min}}{\omega}} \exp(2a\Gamma(\omega_j-\omega_{min}))}{\sum_{i=1}^{n}(1-\omega\Gamma)^{\frac{\omega_i-\omega_{min}}{\omega}} \exp(2a\Gamma(\omega_i-\omega_{min}))} , \tag{3.7}$$

while the average molecular area of adsorbed proteins ω can be expressed as follows:

$$\omega = \frac{\sum_{i=1}^{n}\omega_i(1-\omega\Gamma)^{\frac{\omega_i-\omega_{min}}{\omega}} \exp(2a\Gamma(\omega_i-\omega_{min}))}{\sum_{i=1}^{n}(1-\omega\Gamma)^{\frac{\omega_i-\omega_{min}}{\omega}} \exp(2a\Gamma(\omega_i-\omega_{min}))} . \tag{3.8}$$

The thermodynamic model presented above describes very satisfactorily the adsorption behaviour at low protein concentrations where the simultaneous increase of surface pressure and adsorption is observed [2, 73]. However, assuming the existence of a critical protein concentration, denoted by c^*, π^* and Γ^*, above which the surface pressure remains almost constant while the adsorption often increases, the model can be extended to account for higher concentrated solutions [73]. Thus, for $c > c^*$ the equation of state and the adsorption isotherm become:

$$-\frac{\pi\omega_0}{RT} = \frac{1}{\Psi}[\ln(1-\omega\Gamma) + \Gamma(\omega-\omega_0) + a(\omega\Gamma)^2] , \tag{3.9}$$

and

$$b_j c = \frac{\omega\Gamma_j}{(1-\omega\Gamma)^{\frac{\omega_j}{\omega\Psi}}} \exp\left(-2a\left(\frac{\omega_j}{\Psi\omega}\right)\omega\Gamma\right) , \tag{3.10}$$

respectively, with:

$$\Psi = \frac{\Gamma}{\Gamma^*} \exp\left(\varepsilon\frac{\pi-\pi^*}{RT}\omega\right) , \tag{3.11}$$

where ε represents an adjustable parameter. Finally, the adsorption equilibrium constant b can be expressed as [74]:

$$b = \frac{1}{\rho} \exp\left(- \frac{\Delta G_{ads}}{RT} \right), \tag{3.12}$$

where ρ is the molar concentration of the solvent, assumed to be equal to 56 mol/l for dilute aqueous solutions [186]. It is important to highlight here that the value of ΔG_{ads} was here computed from metadynamics simulations (chapter 2), thus representing the link between the molecular modeling techniques and the macroscopic thermodynamic theory.

3.3 Modeling details

A general description of the macroscopic system to be studied is already provided in section 2.2, together with the adopted simplifications. For the sake of simplicity, here the basic components of the system under investigation are three: the triglyceride with three monounsaturated oleic acid residues which stands for the oil phase, the protein Apovitellenin I coming from the egg yolk LDL, and, finally, water. The presence of salts, small surfactant molecules (phospholipids), or other additives is here neglected since only the emulsifying capacity of the considered egg yolk LDL protein is investigated. Furthermore, the pH of the system is kept constant and equal to 3.8. In order to consider both the complex composition of the emulsion and the equilibration time required by macro-molecules to re-arrange at interfaces, the DPD approach is employed in which the parameter calibration is based on MD simulations. The next sections will present the setup of MD simulations, the DPD model development in which both the coarse-graining procedure and the calibration of parameters are explained, and definitions of the main physical properties investigated here. Finally, the development of the thermodynamic model of protein adsorption is also reported.

3.3.1 MD simulations

The purpose of all-atom MD simulations is to use their results to calibrate the DPD parameter set. Only MD simulations of one protein molecule in bulk phases (water or oil) were performed rather than the entire ternary interfacial system due to the size of the latter which would require excessive computational time. An initial guess of both protein and triglyceride structures was manually made from scratch via a molecule editor. In particular, Figure 3.2a shows the all-atom protein model. It can be clearly seen the disulfide bond links two identical polypeptide chains. Furthermore, the N- and C- terminal amino acid residues and, if applicable, the functional group of side chains were protonated or deprotonated by comparing their corresponding pK_a with the pH of the solution [187]. Thus, at pH 3.8 the net charge of the protein homodimer results equal to 16 e and the protein molecular mass M is 18675.6 Da. MD simulations were performed using the OPLS-AA force field [188, 189], while water was described by the TIP3P water model [190]. A cutoff of 7.5 Å was used for long-range interactions, and both electrostatic and van der Waals interactions were handled using a smooth particle mesh Ewald summation method (SPME) [191]. For the protein and the triglyceride, a first 20-ps simulation in a vacuum with a time step of 1 fs was performed on the single molecule to relax its initial structure. Before solvation with water or oil, the protein was centered in a rectangular box with a minimum distance of any part of the molecule defined to be at least 1 nm from box walls in order to satisfy the minimum image convention when using periodic boundary conditions. According to the reproduced environment, the box was filled with respectively 15994 water or 325 triglyceride molecules, plus 16 Cl^- counterions to ensure the electroneutrality of the system. Thus, the resulting MD box contains a total of 50694 or 56987 atoms in the case of protein in water or oil bulk respectively. After a simple energy minimization to ensure that the system had no steric clashes or inappropriate geometry, a 0.5-ns NPT (i.e., constant number of particles, pressure, and temperature) equilibration simulation at ambient pressure (1 atm) and temperature (298 K) was performed. Pressure and temperature were fixed using the Berendsen barostat and thermostat [192] and the Verlet algorithm was used to integrate the equations of motion with an increased time step of 2 fs. To verify that the system was at equilibrium, the fluctuations in the temperature, pressure, density and potential energy were monitored. In particular, the average density reached during the last 0.2 ns of equilibration simulation was equal to 1059.57 and 921.85 kg/m^3 respectively for the protein in water and in the oil system, both with fluctuations in the 0.1%. Finally, NVT (i.e., constant number of particles, volume, and temperature) production simulations ranging from 2 to 6 ns were performed to collect statistically averaged results by saving particle trajectories every 250 time steps.

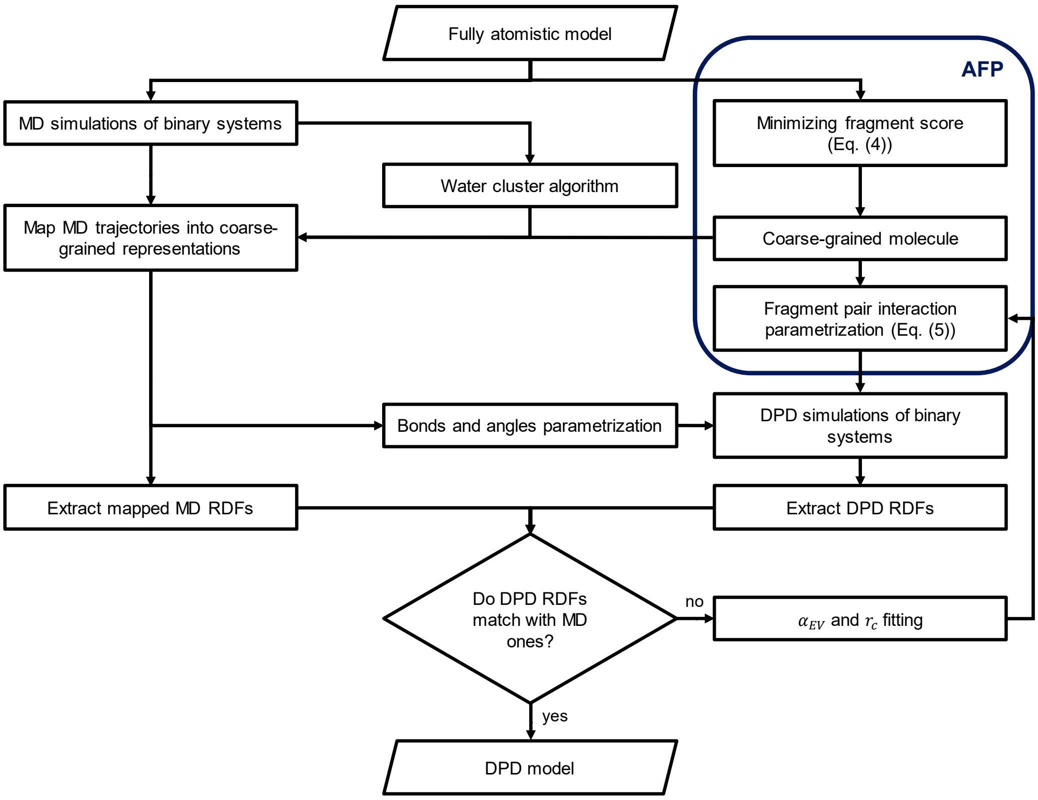

Fig. 3.1 Schematic diagram of the main stages followed in this work to develop the DPD model. See section 3.3.2 for details of each step.

3.3.2 Coarse-graining procedure and parameter calibration

The main steps of the DPD model development are summarized in a schematic diagram in Figure 3.1, in which each stage is explained in this section.

The first step toward a realistic DPD molecular model is to obtain the coarse-grained (CG) representation of the molecules together with their full parameter set of both inter- and intra-molecular interactions. For this scope, the Automated Fragmentation and Parametrization (AFP) method is used and here a very brief introduction to this approach is provided. For a fully detailed discussion on it, the reader can refer to the work Ref. [193].

Starting from their fully atomistic representations, the molecules involved in the investigated system are fragmented according to a scoring function, through a simulated annealing function that cuts through bonds; the optimal bond fission pattern is preserved and the fragments are stored. The scoring function is here

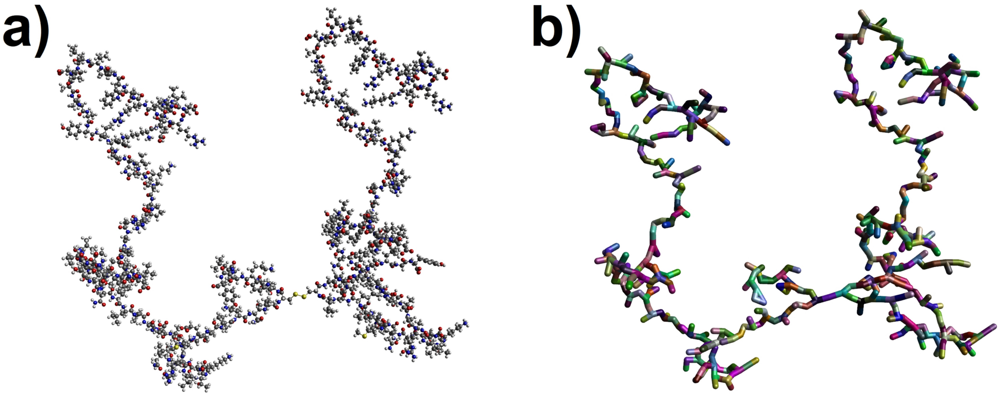

Fig. 3.2 All-atom (a) and corresponding coarse-grained (b) model obtained via AFP of Apovitellenin I. DPD beads are represented by colored fragments, highlighting the bond fission pattern.

defined as:

$$S = \left(1 - \frac{V}{V_0}\right)^2 , \tag{3.13}$$

where V is the volume of the fragment and V_0 is the reference volume of a cluster of three water molecules in its lowest energy conformation (i.e., the reference volume used here is equal to 67.7 Å^3 as in the original AFP work [193]). In this approach, molecule-unique fragmentation is used in order to preserve as much as possible of the properties of the molecule. This means that the fragments are not database-unique, as is customary in coarse-grained simulations, but completely specific to a given molecule. By applying this fragmentation technique, the triglyceride molecule and the homodimer Apovitellenin I are comprised of 20 and 500 beads respectively, while each water bead corresponds to three atomistic water molecules. In particular, Figure 3.2 shows the all-atom (a) and the corresponding coarse-grained (b) representation of the protein molecule.

In the AFP framework, the interaction DPD parameter a_{ij} is split into two contributions, one from the excluded volume and the second from the residual interactions:

$$a_{ij} = \alpha_{EV} v_i v_j + \alpha_{res} \sqrt{v_i v_j} \beta \Delta G_{res,ij} , \tag{3.14}$$

where $v_i = V_i / V_0$ is the scaled molecular volume of fragment i, $\beta = 1/k_b T$, α_{EV} and α_{res} represent two global adjustable parameters and $\Delta G_{res,ij}$ is the residual Gibbs energy of mixing of a *hypothetical* equimolar mixture of fragments i and j. The Gibbs energy of mixing was calculated through COSMO-RS calculations

[194, 195], using the charge envelope of the fragments (the so-called sigma profiles). The COSMO charge envelope is here computed via a modified version of AM1 [196–198], using atomic partial charges derived from the charge equilibration (QEq) method [199]. By definition the residual Gibbs energy of mixing between identical fragments is zero, i.e., $\Delta G_{res,ii} = 0$, thus it follows trivially that a_{ii} is reduced only to the excluded volume contribution and, in particular, for water bead self-interaction $a_{ww} = \alpha_{EV}$. It is also important to point out here that the bead-size effect is taken into account in the definition of DPD a_{ij} parameter given in Eq. (3.14) by considering the fragment volume scaled with respect to the reference volume, V_0, of a cluster of three water molecules. This allows us to consider a constant DPD base unit of length, h, for all fragments irrespective of size or composition. As in the original AFP work [193], here the value of h is assumed equal to 7.65 Å as the yardstick for length in DPD approach. This value corresponds to five 3-mer water clusters per cell of size h^3, or, in terms of the DPD dimensionless unit system, this corresponds to a density of 5 for water under ambient conditions. The soft-core repulsion potential employed here is devoid of the short-range Lennard-Jones divergence. Also, the typical long-range electrostatic Coulomb term is avoided completely by using the close-contact electrostatic interaction of the COSMO model. Both interactions are therefore replaced by a soft repulsive potential that is local, with a length scale limited to the cutoff, r_c. Hence, in the AFP approach, the fragment-specific chemical information is condensed into only one parameter: the DPD a parameter. The magnitude of the repulsion (not the spatial extension) is modified depending on the volume of the underlying molecular fragment, and residual interactions.

In order to map the characteristics of the atomistic models into the DPD system, MD simulations of protein in water and oil bulks were used to extract molecular characteristics such as radial distribution functions as well as the distributions of lengths and angles for molecules bonded with length and angular bonds. To make MD and DPD models physically comparable, it is necessary to map atomistically detailed trajectories into their corresponding coarse-grained representations considering a length scale factor, h, to convert atomistic coordinates and MD box dimensions into a CG model. When dealing with the triglyceride and the protein in which their fragmentation information has been already well-defined through the AFP approach, the mapped MD trajectories of such molecules are easily determined by replacing the fully atomistic coordinates with the center-of-mass positions of provided molecular fragments. However, in the case of atomistic water models, where the water particles move independently, their CG representation has to be dynamically identified. Therefore, a clustering method is required to enable the mapping of multiple water molecules into a single CG bead. Here, the water molecules clustering algorithm proposed in the work Ref. [200] was employed, which is based on a step-wise iterative nearest neighbor search algorithm. The number of water molecules per bead in all clusters is kept constant and equal to the degree of coarse-graining employed here, i.e., a 3 to 1 CG ratio, corresponding to the number of clustering steps performed for each simulation time frame. This represents the major advantage compared to other approaches where, instead, the total number of beads in the system have to be provided [201], leading to some issues converging with the desired number of equally sized clusters. Very briefly, as the algorithm initialization, a grid of fixed-size cubes was superimposed onto the MD simulation box and initial positions of bead centers were generated by randomly choosing coordinates of water molecules from the first time frame. For each step of the algorithm, an iterative search for the unique nearest water molecule was carried out in the area adjacent to the unit cell in which the coarse-grained bead is located. The unique nearest water molecule was defined by means of the Euclidean distance from the center of mass of a CG bead. When all of the CG beads had the same number of molecules assigned to them (equal to the CG ratio), the algorithm finished and the positions of the beads were updated by calculating the center-of-mass of the molecular clusters. Hence, for each MD simulation time frame, the water molecules were divided into equally sized groups based on their proximity.

The mapped MD trajectories were used to extract radial distribution functions (RDFs) of coarse-grained molecules. Thus, using the AFP method as a basis, a further DPD parameter calibration was carried out by using the MD RDFs as reference curves to be compared with those extracted from DPD simulations. Since the RDF is solely determined by the conservative force [202], the repulsion force coefficients were adjusted to match MD and DPD RDFs. As the specific fragment pair interactions were defined in Eq. (3.14), the global adjustable parameters which serve to define the mutual repulsive interaction between *all* the beads belonging to a single type of molecule can be used to calibrate the DPD model. In particular, α_{EV} and the cutoff distance, r_c, were used as fitting parameters, while for all the fragment pairs the DPD-sigma parameter was set to the standard value of 3.0 [42] and α_{res} was kept equal to 6.1 as in the original AFP work [193]. Therefore, from both MD and DPD simulations of protein in water and in oil bulk, only RDFs referring to all beads belonging to water, oil, and protein were extracted and the results of the calibration are presented and discussed in section 3.4. Obviously, from simulations of the binary systems only water-water, oil-oil, water-protein, and oil-protein interactions can be exactly calibrated. However, the remaining interactions, i.e., oil-water and protein-protein, must be determined to build the DPD model of the ternary system. In particular, the oil-water α_{EV} value was obtained by simply fitting the experimental interfacial tension between purified soybean oil and water [65], found to be equal to 31-32 mN/m and independent on the presence of salt [203]. For the protein-protein repulsive interaction, the same α_{EV} value of water-protein was arbitrarily chosen as a first guess. This value could be of paramount importance since the self-protein interaction may affect the structural configuration of the protein as well as the equilibrium and dynamics properties of the ternary system. The study of protein-protein interactions needs therefore a deeper insight, which could be the scope of future works.

The parameterization of intra-molecular interactions (bonds and angles) of CG molecules was also based on MD simulations. The basic concept is to construct the distribution function of each of these quantities from atomistic model simulations. By using again the molecular fragment information obtained via AFP within the atomistic MD trajectories, the distribution functions of bond lengths and bending angles were calculated based on the center of the coarse-grained fragments. Then, a robust and fast approach when dealing with hundreds of bond and angle interaction types generated from the automated coarse-graining procedure employed in this work (AFP) is to derive parameters from distributions directly [57, 204, 205], instead of fitting each bond-stretching and bending angle potential obtained from Boltzmann inversion with a harmonic approximation [206]. When assuming a harmonic bond potential (Eq. (3.3)), the resulting distribution is a Gaussian that can be equated with the distribution of the bonds. It follows that the equilibrium bond length, l_H, is simply the average of the distribution, and the bond constant, k_S, can be expressed in terms of the standard deviation of that distribution [57, 204, 205]. For angles, the same would hold for harmonic potentials (Eq. (3.4)), except that the angle is bounded between 0° and 180°. This means that the distribution for a purely harmonic potential will not be a Gaussian, but rather a Gaussian that is cut off at 180°. However, a reasonable procedure is to simply take the angle where the distribution is maximal and treats that as if it was the average, equating it to the equilibrium angle, θ_H. Taking the standard deviation to calculate the angle potential strength, k_A, also is reasonable [57]. It is important to point out that this procedure is not able to capture multiple maxima and/or minima in bond and angle distributions from atomistic MD simulations [57]. Without further modification, bonded interaction parameters directly derived from MD distributions can be used in DPD simulations by using a shorter time step than that typically used in DPD works (i.e., $\Delta t = \mathcal{O}(0.01)$ [42]). In fact, the exact replication of the MD structures required the strength of bonds to become too large for a relatively long time step, resulting in unstable simulations [55]. Therefore, in order to preserve the distance and angular bond characteristics, a dimensionless time step of $\Delta t = 0.001$ was used to integrate the DPD equations of motion [200].

3.3.3 DPD simulation parameters

To avoid using excessively large or small numbers and to simplify the calculations, DPD systems were usually scaled by arbitrarily chosen base units. As was already discussed in the previous subsection, the conversion factor $h = 7.65$ Å was here employed as the base unit of length. The mass of one water bead consisting of three water molecules equal to 8.974×10^{-26} kg, was used as the base mass unit. Both MD and DPD simulations were performed at ambient temperature (298 K), giving $k_bT = 4.11 \times 10^{-21}$ J used as the base unit for energy, where k_b is the Boltzmann constant. The base time unit τ was estimated by evaluating the diffusion coefficient. This is computed from both MD and DPD simulations by using the standard mean-squared displacement (MSD) method through the well-known Einstein relation [38]. By defining the scaling factor $S = D_{W,Exp}/D_{W,\mathrm{DPD}} = 7.63 \times 10^{-9}$ m^2/s, where $D_{W,Exp}$ and $D_{W,\mathrm{DPD}}$ are respectively the experimental water self-diffusion coefficient at ambient conditions and the simulated one via DPD, the base unit used to convert the reduced DPD time into real unit reads as follows:

$$\tau = \frac{h^2}{S} \approx 77 \text{ ps} . \tag{3.15}$$

Therefore, the real protein diffusion coefficient computed from DPD simulations was simply determined by multiplying the simulated value for the scaling factor, S [207]. Since no experimental measurement is available in the literature, the protein diffusion D computed via MD and DPD were compared with three correlations proposed for the prediction of protein diffusion coefficients in free solution, based on the molecular weight M (Eq. (3.16a) [208]), on the radius of gyration R_g (Eq. (3.16b) [209]), and on both the molecular weight and the radius of gyration of the protein (Eq. (3.16c) [210]), respectively:

$$D = 8.34 \times 10^{-8} \left(\frac{T}{\eta M^{1/3}} \right), \tag{3.16a}$$

$$D = 5.78 \times 10^{-8} \left(\frac{T}{\eta R_g} \right), \tag{3.16b}$$

$$D = 6.85 \times 10^{-8} \left(\frac{T}{\eta \sqrt{M^{1/3} R_g}} \right), \tag{3.16c}$$

where η is the solvent viscosity, i.e., 0.894 and 50 cP at 25 °C for water [211] and for soybean oil [212], respectively.

Several DPD simulation configurations were investigated in this work. In order to match the coarse-grained characteristics from MD simulations, the binary systems were reproduced using DPD. The MD box was scaled according to the length conversion factor h and one CG protein molecule was located at its center. According to the binary environment, the box was then filled with water beads or oil CG molecules to obtain the overall DPD density $\rho = 5$. The DPD simulations were performed with an equilibration period of 10^5 steps, then followed by a production phase of 10^6 steps, saving particle trajectories every 250 steps. Once DPD parameters have been calibrated as explained in the previous subsection, two DPD configurations of the interfacial system were carried out in order to study the equilibrium properties at increasing protein interface concentration c_i and the protein adsorption at the oil/water interface. Both initial configurations consisted of a central water phase segregated by two oil phases, thus forming two planar interfaces in equidistant yz-planes. The 50/50 oil-to-water bead ratio was kept constant for all DPD simulations and both the number of water beads and oil CG molecules were adjusted to keep the same overall DPD density of 5 when the protein molecules were also added in the DPD box. The equilibrium simulations were conducted with increasing protein interface concentration c_i, which is simply calculated by multiplying the number of the protein molecules at each interface for the protein molecular mass M, divided for the constant interface yz-area expressed in real units. The protein molecules were initially located at the oil–water interface to make sure that both interfaces contain the same number at equilibrium in order to perform averages on both interfaces. For equilibrium DPD simulations, the box was an orthorhombic cell of reduced size $L_x \times L_y \times L_z$, where $L_y = L_z = 32$ and L_x was properly adjusted up to 52 based on the protein molecule number to allow both interfaces to be independent. Simulations were run for 2.5×10^5 equilibration steps and for a production period of 10^6 steps, saving time frame data for post-processing every 500 steps. Here the interfacial tension, σ_{DPD}, was computed by integrating the difference between normal and tangential stress across the interface separating the segregated components [213]. Thus, if the normal to the interface lies along the x-direction, the interfacial tension is deduced from the local components of the pressure tensor:

$$\sigma_{\mathrm{DPD}} = \frac{1}{2}\int (p^*_{\mathrm{N}} - p^*_{\mathrm{T}})\, dx = \frac{1}{2}\int \left(p^*_{xx} - \frac{1}{2}\left(p^*_{yy} + p^*_{zz}\right)\right) dx\,, \tag{3.17}$$

where p^*_{N} and p^*_{T} are the normal and tangential components of the pressure tensor profile in reduced DPD units. The factor 1/2 before the integral sign is due to the presence of two symmetric interfaces in the DPD simulation box when using periodic boundary conditions. Since the oil droplets of a food emulsion have a diameter of the order of microns [7], it is reasonable to neglect the curvature effect when modeling the interfacial system at the nano-scale, thus allowing to use of the above formula, valid for planar geometry only [213]. The conversion of σ_{DPD} to real units operates as follows: $\sigma_{\mathrm{calc}} = \frac{k_b T}{h^2}\sigma_{\mathrm{DPD}}$. The quantity σ_{calc} can be directly compared with experimentally measured interfacial tension. The free protein adsorption at the oil/water interface was also studied by locating one protein molecule in the center of an orthorhombic DPD box $L_x \times L_y \times L_z$, where $L_y = L_z = 20$ and L_x was ranged from 40 to 56 in order to properly increase the mutual initial distance between the protein center and the interface. In addition, the adsorption at the oil/water interface was tested for an LDL-like particle configuration by initially creating a small droplet of 15 oil CG molecules surrounded by one protein molecule. These latter DPD simulations were performed with 2×10^5 equilibration steps and a production period of up to 4×10^6 steps, saving simulation time frames every 500 steps to check if the protein adsorption has taken place.

Apart from the water cluster algorithm, which was performed in the MATLAB environment [200], all MD and DPD simulation setup, runs, and post-processing analyzes were conducted within the CULGI software package [214], together with all other tools and algorithms employed here.

Table 3.1 Optimized parameters used in the thermodynamic model of protein adsorption (from Eqs. (3.5) to (3.11)).

Parameter	**Optimized value**
a	0.00625
ω_{min} [m^2/mol]	1.9×10^6
ω_{max} [m^2/mol]	4.9×10^7
n	565
ε	3.9×10^{-4}
π^* [mN/m]	22.5

3.3.4 Details of the thermodynamic model

As regards the thermodynamic model of protein adsorption, the equations of state Eqs. (3.5) and (3.9) were solved together with the expression of the mean molar area Eq. (3.8) to find the value of ω for each Γ value. Then, these values were included in the isotherm of adsorption (Eqs. (3.6) and (3.10)) in order to obtain the surface pressure profile as a function of the protein bulk concentration. To do this, further parameter optimization was performed with Matlab to minimize the error between the optimized curve of Eqs. (3.5) and (3.9) and the data from DPD simulations. The optimized parameters used in the thermodynamic model have listed in Table 3.1.

3.4 Results and discussion

The results of the DPD model calibration explained in section 3.3.2 are shown in Figure 3.3, where the distance is expressed in real units, and in Table 3.2. Using the MD RDFs as references, the DPD RDFs were adjusted in order to best match curve heights and shapes by calibrating both α_{EV} and r_c of molecule bead pairs. These two terms define both the magnitude (via Eq. (3.14)) and the spatial extension of the repulsive force (Eq. (3.2)). Typically, in standard DPD the cutoff value also represents the base unit of length and, therefore, is often set equal to 1 in the dimensionless unit [42]. In contrast, here the dimensionless value of r_c resulting from fitting the first peaks of RDF curves shown in Figure 3.3 was found to be equal to 0.7. Hence, the cutoff, r_c, and the length factor, h, were decoupled in order to assure both the constant DPD number density of 5 and the repulsive force calibration. The results of α_{EV} fitting are summarized in Table 3.2. Although the oil-water α_{EV}

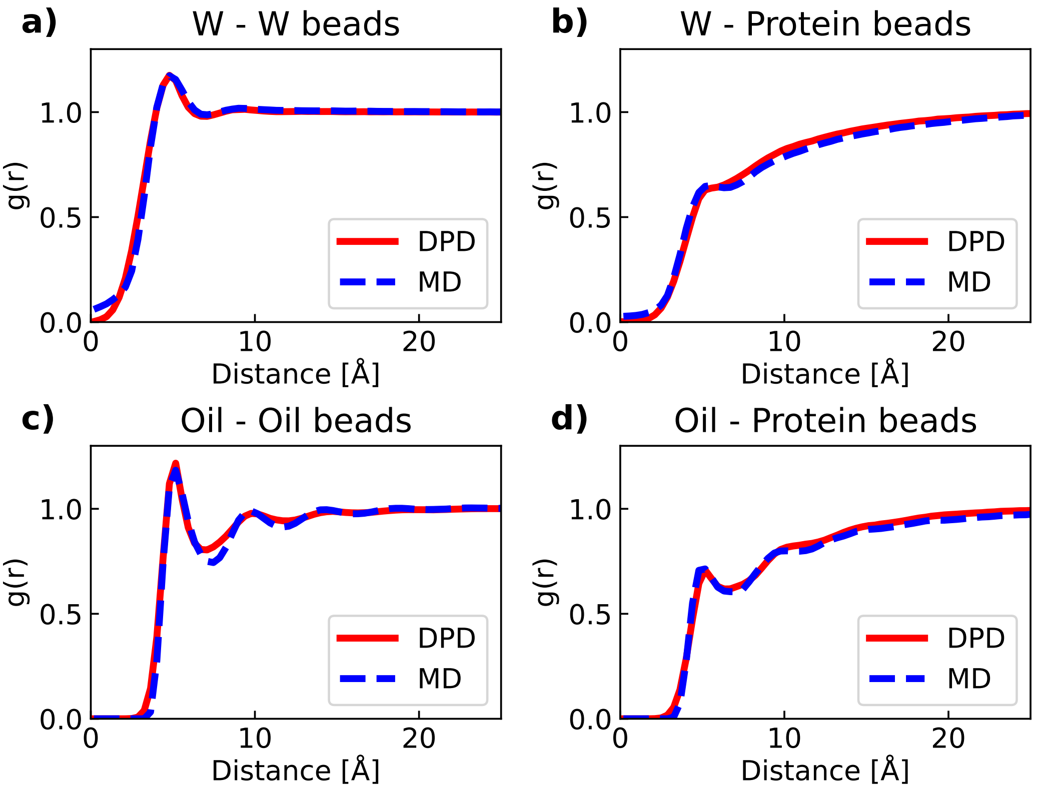

Fig. 3.3 Results of the DPD parameter calibration of water-water (a), water-protein (b), oil-oil (c), and oil-protein (d) interactions based on matching RDFs of the mapped MD reference model (dashed blue line) with corresponding RDFs extracted from DPD simulations (solid red line).

turned out to be substantially smaller than all the others in Table 3.2, the overall repulsion between water and oil beads was properly reproduced due to the two contributions in Eq. (3.14) and a cutoff, r_c, equal to 1 in this specific case, in which a sophisticated calibration was not needed.

The molecular model is tested and the main findings are presented here, paying particular attention to verifying the emulsifying behavior of Apovitellenin I at the oil/water interface. First, preliminary structural and dynamic quantities of the protein are estimated by performing both MD and DPD simulations of one protein molecule in bulk phases. Then, the DPD simulation results of the ternary system are discussed in terms of both equilibrium and dynamic aspects.

Table 3.3 reports End-to-End distance and radius of gyration mean values and standard deviations of Apovitellenin I in water and oil bulks computed via MD and DPD simulations. The MD values were averaged over the simulation time,

Table 3.2 Values of the global parameter α_{EV} used in Eq. (3.14) to define the mutual repulsion between all the beads belonging to water, oil, and protein in the DPD model of this work. The cutoff distance, r_c, is equal to 0.7 unless otherwise specified.

α_{EV}	W	Oil beads	Protein beads
W	25^a	-	-
Oil beads	8.5^b	100	-
Protein beads	40	100	40^c

[a] Exactly corresponding to a_{ww}.
[b] Value obtained by fitting experimental interfacial tension between soybean oil and water [203], with a cutoff distance, r_c, equal to 1.
[c] Arbitrarily chosen equal to the water-protein value.

meanwhile, ten independent DPD simulations with the same initial configuration were carried out from which the reported values are extrapolated by computing their respective arithmetically averaged frequency distributions. It is important to recall that Apovitellenin I is modeled here as a homodimer, so the two polypeptide chains are labeled as 1 and 2 in Table 3.3 where the End-to-End distance is that between the N-terminal and the C-terminal of each chain, while the protein radius of gyration refers to the homodimer itself. By looking at mean values reported in Table 3.3, it can be noticed that a good accordance between the two molecular techniques is achieved. The largest differences are only related to the chain 1 End-to-End distance and the radius of gyration of the protein in the water environment. The MD radius of gyration data suggest that the protein is more compact in water than in the oil environment, while an opposite trend is detected via DPD. Another considerable dissimilarity regards the standard deviation values calculated with the two techniques. Both MD and DPD were able to identify a smaller error of the respective quantity in oil than in water bulk meaning a less flexible protein structure in the former environment than in the latter. However, all the DPD standard deviations are significantly higher than those obtained via MD. This might be due to two main reasons. First, combining distributions from independent DPD simulations into a single arithmetically averaged distribution involves that the variance of the averaged one is always at least as large as the minimum of the variances of input distributions [215]. Secondly, the soft potential applied in the DPD force field can provide less steric hindrance compared to the Lennard-Jones potential used in MD. Moreover, the higher variation in DPD than MD may be related to the lack of additional bond constraints for intra-protein

Table 3.3 End-to-End distance and radius of gyration mean values and standard deviations of Apovitellenin I in water and oil bulk phases computed via MD and DPD simulations.

			MD	**DPD**[a]
Apovitellenin I in Water	**End-to-End distance** [Å]	Chain 1	50.46 ± 2.93	62.06 ± 18.84
		Chain 2	69.84 ± 2.82	65.87 ± 18.37
	Radius of gyration [Å]		24.98 ± 0.50	35.67 ± 5.26
Apovitellenin I in Oil	**End-to-End distance** [Å]	Chain 1	57.22 ± 0.96	58.38 ± 14.59
		Chain 2	64.49 ± 0.49	63.39 ± 14.20
	Radius of gyration [Å]		27.04 ± 0.13	29.39 ± 2.84

[a] The reported values are extrapolated from respective frequency distributions arithmetically averaged over ten independent simulations.

molecular interaction [60, 216] in the present DPD framework, thus assuming a completely flexible nature of Apovitellenin I without a specific secondary structure. This latter explanation can be also given to the opposite trend of the mean value of the protein radius of gyration reported by means of MD and DPD in the two bulk phases.

Table 3.4 shows the comparison of diffusion coefficient values, D, of Apovitellenin I in water and oil bulk calculated by means of three correlations found in the literature (Eq. (3.16) [208–210]) and computed from MD and DPD simulations. MD protein radius of gyration in the respective solution reported in Table 3.3 are used in expressions based on a such property (Eqs. (3.16b) and (3.16c)). Table 3.4 also reports the diffusion errors in terms of ranges of variability. In particular, the accuracy of correlation results was taken from the corresponding previous works [208–210], meanwhile MD and DPD uncertainties were directly estimated from simulations. As can be seen, both correlation and simulation results show a difference in the protein diffusion coefficient of at least one order of magnitude between the water and oil solution. The larger diffusion coefficient in water than in oil is most likely due to the larger oil viscosity than the water one which can be responsible for the limited mobility of Apovitellenin I in the oil phase. By comparing the results for the water environment, MD and DPD give a remarkable agreement between them although all the correlations indicate a slightly higher value. On the other hand,

Table 3.4 Comparison of diffusion coefficient values of Apovitellenin I in water and oil bulk as predicted by three correlations (Eq. (3.16)) and as computed from MD and DPD simulations.

$D \times 10^{-12}$ [m^2/s]		Apovitellenin I in Water	Apovitellenin I in Oil
	Eq. (3.16a) [208]	82.3 – 127.2	1.47 – 2.27
Correlation results	Eq. (3.16b) [209]	65.7 – 89.0	1.10 – 1.45
	Eq. (3.16c) [210]	80.6 – 97.0	1.40 – 1.65
MD		22.7 – 24.0	0.296 – 0.297
DPD[a]		20.9 – 26.1	1.97 – 2.92

[a] Averaged on ten independent simulations.

the accordance with simulation results is relatively lost when dealing with oil bulk, but the DPD value is noticeably close to those predicted via empirical correlations. It is also important to highlight here that the diffusion coefficient of proteins in solution computed by molecular simulation techniques tends to be underestimated when compared to the true value [217]. That being said, although it is really hard to validate the data reported in Tables 3.3 and 3.4 without experimental evidence, it is possible to affirm that molecular modeling techniques lead to very reasonable results.

Let us move now on to the discussion of the ternary system made by oil, water, and protein via DPD simulations. In order to study the equilibrium properties of such a system, the starting configuration of the DPD box consists of two symmetrical interfaces due to the periodic boundary conditions applied in the three directions. Figure 3.4 shows the equilibrated DPD boxes representing the oil-water interface where Apovitellenin I acts as the surfactant at increasing protein surface concentrations and by highlighting the planar interfaces. Figure 3.5 reports profiles of the number density of oil, water, and protein (i) and stress profiles (difference between normal and tangential pressures, $p^*_{\mathrm{N}} - p^*_{\mathrm{T}}$) (ii) along the normalized x-direction normal to the interfaces at increasing protein interface concentrations corresponding to those of Figure 3.4 ((a), (b), and (c)). The dashed lines represent the interface position in the initial DPD configuration. It points out the initial phase separation and the resulting mutual interpenetration of each component at equilibrium. The profile plots show the symmetry of the equilibrated ternary system and define the interfacial region that contains the protein layer and the bulk region that lies between the interfaces. As it can be seen in Figures 3.5 (a.i), (b.i) and (c.i), the most interesting result is that the protein molecules penetrate the water bulk to a much larger extent than the oil bulk, especially at higher interface protein concentrations. As expected by looking at Table 3.2, this is most likely due to the higher overall repulsion between protein and oil than that between protein and water. By looking at Figures 3.5 (a.ii), (b.ii), and (c.ii), the mechanical equilibrium of the system is reached in both oil and water phases since the stress profiles fluctuate with small oscillations around zero in the bulk regions. As a consequence, the local contribution to the interfacial tension is located only at the interfaces, with an increase in the stress in the protein region. Therefore, the accuracy of the interfacial tension calculation is achieved. In order to avoid size effects along x-axis and allow both interfaces to be independent, the bulk phases must be large enough to reach the mechanical equilibrium by increasing the L_x dimension as the number of protein molecules increases keeping the interface yz-area constant.

Figure 3.6 reports the trend of the protein layer thickness (a), the protein mean radius of gyration, $\langle R_{g,Protein} \rangle$ (b), and, finally, the interfacial tension (c) as a function of the interface concentration of Apovitellenin I. Three independent DPD runs were carried out and the averaged values are shown together with the corresponding standard deviations. Error bars are generally smaller than symbols indicating high reproducibility of the current DPD model. The most remarkable result is the interfacial tension decrease as the protein interface concentration increases. This trend clearly evidences the capability of Apovitellenin I to behave as a surfactant. As expected, the minimum value of the interfacial tension is reached at the saturation of the interface, which no longer allows direct interactions between oil and water. As shown in Figure 3.6(c), the saturation is obtained at the protein interface concentration equal to 3.0-3.5 mg/m^2, where the interfacial tension ranges between 8 and 10 mN/m. The maximum protein coverage (about 3.0 mg/m^2) of the present system is in line with that observed in an experimental work where the oil-in-water emulsion stabilized by flexible proteins (caseins) was studied [218]. Moreover, in the work Ref. [132], it is reported that the equilibrium interfacial tension for the oil-water interface with adsorbed LDL film at pH 3 is 9.5 mN/m, which is markedly consistent with our result. It is also important to highlight that when no protein molecules are added, the interfacial tension between the water and oil phase modeled as homotriglycerides is accurately reproduced in agreement with the experimental value [12, 203]. $\langle R_{g,Protein} \rangle$ (Figure 3.6(b)) is computed from the mean value of the protein R_g distri-

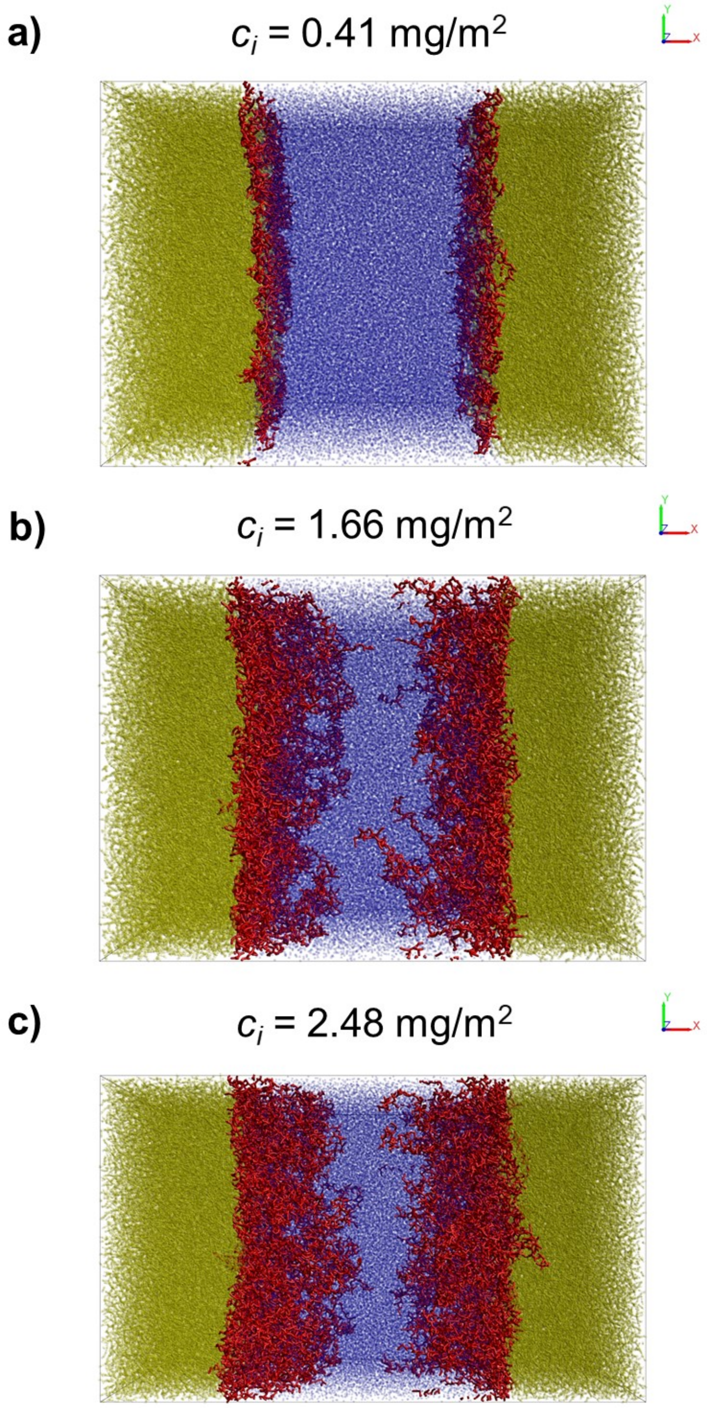

Fig. 3.4 Snapshots of equilibrated DPD boxes of the interface between oil (yellow) and water (blue) where Apovitellenin I (red) acts as the surfactant at increasing protein interface concentration, c_i ((a), (b), and (c)).

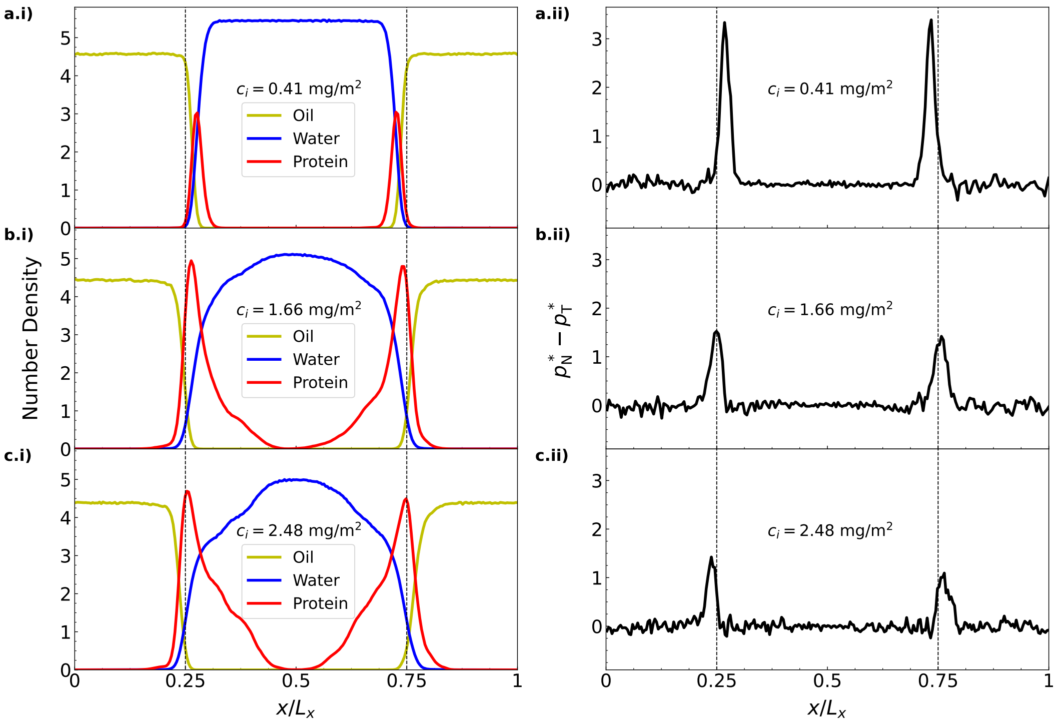

Fig. 3.5 Profiles of the number density of oil, water and protein (i) and of the difference between normal and tangential pressures, $p_{\mathrm{N}}^{*} - p_{\mathrm{T}}^{*}$, (ii) along the normalized x-direction normal to the interfaces at increasing protein interface concentrations ((a), (b), and (c)).

bution, further averaged over three DPD simulations. Therefore, $\langle R_{g,Protein} \rangle$ provides information about the conformation and packing of protein molecules at the interface. At low concentrations, the protein radius of gyration is higher than its corresponding DPD value in both bulk situations (see Table 3.3). This can indicate that, when very few protein molecules are absorbed in the oil-water interface, they assume a more elongated conformation than that in water or oil solution. Meanwhile, at increasing protein concentration, the mean radius of gyration of Apovitellenin I at the interface decreases to a stable value and becomes comparable to that in free solution. Thus, the packing mode of protein molecules at the interface can be considered similar to that observed in bulk phases, when the protein interface concentration is high. Regarding the thickness of the protein layer (Figure 3.6(a)), it is directly derived from the width of the protein density profile along the x-direction normal to the interface surface (see Figures 3.5(i) for reference). As expected, the protein layer thickness increase from 2 to 13 nm as the protein interface concentration increases until the saturation of the interface where the maximum and stable value for the thickness is reached. In the work Ref. [218], it is reported that the adsorbed layer of casein molecules at the maximum coverage of the oil-water interface was about 10 nm thick so that the protein molecules protrude further into the solution, as also shown in this work (Figures 3.4 and 3.5(i)). Moreover, previous works [124, 219] found that the interfacial layer surrounding oil droplets in mayonnaise has an average thickness of around 14 nm, which is comprised of surface-active proteins and lecithin-protein granules from egg yolk. Those findings are reasonably in accordance with our results. It is also straightforward to point out here that the emulsifier behavior of only one LDL apoprotein is tested since it is identified as one of the most surface-active. LDL phospholipids may also have an effect on the interfacial tension of LDL-based emulsion by a further decrease of its saturation value.

In order to study the adsorption of Apovitellenin I at the oil-water interface, DPD simulations of a box containing two equidistant interfaces and one free protein molecule initially located in the center of the water phase were carried out. So, the protein diffusion from the aqueous environment towards the oil-water interface is investigated as represented in Figure 3.7, where an illustrative example shows the three main steps of the protein adsorption mechanism. First, the protein moves to the interface (a), then a portion of the molecule initiates the protein adsorption (b) and, after a certain time, Apovitellenin I is totally adsorbed at the oil-water interface (c). Apparently, there is no specific reason for the protein to be preferably adsorbed at

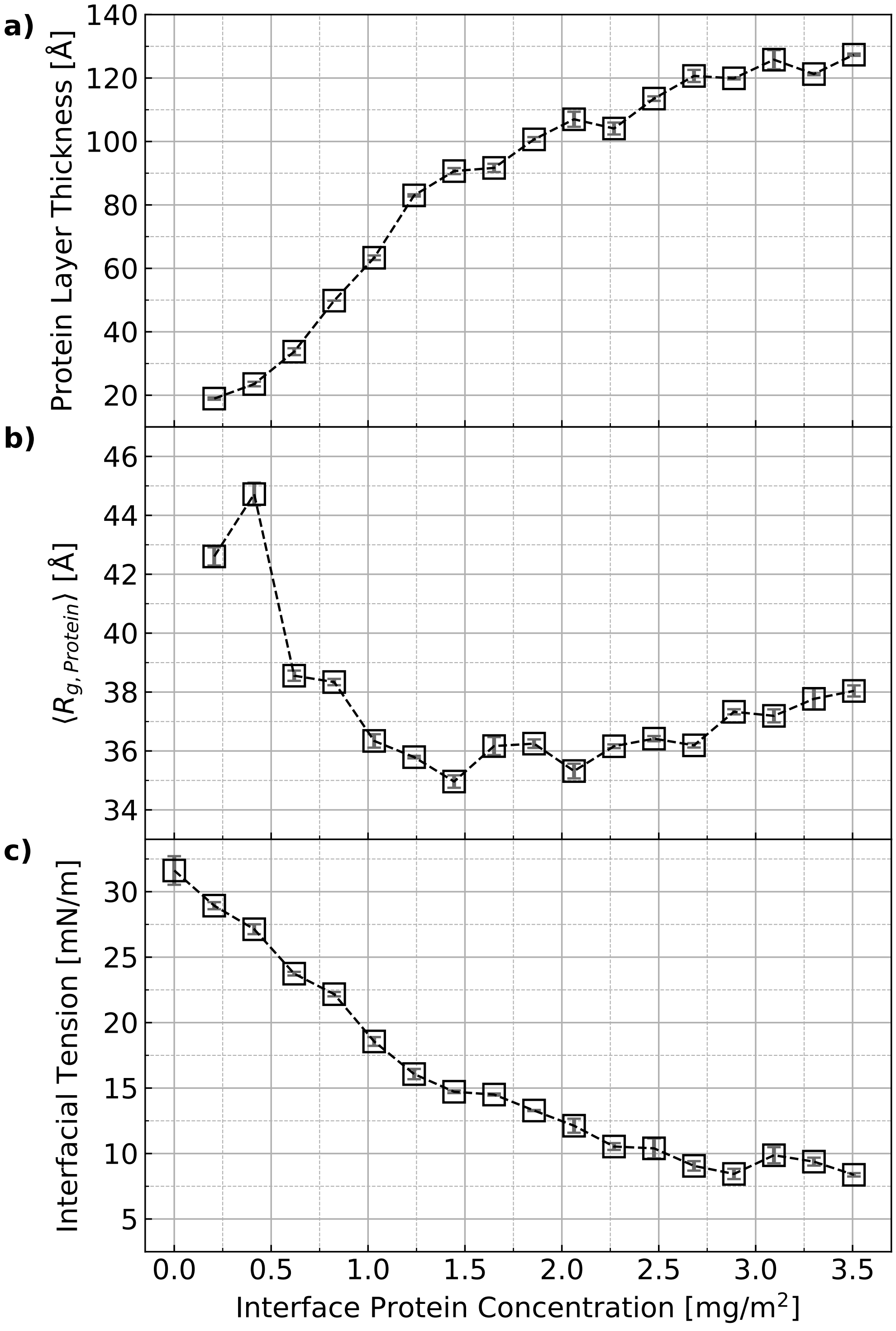

Fig. 3.6 Protein layer thickness (a), protein mean radius of gyration, $\langle R_{g,Protein} \rangle$ (b), and interfacial tension (c) as a function of the interface concentration of Apovitellenin I. Error bars are estimated from three independent DPD simulations.

the right rather than at the left interface as the two sides are symmetrical. Moreover, protein desorption has not been observed meaning that the adsorption process is most likely irreversible as also reported in previous experimental works [1, 19]. To estimate the time required by a protein molecule to be fully absorbed as a function of its distance from the oil-water interface, multiple DPD simulations were performed by increasing the box size in the x-direction normal to the interfaces and the results are summarized in Figure 3.8. Since the oil-to-water bead ratio is kept constant and the protein molecule is placed in the center of the water phase at the beginning of the simulation (see Figure 3.7 for reference), the abscissa of Figure 3.8 represents the initial distance between the geometric center of the protein molecule and the oil-water interface. The y-coordinate of Figure 3.8 expresses the time elapsed from the start of the simulation to the moment in which the protein molecule is totally absorbed in one of the interfaces and it is estimated by visual inspection of simulation time frames. As also done in Figure 3.6, for each point three independent DPD simulations were carried out from which the mean value and the standard deviation were extracted. Although the error bars are relatively large, a linear trend passing through the origin of the axes can be identified in the range of investigated distances. The slope of 0.978 ns/Å can be considered as an estimation of the required time of a liberated Apovitellenin I molecule to be totally adsorbed at a free interface as a function of their mutual distance.

As already stated in section 2.2, LDL particles act as vectors of surfactant constituents (e.g., Apovitellenin I) that could not be soluble in water until they reach the interface. Therefore, a DPD simulation of an LDL-like particle with a lipid core surrounded by one molecule of Apovitellenin I was performed, and the adsorption mechanism at the oil-water interface was tested. Although it is clear that this structure is far from being a realistic representation of an LDL particle, surprisingly the adsorption process proposed in the works Refs. [1, 22] is qualitatively reproduced as it can be seen in Figure 3.9 (Multimedia view). Indeed, first, the LDL-like particle diffuses in the water bulk (a) until the protein situated on the particle surface comes into contact with the interface causing the unfolding of the LDL-like particle (b). Thus, the protein molecule initiates the LDL-like particle disruption by its anchorage at the oil-water interface. Then, the neutral lipids are released from the particle core and merge with the oil phase, while the protein molecule adsorbs at the interface (c) (see also Figure 1.1 for the sake of comparison). Since the system dimensions of Figure 3.9 (Multimedia view) are the same as those represented in Figure 3.7, a

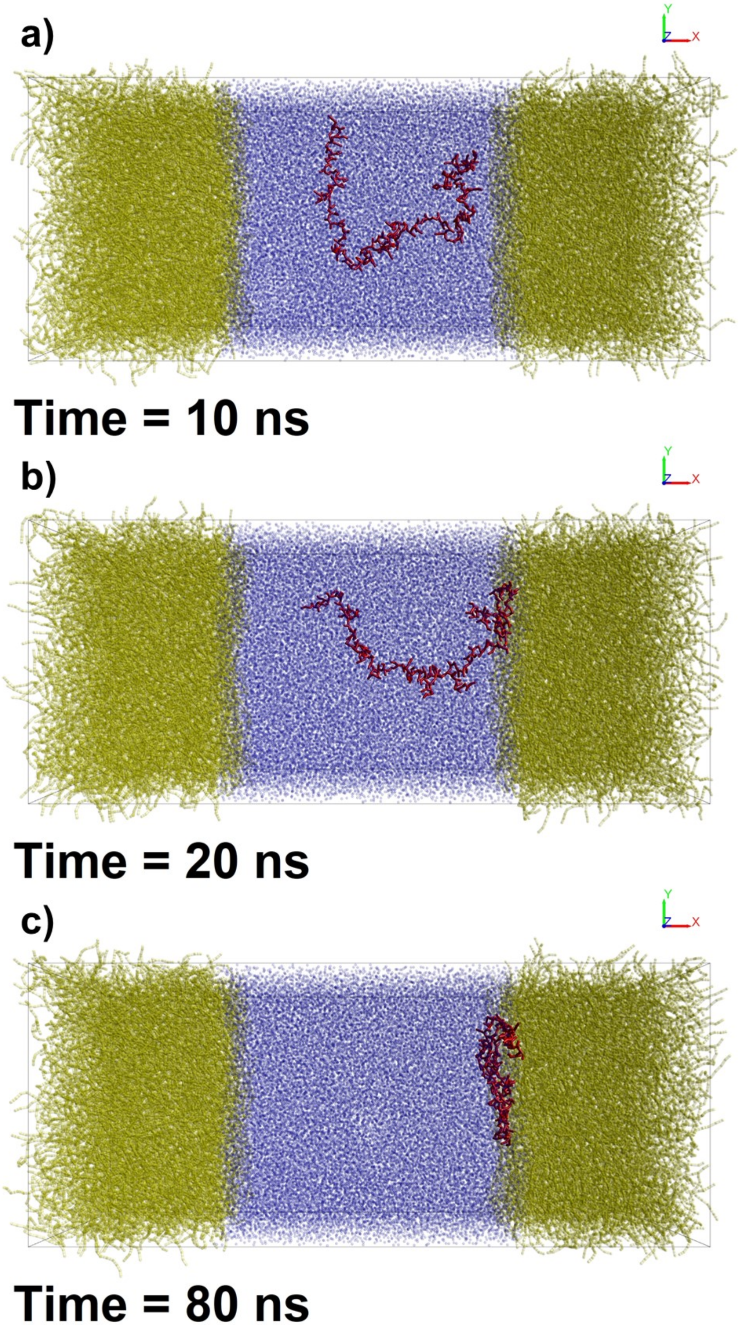

Fig. 3.7 Snapshots of the DPD simulation showing an illustrative example of the adsorption process of Apovitellenin I (one free molecule in red) at the interface between oil (yellow) and water (blue). The most significant steps of the adsorption mechanism are successively represented in (a), (b), and (c).

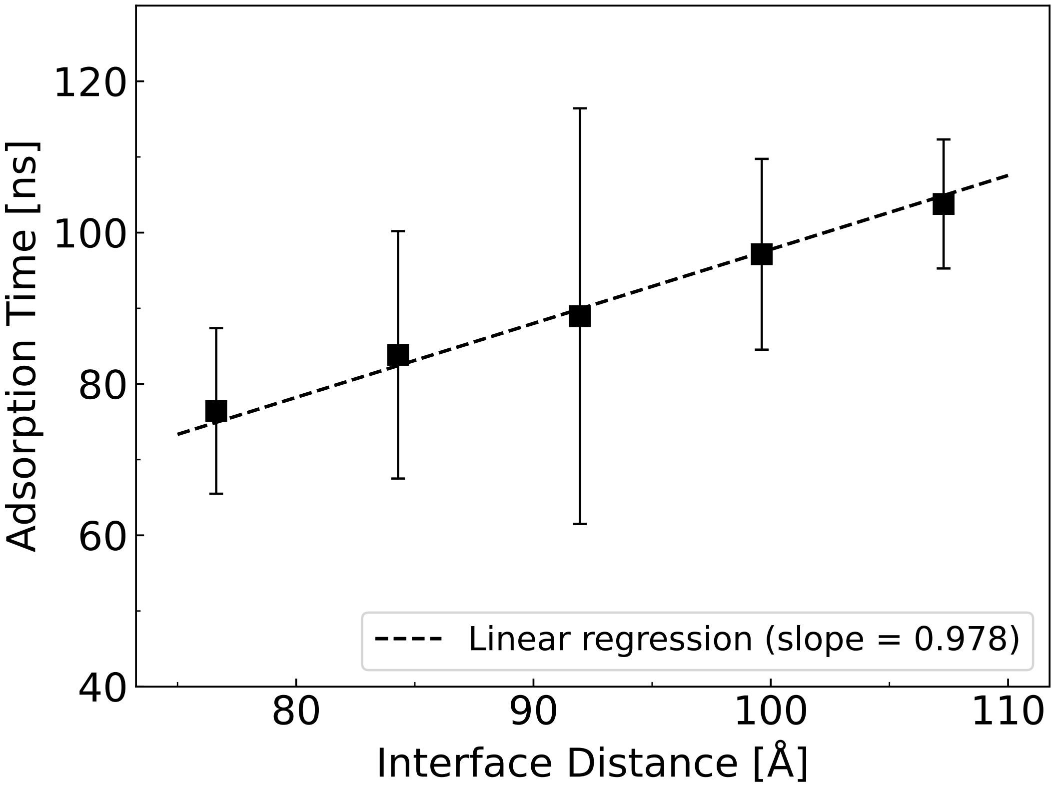

Fig. 3.8 Trend of the time required by one free molecule of Apovitellenin I to be fully adsorbed at the oil-water interface as a function of the initial distance between the protein geometric center and the oil-water interface. Error bars are estimated from three independent DPD simulations.

general comparison can be made between two configurations, namely the liberated protein and the LDL-like particle. In particular, the adsorption time of the LDL-like particle is significantly higher than that of the free protein. This can be intended as a greater stability of Apovitellenin I when surrounding the LDL-like particle rather than as a free molecule, also confirming that the liberated protein is supposed to be almost insoluble in water. Finally, it is important to remark that the representation of the LDL-like particle here presented must be considered qualitative, since both LDL size and its specific composition, namely including also the lipid distribution of the LDL core and all surfactant components situated on the LDL surface (e.g., phospholipids and other apoproteins), were not considered in the analysis.

3.4.1 Application of the thermodynamic model of protein adsorption

Once the optimized parameter set was obtained (Table 3.1), it is verified that the equation of state of the thermodynamic model of protein adsorption (Eqs. (3.5) and (3.9)) fits the data obtained from DPD simulations (Figure 3.6(c)) with an acceptable error as shown in Figure 3.10. Surprisingly, a very good agreement is also noticed between the values of Apovitellenin I with those experimentally obtained for the β-casein at the air-water interface [2]. This shows that these two proteins have a very similar behavior which is typical of flexible protein surfactants [73, 74]. Therefore, this consideration justifies the choice of using the data of β-casein to validate the approach employed here to link different computational methods, namely MetaD and DPD, to obtain a macroscopic property (see also chapter 2 for more details).

To obtain a complete thermodynamic description of adsorption for the Apovitellenin I, there is only the adsorption equilibrium constant b to determine by means of Eq. (3.12). As reported, b only depends on the value of ΔG_{ads}. Therefore, from the metadynamics simulation of Case 1 shown in chapter 2, it was obtained the variation of the Gibbs free energy between the protein in the bulk state and the protein in the adsorbed state (Figure 2.8). Once the constant of adsorption was obtained, it is inserted into the expression of the adsorption isotherm (Eqs. (3.6) and (3.10)) to find the value of the protein bulk concentration for each value of π and Γ obtained from the DPD simulations (Figure 3.6(c)), as reported in Figure 3.11. Although the bulk concentration values appear to be relatively small compared to those of β-casein

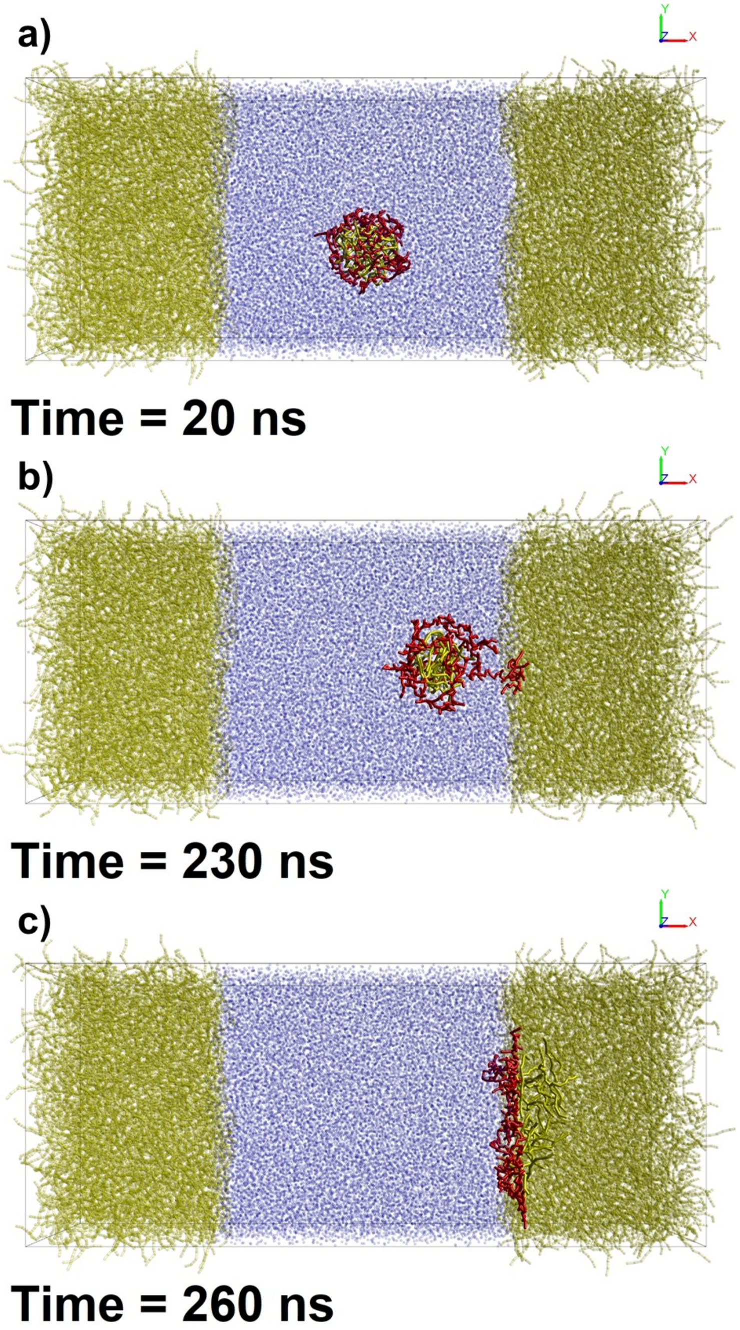

Fig. 3.9 Snapshots of the DPD simulation showing the adsorption process of an LDL-like particle with a lipid core (bright yellow) surrounded by one molecule of Apovitellenin I (red) at the interface between oil (yellow) and water (blue). The most significant steps of the adsorption mechanism are successively represented in (a), (b), and (c) (Multimedia view).

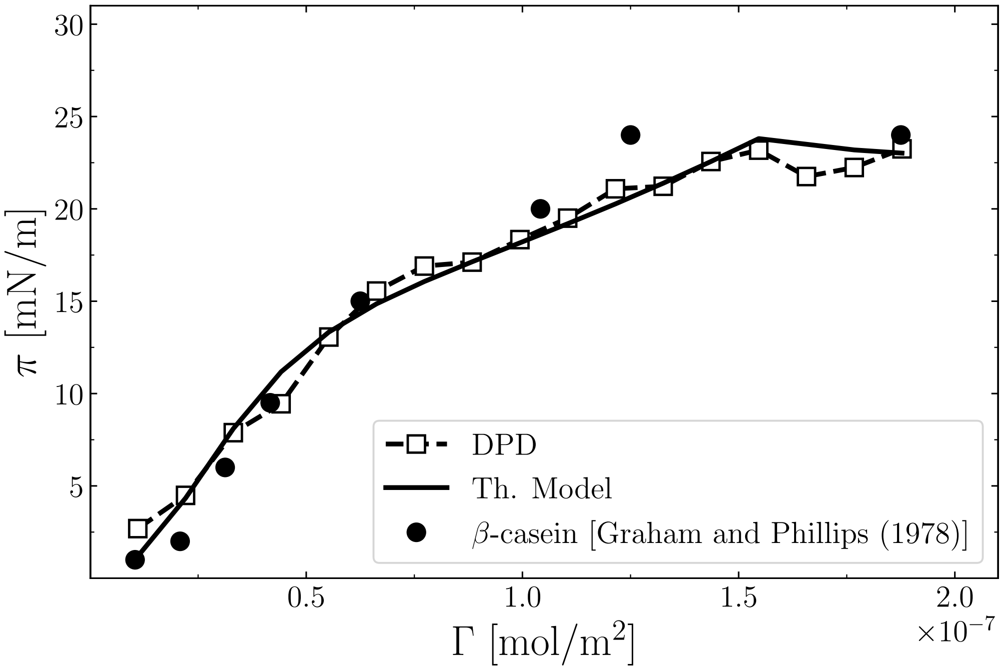

Fig. 3.10 Variation of the surface pressure versus the protein surface molar concentration. The squares represent the data obtained from DPD simulations (Figure 3.6(c)). The continuous line represents the equation of state of the thermodynamic model of protein adsorption (Eqs. 3.5 and 3.9) applied to the Apovitellenin I. The circles represent the experimental data of β-casein at the air-water interface [2].

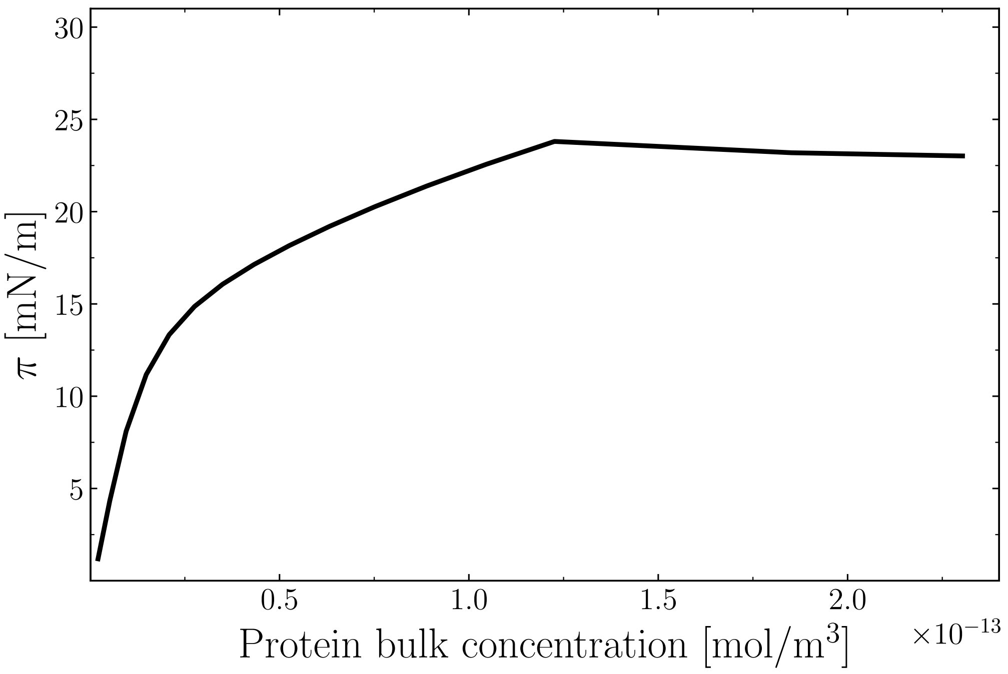

Fig. 3.11 Variation of the surface pressure versus the protein bulk concentration of Apovitellenin I.

[2], there are no experimental data of Apovitellenin I to directly compare this result. Nevertheless, this trend represents a prediction of a macroscopic property that is not easy to experimentally estimate for the protein under investigation. Since this profile only depends on the value of b and, in turn, on the Gibbs free energy of adsorption ΔG_{ads}, the approach and results proposed are eventually validated in section 2.5 by studying the β-casein adsorbing at the air-water interface whose value of ΔG_{ads} is available in the literature [69, 74]. So it is reasonable to consider the trend of Figure 3.11 a valid result.

3.5 Conclusions

Although egg yolk is widely used as an emulsifier in many food emulsion preparations, little experimental research on emulsifying properties of its individual components has been carried out since their extraction and isolation from the egg yolk complex matrix turned out to be difficult. Hence, this work focuses on the molecular model of an oil/water interface stabilized by one of the most surface-active proteins of egg yolk LDLs, called Apovitellenin I. In order to take into account the system size, composition, and the equilibration time needed by macro-molecules to re-arrange at interfaces, the molecular modeling technique here proposed is the Dissipative Particle Dynamics approach. Once the chemical species were determined in section 2.2, especially the biomolecule that should act as a surfactant at the oil/water interface, an automated coarse-graining procedure was carried out on the molecules involved in the ternary system. In DPD systems the intended physical properties are determined by means of a parameter calibration, which was here based on coupling DPD with all-atom Molecular Dynamics simulations of a single protein molecule in two different solvents, water and oil. Thus, both inter- and intra-molecular interactions employed in the DPD system are solely determined by matching the structural data from the atomistic simulations. The model was designed to test the most relevant physical properties of the protein studied, especially its emulsifier behavior. The results of MD and DPD simulations are compared in terms of protein structural and dynamics properties (radius of gyration, end-to-end distance, and diffusion coefficient), showing a good agreement between the two molecular techniques. Then, the oil-water interface system was simulated via the DPD technique. In particular, the present molecular modeling approach was able to properly describe the protein surfactant behavior by interfacial tension decrease at increasing protein surface concentration. The protein density profile, layer thickness, and adsorption time at the oil-water interface were also investigated, giving reasonable results in line with experimental evidence of similar protein systems. In addition, the adsorption mechanism of an LDL-like particle is qualitatively reproduced. A thermodynamic model of protein adsorption was applied to evaluate the increase of the surface pressure at increasing protein surface and bulk concentration. In particular, the equation of state for the Apovitellenin I presents a very similar trend of another protein surfactant, the β-casein. The Gibbs free energy of protein adsorption at the oil-water interface extracted from metadynamics simulations was linked to the DPD simulations to obtain a complete description of Apovitellenin I as a surfactant. Therefore, the modeling method here presented shows how computer molecular simulations can greatly help in the comprehension of food emulsion behavior. In general, this work reports how molecular modeling techniques can be linked together not only to reproduce qualitative behaviors but also to quantitatively predict properties that are difficult to estimate experimentally.

These results are encouraging and could be a starting point to explore the role of other surfactant molecules from egg yolk with an analogous molecular modeling method. In fact, in future works, the thermodynamic model can be applied by considering not only the single protein but also the influence of phospholipids or other competitive proteins for adsorption. Moreover, it can be also interesting to explore the critical surface concentration of phospholipids at which the protein is able to adsorb at the interface. This may represent an important application of the method proposed since the greatest synergistic effect between phospholipids and proteins in decreasing the surface tension can be studied and, as a consequence, a better understanding of the stability of food emulsions can be achieved. Additionally, starting from the thermodynamic model, a kinetic model can be developed to evaluate the decrease of the surface tension over time and, eventually, these findings can be used to improve the mixing time in food emulsion production processes. Moreover, the main findings of this work together with non-equilibrium studies at the mesoscale will pave the way for a better understanding of the breakage and coalescence events of the oil droplets occurring in the food emulsion preparation.

Chapter 4

Scaling of the coarse-grained molecular model

4.1 Introduction

In this chapter, applications of a scaling scheme to oil-water interfacial systems are investigated by means of DPD, also including a coarse-graining procedure for the surfactant molecule referring to chapter 3. Instead of transport processes (viscosity), particular attention is paid to equilibrium properties such as the interfacial tension, highlighting the advantages and limits of the proposed scaling scheme for different levels of coarse-graining. Hence, the combined coarse-graining and scaling procedure are tested for planar interfaces with and without surfactants and the main findings are, eventually, compared with those of the previous chapter. Finally, an example of simulating a droplet configuration is also illustrated and discussed. Therefore, the main aim of this chapter is to study the effects of up-scaling the DPD model to different coarse-graining levels by conserving the equilibrium properties of interfacial systems.

This chapter is structured as follows: in section 4.2 a general background of the scaling relations is illustrated; simulation details are provided in section 4.3, together with all assumptions and simplifications of the modeling approach employed; then, the main results are shown and discussed in section 4.4, and, finally, section 4.5 reports conclusions of this chapter.

4.2 Theoretical background

An overview of the standard Dissipative Particle Dynamics (DPD) method is already provided in section 3.2.1 and can be also found elsewhere in the literature [40–42, 87, 185]. Therefore, here only the main concepts of the scaling procedure employed in this chapter are presented.

Only the definition of the conservative force is recalled since it is involved in studying the static properties of equilibrium systems [42, 87, 200, 220]. In this chapter the conservative force $\mathbf{F}_{ij}^{\mathrm{C}}$ felt by bead i includes contributions from repulsive interactions with surrounding beads and, possibly, contributions due to the springs connecting bead i to other beads in the same molecule. The repulsive force $\mathbf{F}_{ij}^{r}$, which is modeled as a soft repulsion between beads i and j, is already defined in Eq. (3.2). When dealing with a chain molecule, an additional conservative term is considered to maintain bonds between neighbor beads. In this study, the bonds were modeled using a harmonic spring quadratic potential given in Eq. (3.3).

4.2.1 Scaling Relations

In this section, the basic concepts of scaling DPD simulations are presented, together with the nomenclature and notation originally used in the work Ref. [93].

As already stated, the operation of coalescing ν physical particles into one DPD bead is denoted as "coarse-graining" [221]. Being N the total number of DPD beads in a simulation, it holds that $\nu N = N_{phys}$, with N_{phys} is the number of physical molecules represented in the simulation. In order to compare DPD simulations with different coarse-graining levels ν and ν', the scaling ratio $\phi = N/N' = \nu'/\nu$ is introduced. Therefore, functions of ϕ are identified to describe the scaling of various quantities at different coarse-graining levels and these scaling expressions refer to relations between the respective parameters of two systems with different coarse-graining levels ν and ν'. When $\phi > 1$, this means that the same physical space ($L' = L$) is represented by a smaller particle density since each DPD bead in the system denoted by ν' contains a larger number of physical particles. In contrast with the results of work Ref. [221] where the bead density ρ is decreased to ρ' while keeping relevant properties (in particular the particles' radius of interaction) constant, here an alternative scaling process is employed. When changing the level of coarse-graining for the DPD particles, their number is accordingly scaled and their size (radius of interaction) is adjusted in order to keep instead the relative overlap of the interacting particles constant. Hence when a system with many DPD beads is mapped onto one with fewer but larger and heavier particles, the interaction parameters have to be changed in order to maintain the overall system properties. The following scaling relations in three dimensions are therefore here employed [93]:

$$\begin{aligned} v' &= \phi v \,, & N' &= \phi^{-1} N \,, \\ m_i' &= \phi m_i \,, & \rho' &= \phi^{-1} \rho \,, \\ a_{ij}' &= \phi^{2/3} a_{ij} \,, & r_{c,ij}' &= \phi^{1/3} r_{c,ij} \,, \\ \sigma_{ij}' &= \phi^{5/6} \sigma_{ij} \,, & \gamma_{ij}' &= \phi^{2/3} \gamma_{ij} \,, \\ \varepsilon' &= \phi \varepsilon \,, & \tau' &= \phi^{1/3} \tau \,, \end{aligned} \tag{4.1}$$

where $\varepsilon = k_b T$ and τ are energy and time scales, respectively, while k_b stands for the Boltzmann constant and T for the temperature. With these scaling relations, the same physical system shares properties, such as mass density, temperature, and compressibility [93, 95], but it is represented by different coarse-graining levels, using different length and time scales. As it is customary in DPD modeling, energy, mass, time, and length are expressed in reduced units while parameters in Eq. (4.1) have to be considered as dimensional quantities [93]. Indeed, the mass of a single DPD particle, force cutoff radius, and thermal energy are typically employed as basic units in DPD. The length, mass, time, and energy of the system are, thus, not defined explicitly but in terms of these DPD units [42]. It is also shown that the velocity increments $\Delta \mathbf{v}$ obtained from integrating the forces are unchanged when the scaling is combined with the according reduction of units, which implies that the relative particle motions are unaffected by scaling in the reduced unit systems (denoted by a tilde) [93]. Then when going to the reduced units of the primed system, it gives that for the reduced parameter $\widetilde{a_{ij}}$:

$$\widetilde{a_{ij}}' = a_{ij}' \frac{r_{c,ij}'}{\varepsilon'} = \frac{\phi^{2/3} \phi^{1/3}}{\phi} a_{ij} \frac{r_{c,ij}}{\varepsilon} = \widetilde{a_{ij}} \,, \tag{4.2}$$

since a_{ij} scales like energy over length. Similarly, it follows for the reduced $\widetilde{\gamma_{ij}}$:

$$\widetilde{\gamma_{ij}}' = \gamma_{ij}' \frac{r_{c,ij}'^2}{\varepsilon' \tau'} = \frac{\phi^{2/3} \phi^{2/3}}{\phi \phi^{1/3}} \gamma_{ij} \frac{r_{c,ij}^2}{\varepsilon \tau} = \widetilde{\gamma_{ij}} \,, \tag{4.3}$$

since γ_{ij} scales like energy over length and velocity. Finally, from the fluctuation-dissipation relation [42] it gives again that:

$$\widetilde{\sigma_{ij}}' = \widetilde{\sigma_{ij}} \, . \tag{4.4}$$

These relations indicate that the two coarse-graining systems are stochastically equivalent and, therefore, every system with the same values of the reduced variables $\widetilde{a_{ij}}$, $\widetilde{\gamma_{ij}}$, and $\widetilde{\sigma_{ij}}$ have the same state space [93, 95]. This implies that, in reduced units, a DPD calculation performed for a system with small extensions and over a small time interval is numerically identical to one for a much larger system and covering a longer time range. As a result, it can be shown that DPD is a scale-free (truly mesoscopic) method when dealing with simple bulk fluids [93, 95]. The independence of scale for these systems cannot necessarily be upheld for other types of interactions, namely binary mixtures of liquids A and B where more conservative interaction parameters are employed to describe the relative repulsion, such as a_{AA}, a_{AB}, and a_{BB}. Following the scaling relations in Eq. (4.1), the scale independence holds for bulk interactions (a_{AA} and a_{BB}) because the energy associated with an individual DPD particle scale linearly with ϕ, i.e., it is made proportional to the number of molecules a DPD bead represents. On the other hand, a_{AB} is a surface-dependent interaction parameter that determines interfacial energy and therefore may be expected to scale differently [93, 94]. However, in this work, the original scaling relations in Eq. (4.1) are used for any pair interaction i, j and the relative effects will be discussed in section 4.4, in particular as regards the interfacial tension.

When dealing with bonded interactions, the following scaling relations for the parameters k_S and l_H of the harmonic spring quadratic potential (Eq. (3.3)) are employed:

$$k_S' = \phi^{1/3} k_S \, , \;\; l_H' = \phi^{1/3} l_H \, , \tag{4.5}$$

simply obtained by dimensional analysis of units, instead of a more sophisticated method [97]. Indeed, the stiffness parameter k_S scales like energy over squared length, while l_H scales like the length as being the equilibrium length of the bond constraint.

4.3 Simulation details

In this section, the details of DPD simulations performed are presented, together with the appropriate approximations and simplifications adopted. Two case studies are investigated here: first, the interfacial system of a binary mixture modeled via a standard parameterization for the oil and water liquids; second, the ternary system where a protein surfactant molecule is introduced and modeled accordingly to chapter 3. For the first case, the effects of applying the scaling relations in Eq. (4.1) even to a standard interfacial system are studied and the resulting outcome is used for the second case to scale up the ternary system by comparing the equilibrium proprieties of the reference model with those of the up-scaled one. The last example of a droplet configuration is also provided in order to illustrate the capability of the scaling approach to maintain the domain conformation for multi-component systems.

The simple oil/water interfacial system was simulated in an orthorhombic box of constant size $2L \times L \times L$ with $L = 50$ (in absolute units) with periodic boundary conditions, representing the same physical space for different coarse-graining level ratio ϕ where DPD beads have different radii. This can be seen in Figure 4.1 where an example of the simulating boxes of the interfacial oil/water system for $\phi = 1$ (a) and for $\phi = 100$ (b) are reported, highlighting the decrease of the DPD particle number density due to the scaling approach. The initial configuration consisted of a central water phase segregated by two oil phases, thus forming two planar interfaces in equidistant yz-planes. The 50/50 oil-to-water bead ratio was kept constant for all DPD simulations for this case at increasing coarse-graining ratio ϕ. By denoting the oil bead with O and the water bead with W, typical simulation parameters [42] in absolute units for $\phi = 1$ are $r_{c,OO} = r_{c,WW} = r_{c,WO} = 1$, $m_O = m_W = 1$, $\rho = 3$, $\gamma_{OO} = \gamma_{WW} = \gamma_{WO} = 4.5$, $\sigma_{OO} = \sigma_{WW} = \sigma_{WO} = 3$, $a_{OO} = a_{WW} = 25$, and a_{WO} ranging from 50 to 100. These parameters have then been scaled according to Eq. (4.1) for other coarse-graining values of ϕ. Following the energy and time scaling in Eq. (4.1), DPD simulations were run with a time step $\Delta t = 0.02\tau$ for 10^4 equilibration steps and for a production period of 5×10^4 steps. Pressure and interfacial tension were then measured from simulations. In particular, the interfacial tension (IFT) was computed by integrating the difference between normal and tangential stress across the interface separating the segregated components [213], following the same definition given in Eq. (3.17) here considered in physical units.

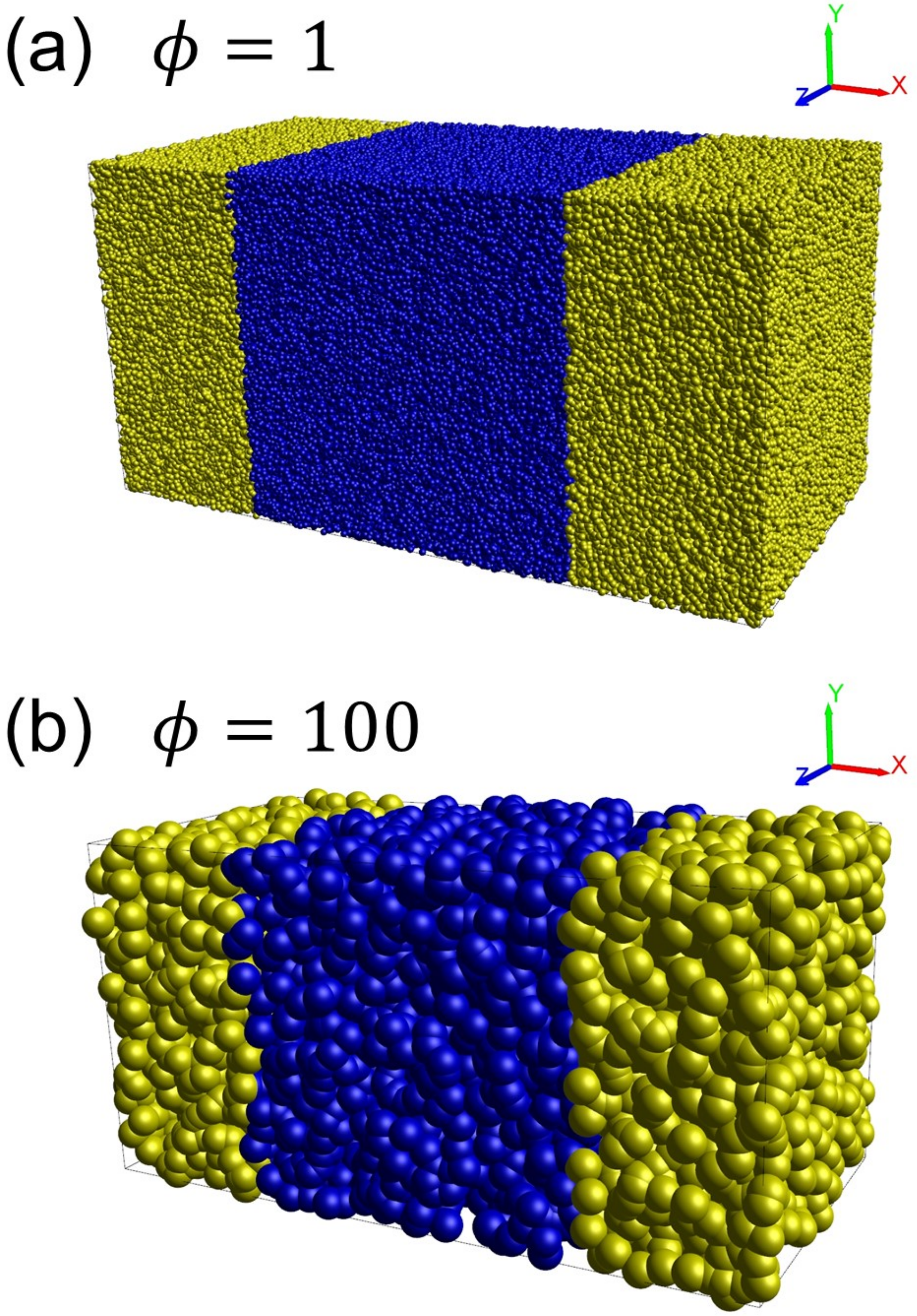

Fig. 4.1 Snapshots of DPD boxes of the planar interfaces between oil (yellow) and water (blue) for $\phi = 1$ (a) and for $\phi = 100$ (b).

The second case, where the scaling approach was tested, focused on reproducing a ternary system made by water, oil, and protein surfactant, which was investigated in chapter 3, thus labeled here as the reference model for $\phi = 1$. The general idea is therefore to scale the DPD model up to the protein molecule level by maintaining the appropriate differences between the three phases. In the reference model, the protein surfactant was modeled as a chain molecule with bonded interactions. Here this level of detail will be lost but favoring instead the mutual repulsion with the remaining two phases (oil and water). First of all, the new coarse-graining level ν' (and ϕ) was decided in order to represent the protein molecule as a single DPD particle or as two bonded beads. In line with the volume equivalence of DPD particles employed in previous works [83, 193, 200], the coarse-graining level ratio $\phi = \nu'/\nu$ was chosen by referring to the protein molecule size, namely by comparing the bead volume of the primed system with that of the reference model. As it has been shown, the protein molecule assumed an almost stable mean radius of gyration of about 36.5 Å after a certain surface concentration at the oil/water interface (Figure 3.6(b)). As a first guess when the protein molecule was modeled with a single DPD bead, this value is then assumed as the radius of the sphere whose volume is compared with that used in the reference model for defining the coarse-graining level ν, namely the volume of a cluster of three water molecules [193]. This leads to preserving bead-size effects when dealing with chain molecules [97, 193], instead of simply comparing the number of beads representing the protein molecule in the reference model. So the coarse-graining ratio ϕ was defined as the ratio of particle volumes: 3008 and 1504 for coarse-graining the protein as a single bead (P) and as two bonded beads (H and T), respectively (Figure 4.2). Therefore, the scaling procedure was applied to the ternary system with these values of ϕ, making the comparison with the reference model. Water (W) and oil (O) beads are then represented by taking into account the coarse-graining ratio ϕ respectively employed. While the water bead in the primed system is made by coalescing ν' number of physical water molecules, oil was also modeled as a chain molecule in the reference system, thus the ratio between the protein and oil molecular volumes gives the number of oil molecules gathered to represent the O bead in the primed system.

As it was done for the simple O/W interfacial system, all DPD simulations of the ternary interfacial system were performed in an orthorhombic box of constant size $2L \times L \times L$ with $L = 128$ (in absolute units) with periodic boundary conditions. This box size was employed in order to simulate a number of total particles N' large

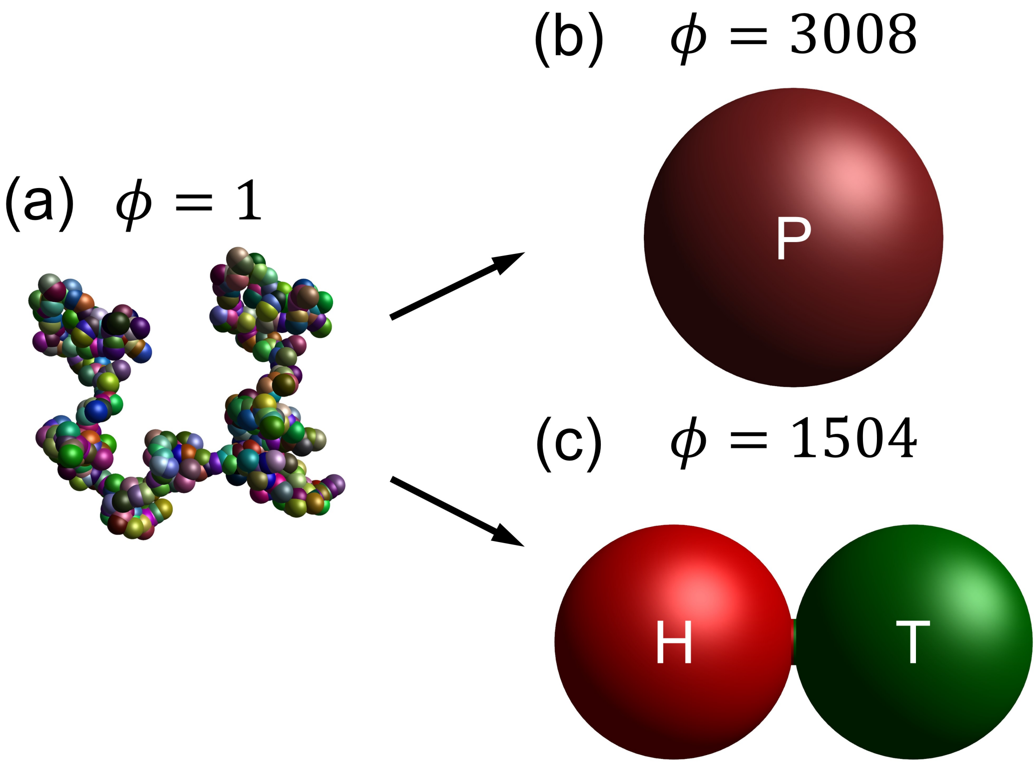

Fig. 4.2 Schematic representation of the coarse-grained protein molecule in the reference DPD model (chapter 3) with $\phi = 1$ (a) and in the up-scaled DPD model with $\phi = 3008$ (b) and $\phi = 1504$ (c).

enough to gather statistically relevant results. For the interfacial system, the 50/50 oil-to-water bead ratio was again kept constant, and both the number of water and oil beads filling the simulation box was adjusted to keep the same overall number density ρ' when the protein beads were also added in the DPD box. Indeed, simulations were performed to study equilibrium proprieties of the interfacial system, such as the interfacial tension, at increasing protein surfactant concentration, where its surface number density was calculated as will explain in Appendix A. The initial configuration again here consisted of a central water phase segregated by two oil phases, thus forming two planar interfaces in equidistant yz-planes. The protein molecule beads were initially located at the oil–water interface to make sure that both interfaces contain the same number of surfactants in order to perform averages on both interfaces. In line with chapter 3 for $\phi = 1$, simulation parameters in absolute units are $\rho = 5$ and $\gamma_{ij} = 4.5$, $\sigma_{ij} = 3$, for any bead pair ij, then scaled according to Eq. (4.1) for corresponding coarse-graining values of ϕ (3008 or 1504). $m'_P = 2m'_H = 2m'_T$ is determined by the ratio between the molecular mass of the protein and that of three water molecules, while m'_O by the ratio of the oil molecule mass and that of three water molecules multiplied for the number of oil molecules coalesced in the O particle based on the ϕ value used. As regards the repulsion a_{ij} parameters, they are listed in Table 4.1 and, apart from $r_{c,WO} = 1$, $r_{c,ij}$ is equal to 0.7 according to chapter 3 for $\phi = 1$. Also, these parameters have been scaled following Eq. (4.1). It is straightforward to underline here that self-repulsion parameters of oil and water (a_{WW} and a_{OO}) have been obtained by respective bulk simulations. Since the pressure of bulk fluids is independent of the coarse-graining ratio ϕ by means of Eq. (4.1) [93], a_{WW} was exactly the same used in the reference model (chapter 3), while a_{OO} was determined by letting the oil bulk phase pressure in the primed system being the same as for $\phi = 1$ (results not shown). The inter-repulsion parameters were obtained in order to give the best matching with the interfacial tension values as it will be shown in section 4.4. In particular, three parameterization cases have been tested for the P bead when the protein molecule was modeled as a single particle while a clear distinction between the hydrophilic (H) and hydrophobic (T) part was made if the protein was described by two beads. Therefore, when applying such a coarse-graining procedure, the obtained repulsion parameters were still representative of surfactant interactions, however, the level of molecular details was much smaller than the case of $\phi = 1$. Moreover, the harmonic potential parameters used for the bond between H and T beads are $k_S = 400$ and $l_H = 1$, as a first guess, then scaled

Table 4.1 Repulsion parameters a_{ij} used in this chapter. Note that these parameters have been then scaled according to Eq. (4.1) based on the value of ϕ employed.

a_{ij}		W	O	P	H	T
W		25	-	-	-	-
O		16.5	50	-	-	-
P	case 1	60	90	30	-	-
	case 2	70	105	35	-	-
	case 3	80	120	40	-	-
H		20	200	-	15	-
T		90	40	-	15	15

according to Eq. (4.5). Following again the time and energy scaling in Eq. (4.1), these DPD simulations were performed with a time step $\Delta t = 0.001\tau$ for 3×10^4 equilibration steps and a production period of 10^5 steps. Density profiles, pressure, and interfacial tension were then measured from simulations. Here the interfacial tension was calculated again as reported in Eq. (3.17).

An illustrative test was also conducted by simulating an oil droplet in water bulk in presence of protein surfactants at equilibrium in order to investigate the capability of the parameterization employed and the scaling procedure for an additional interfacial system setup. For both $\phi = 3008$ and $\phi = 1504$, the initial conditions and the physical space simulated are the same. Being $R = 65$ the initial radius of the sphere containing the oil phase, DPD simulations were performed in a cubic box with $L = 4R$. As in the previous case, these box dimensions were used to simulate a number of total particles N' large enough to gather statistically relevant results. The sphere was then filled with oil beads and the remaining space with 700 protein molecules (single bead or two-bead molecule depending on the value of ϕ adopted) and with a number of water particles in order to have an overall $\rho = \phi\rho'$ equal to 5. The same simulation parameters were employed and, in particular, only case 3 of Table 4.1 was studied for the P bead type parameterization. Simulations were run for a total of 2.5×10^5 steps, out of which 5×10^4 steps are used to equilibrate the system, saving time frame data for post-processing every 250 steps. Thus, the time-averaged distributions of the radius of gyration of the oil droplet surrounded by protein molecules were then measured for both ϕ cases.

All DPD simulation setup, runs, and post-processing analyzes were conducted within the CULGI software package [214], together with all other tools and algorithms employed in this chapter.

4.4 Results and discussion

In this section, the main findings are presented and discussed. First, the analysis of the simple DPD O/W interface is carried out, and, then, applications of the scaling procedure to more complex systems are reported.

Figure 4.3 shows the pressure (a) and IFT′ (b) trends with varying the coarse-graining ratio ϕ for the simple O/W interface, for three values of the a_{WO} parameter. A relatively small non-linear increment is detected as regards pressure values at increasing ϕ. In the work Ref. [93], it is already reported that pressure in a DPD simulation of a bulk fluid with periodic boundary conditions for different self-repulsion parameters a and for various ϕ values is independent of the coarse-graining. Therefore applying the scaling relations in Eq. (4.1) to a binary system leads to the loss of pressure independence of the coarse-graining ratio. This can be related to the use of the same scaling expression also for the surface term a_{WO} [93]. On the other hand, for each a_{WO} value it is clearly evident that the interfacial tension (in physical unit) IFT′ computed from DPD simulations (Eq. (3.17)) scales with ϕ^{C}, where $C = 1/3 \leq 1$ as suggested in the work Ref. [93], so that:

$$\mathrm{IFT}' = \phi^{1/3}\mathrm{IFT}\ . \tag{4.6}$$

It is important to highlight here that this result is in line with the works Ref. [94, 222]. Such scaling relation for the interfacial tension can be expected by dimensional analysis of units in Eq (4.1). In fact, following the notation of reduction of units from the work Ref. [93], it is also possible to show that:

$$\widetilde{\mathrm{IFT}'} = \mathrm{IFT}'\frac{r_c'^2}{\varepsilon} = \phi^{1/3}\mathrm{IFT}\frac{\phi^{2/3}r_c^2}{\phi\varepsilon} = \widetilde{\mathrm{IFT}}\ , \tag{4.7}$$

since interfacial tension reduces as energy over squared length. Hence, scaling and unit reduction precisely cancel each other. As a result, in the DPD framework, the reduced interfacial tension $\widetilde{\mathrm{IFT}}$ is scale-free, meaning that the calculation of this equilibrium property with a single set of parameter values represents interfaces at arbitrary length scales. In order to study how the scaling relations affect the interfacial tension calculation, the stress profiles of the simple O/W system along the normalized x-direction normal to the interfaces at increasing coarse-graining ratios ϕ are shown in Figure 4.4. The mechanical equilibrium of the system is reached in both the oil and water phases since the stress profiles fluctuate with small oscillations around zero in the bulk regions. As a consequence, the local contribution to the interfacial tension is located only at the interfaces, with an increase in the stress in the O/W interface region. Therefore, the accuracy of the interfacial tension calculation is achieved. As it can be seen, both pick heights and interface region width increase as the coarse-graining ratio ϕ increases, determining an increment in the IFT$'$ value (see Eq. (3.17)). This can be referred to as a combined effect of scaling both $r_{c,ij}$ and a_{ij} parameters according to Eq. (4.1).

Let us move now on the discussion of the ternary system made by oil, water, and surfactant (protein) when applying the scaling relations (Eq. (4.1)) to a reference system ($\phi = 1$) investigated in chapter 3, for two coarse-graining ratios ϕ. In order to study the equilibrium properties of such a system, the starting configuration of the DPD box consists of two symmetrical interfaces due to the periodic boundary conditions applied in the three directions. Figure 4.5 shows the equilibrated DPD boxes representing the oil-water planar interfaces covered by surfactant molecules for $\phi = 3008$ (case 3 in Table 4.1) (a) and $\phi = 1504$ (b). Figure 4.6 reports the number density profiles of oil, water, and surfactant beads along the normalized x-direction for the coarse-graining ratios ϕ investigated here at two surfactant molecule number density c_p. By looking at Figures 4.5 and 4.6, the symmetry of the equilibrated ternary system can be seen. Density profiles define the interfacial region that contains the surfactant layer and the bulk region that lies between the interfaces, highlighting the mutual interpenetration of each component at equilibrium. Therefore, the parameterization of the three species combined with the scaling procedure explained in section 4.2.1 are able to maintain the structural properties of the interfacial system, even at a high level of coarse-graining ratio ϕ. In Figure 4.6, it is straightforward to note that number density values are expressed as $\phi\rho'$ to make profiles comparable between ϕ equal to 3008 and 1504. Although the overall number density ρ is kept constant, the local bulk density of oil and water beads fluctuates around a value different from 5 due to the fact that self-repulsion parameters used in this work for oil and water (a_{OO} and a_{WW} in Table 4.1, respectively) are not the same value

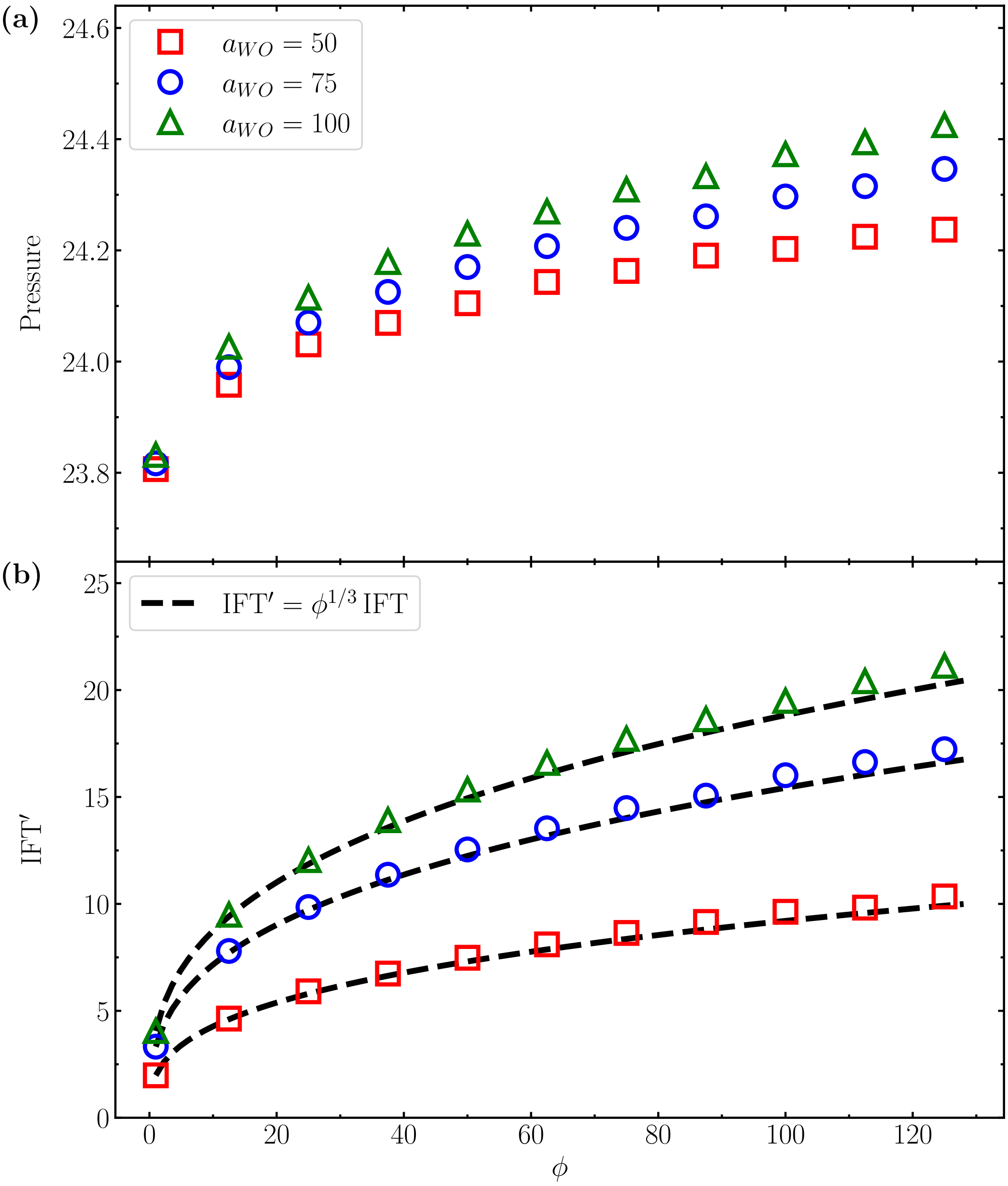

Fig. 4.3 Pressure (a) and IFT′ (b) trends with varying the coarse-graining ratio ϕ for the simple O/W interface. Empty symbols stand for the results of DPD simulations with the repulsion parameter a_{WO} equal to 50 (red squares), 75 (blue circles), and 100 (green triangles), respectively. Black dashed lines represent the scaling relation for the interfacial tension: $\mathrm{IFT}' = \phi^{1/3}\mathrm{IFT}$.

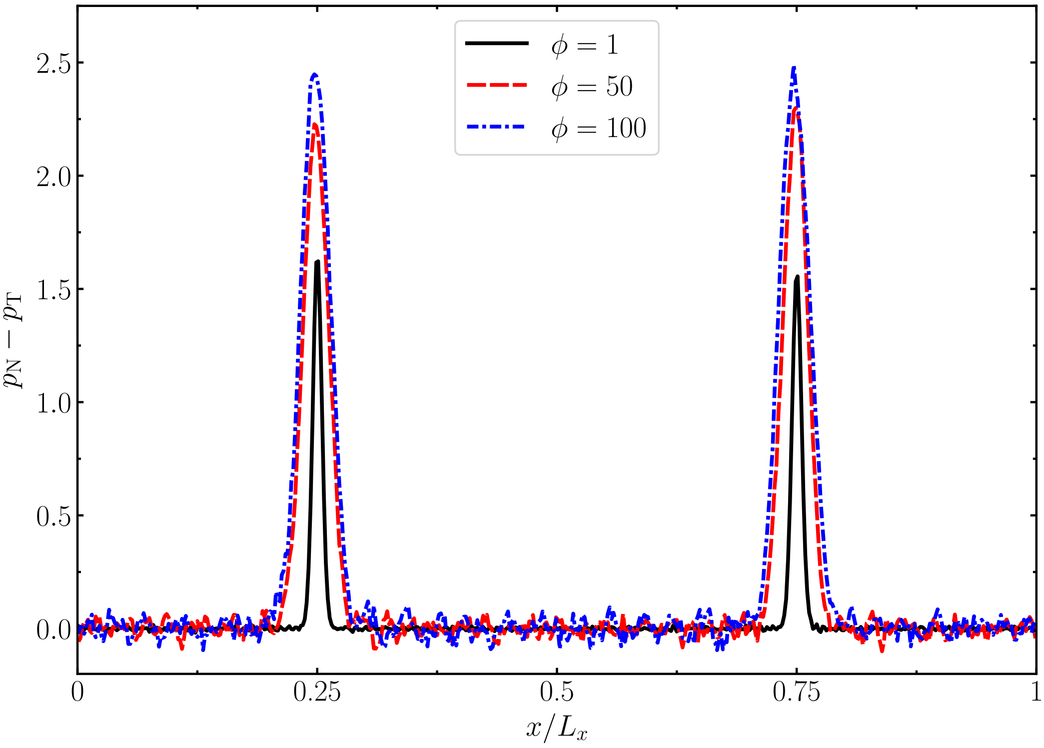

Fig. 4.4 Stress profiles (difference between normal and tangential pressures, $p_{\mathrm{N}} - p_{\mathrm{T}}$) along the normalized x-direction normal to the interfaces at increasing coarse-graining ratios ϕ for the simple DPD O/W system with $a_{WO} = 50$.

[223]. A closer look at the surfactant density profiles reveals that an appreciable number of surfactant beads are not adsorbed at interfaces since surfactant density values are not zero at the oil and water bulk regions. This effect is more relevant at higher c_p and for the case of $\phi = 3008$. In fact, at the same c_p the surfactant density peaks are higher for $\phi = 1504$ than for $\phi = 3008$, meaning that a higher number of surfactants molecules are adsorbed at the interface in the former case than in the latter. This effect justifies the quantification of the surfactant molecules actually adsorbed at the interface at increasing surfactant concentration. This is obtained from the surfactant density profiles by implementing an automatic procedure to determine the protein surface density at equilibrium as explained in Appendix A. However, Figure 4.6 also shows that, when using the up-scaled DPD model, a clear distinction between hydrophilic and hydrophobic parts in the surfactant molecule as done for $\phi = 1504$ (see Figure 4.2 and Table 4.1) provides better results in terms of preserving the reference conformation at equilibrium. In particular, for $\phi = 1504$ the surfactant molecules penetrate the water bulk to a much larger extent than the oil bulk, especially at higher c_p values as already reported in section 3.4.

Figure 4.7 represents the most interesting result of this chapter. It reports the interfacial tension as a function of the surfactant (protein) surface number density by comparing the reference results for $\phi = 1$ from section 3.4 [83] with those obtained in this chapter with $\phi = 3008$ (a) and $\phi = 1504$ (b). Three independent DPD runs were carried out and the averaged values are shown together with the corresponding standard deviations. Error bars are generally smaller than symbols indicating high reproducibility of the current DPD model. As it is shown that the interfacial tension scales following the Eq. (4.6), it is expressed here as $\mathrm{IFT}'/\phi^{1/3}$ in order to make its values comparable at different coarse-graining ratios ϕ. When no surfactant is added to the simulation box, it is important to highlight that, besides the scaling relation, the interfacial tension value between the oil and water phase is accurately reproduced by using the same parameterization of water and oil beads for different ϕ (Table 4.1). As it can be seen, a very good agreement is achieved for both ϕ values investigated here at increasing protein surface number density. Apart from a simple a parameters fine-tuning, then it is possible to preserve the interfacial tension trend in an up-scaled DPD model with surfactant (protein) molecules. In both cases, the interfacial tension decreases as the protein surface density increases until it reaches a minimum value at the saturation of the interface. As it is shown, a further increase in protein surface concentration has almost no effect on the interfacial tension, which is

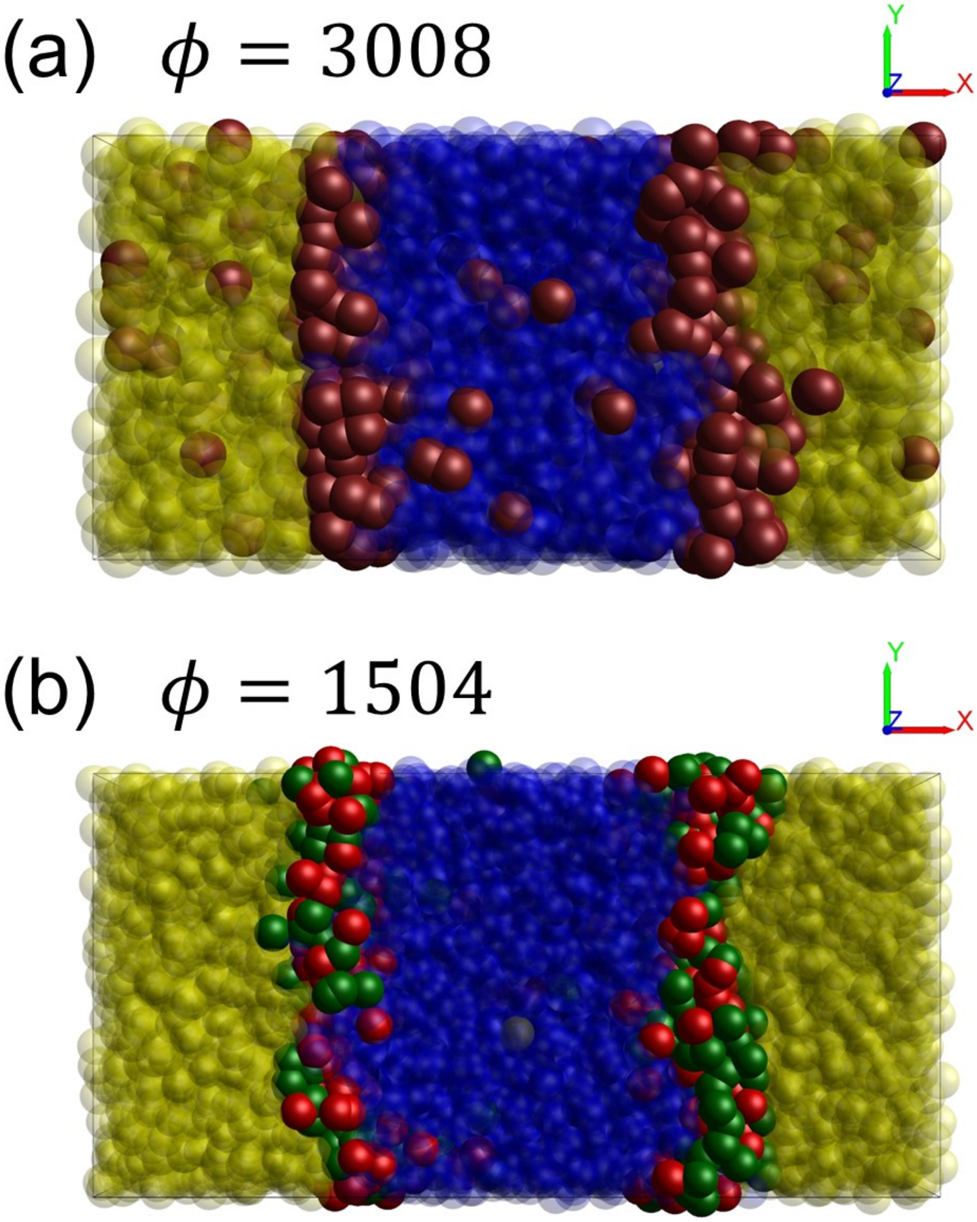

Fig. 4.5 Snapshots of equilibrated DPD boxes of the planar interfaces between oil (yellow) and water (blue) covered by surfactant molecules (brown beads for $\phi = 3008$ (case 3 in Table 4.1) (a), green and red beads for $\phi = 1504$ (b)), at the surfactant molecule number density c_p equal to 3.05×10^{-4} [numbers per unit volume].

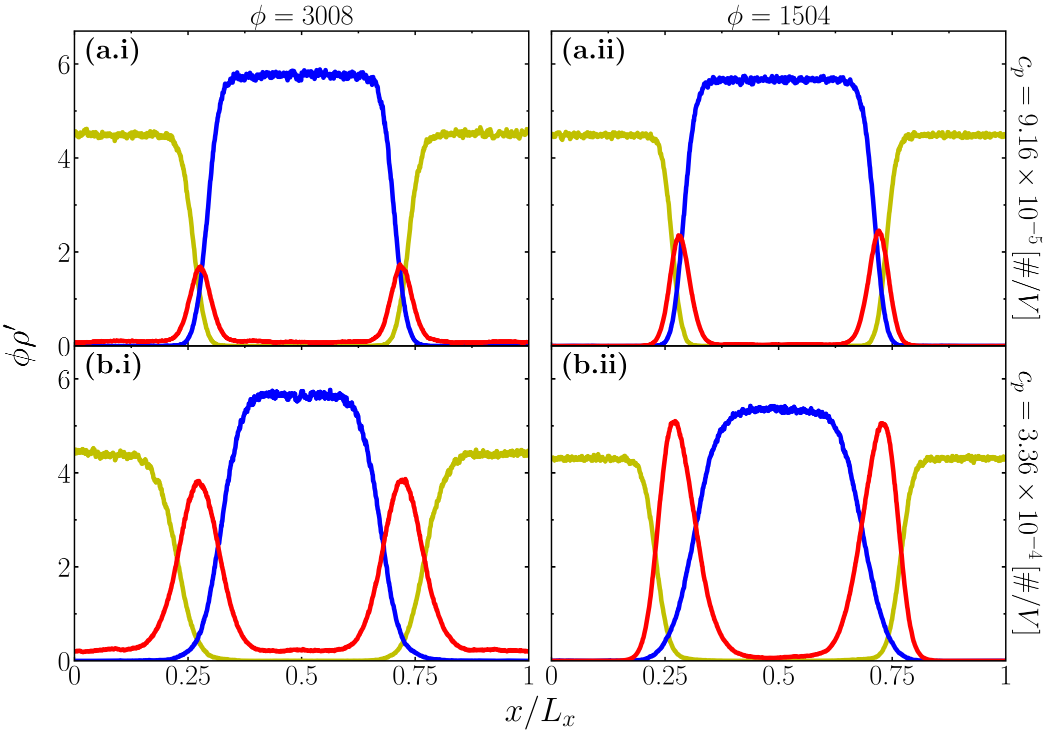

Fig. 4.6 Number density profiles of oil (yellow lines), water (blue lines), and surfactant (red lines) along the normalized x-direction normal to the interfaces with the coarse-graining ratio ϕ equal to 3008 (case 3 in Table 4.1) ((a.i) and (b.i)) and 1504 ((a.ii) and (b.ii)) at two surfactant molecule number densities c_p ((a.i), (a.ii) and (b.i), (b.ii), respectively).

a typical behavior of an interfacial system stabilized by protein surfactants [2, 73]. However, some differences are identified with respect to the reference system with $\phi = 1$. As regards $\phi = 3008$, all three protein bead parameterization leads to larger deviations from the reference data at lower protein concentrations while smaller ones correspond to the protein parameterization of case 3 in Table 4.1 at higher protein concentrations. On the other hand, concerning $\phi = 1504$, an almost perfect match with the reference case is obtained at lower protein concentrations. Nevertheless, the interfacial tension reaches the minimum value at the saturation of the interface at a lower protein concentration than that of $\phi = 1$. The values of protein surface number density are obtained as explained in Appendix A. As already illustrated in Figure 4.6, each symbol corresponds to the same initial protein volume number density c_p in Figure 4.7, thus the effect of the different numbers of molecules adsorbed at the interface depending on the coarse-graining ratio ϕ is here even more evident. In fact, when ϕ is equal to 3008 increasing oil, water and self-repulsion parameters of P bead type (from case 1 to case 3 of Table 4.1) leads to a better absorbing capability but a worse surfactant behavior in terms of the interfacial tension reduction. If the protein molecule is modeled as two bonded beads by distinguishing between the hydrophobic and the hydrophilic contribution as done for $\phi = 1504$, the best adsorbing activity is obtained. In Figure 4.8 the pressure trends for different ϕ values are then reported at increasing protein volume number density. When the oil/water interface is free of protein molecules, the pressure value increases non-linearly going from the case of $\phi = 1$ up to $\phi = 3008$ as expected by looking at Figure 4.3(a). Then, clear differences in the pressure trends are observed. Although pressure decreases slight linearly for $\phi = 1$ at increasing protein concentration, it increases non-linearly for $\phi = 3008$. This appears to be related to the protein coarse-grained model used for $\phi = 3008$. In fact, if $\phi = 1504$ and the protein molecule is represented by at least two bead types, the pressure trend is decreasing as well. Nevertheless, its slope is relatively larger in absolute value than that of $\phi = 1$. Therefore, it seems that the pressure profile cannot be precisely reproduced at higher coarse-graining levels when most molecular details are lost.

As the last result of this chapter, Figure 4.9 shows an illustrative example of using the scaling procedure to simulate an oil droplet in water bulk in presence of surfactants. As explained in section 4.3, the initial conditions and the physical space simulated are the same for $\phi = 3008$ and for $\phi = 1504$. Hence similarities and differences between the two coarse-graining ratio cases are investigated. In both

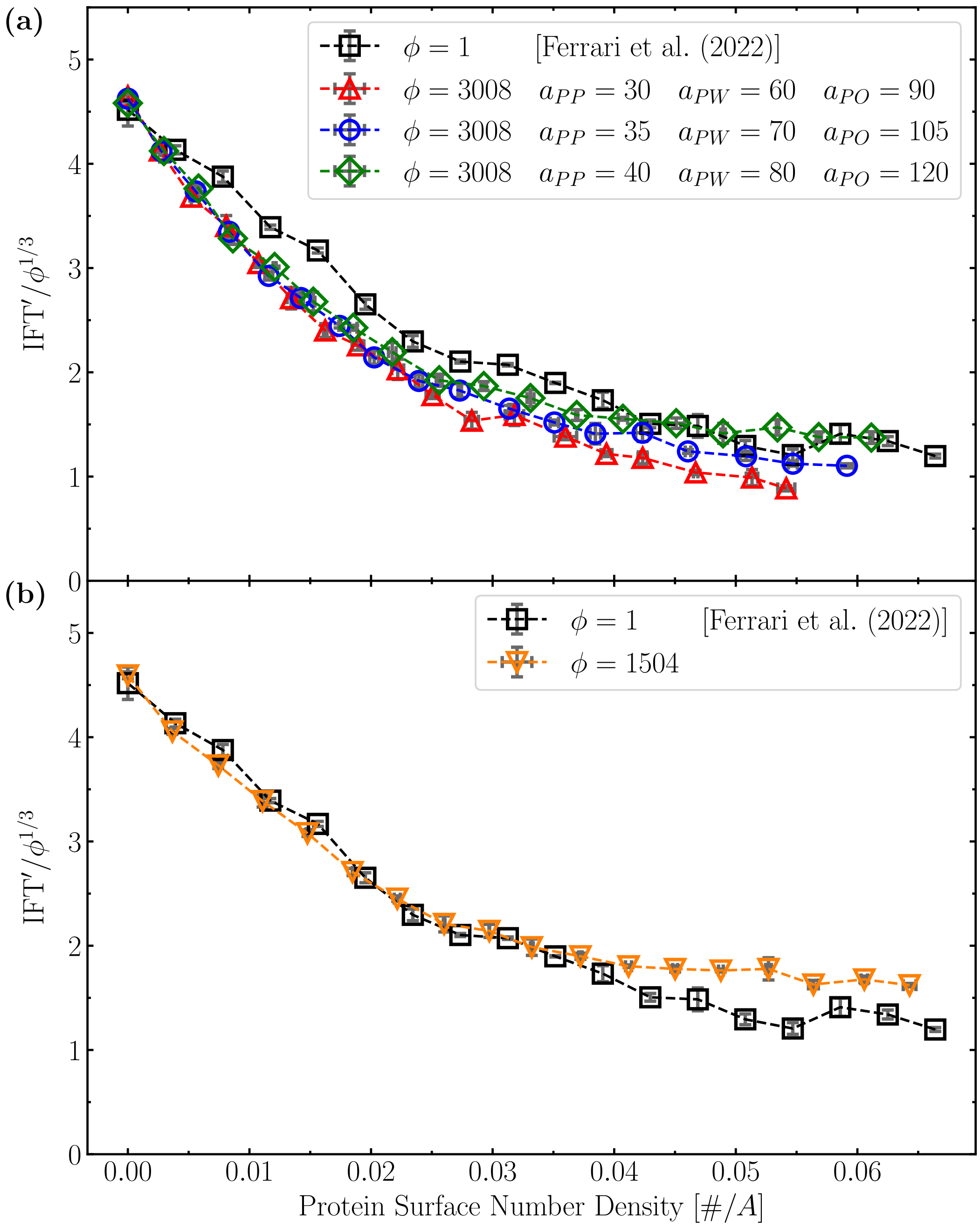

Fig. 4.7 Interfacial tension as a function of the protein surface number density, comparing between reference results for $\phi = 1$ and for $\phi = 3008$ (a) and $\phi = 1504$ (b). Error bars are estimated from three independent DPD simulations.

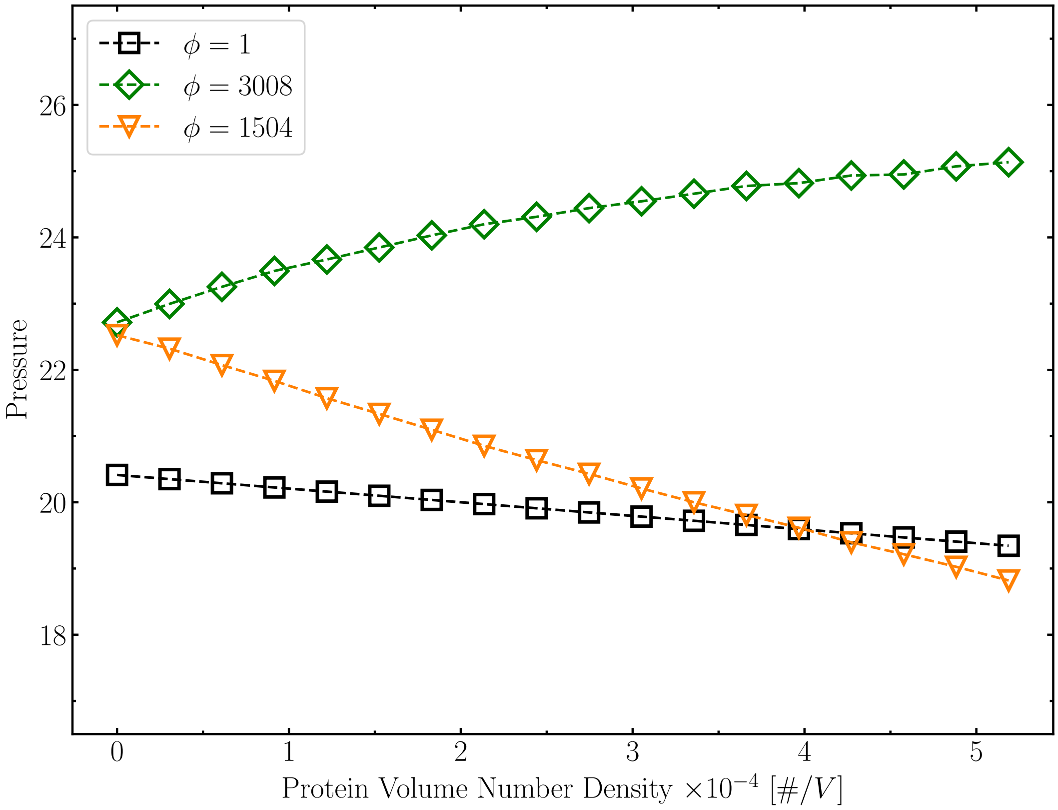

Fig. 4.8 Pressure trends for different ϕ values at increasing protein volume number density. Similar data are obtained with different parameterizations of P bead type, thus results for $\phi = 3008$ only referring to case 3 of Table 4.1 are reported. Error bars related to three independent DPD simulations are much smaller than the symbol size, thus they are not shown.

of them, it is important to highlight that the equilibrium configuration as a single droplet is observed due to the parameterization and the scaling procedure employed. This can demonstrate once again that the scaling relations in the DPD framework are able to describe different structural conformations. However, by comparing the $\phi = 3008$ case with the $\phi = 1504$ one it is again shown that the adsorbing capability of protein molecules is better reproduced if they are modeled by two bonded beads than a single bead. This can be seen by looking at the time-frequency distributions of the radius of gyration value of the oil droplet covered by surfactant molecules and at the corresponding snapshots of clipped simulation boxes in Figure 4.9. In fact, the protein beads appear to be more dispersed in the simulation box for $\phi = 3008$ than for $\phi = 1504$, also represented by a bit smaller mean value of the droplet radius of gyration, meaning fewer protein molecules adsorbed at the oil droplet interface with respect to the case of $\phi = 1504$. Moreover, the smaller standard deviation of the frequency distribution and the better quality of the fitting through the Gaussian distribution indicate more stability of the droplet modeled with $\phi = 1504$ than with $\phi = 3008$. If the same length conversion factor is used from section 3.3.2, then the corresponding mean values of the droplet radius of gyration are 43.7 and 45.4 nm for $\phi = 3008$ and for $\phi = 1504$, respectively. However, it must be stated that these numbers are based on speculative assumptions on spatial and time scales associated with DPD units. However, this seems in line with respect to previous works on simulating a single droplet via DPD [224–226].

4.5 Conclusions

In this chapter, we explored the possibility to use classical DPD to describe an oil-water and an oil-water-surfactant system using the concept of level of coarse-graining, with the aim to obtain a simplified model capable of reproducing properly the drop of interfacial tension observed with more detailed mesoscale simulations. We found that the classical DPD model is invariant with respect to the proper definition of the level of coarse-graining, as argumented in the work Ref. [93]. When dealing with interfacial systems which are one of the most successful applications of the DPD method, they tend to exhibit a typical length scale due to the domain formation. This means that the independence of the length scale cannot anymore be achieved. However, in this chapter, we showed that, if an interfacial system can be simulated

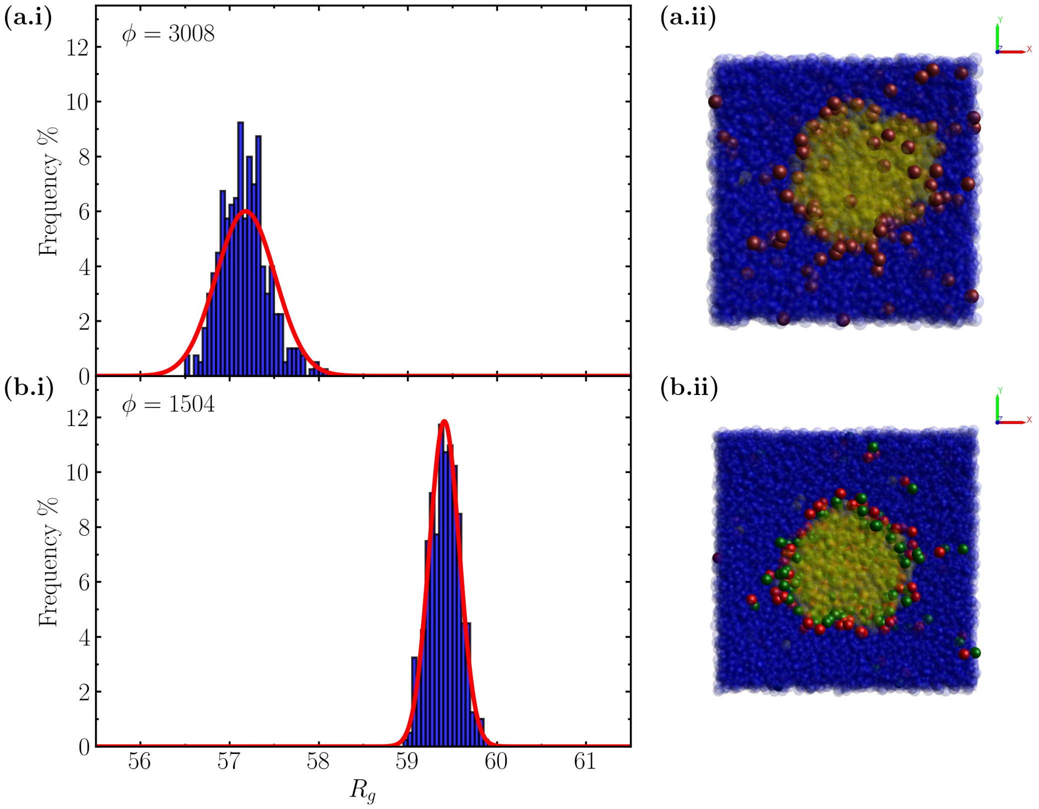

Fig. 4.9 Time-frequency distributions (blue histograms) of the radius of gyration value of an oil droplet covered by surfactant molecules in water bulk for $\phi = 3008$ (case 3 of Table 4.1) (a.i) and for $\phi = 1504$ (b.i) and the relative Gaussian fitting curves (red lines). Corresponding snapshots of clipped simulation boxes are shown in (a.ii) and (b.ii), where oil and water are represented by yellow and blue beads respectively while protein molecules by brown beads for $\phi = 3008$ and green and red beads for $\phi = 1504$.

with DPD on a small scale, the scaling of interactions does not prevent a simulation on a larger scale unless specific issues are dealt with. Indeed, equilibrium proprieties of planar interfaces with and without a protein surfactant for different ratios of the level of coarse-graining were investigated by applying the scaling scheme. Although the level of description is much smaller, it was shown that the equilibrium interfacial tension trend can be conserved for different coarse-graining ratios besides a scaling factor. This can be achieved by a simple representation of molecules involved, meaning that very few interaction parameters need to be set, thus decreasing the model complexity. The same approach for planar interfaces was also employed for a droplet configuration, showing that in both cases it is possible to maintain the domain conformation by applying an appropriate combined scaling procedure and coarse-graining parameterization. On the other hand, the pressure of interfacial systems appears to be not independent of the coarse-graining ratio, in contrast with the result of bulk fluids. The surface concentration of surfactants also seems to be related to the coarse-graining level and parameterization. Hence, possible applications of such findings will focus on investigating droplet coalescence and breakage events, which occur at a time- and space-scale larger than that of thermal fluctuations of single particles.

Chapter 5

Meso-scale model

5.1 Introduction

This chapter focuses on numerical simulations of two immiscible fluids in the presence of soluble surfactants via mesoscopic approaches, namely Lattice Boltzmann Model (LBM) and Dissipative Particle Dynamics (DPD). Although both techniques have been successfully employed in modeling these systems, they are conceptually different. Indeed, the former is a particle-based model solving Newton's second law of motion for a system consisting of *N* particles, while the latter models the fluid consisting of fictive particles (particle populations). Such particles perform consecutive propagation and collision processes over a discrete lattice, thus solving the discrete-velocity Boltzmann equation, that approximates the Navier-Stokes equation in the nearly-incompressible limit. Both the thermodynamic and hydrodynamic description of a realistic ternary system consisting of oil, water, and surfactants is represented by the phase-field model within the LBM framework. Based on a DPD study, the LBM was tested to compare the two mesoscopic models of immiscible liquids in presence of surfactants in terms of equilibrium properties. In particular, the reduction of the interfacial tension at increasing surfactant concentration was studied. Hence, the equilibrium properties were analyzed to check if the LBM approach can describe the same outcome of DPD simulations with the aim of finding a possible link between the molecular and the continuum modeling approaches.

The rest of this chapter is organized as follows: section 5.2 represents the governing equations of the phase field method and the LBM technique; the numerical analysis is explained in section 5.3, together with analytical simplifications and details of the DPD simulations; then, section 5.4 presents the results obtained here and, finally, conclusions are reported in section 5.5.

5.2 Theoretical background

5.2.1 Phase field method

The ternary system consists of a non-ionic surfactant and two immiscible liquids (i.e., binary fluid-surfactant system) can be represented by introducing two order parameters ϕ and ψ: the former represents the bulk phases with the diffuse interface and the latter describes the soluble surfactant. ϕ is the difference between the local concentrations (i.e., mass or volume fractions) of two immiscible liquids [227]. It varies from -1 to $+1$, where $\phi = +1$ and $\phi = -1$ indicate the dispersed and continuous phases, respectively. ψ is the volume or mole fraction (i.e., concentration) of the surfactant ranging from 0 to 1.

The hydrodynamics of the binary fluid-surfactant (BFS) system is governed by four equations: the continuity equation for density, the momentum equation for velocity, and two Cahn-Hilliard-type convection-diffusion equations describing the transport of ϕ and ψ [101]:

$$\partial_t \rho + \partial_\alpha (\rho u_\alpha) = 0 \, , \tag{5.1a}$$

$$\partial_t (\rho u_\alpha) + \partial_\beta (\rho u_\alpha u_\beta) = -\partial_\beta P^{th}_{\alpha\beta} + \partial_\beta \nu (\rho \partial_\alpha u_\beta + \rho \partial_\beta u_\alpha) \, , \tag{5.1b}$$

$$\partial_t \phi + \partial_\alpha (\phi u_\alpha) = M_\phi \partial^2_{\beta\beta} \mu_\phi \, , \tag{5.1c}$$

$$\partial_t \psi + \partial_\alpha (\psi u_\alpha) = M_\psi \partial^2_{\beta\beta} \mu_\psi \, . \tag{5.1d}$$

The equations are written in the Einstein notation, where α and β represent the spatial coordinates x, y, and z; t stands for time; ρ and ν are the fluid density and kinematic viscosity, respectively; u_α is the fluid velocity; the mobilities M_ϕ and M_ψ corresponding to ϕ and ψ are assumed constant; the thermodynamic pressure tensor, $P^{th}_{\alpha\beta}$, is the driving force of the BFS system; the chemical potential of bulk phases, μ_ϕ, and the chemical potential of the surfactant, μ_ψ, govern the mass transport of ϕ and ψ, respectively.

The thermodynamics of the ternary system is defined by a choice of free energy functional. The total free energy functional, F_{total}, suggested in the work Ref. [105] is used in the present study as follows:

$$F_{total} = F(\rho,\phi,\psi) = \int \left[\mathscr{F}_{\phi} + \mathscr{F}_{\psi} - \frac{C}{2}\psi^2 - E\phi\psi + \mathscr{F}_0 + \mathscr{F}_{ex} + \rho T \ln\rho \right] dV \ , \tag{5.2}$$

where:

- $\mathscr{F}_{\phi}$ is the Cahn-Hilliard free energy density functional used to represent a binary mixture [228] defined as follows:

  $$\mathscr{F}_{\phi} = \frac{A}{2}\phi^2 + \frac{B}{4}\phi^4 + \frac{\kappa_{int}}{2}(\partial_\alpha \phi)^2 \ . \tag{5.3}$$

  The first two terms represent the double well potential function which has two minima representing two bulk phases of the binary fluid mixture as $\pm\phi_b = \pm\sqrt{-A/B}$. The last term accounts for the interfacial free energy density due to the diffuse interface approximation. κ_{int} is a positive constant.

- $\mathscr{F}_{\psi}$ is the ideal entropy of mixing two immiscible liquids and the surfactant suggested in the work Ref. [102] from the sharp interface model [229]:

  $$\mathscr{F}_{\psi} = k_b T[\psi \ln(\psi) + (1-\psi)\ln(1-\psi)] \ . \tag{5.4}$$

  The term $k_b T$ represents the thermal energy, where k_b is the Boltzmann constant.

- The term $-\frac{C}{2}\psi^2$ describes the free energy density of lateral interaction between two adjacent surfactants. This term prevents the surfactant from forming clusters [227]. The parameter C describes the self-interaction strength between surfactants.

- The term $-E\phi\psi$ describes the free energy density due to the different solubility of surfactant in bulk phases. The parameter E describes the difference in the solubility strength of surfactant in two bulk phases.

- $\mathscr{F}_0$ is the free energy density contribution from the adsorption of surfactant on the liquid-liquid interface defined as follows:

$$\mathscr{F}_0 = -\frac{D}{2}\psi\hat{\delta}(x) \; , \tag{5.5}$$

  where $\hat{\delta}(x)$ is a nascent delta function incorporating the diffuse representation of the surface free energy density. The different representations of $\hat{\delta}(x)$ lead to the different types of coupling between the surfactant and bulk phases [102, 230]. The parameter D is related to the surface free energy density due to surfactant molecules.

- The extra free energy density $\mathscr{F}_{ex}$ due to the presence of the surfactant in bulk phases is incorporated to numerically stabilize the diffuse interface model for microemulsions [231]:

$$\mathscr{F}_{ex} = \frac{W}{2}\psi\phi^2 \; , \tag{5.6}$$

  where W is the parameter related to the excess free energy density. The term $\mathscr{F}_0$ locally attracts surfactant to an existing interface, whereas the term $\mathscr{F}_{ex}$ globally counteracts the occurrence of free surfactant in bulk regions [230].

- The last term in Eq. (5.2) ensures the incompressibility of the fluid in the Lattice Boltzmann model and compressibility errors can be reduced by increasing the value of temperature T [232]. This term has no influence on phase behavior.

From thermodynamic relations, the chemical potentials μ_ϕ and μ_ψ can be derived by taking the functional derivatives of the total free energy functional of the BFS system with respect to ϕ and ψ as follows:

$$\mu_\phi = \frac{\delta F_{total}}{\delta\phi} = A\phi + B\phi^3 - (\kappa_{int} - D\psi)\partial^2_{\alpha\alpha}\phi - E\psi + D(\partial_\alpha\phi)(\partial_\alpha\psi) + W\psi\phi \; , \tag{5.7a}$$

$$\mu_\psi = \frac{\delta F_{total}}{\delta\psi} = k_bT[\ln(\psi) - \ln(1-\psi)] - C\psi - E\phi - \frac{D}{2}(\partial_\alpha\phi)^2 + \frac{W}{2}\phi^2 \; . \tag{5.7b}$$

For these derivations, the square gradient of ϕ is considered as the approximation of the Dirac delta function $\hat{\delta}(x) \approx (\partial_\alpha\phi^2)$ [102] in Eq. (5.5). This particular representation can be derived from the sharp interface models proposed in the works Refs. [229, 233].

According to the work Ref. [234], the term $D\psi\partial^2_{\alpha\alpha}\phi + D(\partial_\alpha\phi)(\partial_\alpha\psi) + W\psi\phi$ in Eq. (5.7a) makes the interfacial profile sharpen (i.e., thin interface) for the square gradient approximation. Following this observation, the term is neglected hereafter to ensure the physical interfacial behavior.

From the Gibbs-Duhem equality, the divergence of thermodynamic pressure tensor $P^{th}_{\alpha\beta}$ can be represented in terms of the excess chemical potential gradients which act as the thermodynamic force density (i.e., unit volume). The divergence of the thermodynamic pressure tensor can be defined as [101]:

$$\partial_\alpha P^{th}_{\alpha\beta} = [\phi(\partial_\alpha\mu_\phi) + \psi(\partial_\alpha\mu_\psi)]\delta_{\alpha\beta} \ . \tag{5.8}$$

The thermodynamic pressure tensor can be decomposed into two parts as follows [231]:

$$P^{th}_{\alpha\beta} = p\delta_{\alpha\beta} + P^{chem}_{\alpha\beta} \ , \tag{5.9}$$

where the thermodynamic pressure p is the isotropic part of the thermodynamic pressure tensor and a scalar that can be derived using thermodynamic relations as:

$$p = \phi\mu_\phi + \psi\mu_\psi + \rho\frac{\delta F_{total}}{\delta\rho} - F_{total} \ . \tag{5.10}$$

After inserting μ_ϕ, μ_ψ, and F_{total} from Eqs. (5.7a), (5.7b), and (5.2) in Eq. (5.10), the expression of p can be written as:

$$p = \frac{A}{2}\phi^2 + \frac{3B}{4}\phi^4 - \frac{\kappa_{int}}{2}(\partial_\alpha\phi)^2 - \kappa_{int}\phi\partial^2_{\alpha\alpha}\phi - k_bT[\ln(1-\psi)] - \frac{C}{2}\psi^2 - E\phi\psi + \rho T \ . \tag{5.11}$$

The chemical pressure tensor $P^{chem}_{\alpha\beta}$ accounts for the contribution of non-isotropic forces exerted by the interface [231]. To satisfy Eq. (5.8), $P^{chem}_{\alpha\beta}$ can be formulated as follows:

$$P^{chem}_{\alpha\beta} = (\kappa_{int} - D\psi)(\partial_\alpha\phi)(\partial_\beta\phi) \ . \tag{5.12}$$

5.2.2 Lattice Boltzmann model

The set of governing equations (Eq. (5.1)) representing the BFS system is solved numerically using a Lattice Boltzmann model (LBM) formulation. The diffuse interface free energy LBM [235] is extended to accommodate for the presence of surfactants following the work Ref. [105]. In the LBM framework, the macroscopic properties such as mass density ρ and momentum density ρu_α can be defined based on the single particle distribution function (i.e., discrete-velocity distribution function). In a similar way, the order parameters ϕ and ψ can also be obtained by introducing two more particle distribution functions. Overall, three particle distribution functions $f(\vec{r},t)$, $g(\vec{r},t)$, and $h(\vec{r},t)$ are used to solve the set of continuity and Navier-Stokes equations, and the Cahn-Hilliard equations for ϕ and ψ. The number of discrete velocity directions required to represent the continuous particle velocity space depends on the consistent approximations of governing equations with minimum computational resources. In this study, the D3Q19 velocity set is selected for three populations f, g, and h considering the accuracy as well as efficiency of the LBM scheme. The D3Q19 set indicates the discretization of velocity space into nineteen velocity stencils ($q \in 0, ..., 18$) spanning over three Cartesian coordinates x, y, and z. The D3Q19 velocity set is described in Appendix B.

The discretized Boltzmann equation describes the evolution of particle distribution functions with respect to time, space, and velocity as follows:

$$f_q(\vec{r}+\vec{c}_q\Delta t, t+\Delta t) = f_q(\vec{r},t) + \Omega_q^f(\vec{r},t) \ , \tag{5.13a}$$

$$g_q(\vec{r}+\vec{c}_q\Delta t, t+\Delta t) = g_q(\vec{r},t) + \Omega_q^g(\vec{r},t) \ , \tag{5.13b}$$

$$h_q(\vec{r}+\vec{c}_q\Delta t, t+\Delta t) = h_q(\vec{r},t) + \Omega_q^h(\vec{r},t) \ . \tag{5.13c}$$

These equations can be interpreted as the advection equations: it represents that the discrete particle populations travel from the initial lattice position $\vec{r}$ to the neighboring lattice position $\vec{r}+\vec{c}_q\Delta t$ with a velocity $\vec{c}_q = (c_{qx}, c_{qy}, c_{qz})$ during the time step Δt. This leads to the collision of particles which is incorporated by a collision operator Ω_q as a source term on the right side of the equations. The grid spacing Δx and time step Δt are scaled in lattice units (lu) such that Δx = 1 and Δt = 1. The conversion from lattice units to SI base units is achieved by the scaling of physical parameters, the analysis of relevant dimensionless numbers, and the exploitation of the law of similarity (see the work Ref. [103] for more details). The system of governing equations (Eq. (5.1)) can be obtained from the set of Eq. (5.13) by the Chapman-Enskog expansion.

The collision operator Ω_q accounts for the relaxation of the particle populations towards the equilibrium distributions after collisions between them. The selection of collision operator affects the stability and accuracy of numerical results. In the present study, the Bhatnagar-Gross-Crook (BGK) collision operator (i.e., single-relaxation-time (SRT) collision operator) [236] is considered for the particle populations g and h. The collision operators Ω_q^g and Ω_q^h in Eqs. (5.13b) and (5.13c) can be written as follows:

$$\Omega_q^g = -\frac{g_q - g_q^{eq}}{\tau_g}\Delta t \ , \tag{5.14a}$$

$$\Omega_q^h = -\frac{h_q - h_q^{eq}}{\tau_h}\Delta t \ , \tag{5.14b}$$

where τ_g and τ_h are the relaxation times representing the time that the particle populations g and h take to reach their equilibrium distributions g_q^{eq} and h_q^{eq}, respectively.

The major drawback of the BGK collision operator is its inability to increase the velocity or decrease the viscosity to incorporate larger Reynolds numbers (i.e., turbulent flow) as it decreases the stability and accuracy of the LBM scheme [98]. Also, increasing the grid size is not computationally efficient. Hence, the multiple-time-relaxation (MRT) collision operator is used for the particle population f that ensures the consistent numerical results at higher Reynolds numbers by relaxing the collision of particles in the moment space instead of the population space with individual collision rates for $q \in 0, ..., 18$. The collision operator Ω_q^f in Eq. (5.13a) can be represented as follows:

$$\Omega_q^f = -\mathbf{M}^{-1}\mathbf{S}\mathbf{M}(f_q - f_q^{eq})\Delta t \ , \tag{5.15}$$

where f_q^{eq} represents the equilibrium distribution of particle population f. The transformation from the population space to moment space and implementation of different relaxation rates are performed by the transformation matrix $\mathbf{M}$ and relaxation matrix $\mathbf{S}$, respectively. Then, the multiplication by $\mathbf{M}^{-1}$ refers to the mapping from moment to population space after the relaxation. These matrices are constructed for the D3Q19 velocity set from the guidelines suggested in the work Ref. [237]. The MRT collision operator is incorporated into the LBM algorithm using the work Ref. [238]. The representation of transformation and relaxation matrices are provided in Appendix C.

The local macroscopic variables such as density, momentum density, and the order parameters at any given lattice site can be determined by the moments of the particle distribution functions. The moments are defined as the summation or weighted summation of particle populations over the discretized velocity space:

$$\sum_q f_q = \rho \ , \quad \sum_q f_q c_{q\alpha} = \rho u_\alpha \ , \tag{5.16a}$$

$$\sum_q g_q = \phi \ , \quad \sum_q g_q c_{q\alpha} = \phi u_\alpha \ , \tag{5.16b}$$

$$\sum_q h_q = \psi \ , \quad \sum_q h_q c_{q\alpha} = \psi u_\alpha \ . \tag{5.16c}$$

In LBM, the macroscopic properties such as the kinematic viscosity and the mobility can be described in terms of the speed of sound and the relaxation time. The kinematic viscosity ν of the BFS system can be defined as:

$$\nu = c_s^2 \left(\tau_f - \frac{1}{2} \right) \Delta t \ , \tag{5.17}$$

where τ_f is the relaxation time of particle population f. The mobilities M_ϕ and M_ψ can be described as follows:

$$M_\phi = \Gamma_\phi \left(\tau_g - \frac{1}{2} \right) \Delta t \ , \tag{5.18a}$$

$$M_\psi = \Gamma_\psi \left(\tau_h - \frac{1}{2} \right) \Delta t \ , \tag{5.18b}$$

where τ_g and τ_h are the relaxation times of particle populations g and h, respectively. Their values should be $\tau_g = \tau_h = 1/(3 - \sqrt{3})$ to get more accurate and stable numerical results for the convection-diffusion scheme [239].

The moments of the equilibrium distribution functions f_q^{eq}, g_q^{eq}, and h_q^{eq} represent the set of equations as same as Eq. (5.16). In addition, the higher order moments of these functions are related to the thermodynamic pressure tensor, the coefficient of mobilities Γ, and the chemical potentials according to the LBM schemes suggested in the works Refs. [231, 235] as follows:

$$\sum_q f_q^{eq} c_{q\alpha} c_{q\beta} = P_{\alpha\beta}^{th} + \rho u_\alpha u_\beta \ , \tag{5.19a}$$

$$\sum_q g_q^{eq} c_{q\alpha} c_{q\beta} = \Gamma_\phi \mu_\phi \delta_{\alpha\beta} + \phi u_\alpha u_\beta \ , \tag{5.19b}$$

$$\sum_q h_q^{eq} c_{q\alpha} c_{q\beta} = \Gamma_\psi \mu_\psi \delta_{\alpha\beta} + \psi u_\alpha u_\beta \ . \tag{5.19c}$$

The mathematical formulation of equilibrium distribution functions f_q^{eq}, g_q^{eq}, and h_q^{eq} is described in Appendix B.

The value of temperature T in Eq. (5.2) is chosen to be $1/3$ considering the numerical accuracy and stability [105]. This represents the ideal gas type contribution with the ideal gas pressure $p_{id} = \rho T$. In LBM, the speed of sound is represented as $c_s^2 = (1/3)\Delta x^2/\Delta t^2 = 1/3$ as $\Delta x = \Delta t = 1$ in lattice units. Hence, the last term $\rho T \ln\rho$ in Eq. (5.2) can be rewritten as $\rho c_s^2 \ln\rho$ for this case.

The relationship between the parameters D and W can be described by defining a dimensionless number: $Ex = \frac{D}{W\xi^2}$ where ξ is the scale of the interface thickness. Ex represents the bulk surfactant solubility parameter [230].

5.3 Numerical details

5.3.1 Analytical equations

For analytical derivations, $E = 0$ (i.e., the equal solubility in bulk phases) is considered. Moreover, both Langmuir and Frumkin adsorption isotherms for surfactants are taken into account by setting $C = 0$ or $C > 0$, respectively [101, 105].

Here, the analysis is restricted to planar interfaces normal to the x-direction in the simulation domain. At thermodynamic equilibrium, the chemical potential of bulk phases μ_ϕ is uniform throughout the BFS system. Hence, the expression for the order parameter ϕ can be derived by equating the chemical potential of ϕ at any location x to the chemical potential of ϕ at the interface:

$$\mu_{\phi,x} = \mu_{\phi,0} \ , \tag{5.20a}$$

$$A\phi + B\phi^3 - \kappa_{int}\partial^2_{\alpha\alpha}\phi = 0 \ , \tag{5.20b}$$

$$A\phi + B\phi^3 = \kappa_{int}\partial^2_{\alpha\alpha}\phi \ . \tag{5.20c}$$

Dividing both sides of the above equation by $-A\phi_b$ and simplifying, it follows:

$$\frac{\phi}{\phi_b} - \frac{B\phi^3}{A\phi_b} = -\frac{\kappa_{int}}{A}\partial^2_{\alpha\alpha}\left(\frac{\phi}{\phi_b}\right) \ . \tag{5.21}$$

Using the definition of bulk phase $\phi_b^2 = -\frac{A}{B}$ and introducing the dimensionless parameter $\hat{\phi} = \frac{\phi}{\phi_b}$, it follows as:

$$\hat{\phi}^3 - \hat{\phi} = -\frac{\kappa_{int}}{A}\partial^2_{\alpha\alpha}\hat{\phi} \ , \tag{5.22a}$$

$$-\frac{A}{\kappa_{int}}\iint(\hat{\phi}^3 - \hat{\phi})dxdx = \iint(\partial^2_{\alpha\alpha}\hat{\phi})dxdx \ . \tag{5.22b}$$

Integrating the above equation gives the equilibrium profile of ϕ as follows:

$$\phi(x) = \phi_b \tanh\left(\frac{x}{\xi}\right) \ , \tag{5.23}$$

where x is a coordinate normal to the interface and the interface thickness $\xi = \sqrt{\frac{2\kappa_{int}}{-A}}$. The interfacial tension of a clean interface (i.e., without surfactant loading) can be defined as:

$$\sigma_0 = \frac{4\kappa_{int}\phi_b^2}{3\xi} \ . \tag{5.24}$$

Similarly, for ψ, comparing the chemical potential of ψ at any location x with that in the bulk phase, it follows as:

$$\mu_{\psi,x} = \mu_{\psi,b} \ , \tag{5.25a}$$

$$\begin{aligned} k_bT[\ln(\psi) - \ln(1-\psi)] - C\psi - E\phi - \frac{D}{2}(\partial_\alpha\phi)^2 + \frac{W}{2}\phi^2 = \\ = k_bT[\ln(\psi_b) - \ln(1-\psi_b)] - C\psi_b - E\phi_b + \frac{W}{2}\phi_b^2 \ , \end{aligned} \tag{5.25b}$$

$$\psi(x) = \frac{\psi_b}{\psi_b + (1-\psi_b)\psi_c(x)} \ , \tag{5.25c}$$

where $\psi_c(x)$ is represented as:

$$\psi_c(x) = \exp\left\{ -\frac{1}{k_bT}\left[C(\psi - \psi_b) + \frac{D}{2}(\partial_\alpha\phi)^2 - \frac{W}{2}(\phi^2 - \phi_b^2) - E(\phi - \phi_b) \right] \right\} . \tag{5.26}$$

At the interface, $\psi_c(0)$ can be defined as follows:

$$\psi_c(0) = \exp\left\{ -\frac{1}{k_bT}\left[C(\psi_0 - \psi_b) + \frac{D}{2\xi^2}\phi_b^2 + \frac{W}{2}\phi_b^2 + E\phi_b \right] \right\} . \tag{5.27}$$

Eqs. (5.23) and (5.25c) are used here as the initialization of ϕ and ψ profiles in numerical simulations.

For interfaces loaded with surfactants, the interfacial tension is an important thermodynamic measure. Here, it is derived from the grand potential Ω following the definition given in the works Refs. [101, 240]. The total surface tension σ is computed by the integral over a flat interface, with direction x perpendicular to the interface:

$$\sigma = \int_x (\Omega - \Omega_b)dx \ , \tag{5.28}$$

with Ω_b the grand potential in the bulk phase, where the surfactant is solubilized.

5.3.2 DPD study

In order to compare LBM results, a DPD study was here used as a reference. The theoretical background about this technique has already been explained in section 3.2.1 and can be also found in the literature [40–42, 185]. Therefore, only details on DPD simulations are here presented. For sake of the comparison, the work Ref. [226]

is here reported since it deals with an oil-water interface in presence of non-ionic surfactants which is the base of the phase-field model presented in section 5.2.1. Indeed, in the DPD work the surfactant molecule is modeled as a typical non-ionic single-chained amphiphilic molecule with a hydrophilic head and a hydrophobic tail. The adsorption of this type of surfactant can be described with a Langmuir or Frumkin isotherm and, therefore, it is substantially different from the one used in previous chapters. In fact, the use of protein surfactant introduces a level of complexity in the thermodynamic model (see section 3.2.2) which is not represented in the current LBM scheme. This justifies the choice to use a DPD work found in the literature to compare the two mesoscopic modeling techniques.

The densities of the water and oil phases are considered to be equal to each other in the DPD work in agreement with the definition of the order parameter ϕ in the LBM framework. By varying the amount of surfactant added to the system, the interfacial tension corresponding to different surfactant densities at interface d_s can be calculated, where d_s is defined as the average number of surfactant molecules divided by twice the interface area. It is also assumed that the concentration of surfactant added to the system is lower than the critical micelle concentration, so one can assume that the total number of surfactant molecules must be adsorbed in the interfacial region at the steady state. The calculation of the interfacial tension was performed in a DPD simulation box of $20 \times 20 \times 40$ with periodic boundary conditions in three directions and the initial location of the water, oil, and surfactant molecules constituted two planar interfaces perpendicular to the z-direction. The relation between the interfacial tension Γ and the percent interface coverage reads as follows:

$$\Gamma - \Gamma_0 = d_s^{\infty} RT \ln(1-c) - \frac{kc^2}{2} \, , \tag{5.29}$$

where Γ_0 is the interfacial tension of the free interface, d_s^{∞} is the maximum surfactant density at the interface, R is the ideal gas constant, $c = d_s/d_s^{\infty}$ is the percent interface coverage of surfactant and k is a constant parameter. By fitting the results of the interfacial tension DPD simulations with Eq. (5.29), the following relation was obtained [226]:

$$\Gamma - 3.568734 = 1.553019 \times \left[\ln\left(1 - \frac{d_s}{1.3}\right) \right] - 2.7 \times \left(\frac{d_s}{1.3}\right)^2 \, . \tag{5.30}$$

Eq. (5.30) represents a target relation to fit with the results of LBM simulations of the same system. An explicit definition of the quantity c in the LBM framework is needed in order to correctly compare the results of both modeling techniques as explained below.

In most of the LBM work of the BFS system [100, 102, 105], the interfacial tension comes from the thermodynamic analysis. According to the work Ref. [241], the variation in the surface tension can be expressed in terms of the surface excess quantities. From the Gibbs adsorption equation at a constant temperature, it can be represented in general as follows:

$$d\sigma = -C_{xs} d\mu \ . \tag{5.31}$$

Here, a subscript xs indicates the surface excess quantity, and C_{xs} is the excess concentration. These excess quantities account for the local variation of the quantity in the interfacial region. Following this, the equation of state for the diffuse interface model can be represented as:

$$d\sigma = -\psi_{xs} d\mu_{\psi} \ , \tag{5.32}$$

where ψ_{xs} is the total amount of surfactant over the interfacial region (i.e., diffuse interface) and the integration of ψ over the diffuse interface can not be analytically obtained [102, 105]. Due to this problem, it was concluded that the excess surfactant concentration ψ_{xs} is made proportional to ψ_0 (i.e., $\psi_{xs} = \alpha\psi_0$) by a proportionality coefficient α. This implies that the equation of state can be derived as follows:

$$\begin{aligned} d\sigma &= -\psi_{xs} d\mu_{\psi} \ , \\ &= -\alpha\psi_0 d\mu_{\psi_0} \ , \\ \sigma(\psi_0) - \sigma_0 &= \alpha\left[k_B T \ln(1-\psi_0) + \frac{C}{2}\psi_0^2\right] \ . \end{aligned} \tag{5.33}$$

This states that the lowering of interfacial tension for diffuse models is proportional to that of the sharp interface model. α must account for the quantity of surfactant concentration in the interfacial region excluding ψ_0, thus it depends only on $Ex = \frac{D}{W\xi^2}$ after fixing ξ [105].

The definition of concentration of surfactant ψ is arbitrary as it can be defined as the volume fraction of surfactant [102] or the mole fraction of surfactant [242] and it is a local property. Here, ψ is interpreted as the mole fraction of surfactants. Therefore, ψ can be defined as:

$$\psi(x) = \frac{n_S(x)}{n_S(x) + n_{BL}(x)} \,, \tag{5.34}$$

where $n_S(x)$ and $n_{BL}(x)$ are the moles of surfactant and binary liquids on any location x, respectively. Following this definition, ψ must be a local property and it can locally vary from 0 to 1 since it accounts for the relative local presence of surfactants and binary liquids.

Now, the interface coverage of surfactant c in Eq. (5.29) can be related to the surfactant concentration at the interface ψ_0. From the Avogadro number, one can correlate the number of molecules to the number of moles present in the system. Using this argument, the definition of c can be simplified as follows:

$$\begin{aligned} c = \frac{d_s}{d_s^\infty} &= \frac{\text{the number of surfactant molecules in the interfacial region}}{\text{the maximum number of surfactant molecules in the interfacial region}} \,, \\ &= \frac{\text{the moles of surfactant in the interfacial region}}{\text{the maximum moles of surfactant in the interfacial region}} \,, \\ &= \frac{\psi_{xs}}{\psi_{xs}^\infty} \,. \end{aligned} \tag{5.35}$$

As already stated, ψ_{xs} is the total amount or mole fraction of surfactant over the interfacial region (i.e., interface thickness). The moles of surfactant in the interfacial region are assumed to be proportional to ψ_{xs}. Due to the fact that we are interested in the ratio of ψ_{xs} not in the absolute values, this unknown proportionality coefficient is canceled out in taking the ratio of ψ_{xs}. Hence, one can correlate c and ψ_{xs} as expressed above. Following the suggestion of the work Ref. [102], ψ_{xs} in the above expression can be simplified once more as follows:

$$c = \frac{d_s}{d_s^\infty} = \frac{\psi_{xs}}{\psi_{xs}^\infty} = \frac{\cancel{\alpha}\psi_0}{\cancel{\alpha}\psi_0^\infty} = \frac{\psi_0}{\psi_0^\infty} \,. \tag{5.36}$$

Here, ψ_{xs}^∞ is the maximum amount of surfactant over the interfacial region. α depends only on Ex after fixing ξ and it has no relation with ψ_0 [105], so one can assume that the value of α maintains the equality of the above expression. ψ_0^∞ is the maximum mole fraction of surfactant at the interface in the case of maximum packing of the interfacial area. One can theoretically take $\psi_0^\infty = 1$ as it is defined as a relative local property (Eq. (5.34)). Therefore, when the maximum packing of the interfacial region occurs, it means that only surfactants are ideally present at the interface without binary liquids. Following this explanation, c can be finally represented as:

$$c = \frac{d_s}{d_s^\infty} = \psi_0 \,. \tag{5.37}$$

Following this relation, it is then possible to directly compare the DPD results [226] with LBM simulations. In fact, for different values of $c = \frac{d_s}{d_s^\infty}$, the percentage reduction of the interfacial tension in presence of surfactants compared to the one of the clean interface is different. For example, at $c = \frac{d_s}{d_s^\infty} = \frac{0.5}{1.3} = 0.3846$, the reduction in the interfacial tension observed is around 30% [226].

5.4 Results and discussion

First, the phase field model's capability for the prediction of the profile of surfactant concentration at a planar oil-water interface was numerically tested. LBM simulations are performed in a domain size of $128 \times 128 \times 128$ in lattice units [lu] with two planar interfaces equidistant in x direction, where the dispersed phase is initially positioned at $32 \leq x \leq 96$. The interface locations are fixed at $x_{01} = 32$ and $x_{02} = 96$. The periodic boundary conditions are imposed at all the boundaries. The values of ϕ and ψ were initialized using the analytical expressions (Eqs. (5.23) and (5.25c), respectively). For this case, we consider $-A = B$ (i.e., $\phi_b = 1$), $C = 0$, $D = \kappa_{int}$, $E = 0$, $\psi_b = 0.01$, $\psi_c = 0.017$, $Ex = 0.17$, $\sigma_0 = 0.02$, $M_\phi = 0.2$, $M_\psi = 0.02$, $\tau_f = 0.53$, and $\xi/\Delta x = 2$. The parameters A, B, κ, k_bT, and W are obtained from the values of $\xi/\Delta x$, σ_0, ψ_c, and Ex. As shown in Figure 5.1, the numerical results are in good agreement with the analytical solutions.

Then, the comparison between LBM and DPD simulations [226] was performed by computing the reduction in the interfacial tension value for different values of Ex, ψ_b, and C. As it can be seen in Figure 5.2, a very good agreement was achieved between the DPD and LBM simulations. The goodness of curve fitting was evaluated by computing the Root Mean Squared Error (RMSE). Langmuir and Frumkin's isotherms were tested and the best results were obtained for $Ex = 0.18$, $C = 0$ and $Ex = 0.17$, $C = 0.1k_bT$, respectively. Moreover, Figure 5.3 shows the range of the bulk concentration ψ_b investigated, together with the corresponding values of

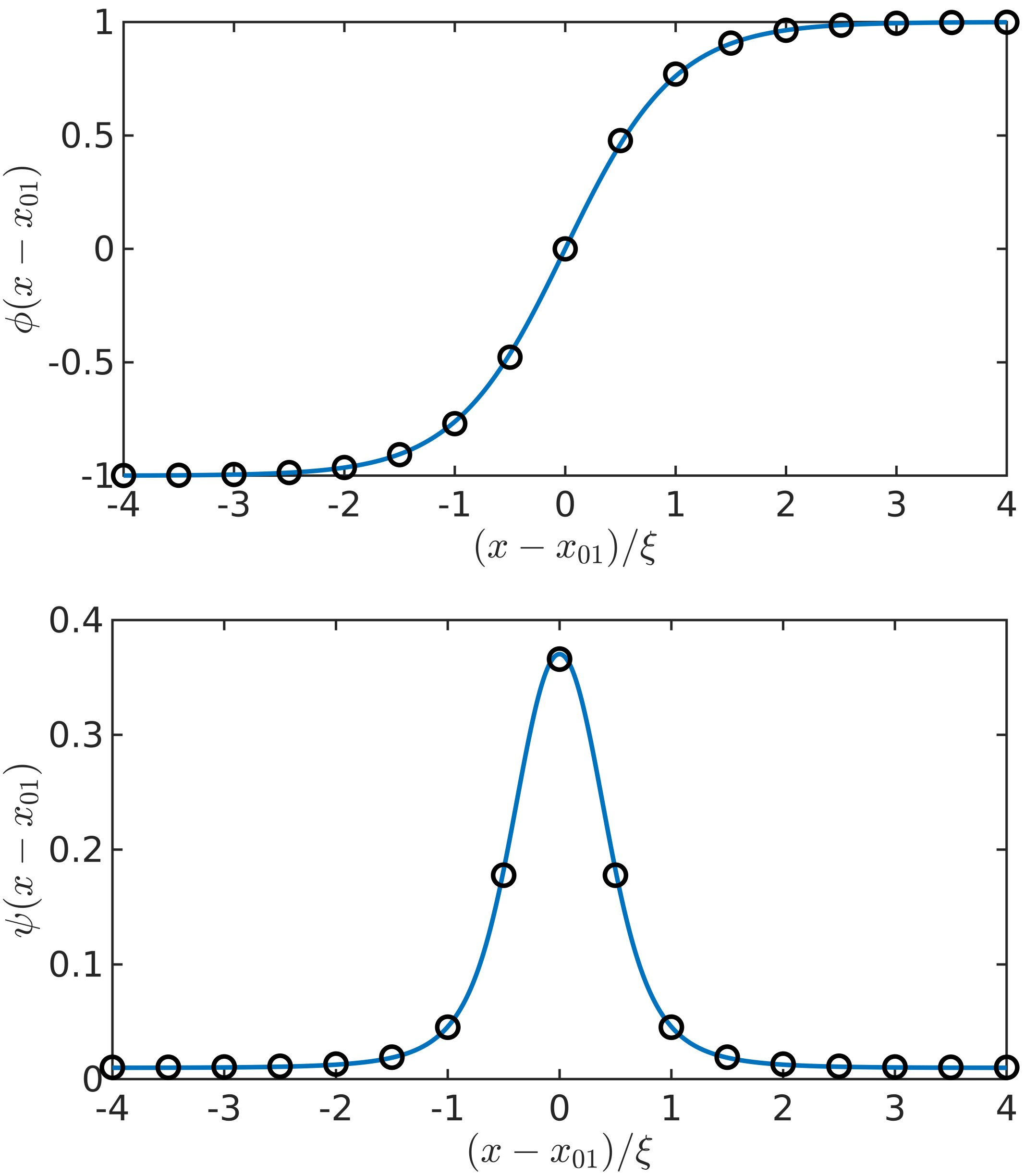

Fig. 5.1 Equilibrium ϕ (top) and ψ (bottom) profiles for $\psi_b = 0.01$. Simulation results (symbols) follow analytical expressions (blue lines).

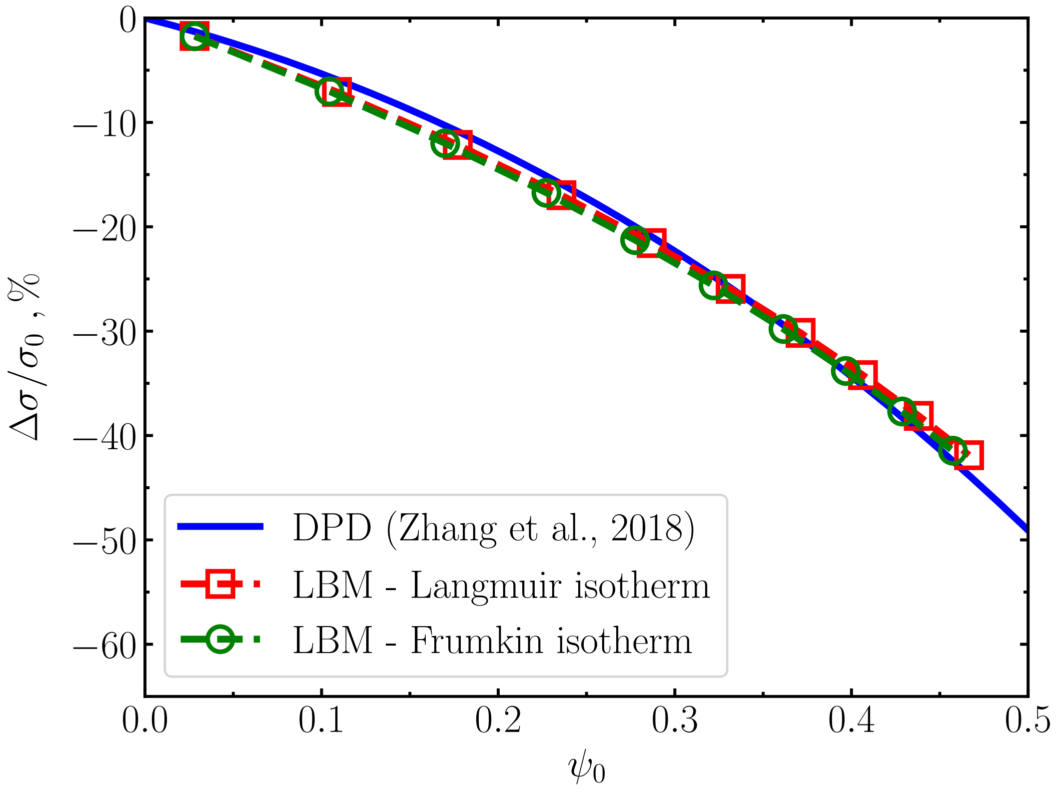

Fig. 5.2 Comparison of interfacial tension trend at increasing surfactant concentration between DPD and LBM simulations.

the surfactant loading ψ_0. As it can be seen and already pointed out in previous works [100, 101], the model can correctly reproduce both the Langmuir and Frumkin isotherms since simulations results follow the analytical prediction given by:

$$\psi_0 = \frac{\psi_b}{\psi_b + \psi_c \exp\left(-\frac{C}{k_b T}\psi_0\right)} , \tag{5.38}$$

with:

$$\psi_c = \exp\left[-\frac{1}{2k_b T}\left(\frac{D}{\xi^2} + W\right)\phi_b^2 + \frac{E}{k_b T}\phi_b\right] . \tag{5.39}$$

In fact, Eq. (5.38) represents the equilibrium adsorption isotherm obtained by reducing Eq. (5.25c) in the case of a dilute solution where the bulk surfactant concentration is much smaller than unity, i.e., $\psi_b \ll 1$ (Figure 5.3) [100, 101]. Therefore, the model can recover the Frumkin adsorption isotherm (see Eq. (5.38)), which reduces to the well-known Langmuir adsorption isotherm if $C = 0$.

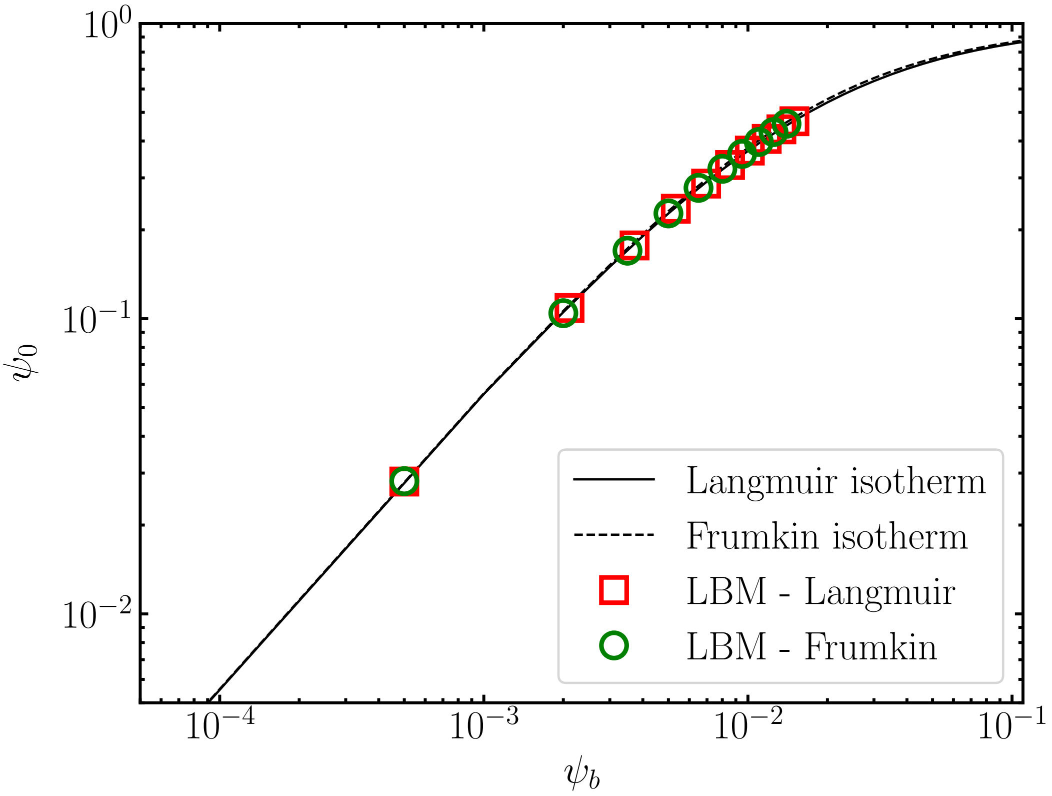

Fig. 5.3 Simulation results (symbols) following the Langmuir and Frumkin isotherms (solid and dashed line, respectively).

5.5 Conclusions

In this chapter, the phase field model in the Lattice Boltzmann scheme was applied to simulate immiscible binary fluid flows in the presence of soluble surfactant. It was modeled as a typical non-ionic single-chained amphiphilic molecule with a hydrophilic head and a hydrophobic tail. From equilibrium numerical simulations, this method can lead to the commonly-used surfactant adsorption isotherms, i.e., the Langmuir and Frumkin isotherms. Based on a DPD study, the LBM was tested to compare the two mesoscopic models in terms of reducing the interfacial tension at increasing surfactant concentration. Although both DPD and LBM have been successfully employed in modeling such systems, they are conceptually different. However, the comparison of the two methods showed that a link can be found in order to bridge the gap between the molecular and the continuum modeling approaches.

These promising results will pave the way for further investigation of the dynamic properties of binary fluids in presence of surfactants. Indeed, future works will deal with numerical simulations of an oil droplet covered by surfactants in shear flow. Therefore, the droplet deformation and break up for different operating conditions will be studied by means of the LBM framework and, eventually, compared with DPD results.

Chapter 6

Macro-scale model

6.1 Introduction

Here, we aim to model the last step of the mayonnaise production process in a cone mill by means of 2D and 3D computational fluid dynamics (CFD) simulations and population balance modeling (PBM) in order to: (1) properly describe the non-Newtonian dynamics of the emulsion, (2) investigate the role of the pre- and post-mixing zones, and (3) clarify the importance of the local type of flow. In particular, although mayonnaise consists of two distinct phases, high internal phase emulsions can be considered as a shear-thinning pseudo-single phase system with an apparent density and viscosity [6, 7]. The apparent emulsion viscosity, as a function of oil content, was evaluated through the fitting of experimental data, by using a power law model with a plateau at the high shear rate end [6]. In order to describe the evolution of the DSD, the Population Balance Equation (PBE) is employed, in which the coalescence and breakage of the oil droplets are taken into account by appropriate kernels, which in turn depend on the local flow conditions, which range from rotation to pure-shear and finally to elongation, depending on the relative contribution of rotation and strain. Previous PBM works were not capable of providing accurate predictions due to their restrictive assumptions, since coalescence was neglected [111, 112]. In fact, although cone mills are designed to promote drop breakage, colliding droplets may coalesce under certain conditions [106, 243]. The Quadrature Method of Moments (QMOM) [244–249] is used in order to solve the PBE, whereas CFD simulations are performed with the open source CFD code OpenFOAM (version 6.0) [250, 251].

This chapter is organized as follows: section 6.2 summarizes the main equations used to describe the flow field and the DSD evolution, section 6.3 reports the details about the simulation test cases and their implementation into OpenFOAM, section 6.4 focuses on the most important results obtained, and, finally, section 6.5 presents the main conclusions of this chapter.

6.2 Theoretical background

The emulsification within the rotor-stator system investigated in this chapter is a steady-state process. Therefore, the well-known momentum balance equation for an incompressible, non-Newtonian, and stationary flow is solved in order to obtain the flow field [252]. In this geometry, the centrifugal force that acts on the rotating fluid is not perpendicular to the rotor and stator surfaces. The flow field between two coaxial conical cylinders can present instabilities, known as Taylor vortices [114]. These vortices are superimposed to the main Couette flow with an axial throughput [119]. For such a particular system, very different flow patterns can develop inside the cone mill with varying operating conditions [118]; however, as it will be shown in section 6.4, the conditions investigated here only result in the appearance of laminar Taylor vortices. Therefore, the implementation of a turbulence model is not necessary.

In order to evaluate this particular flow pattern, the Reynolds number is calculated as follows:

$$\mathrm{Re} = \frac{\omega R_{max} d}{\bar{\nu}_{emul}} , \tag{6.1}$$

where ω is the angular velocity of the rotor and d is the distance (gap) between the rotor and the stator. In general, the Reynolds number for the investigated system is not constant, since the rotor radius increases from the top to the bottom of the cone mill, and the viscosity changes locally as a function of the local shear rate $\dot{\gamma}$. Therefore, the maximum rotor radius R_{max} and the volume-averaged kinematic apparent viscosity of the emulsion $\bar{\nu}_{emul}$ are used in Eq. (6.1). This corresponds to the definition used in the previous simulation works with whose results we compared our work [116–118]. For specific operating conditions, it is a good approximation to only consider the volume average of the emulsion viscosity $\bar{\nu}_{emul}$ since the local shear rate inside the gap section of the cone mill mostly depends on the tangential velocity gradient. As it will be shown in section 6.4, the tangential component of velocity shows a linear profile (and a constant gradient) along the gap width for a specific rotor radius. On the other hand, along the height of the cone mill, there is just little variation of the tangential velocity gradient, since the difference between the maximum and the minimum rotor radius is small (see Figure 6.2).

6.2.1 Non-Newtonian rheology model

In order to properly describe the non-Newtonian dynamics of the emulsion, the fluid is considered as a shear-thinning pseudo-single phase system, with an apparent emulsion viscosity η_{emul} evaluated through a power law model with a plateau at high shear rates fitted with experiments and reasonably accurate in the range of the local shear rate $\dot{\gamma}$ developed inside the cone mill mixer ($10^3 - 10^5$ s^{-1}) [6, 7]:

$$\frac{\eta_{emul}}{\eta_c} = \eta_r = \eta_{r,\infty} + K\dot{\gamma}^m \ . \tag{6.2}$$

In Eq. (6.2), η_r is the dimensionless relative viscosity, expressed as the ratio of apparent emulsion viscosity η_{emul} to continuous water phase viscosity η_c. The continuous phase consists of egg yolk, salt, and vinegar dissolved in water (section 2.2), and its viscosity was measured to be Newtonian over the range of shear rates investigated and equal to 10 mPa · s [6, 7]. In Eq. (6.2), $\eta_{r,\infty}$ is the relative plateau viscosity for high shear rates. The parameters $\eta_{r,\infty}$, K, and m result from experimental data fitting and they only depend on the oil concentration [6]. The kinematic apparent emulsion viscosity is $\nu_{emul} = \eta_{emul}/\rho_{emul}$, where ρ_{emul} is the apparent emulsion density, calculated as $\rho_{emul} = \rho_{oil}\phi_v/\phi_w$. Here, ϕ_v and ϕ_w are respectively the oil volume and the oil weight fractions, as reported in the reference experimental work [6, 7]. It is important to point out here that, in the works Refs. [6, 7], it is provided a relationship for the apparent emulsion viscosity as a function of the mean oil droplet diameter in order to link the evolution of the DSD with the macroscopic rheological properties. However, here the approach described in Eq. (6.2) is employed to describe the non-Newtonian dynamics of the emulsion for sake of the computational simplicity (see section 6.3).

6.2.2 CFD and PBM description

As mentioned, the flow field of the liquid-liquid emulsion in the cone mill is described by solving the steady-state continuity and momentum balance equations for an incompressible pseudo-single phase non-Newtonian flow, as detailed in previous works [253, 254]. By solving these equations the emulsion velocity in the cone mill, **U**, described as a pseudo-single phase fluid is calculated. Numerous interesting flow features can be extracted via this variable. For example, the local shear rate is calculated as follows:

$$\dot{\gamma} = 2\sqrt{II_{\mathbf{E}}}\ , \tag{6.3}$$

where $II_{\mathbf{E}}$ is the second invariant of the symmetric rate-of-strain tensor **E**, which is in turn defined as:

$$\mathbf{E} = \frac{1}{2}\left[\nabla\mathbf{U} + (\nabla\mathbf{U})^T\right]\ . \tag{6.4}$$

Another interesting flow feature is the so-called Manas-Zloczower mixing index [255], defined as follows:

$$\alpha = \frac{\sqrt{II_{\mathbf{E}}}}{\sqrt{II_{\mathbf{E}}} + \sqrt{II_{\mathbf{\Omega}}}}\ , \tag{6.5}$$

where $II_{\mathbf{\Omega}}$ is the second invariant of the skew-symmetric rate-of-rotation tensor **Ω**, which in turn is defined as:

$$\mathbf{\Omega} = \frac{1}{2}\left[\nabla\mathbf{U} - (\nabla\mathbf{U})^T\right]\ . \tag{6.6}$$

The mixing index α has a $0-1$ range, with 0 indicating a rotational motion, and 0.5 and 1 indicating pure shear and pure elongational flows, respectively [255]. As it will see later, both $\dot{\gamma}$ and α play an important role during droplet breakup.

The evolution of the droplet size distribution (DSD) is properly described by the PBE, accounting for the birth and death of droplets due to coalescence and breakage events. Assuming the emulsification process at the steady-state and omitting explicit indications of space and time dependencies, the PBE can be written as follows [256]:

$$\begin{aligned} \nabla\cdot(\mathbf{U}n(L)) = {} & \frac{L^2}{2}\int_0^L \frac{C\left(\left(L^3-L'^3\right)^{1/3}, L'\right)}{\left(L^3-L'^3\right)^{2/3}} n\left(\left(L^3-L'^3\right)^{1/3}\right) n\left(L'\right) dL' \\ & - n(L)\int_0^\infty C\left(L,L'\right) n\left(L'\right) dL' + \int_L^\infty g\left(L'\right)\beta\left(L|L'\right) n\left(L'\right) dL' - g(L)n(L)\ , \end{aligned} \tag{6.7}$$

where $n(L)$ is the DSD [247], L is the droplet diameter as well as the internal coordinate of the PBE. The right-hand side of Eq. (6.7) is the source term due to the coalescence and breakage of the oil droplets, which are described by means of phenomenological models called kernels [257]. The coalescence kernel, $C(L,L')$, and the breakage kernel, $g(L)$, quantify the rate with which droplets coalesce and break. The daughter-size distribution function, $\beta(L|L')$, defines instead the size distribution of the droplets formed by the breakup of a droplet of size L'.

Thanks to the assumption of considering the emulsion as a shear-thinning pseudo-single phase, **U** in Eq. (6.7) is the fluid velocity obtained by solving the flow field equation (as explained above). Therefore, **U** represents the first coupling variable used in this work, and from the flow field, it is possible to calculate the local shear rate $\dot{\gamma}$ [252]. As previously mentioned, in this work QMOM [245, 246] is employed to solve the PBM (Eq. (6.7)). The general idea behind this method is to solve transport equations for the moments of the DSD. By approximating the unknown DSD, $n(L)$, as a summation of Dirac functions and using a quadrature approximation of order N, QMOM leads to the following expression for the moment of order k [246]:

$$M_k = \int_0^{+\infty} n(L) L^k \mathrm{d}L \approx \sum_{\alpha=1}^{N} w_\alpha L_\alpha^k \quad \text{with} \quad k \in 0,...,2N-1 \; , \tag{6.8}$$

where w_α and L_α are the N quadrature weights and N quadrature abscissas, in turn, calculated from the first $2N$ lower-order moments through so-called moment inversion algorithms, such as the Product-Difference (PD) [247] algorithm employed here. The reader can refer to the literature for further details [244–247, 257, 258]. Moreover, it is important to remark that the moments represent integral properties of the DSD. For example, in the case investigated here, M_0 represents the number of oil droplets per unit volume, while M_3, if multiplied by a shape volume coefficient equal to $\pi/6$ due to the spherical shape of the droplets, is equal to the oil volume fraction. Most importantly, the mean Sauter diameter used here for evaluating the evolution of the DSD is simply defined as follows: $d_{32} = M_3/M_2$.

Three important functions appear in Eq. (6.7) which determine the evolution and the final shape of the DSD: the coalescence kernel $C(L,L')$, the breakage kernel $g(L)$, and the daughter-size distribution function $\beta(L|L')$. The coalescence kernel $C(L,L')$, quantifying the rate of coalescence of droplets of diameter L and L', and the breakage kernel $g(L)$, quantifying the rate of breakage of droplets of size L, take respectively the following forms [106]:

$$\begin{aligned} C(L,L') &= K_1 \frac{\pi}{6}\left(\frac{\dot{\gamma}}{1-\phi_v}\right)(L+L')^3 \exp\left(-K_2 \lambda \mathrm{Ca}^{\frac{3}{2}}\left(\frac{8\pi\sigma R_{eq}^2}{A_H}\right)^{\frac{1}{3}}\right) , \\ g(L) &= K_3 \dot{\gamma} \exp\left(-K_4 \frac{\mathrm{Ca_{cr}}}{\mathrm{Ca}}\right) , \end{aligned} \tag{6.9}$$

where ϕ_v is the oil volume fraction, A_H is the Hamaker constant, λ is the ratio between the oil viscosity η_{oil} and the apparent emulsion viscosity η_{emul}, and K_1, K_2, K_3, and K_4 are free adjustable model parameters to be fitted with experimental data. R_{eq} is the equivalent radius of colliding drops of diameter L and L', defined as: $R_{eq} = 2/(2/L + 2/L')$. The interfacial tension σ in Eq. (6.9) is dynamic for an oil-in-water emulsion as it varies according to local flow conditions and surfactant concentrations [1], as it was shown in chapters 3 and 4. In fact, this information could be used as a link with a scale lower than that investigated here. For sake of the computational simplicity, a reasonable assumption is to consider the interfacial tension constant and equal to 10 mN/m since it was shown that this value is reached at the saturation of the oil/water interface (see chapter 3). In Eq. (6.9), Ca is the capillary number, defined as:

$$\mathrm{Ca} = \frac{\eta_{emul}\dot{\gamma}L}{2\sigma} , \tag{6.10}$$

where η_{emul} is the apparent emulsion viscosity and $\dot{\gamma}$ is the local shear rate.

The high shear rates developed inside the mixer tend to stretch the oil droplets and droplet breakage is assumed to follow the capillary instability mechanism [6, 7, 106]. This means that, when the ratio of the viscous stress acting on the drops to the interfacial tension force, i.e., Ca, exceeds a critical value, i.e., the critical capillary number $\mathrm{Ca_{cr}}$, a mother droplet breaks into two or more daughter droplets, depending on the form of the daughter-size distribution function $\beta(L|L')$. The critical capillary number $\mathrm{Ca_{cr}}$ determines the stability of the droplet and depends on the ratio between the viscosity of the disperse and continuous phases, λ, and on the type of flow inside a specific geometry [259–261]. Its expression can be usually derived from experiments and here two empirical correlations are used. The first one refers to the case of pure shear flow (i.e., mixing index, α, equal to 0.5) [262] as the result of single droplet breakup experiments between two concentric cylinders:

$$\log_{10}\mathrm{Ca}_{\mathrm{cr}} = -0.506 - 0.0994\log_{10}\lambda + 0.124(\log_{10}\lambda)^2 - \frac{0.115}{\log_{10}\lambda - 0.611} \,. \quad (6.11)$$

It is worth mentioning that this expression is valid for $\lambda < 4$, as for $\lambda > 4$ the critical capillary number tends to infinity, implying that for $\lambda > 4$ pure shear flow is not effective in breaking the droplets. The second one refers to the case of flows with an elongational component (i.e. $0.5 < \alpha \leq 1.0$) [261] and reads as follows:

$$\mathrm{Ca}_{\mathrm{cr}} = \frac{0.14\lambda^{-1/6}}{\alpha^{1/2}} \,, \quad (6.12)$$

Figure 6.1 reports the dependency of the critical capillary number versus the viscosity ratio for two values of the mixing index, namely pure shear flow, $\alpha = 0.5$ (Eq. (6.11)), and pure elongational flow for $\alpha = 1.0$ (Eq. (6.12)). As it can be seen, for every reported value of the viscosity ratio λ, the critical capillary number for pure elongational flow is smaller than for pure shear flow, indicating that flows with an elongational component are more effective in breaking droplets. This is particularly true for highly viscous disperse phases, where $\lambda > 4$. In these cases, in fact, the critical capillary number for pure shear flows is practically infinitely large, implying that pure shear flow cannot break the droplets, no matter how intense is the shear rate. When $\lambda > 4$ only an elongational component can reduce the drop size [260, 261].

As far as the viscosity ratio, $\lambda = \eta_{oil}/\eta_c$, is concerned, this is usually evaluated as the ratio between the dispersed and continuous phase viscosity. It is however very common, in the case of high content of the oil phase in emulsions, to use the apparent emulsion viscosity η_{emul} instead of the continuous phase viscosity η_c, as in high disperse phase emulsions, droplets perceive a surrounding continuous phase with the emulsion viscosity [106, 263]. This is also consistent with simulating the flow field in the device by using the pseudo-single phase approach [6, 7, 106].

The coalescence kernel $C(L,L')$ in Eq. (6.9) is incorporated in the model since colliding drops may coalesce despite the cone mill being designed to promote droplet breakage [106, 243]. The coalescence rate is determined by the product of the frequency of droplet collisions and the probability that a collision event will produce coalescence. The collision frequency depends on the local flow field [264], and the coalescence probability depends on the capillary number Ca and the viscosity ratio λ [265]. Further details about the expressions of kernels used here can be found in the

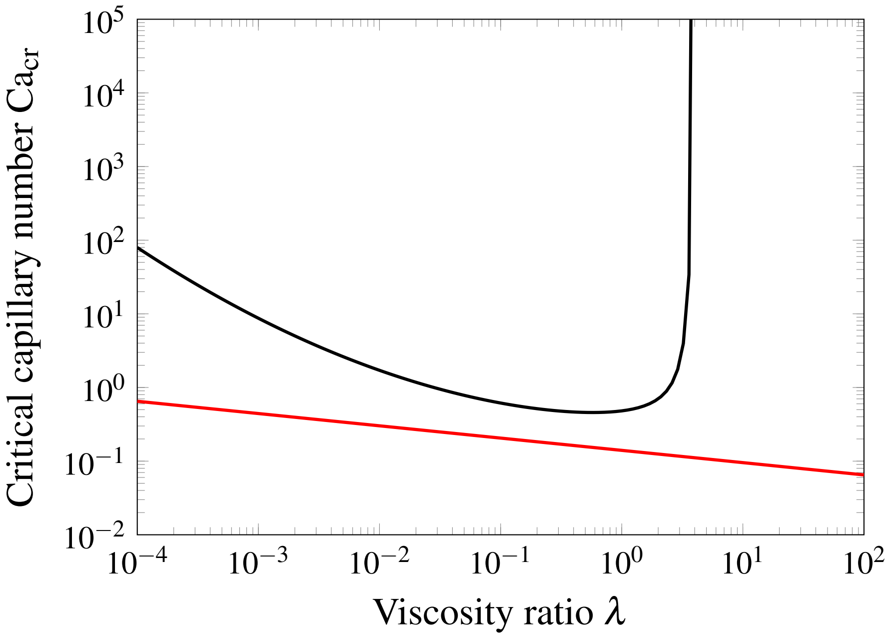

Fig. 6.1 Dependency of the critical capillary number versus the viscosity ratio for pure shear flow (black line $\alpha = 0.5$) (Eq. (6.11)) and pure elongational flow (red line $\alpha = 1.0$) (Eq. (6.12)).

literature [6, 7, 106]. As can be seen from Eqs. (6.9) to (6.12), the coalescence and the breakage kernels are calculated as functions of the local shear rate $\dot{\gamma}$ and of the local apparent emulsion viscosity η_{emul}, both resulting from solving the flow field.

Regarding the daughter-size distribution $\beta(L|L')$, it states the size distribution of daughter droplets originating from a mother droplet after a breakage event. Here a beta function is employed [266]:

$$\beta(L|L') = 180\left(\frac{L^2}{L'^3}\right)\left(\frac{L^3}{L'^3}\right)^2\left(1-\frac{L^3}{L'^3}\right)^2 , \tag{6.13}$$

where L and L' are the sizes of the daughter and mother droplets. Eq. (6.13) assumes that two droplets are formed from a mother and that symmetric breakage is the most likely event. It is important to remind here that the choice of the daughter-size distribution function has a large impact on the final DSD [6, 7, 106], but much less on the mean Sauter diameter [267], used to evaluate the evolution of the DSD in this work. Therefore, the form of the daughter-size distribution function is of secondary importance here.

Finally, the coupling between CFD and PBM is realized here by using two approaches. Some of the simulations are run with the classical on-the-fly coupling, where the governing equations are solved simultaneously [267]; whereas another part of the simulations is run with the off-line coupling, where, first, the CFD equations for the flow field are solved and the relevant information for the flow field is extracted (i.e., the shear rate and the mixing index). Finally, a volume-averaged PBM is solved for the evolution of the DSD [268, 269].

6.3 Numerical details

As already mentioned, we simulated the last step of the mayonnaise production process, i.e., the cone mill mixer, by using CFD and PBM as described in section 6.2. The information about the experiments is taken from the works Refs. [6, 7]. More in detail, three types of mayonnaise were prepared with different concentrations of soybean oil (0.65, 0.70, 0.75 kg/kg), whose density ρ_{oil} and viscosity η_{oil} are respectively equal to 917 $\mathrm{kg/m^3}$ and 50 $\mathrm{mPa \cdot s}$ [106]. Before pumping it into the cone mill, the mayonnaise is characterized by a coarse DSD, whose shape only depends on the initial oil content. After the continuous mixing process into the cone mill, the desired product structure is obtained, i.e., the final DSD is reached. Upstream and downstream DSD measurements are available in the literature for model validation [6, 7].

Each one of these three types of mayonnaise was processed under the three different operating conditions reported in Table 6.1. The last column reports the corresponding Reynolds numbers for the intermediate soybean oil concentration (0.70 kg/kg). As it can be seen, only for Experiment no. 1 the Reynolds number exceeds the critical Reynolds number (also corresponding to the highest Taylor number), highlighting for this operating condition the presence of Taylor vortices [116, 117] (see section 6.4.1).

A sketch of the cone mill mixer is reported in Figure 6.2, together with its 2D and 3D representations. It consists of a solid conical frustum rotor, which rotates clockwise inside a slightly larger stator of the same shape. This configuration forms a small gap in which the emulsion flows from the top to the bottom of the cone mill. The chambers before and after the small gap ensure a homogeneous composition of the emulsion but their role in determining the final DSD is not fully

Table 6.1 Design of experimental test cases from the works Refs. [6, 7] and corresponding Reynolds numbers at oil concentration equal to 0.70 kg/kg (70 wt%).

Exp. no.	**Rotor speed [rpm]**	**Gap [mm]**	**Inlet mass flow rate [kg/h]**	**Re**	
1	6039	0.624	31	140.0	$> \mathrm{Re}_c$ [118]
2	6784	0.208	15	61.2	
3	3170	0.624	64	64.6	

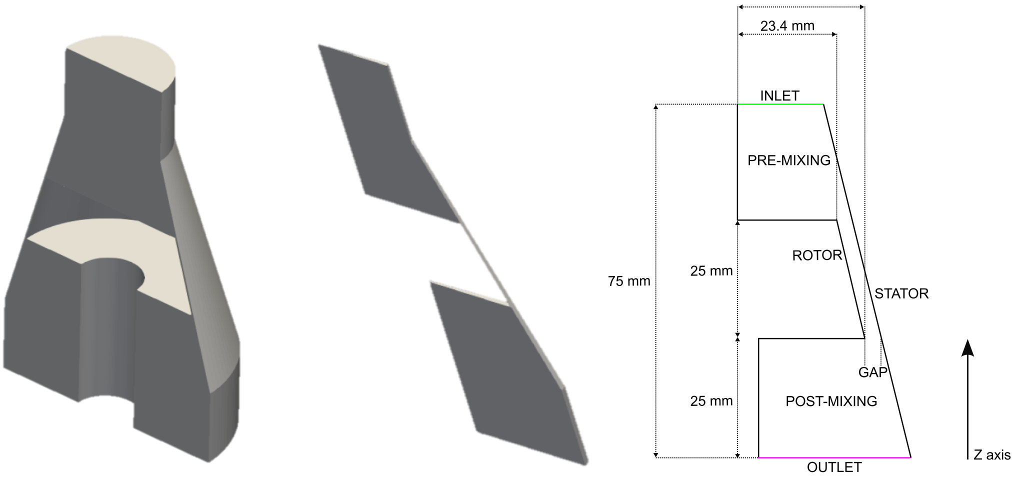

Fig. 6.2 Sketch of the cone mill mixer (right) and corresponding 3D (left) and 2D (center) representations.

clear [6, 7]. This is the reason why different geometries for the simulations are considered, including 2D and 3D representations of the gap region, with and without the pre- and post-mixing chambers. Finally, it is worth mentioning that the pilot scale apparatus (manufactured by IKA) employed in experimental measurements has a more complex geometry, but the representation reported in Figure 6.2 is a reasonable compromise between computational costs and accuracy [6].

All the simulations were performed with the open-source CFD software OpenFOAM (version 6.0). In order to evaluate the flow field, the SRFSimpleFoam solver is employed, which is a steady-state solver for incompressible flows in a single rotating frame. This solver adopts the SIMPLE algorithm for the solution of velocity and pressure coupling. The viscosity model of the emulsion described in section 6.2.1 is implemented as an add-on library.

Table 6.2 Grid independence study on a 2D geometry without pre- and post-mixing chambers for Experiment no. 1 and for a dispersed phase concentration of 0.65 kg/kg (65 wt%).

	Grid 1	**Grid 2**	**Grid 3**	**Grid 4**	**Grid 5**	**Grid 6**
Number of cells along the radial direction	10	15	20	25	30	35
Number of cells along the axial direction	150	220	285	360	430	500
Total number of cells	1500	3300	5700	9000	12900	17500
Number of Taylor vortices	3	16	19	21	21	21
Volume-averaged shear rate [1/s]	28991	29733	30339	30540	30605	30758

In order to properly describe the flow field in the cone mill, a grid independence study was conducted. The six different grids described in Table 6.2 were tested. These six grids refer to the 2D geometry limited to the gap, without pre- and post-mixing chambers. Table 6.2 reports the grid resolution along the axial and radial directions, the total number of cells, the resulting number of Taylor vortices observed, and the volume-averaged shear rate. Only the fine resolution of Grids 4, 5, and 6 makes it possible to properly describe the flow field in terms of both the number of Taylor vortices and the volume-averaged shear rate. Similar information is reported in Figure 6.3, where a contour plot of the shear rate is reported for Experiment no. 1 for Grid 1 and Grid 4 at the oil concentration equal to 0.65 kg/kg (65 wt%). As can be seen, the vortex structure emerges and is correctly described only at the latter grid resolution. All subsequent results refer to a grid resolution of at least 25×360 cells in the gap.

The PBM is solved by means of the QMOM with a three node quadrature, meaning that the first six moments of the DSD are transported. Although in general the evolution of the DSD has an effect on the emulsion viscosity [113], the rheology model here implemented depends only on the dispersed phase volume fraction and not on the oil droplet size. Therefore, the hydrodynamics of the emulsion does not depend on the DSD (see section 6.2.1). As a consequence, in all simulations,

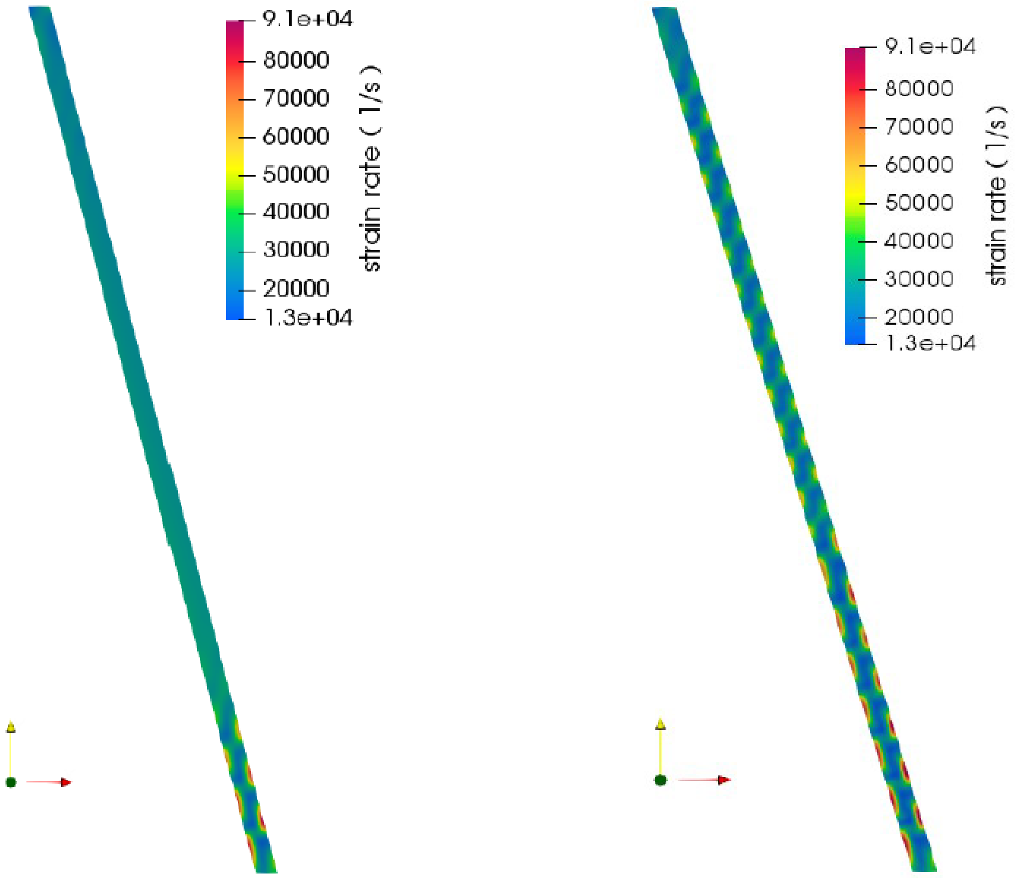

Fig. 6.3 Contour plots of the shear rate reported for Experiment no. 1 for Grid 1 (left) and Grid 4 (right) at the oil concentration equal to 0.65 kg/kg (65 wt%).

Table 6.3 Numerical schemes and boundary conditions used in CFD-PBM simulations.

Variable	**Scheme**	**Boundary condition**			
		Rotor wall	**Stator wall**	**Inlet**	**Outlet**
Pressure	Second-order central scheme	Zero gradient	Zero gradient	Zero gradient	Fixed value
Fluid velocity	Bounded second-order upwind	Rotor speed	No-slip	Constant profile	Zero gradient
Moments	Bounded first-order upwind	Zero gradient	Zero gradient	Fixed value	Zero gradient

at first, only the governing equations of SRFSimpleFoam are solved in order to obtain steady-state flow field information. Then, the variables linking CFD and PBM together, i.e., viscosity and velocity fields (see section 6.2.2), are transferred to the PBM model. As mentioned, in this work two approaches are used. For a limited number of cases, the viscosity and velocity field are transferred to the modified scalarTransportFoam in order to solve the PBM within the CFD code but assuming the flow field was frozen. Further details about this implementation can be found in previous works [250, 251, 258, 270]. Here, the six moments are considered as scalars and their transport equations are incorporated in the scalarTransportFoam module of OpenFOAM that provides a solver for steady or transient transport equation for a single passive scalar, obtaining a modified solver for the solution of the six equations simultaneously. The coalescence and breakage kernels described in section 6.2.2 are used to evaluate the droplet coalescence and breakage rates. Alternatively, the shear rate, $\dot{\gamma}$, and the mixing index, α, within the cone mill are extracted and the PBM is solved in a simplified form as described in a previous work [269].

An overview of the numerical schemes and the boundary conditions used here can be found in Table 6.3. Regarding inlet boundary conditions, the zero gradient condition is set for the pressure, whereas for the velocity an inlet constant profile is imposed, whose value is calculated from the inlet mass flow rate corresponding to experiments reported in Table 6.1. The values of inlet moments (and consequentially the inlet d_{32} value) are calculated from the experimentally measured inlet DSD.

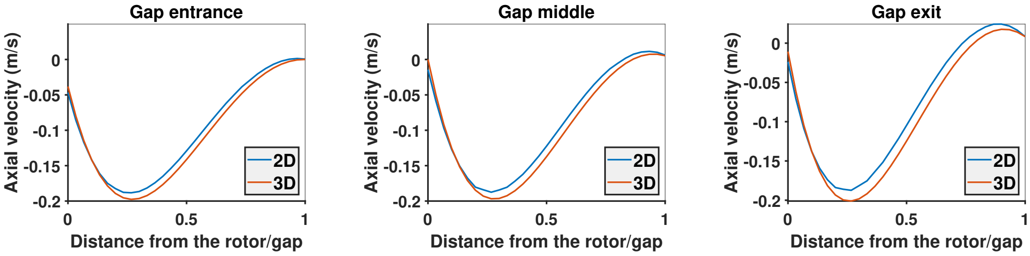

Fig. 6.4 Axial velocity across the gap (normalized distance from the rotating wall) at the gap inlet, center, and outlet, as predicted by 2D and 3D simulations for Experiment no. 1 (Table 6.1) and for a dispersed phase concentration of 0.70 kg/kg (70 wt%).

6.4 Results and discussion

In this section, the most significant results of the simulations performed will be presented. First, the flow field of the emulsion inside the mixer is shown, then, the results of the PBM simulations are also discussed and compared with experimental data.

6.4.1 Flow field results

It is interesting to compare the CFD results obtained with the 2D and 3D geometries with the pre- and post-mixing chambers. Figure 6.4 reports this comparison in terms of the axial velocity across the gap for three different axial positions (inlet, center, and outlet) for one operating condition, namely Experiment no. 1 of Table 6.1. As can be seen, no significant difference is observed between the 2D and the 3D predictions, probably due to the intrinsic axial symmetry of the cone mill. For this reason from now on only 2D results will be presented and discussed. The streaklines for one operating condition are also reported in Figure 6.5. As can be seen, two large recirculation zones are identified in the pre- and post-mixing chambers.

As expected, the CFD simulations show a high velocity gradient due to the high rotational speed, in particular, the highest velocity corresponds to the tip velocity of the rotor, as it can be seen in Figure 6.6, which shows the contour plot of the velocity magnitude in a magnified longitudinal section of the cone mill gap with the oil concentration equal to 0.70 kg/kg (70 wt%) and at operating conditions corresponding to Experiment no. 1 (Table 6.1). Since the rotational speed of the rotor is considerably higher than the inlet fluid velocity, the tangential component of

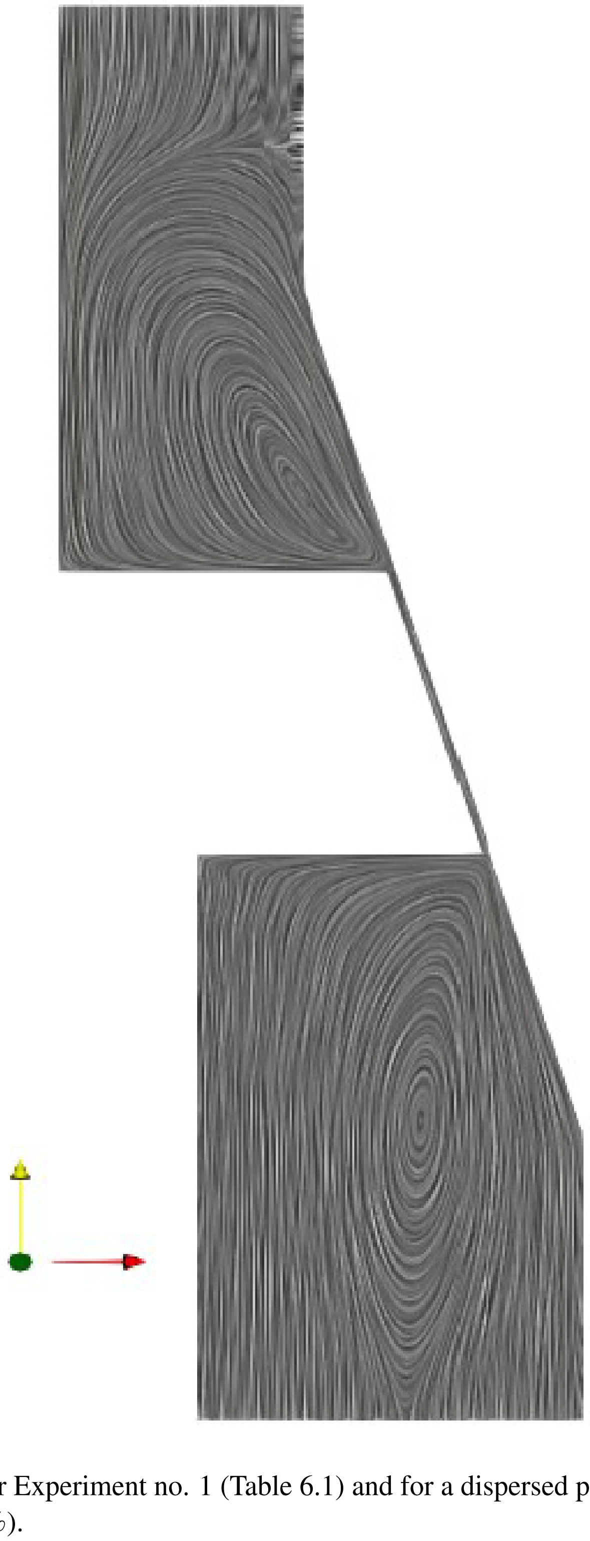

Fig. 6.5 Streaklines for Experiment no. 1 (Table 6.1) and for a dispersed phase concentration of 0.65 kg/kg (65 wt%).

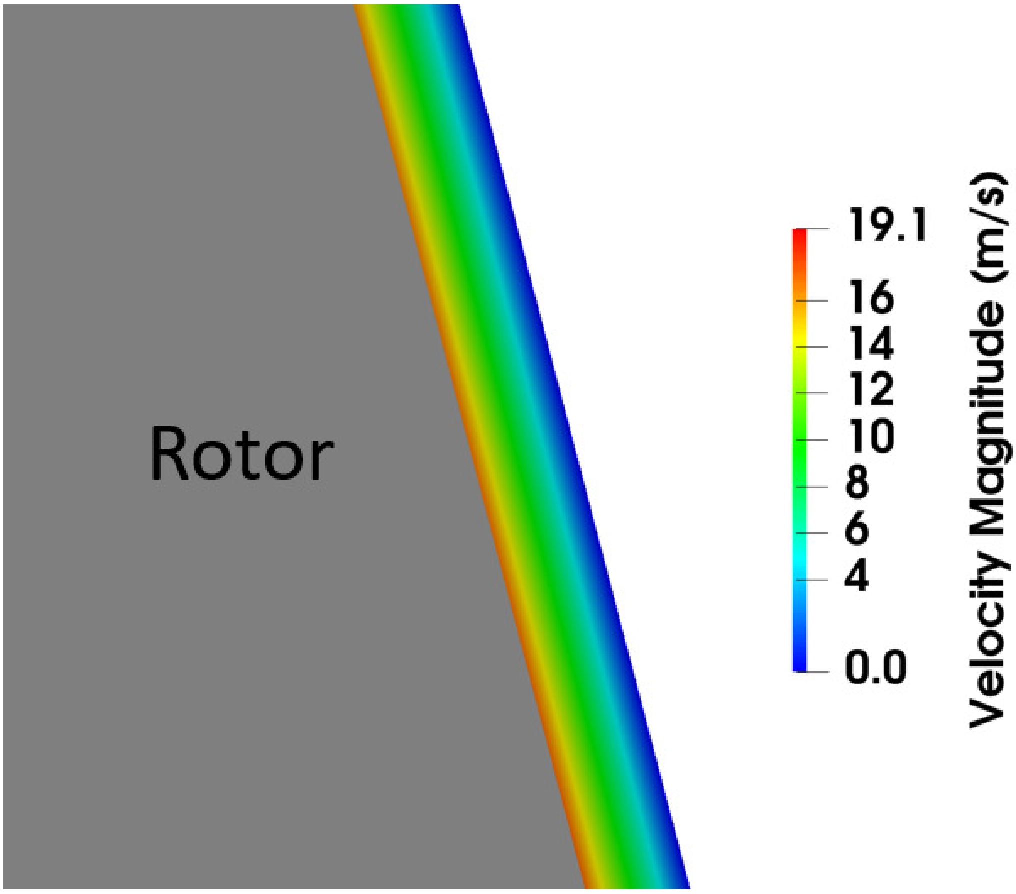

Fig. 6.6 Contour plot of the velocity magnitude in a magnified longitudinal section of the cone mill gap with the oil concentration equal to 0.70 kg/kg (70 wt%) and at operating conditions corresponding to Experiment no. 1 (Table 6.1).

velocity is larger than the axial and radial one and the contour plot of the tangential velocity is very similar to the one reported in Figure 6.6. Moreover, the contour plot shows that the tangential velocity has a linear profile along the gap, with the maximum value at the rotor wall and the minimum one at the stator wall, like in a Couette flow.

Although the main velocity component is the tangential one, it is more interesting to observe the trend of the axial component of the emulsion velocity (z-component). Figure 6.7 reports the axial velocity profiles versus the normalized distance from the rotor wall at half height of the cone mill gap, with the oil concentration equal to 0.70 kg/kg (70 wt%), and for different operating conditions (see Table 6.1). In Experiments no. 2 and 3 the axial velocity presents a parabolic profile, in which the maximum value depends on the inlet flow rate. It is worth reminding here that the fluid flow enters where the cone mill has the smaller radius (top) and exits where it has the larger one (bottom) (see Figure 6.2), explaining the reason for the negative values of velocity. Experiment no. 1 presents a different shape of the axial velocity. Close to the rotor wall, the axial velocity points downward, while its direction is opposite close to the stator wall. Therefore, the presence of such backflow suggests that a large vortex appears for this operating condition, extending over the entire height of the cone mill. This situation has already been observed in previous works, performed with null axial flow [116, 117]. For a better understanding of the fluid flow, Reynolds numbers defined in Eq. (6.1) are calculated for the same conditions of Figure 6.7, and the results are summarized in Table 6.1. For Experiment no. 1 Re is higher than $\mathrm{Re_c}$ (equal to 132 [118]), at which value the flow starts to become unstable and the first large Taylor vortex appears. Although it has been shown experimentally that the axial flow has a stabilizing effect on the formation of instabilities, increasing the value of $\mathrm{Re_c}$ [119], Reynolds number (and, correspondingly, Taylor number) shown in Table 6.1 for Experiment no. 1 is high enough to justify the axial velocity trend shown in Figure 6.7 and to imply the presence of a large vortex filling the entire height of the cone mill.

At last, it is interesting to discuss the predictions for the shear rate, the mixing index, and the corresponding capillary number. Figure 6.8 reports the contour plots for the ratio between the capillary number and the critical capillary number, calculated by using the emulsion viscosity and the viscosity of the continuous phase (Eqs. (6.11) and (6.12)), as well as the mixing index for Experiment no. 1 at the oil concentration equal to 0.65 kg/kg (65 wt%) and no. 3 at the oil concentration equal to 0.70 kg/kg (70 wt%). Closer observation of Figure 6.8 highlights that most of the breakage occurs in the gap, where the capillary number is larger than its critical value due to pure shear flow, namely $\alpha \approx 0.5$. Larger values of the mixing index, namely $\alpha \approx 1$, are observed in the pre- and post-mixing chambers, where, however, the shear rate is not large enough to ensure a value of the capillary number greater than its critical value. This is also confirmed by the results reported in Figure 6.9, where the volume distribution of shear rate and mixing index across the cone mill are reported for the three investigated operating conditions (Table 6.1) at the oil concentration equal to 0.70 kg/kg (70 wt%). As can be seen, the highest shear rates ($\dot{\gamma} \geq 10^3$ 1/s) are observed in regions characterized by a mixing index approximately equal to 0.5. We can therefore conclude that, although the elongational flow, generally more effective in breaking droplets, is observed in the pre- and post-mixing chambers,

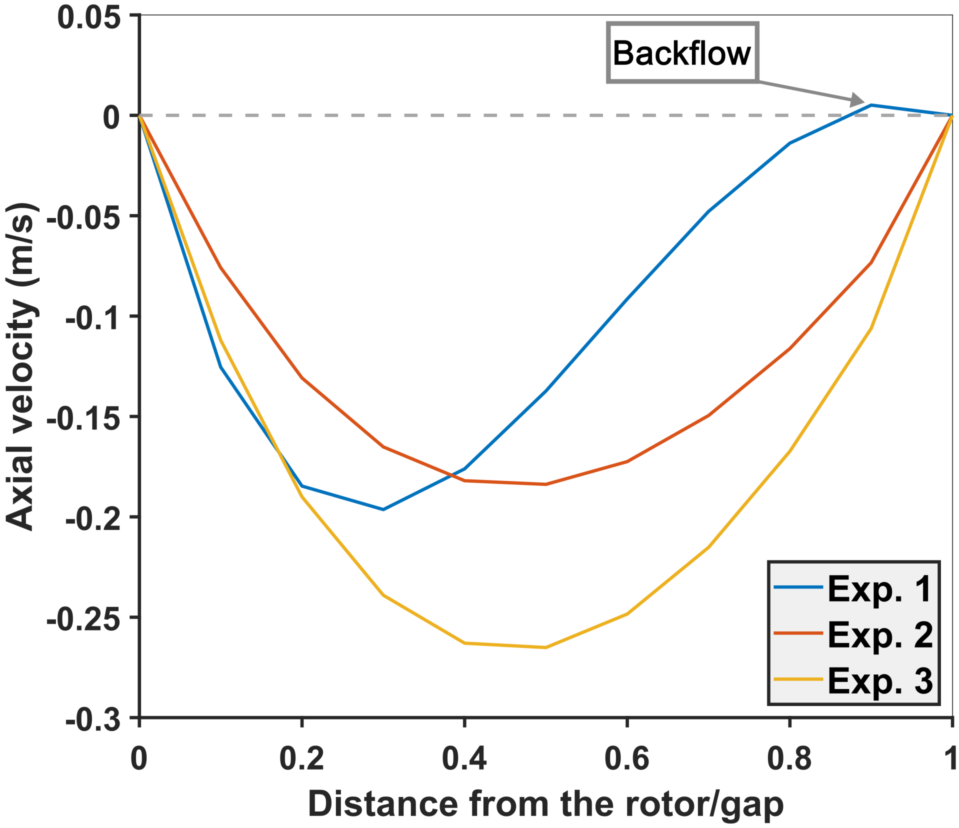

Fig. 6.7 Axial velocity profiles versus the normalized distance from the rotor wall at half height of the cone mill gap with the oil concentration equal to 0.70 kg/kg (70 wt%) and for different operating conditions (see Table 6.1).

most of the droplet breakup occurs within the cone mill gap due to the pure shear flow.

6.4.2 PBM results

As already mentioned, the high rotational speed of the cone mill mixer develops a high-shear rate inside a narrow gap in order to obtain the final product with the desired features. Figure 6.10 reports the trend of the number of the oil droplets per unit volume, corresponding to the moment of order zero of the DSD, and the oil volume fraction, proportional to the moment of order three of the DSD, along the normalized distance from the middle point of the inlet to the middle point of the outlet of the cone mill mixer gap for different oil concentrations. Since the oil concentration does not change due to droplet coalescence and breakage, the third-order moment, which is proportional to the oil volume fraction, remains constant along the gap and is equal to the corresponding values of different types of mayonnaise, as reported in a previous work [7]. On the other hand, the number of oil droplets per unit volume (the moment of order zero) increases, meaning that droplets break moving through the mixer since the total oil amount is constant. In addition, it is important to note that the number of oil droplets is larger for higher oil concentrations.

The evolution of the DSD is reported in terms of the mean Sauter diameter d_{32}, calculated as the ratio between the third and second-order moments. Thanks to the link between PBM and CFD, as described in section 6.2.2, it is possible to highlight the influence of the flow field and, in particular, the high shear rates and the axial velocity on the trend of d_{32}. Figure 6.11 reports the contour plot of d_{32} along a longitudinal section of the cone mill gap with oil concentration equal to 0.70 kg/kg (70 wt%) for Experiments no. 1 and 3. As it can be seen, d_{32} decreases along the flow direction, since droplets undergo breakage induced by the high shear rates inside the mixer. These trends exactly reproduce what it is expected from experimental observations [6, 7]. The insets in Figure 6.11 are magnified sections of the cone mill gap that show in detail how the flow field and, in particular, the axial velocity influence d_{32} trends. For Experiment no. 3, the d_{32} presents a parabolic profile along the gap width, with the higher value at the center of the gap and the lower at the walls, similarly to the respective axial component of velocity (see Figure 6.7). For Experiment no. 1, the situation is different from Experiment no. 3. In this case, it is represented very clearly how the flow field can influence the local DSD. As it is

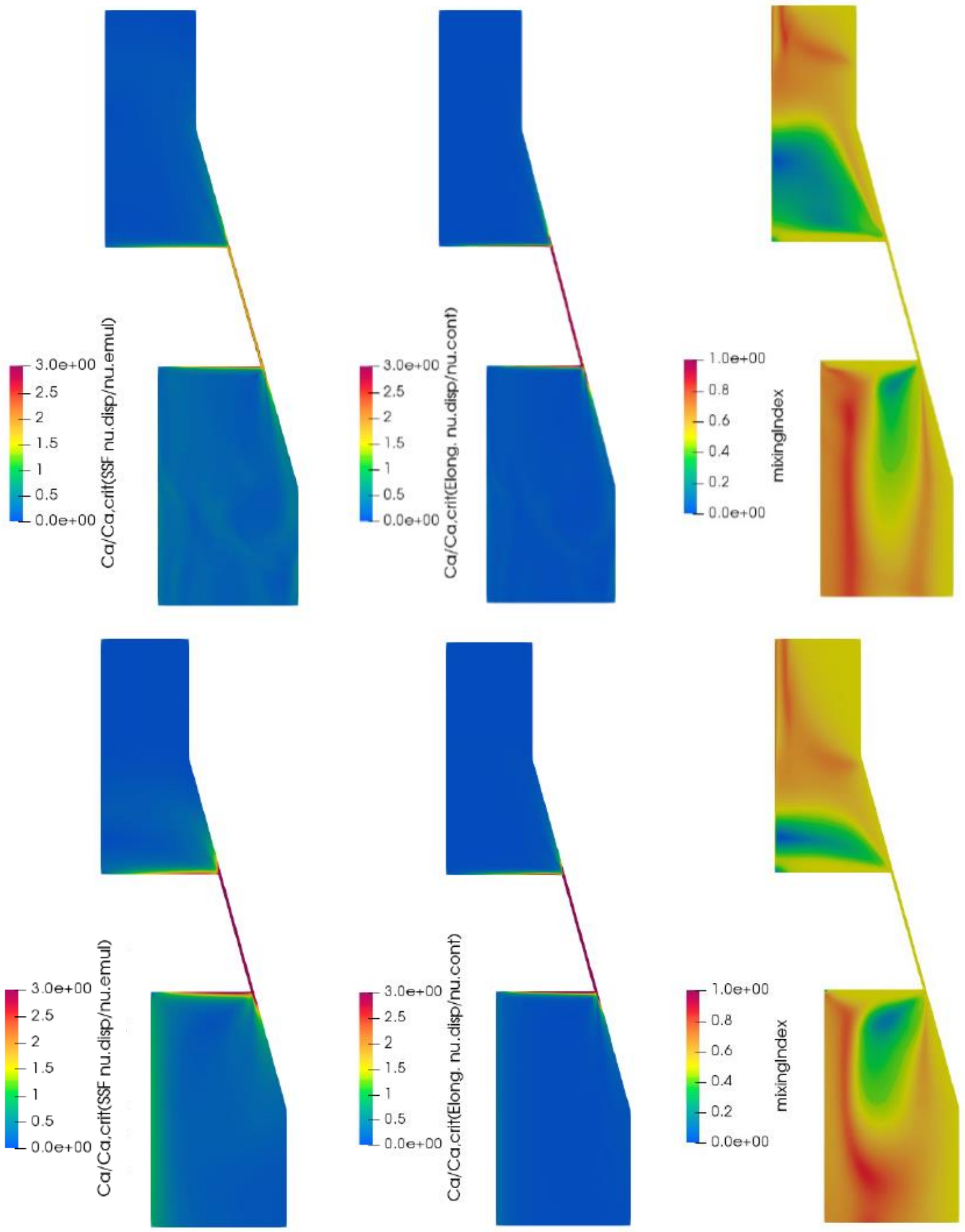

Fig. 6.8 Contour plots for the ratio between the capillary number and the critical capillary number, calculated by using the emulsion viscosity (left) and the continuous phase viscosity (center) (Eqs. (6.11) and (6.12)), and the mixing index, α (right), for Experiment no. 1 at the oil concentration equal to 0.65 kg/kg (65 wt%)(top) and no. 3 at the oil concentration equal to 0.70 kg/kg (70 wt%)(bottom).

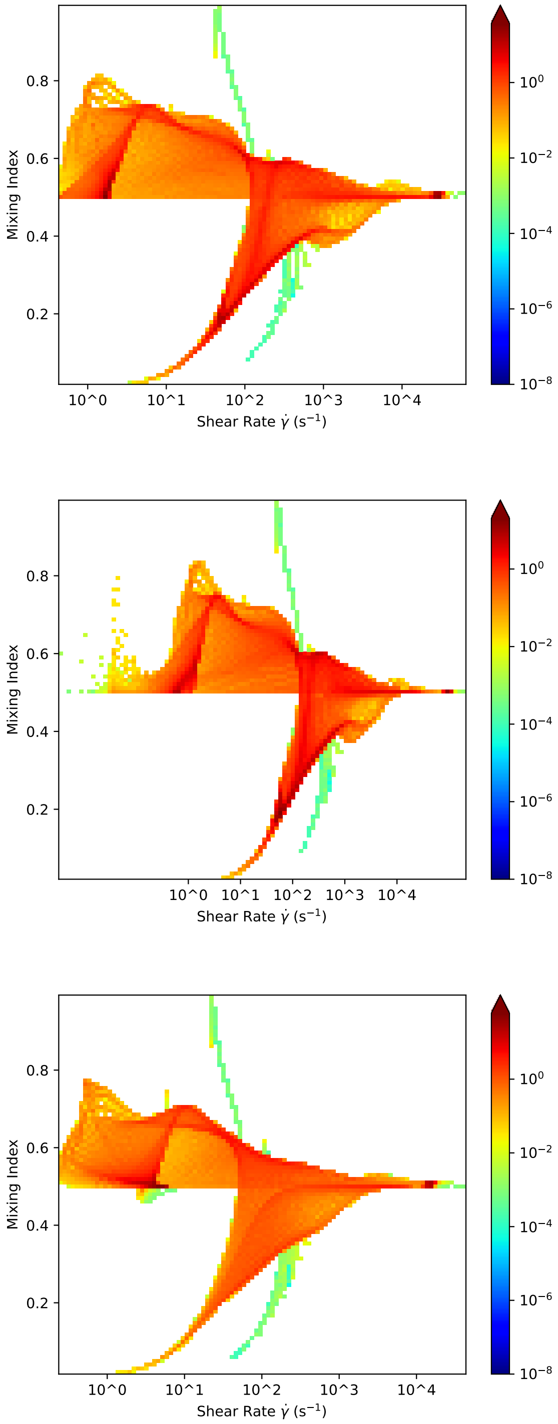

Fig. 6.9 Volume distribution of mixing index and shear rate for operating conditions corresponding to Experiment no. 1 (top), no. 2 (middle) and no. 3 (bottom) at the oil concentration equal to 0.70 kg/kg (70 wt%) (see Table 6.1).

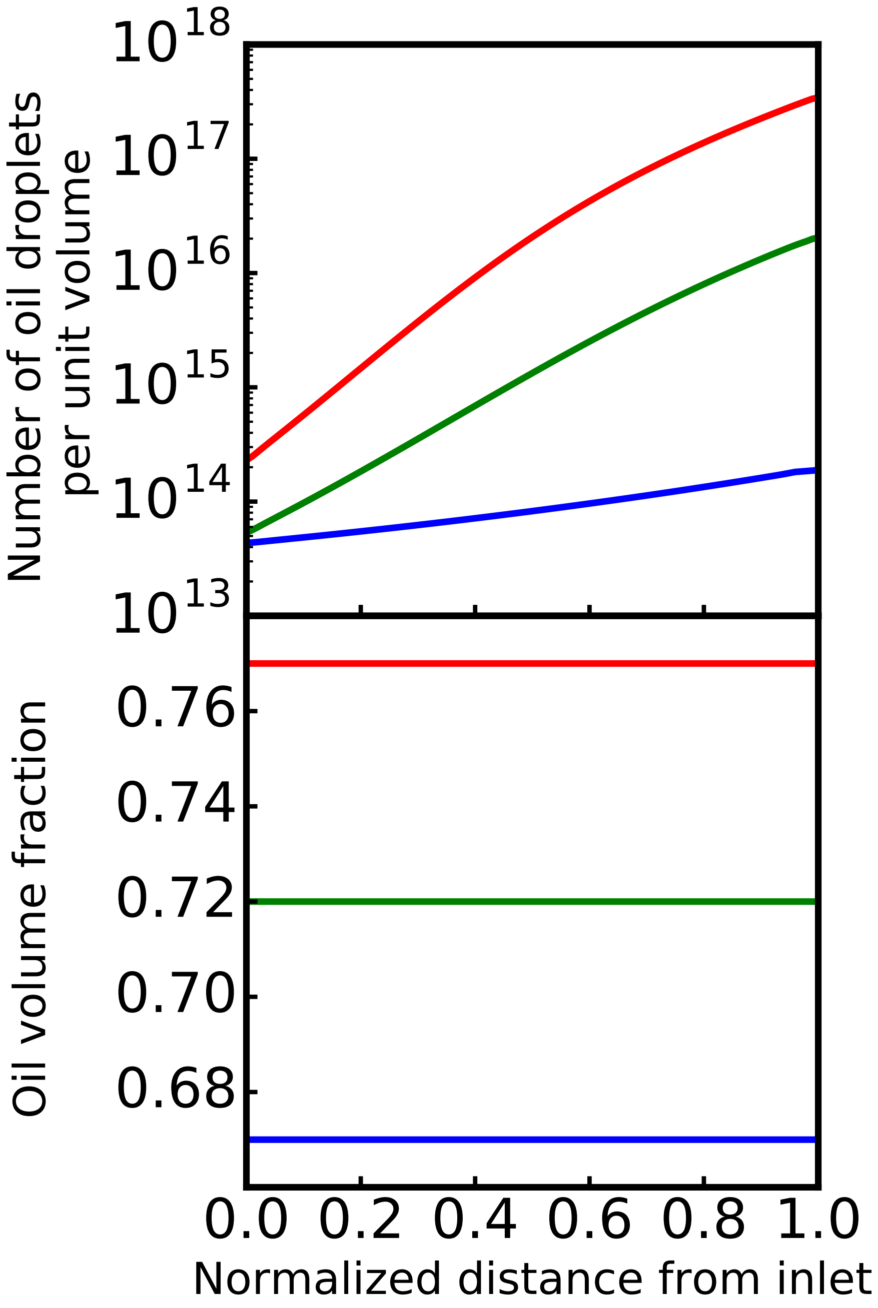

Fig. 6.10 Trend of the number of oil droplets per unit volume (M_0, top) and oil volume fraction ($\pi/6\,M_3$, bottom) along the normalized distance from the middle point of the inlet to the middle point of the outlet of the cone mill mixer gap, for oil concentrations equal to 0.65 kg/kg (blue line), 0.70 kg/kg (green line), and 0.75 kg/kg (red line) in the Experiment n.3 (see Table 6.1).

Table 6.4 Comparison between PBM predictions and experimental measurements for the mean Sauter diameter for Experiments no. 1 and 3 at the oil concentration equal to 0.70 kg/kg (70 wt%) for different values of the coalescence kernel constants, K_1 and K_2, and the breakage kernel constants, K_3 and K_4.

Exp. no.	K_1	K_2	K_3	K_4	d_{32}^{Model} [μm]	d_{32}^{Exp} [μm]
1	1×10^{-6}	1.077×10^{2}	2.154×10^{-4}	1.744×10^{-3}	6.9	6.6
	2.154×10^{-4}	1.498×10^{-6}	4.642×10^{-2}	2.684	3.6	
	1×10^{1}	1.077×10^{2}	2.154×10^{-4}	2.684	23.7	
3	1×10^{-6}	1.077×10^{2}	2.154×10^{-4}	1.744×10^{-3}	29.1	7.7
	2.154×10^{-4}	1.498×10^{-6}	4.642×10^{-2}	2.684	6.7	
	1×10^{1}	1.077×10^{2}	2.154×10^{-4}	2.684	32.0	

reported in section 6.4.1 and Figure 6.7, the presence of Taylor instability inside the mixer leads to a particular shape of the velocity profile. Therefore, the link between CFD and PBM is able to show that the oil droplets are bigger close to the rotor and smaller close to the stator. The average outlet values of d_{32} shown in Figure 6.11 are equal to 7.1 μm for case no. 3 and 5.4 μm for case no. 1, whereas the experimental ones are respectively 7.7 μm and 6.6 μm [7], with a relative error under 20%. These outcomes are obtained by suitably adjusting the free parameters that appear in coalescence and breakage kernels, through a trial and error procedure and more details on this are given below. It is important to point out that the results reported here have illustrative purposes, to show the capabilities of the CFD-PBM approach. Achieving a unique and generic set of free parameters that matches all the experimental data, using optimization and uncertainty quantification techniques, will be the scope of future works.

As just mentioned, the predictions of the PBM are highly affected by the values of the model parameters appearing in the coalescence kernel, K_1 and K_2, and the breakage kernel, K_3 and K_4. Due to the semi-empirical nature of these kernels and the many approximations adopted in their derivation, their values cannot be predicted by the theory but have to be fitted with experiments. An example of the influence of the model parameters on the final predictions can be found in Table 6.4. As expected by increasing K_1, coalescence becomes more important and the mean Sauter diameter increases, and conversely, by increasing K_3 or K_4 breakup becomes more important and the mean Sauter diameter decreases.

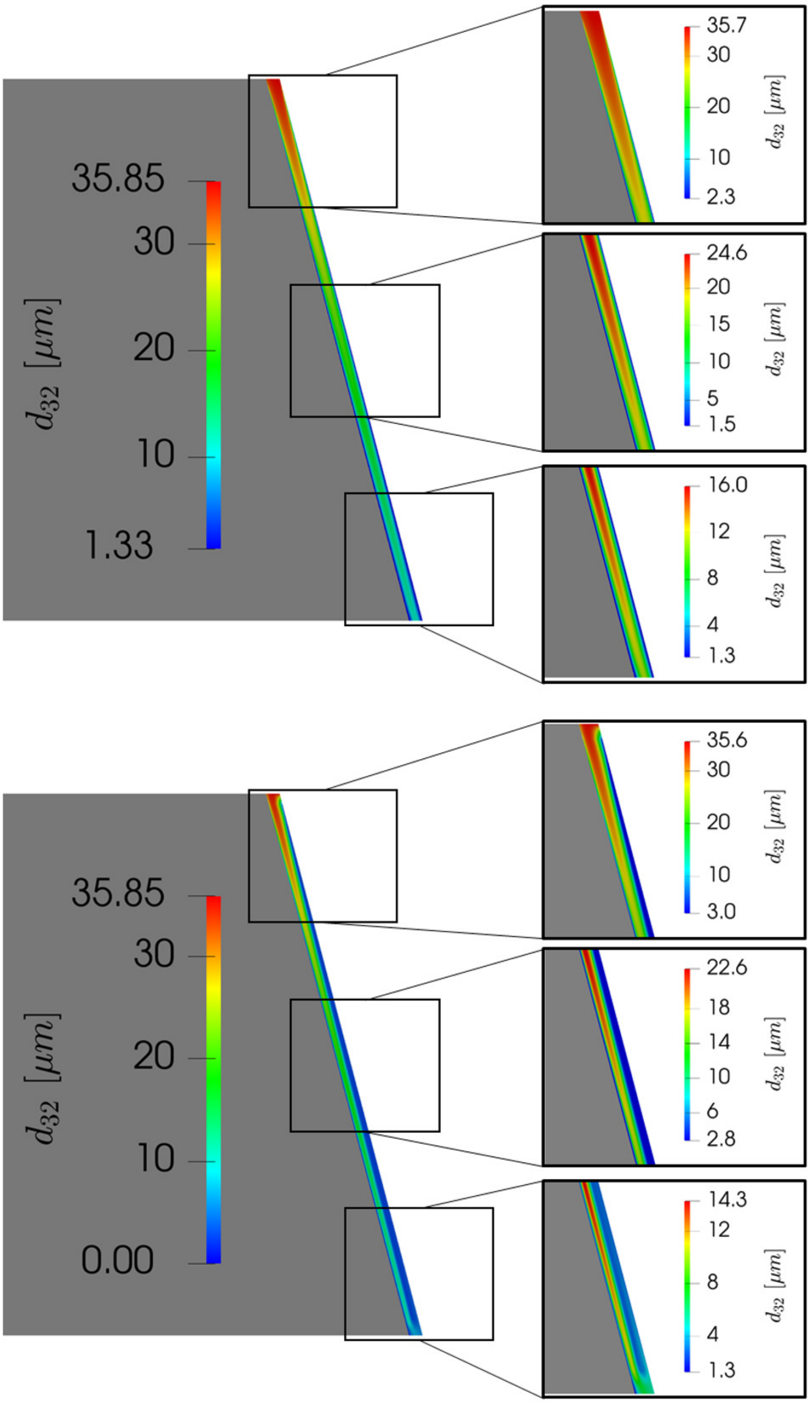

Fig. 6.11 Contour plots of the mean Sauter diameter d_{32} of oil droplets along a longitudinal section of the cone mill gap with oil concentration equal to 0.70 kg/kg (70 wt%) for the Experiments no. 3 (top) and no. 1 (bottom) (see Table 6.1). Insets are magnified gap sections.

Table 6.5 Final comparison between the mean Sauter diameter predicted by the PBM and measured experimentally for Experiments no. 1, 2, and 3 and for the three dispersed phase concentrations investigated here.

Exp. no.	**Mayonnaise 1 (0.65 kg/kg)**		**Mayonnaise 2 (0.70 kg/kg)**		**Mayonnaise 3 (0.75 kg/kg)**	
	exp. data [μm]	model pred. [μm]	exp. data [μm]	model pred. [μm]	exp. data [μm]	model pred. [μm]
1	7.206	9.530	6.587	5.180	4.647	3.180
2	8.787	9.250	5.844	4.780	4.815	2.950
3	12.364	11.99	7.713	6.130	6.063	3.830

In order to optimize the model parameters K_1, K_2, K_3, and K_4, the PBM, solved in the simplified form described in a previous work [269], was coupled with the covariance matrix adaptation evolution strategy (CMA-ES) algorithm [271]. The algorithm minimizes the normalized distance between the predicted mean Sauter diameter and the corresponding experimental values, resulting in the final predictions reported in Table 6.5. The optimization was performed with the PBM implemented in its simplified form, rather than with the full CFD-PBM due to the computational costs associated with the full CFD-PBM which are prohibitive for these applications. As it can be seen from Table 6.5, the comparison is satisfactory as the PBM is capable of capturing the most important trends for the investigated operating conditions.

6.5 Conclusions

In this chapter, a modeling approach for food emulsion production in a high-shear mixer was presented. A flow field analysis performed with CFD shows that recognizable patterns for the investigated geometry are in agreement with previous experimental works. In particular, the tangential component of the emulsion velocity shows a Couette flow, whereas the axial velocity trends depend on Reynolds number: for $\mathrm{Re} < \mathrm{Re}_c$, a Poiseuille flow develops inside the gap of the mixer, but above Re_c the first instability appears and backflow occurs. Thanks to the coupling between CFD and PBM, demonstrated with two approaches, it is possible to obtain a better understanding of the flow influence on the evolution of the droplet size distribution. In particular, the role of the type of flow, elongational versus pure shear, and the role of the pre- and post-mixing chambers in the cone mill were elucidated. This model accounts for both the coalescence and the breakage of the oil droplets, which depend, in turn, on the local flow conditions. From the evaluation of the mean oil droplet diameter, the simulations are able to show that the breaking of the oil droplets promoted by the high shear rates prevails over the coalescence phenomenon, reproducing correctly the experimental data. As a powerful and convenient method for such kind of applications, QMOM is employed for the solution of the population balance equation, taking into account the actual hydrodynamics of the emulsion in order to provide a more accurate prediction of the droplet size distribution.

The results presented here will also serve as the basis for future extension of this work in several directions. First, an optimization procedure will be employed in order to identify an accurate and generic set of kernel constants reproducing the available experimental data. Then, these simulations can be included in a more general multi-scale framework in which the effect of the DSD on the emulsion viscosity can be taken into account via detailed front-tracking simulations. Moreover, the interfacial tension can be directly made dependent on the definition of the local surfactant concentration, thus better including the results on smaller scales from the previous chapters.

Chapter 7

Conclusions and final remarks

This work focused on the multiscale modeling approach for simulating food emulsion production at different space and time scales, namely from the molecular to the equipment level. The main physical phenomena involved in the process are droplet breakage and coalescence, which, in turn, depend on several aspects playing a role at different levels of description. At the molecular scale, the type of surfactant, its adsorption mechanism, and the thermodynamic behavior are essential information to define the interfacial force acting on the oil droplet surface. On the other hand, the type of flow experienced by oil droplets inside the production device, the non-Newtonian viscosity of the emulsion, and the different operating conditions can be studied at the macroscale level of description. Therefore, based on the properties to be investigated, many modeling techniques were here employed to provide useful insight into the physics of the food emulsion. As done in typical multiscale studies, information was transferred from a smaller to a larger scale, thus proposing possible links between different modeling methods. Since each chapter of the thesis was dedicated to a specific technique according to the topic investigated, an overview of the main conclusions obtained is here restated and final remarks are drawn.

In chapter 2, the adsorption of one of the proteins responsible for the stability of food emulsions, the so-called Apovitellenin I, was studied using fully atomistic Molecular Dynamics and Metadynamics simulations. First, it was verified that this protein can actually act as a surfactant at the oil-water interface by analyzing its adsorption behavior. Then, the influence of co-surfactants (phospholipids) on protein adsorption was also investigated showing competitive and/or cooperative interactions based on their spatial configuration. The methodology employed here showed an important advantage to estimating properties that are difficult to obtain experimentally, especially the Gibbs free energy of adsorption which is then used in the coarse-grained model.

In chapter 3, the oil-water interface system stabilized by protein surfactants was simulated via a coarse-grained model, i.e., the Dissipative Particle Dynamics technique coupled with Molecular Dynamics simulations. In particular, this method was able to properly describe the protein surfactant behavior by representing the interfacial tension decrease at increasing protein surface concentration. Reasonable results were obtained in line with experimental evidence of similar protein systems. The present approach was linked to Metadynamics results through a thermodynamic model of protein adsorption to obtain a complete description of Apovitellenin I as a surfactant. Indeed, this procedure can predict a macroscopic property of liquid-liquid interfacial systems, namely the increase of the surface pressure at increasing protein bulk concentration.

In chapter 4, a scaling scheme for classical Dissipative Particle Dynamics simulations was applied to ternary interfacial systems in order to obtain a simplified model that can properly reproduce the decrease of interfacial tension determined with more detailed mesoscale simulations. By applying an appropriate scaling procedure and parameterization, it is possible to conserve the equilibrium interfacial tension trend and maintain the domain conformation even for a simple coarse-grained representation of the molecules involved in the ternary system. Therefore, if an interfacial system can be simulated with classical Dissipative Particle Dynamics on a smaller scale, the scaling of interactions does not prevent a simulation on a larger scale under certain conditions.

In chapter 5, the phase field model was applied for the numerical simulations of immiscible binary fluids in the presence of soluble surfactant within the Lattice Boltzmann model. When dealing with amphiphilic molecules, this approach can describe the typical surfactant adsorption isotherms. By comparing the present method with a Dissipative Particle Dynamics work, it was shown that it is possible to find a link between the two mesoscopic techniques and, in turn, between the particle-based and continuum modeling approaches.

In chapter 6, Computational Fluid Dynamics simulations were coupled with Population Balance Model for describing the last step of the food emulsion production process taking place in a high-shear mixer. The model took into account both the coalescence and breakage of oil droplets, depending on local flow conditions. As the most important property of the food emulsion, the droplet size distribution was correctly reproduced by a comparison with experimental data. A better understanding of the flow influence was achieved showing that the oil droplet breakup promoted by the high shear rates prevails over coalescence events.

Finally, the modeling methods here presented showed how computer simulations can greatly help in the comprehension of food emulsion behavior. Although some issues still need to be addressed for a complete description of the topic studied, however, the multiscale approach can be considered a suitable tool for the investigation of such problems where several physical phenomena are involved at different scales. In general, this work reported how various modeling techniques can be linked together not only to reproduce qualitative behaviors but also to quantitatively predict properties that are difficult to estimate experimentally. This represents a remarkable advantage, especially when dealing with very complex systems as in food science where experimental research can be hindered by difficulties in isolating individual components and their relative contributions to the properties of interest.

References

[1] M. Anton. Egg yolk: structures, functionalities and processes. *Journal of the Science of Food and Agriculture*, 93(12):2871–2880, 2013.

[2] D. E. Graham and M. C. Phillips. Proteins at liquid interfaces: II. Adsorption isotherms. *Journal of Colloid and Interface Science*, 70(3):415–426, 1979.

[3] E. G. Perkins. Chapter 2 - Composition of Soybeans and Soybean Products. In D. R. Erickson, editor, *Practical Handbook of Soybean Processing and Utilization*, pages 9–28. AOCS Press, 1995.

[4] M. Anton. Composition and Structure of Hen Egg Yolk. In R. Huopalahti, R. López-Fandiño, M. Anton, and R. Schade, editors, *Bioactive Egg Compounds*, pages 1–6. Springer Berlin Heidelberg, Berlin, Heidelberg, Germany, 2007.

[5] A. H. Ali, X. Zou, J. Lu, S. M. Abed, Y. Yao, G. Tao, Q. Jin, and X. Wang. Identification of phospholipids classes and molecular species in different types of egg yolk by using UPLC-Q-TOF-MS. *Food Chemistry*, 221:58–66, 2017.

[6] A. Dubbelboer. *Towards optimization of emulsified consumer products : modeling and optimization of sensory and physicochemical aspects*. PhD thesis, Technische Universiteit Eindhoven, Department of Chemical Engineering and Chemistry, 2016.

[7] A. Dubbelboer, J. J. M. Janssen, H. Hoogland, E. Zondervan, and J. Meuldijk. Pilot-scale production process for high internal phase emulsions: Experimentation and modeling. *Chemical Engineering Science*, 148:32–43, 2016.

[8] L. J. Harrison and F. E. Cunningham. Factors influencing the quality of mayonnaise: a review. *Journal of Food Quality*, 8(1):1–20, 1985.

[9] K. P. Das and J. E. Kinsella. Stability Of Food Emulsions: Physicochemical Role Of Protein And Nonprotein Emulsifiers. volume 34 of *Advances in Food and Nutrition Research*, pages 81–201. Academic Press, 1990.

[10] D. J. Mcclements. Critical Review of Techniques and Methodologies for Characterization of Emulsion Stability. *Critical Reviews in Food Science and Nutrition*, 47(7):611–649, 2007.

[11] J. P. Mackson and S. P. Singh. The effect of temperature and vibration on emulsion stability of mayonnaise in two different package types. *Packaging Technology and Science*, 4(2):81–90, 1991.

[12] D. J. McClements. *Food Emulsions: Principles, Practice, and Techniques*. CRC Press, Boca Raton, FL, 2005.

[13] S. Friberg, J. Sjoblom, and K. Larsson. *Food Emulsions*. CRC Press, Boca Raton, FL, 2003.

[14] D. G. Dalgleish. Food emulsions. In J. Sjoblom, editor, *Emulsions and emulsion stability*, page 287–325. Marcel Dekker Inc., 1996.

[15] R. W. Burley. Isolation and properties of a low-molecular-weight protein (apovitellenin I) from the high-lipid lipoprotein of emu egg yolk. *Biochemistry*, 12(7):1464–1470, 1973.

[16] R. W. Burley. Studies on the Apoproteins of the Major Lipoprotein of the Yolk of Hen's Eggs I. Isolation and Properties of the Low-molecular-weight Apoproteins. *Australian Journal of Biological Sciences*, 28:121–132, 1975.

[17] J. A. Depree and G. P. Savage. Physical and flavour stability of mayonnaise. *Trends in Food Science & Technology*, 12(5):157–163, 2001.

[18] G. Urbina-Villalba. Effect of Dynamic Surfactant Adsorption on Emulsion Stability. *Langmuir*, 20(10):3872–3881, 2004.

[19] M. Anton, V. Martinet, M. Dalgalarrondo, V. Beaumal, E. David-Briand, and H. Rabesona. Chemical and structural characterisation of low-density lipoproteins purified from hen egg yolk. *Food Chemistry*, 83(2):175–183, 2003.

[20] P. Jolivet, C. Boulard, V. Beaumal, T. Chardot, and M. Anton. Protein Components of Low-Density Lipoproteins Purified from Hen Egg Yolk. *Journal of Agricultural and Food Chemistry*, 54(12):4424–4429, 2006.

[21] R. W. Burley. Studies on the Apoproteins of the Major Lipoprotein of the Yolk of Hen's Eggs III. Influence of Salt Concentration During Isolation on the Amount and Composition of the Apoproteins. *Australian Journal of Biological Sciences*, 31(6):587–592, 1978.

[22] V. Martinet, P. Saulnier, V. Beaumal, J.-L. Courthaudon, and M. Anton. Surface properties of hen egg yolk low-density lipoproteins spread at the air–water interface. *Colloids and Surfaces B: Biointerfaces*, 31(1):185–194, 2003.

[23] W. Norde. *Colloids and Interfaces in Life Sciences and Bionanotechnology*. CRC Press, Boca Raton, FL, 2011.

[24] C.-A. Palma, M. Cecchini, and P. Samorì. Predicting self-assembly: from empirism to determinism. *Chemical Society Reviews*, 41(10):3713–3730, 2012.

[25] A. J. Stone. *The Theory of Intermolecular Forces*. Oxford University Press, Oxford, U.K., 2013.

[26] A. D. Lavino, M. Ferrari, A. A. Barresi, and D. Marchisio. Effect of different good solvents in flash nano-precipitation via multi-scale population balance modeling-CFD coupling approach. *Chemical Engineering Science*, 245:116833, 2021.

[27] S. R. Euston. Computer simulation of proteins: adsorption, gelation and self-association. *Current Opinion in Colloid & Interface Science*, 9(5):321–327, 2004.

[28] L. A. Pugnaloni, E. Dickinson, R. Ettelaie, A. R. Mackie, and P. J. Wilde. Competitive adsorption of proteins and low-molecular-weight surfactants: computer simulation and microscopic imaging. *Advances in Colloid and Interface Science*, 107(1):27–49, 2004.

[29] D. Zahn. On the role of the solvent in biosystems: atomistic insights from computer simulations. *Frontiers in Bioscience-Landmark*, 14(9):3586–3593, 2009.

[30] E. Dickinson. Structure and rheology of colloidal particle gels: Insight from computer simulation. *Advances in Colloid and Interface Science*, 199-200:114–127, 2013.

[31] S. R. Euston. 14 - Modelling and computer simulation of food structures. In V.J. Morris and K. Groves, editors, *Food Microstructures*, Woodhead Publishing Series in Food Science, Technology and Nutrition, pages 336–385. Woodhead Publishing, 2013.

[32] A. Jusufi. Molecular simulations of self-assembly processes of amphiphiles in dilute solutions: the challenge for quantitative modelling. *Molecular Physics*, 111(21):3182–3192, 2013.

[33] J.-W. Handgraaf and F. Zerbetto. Molecular dynamics study of onset of water gelation around the collagen triple helix. *Proteins: Structure, Function, and Bioinformatics*, 64(3):711–718, 2006.

[34] A. D. Lavino, N. Di Pasquale, P. Carbone, and D. L. Marchisio. A novel multi-scale model for the simulation of polymer flash nano-precipitation. *Chemical Engineering Science*, 171:485–494, 2017.

[35] A. D. Lavino, P. Carbone, and D. Marchisio. MARTINI coarse-grained model for poly-ε-caprolactone in acetone-water mixtures. *The Canadian Journal of Chemical Engineering*, 98(9):1868–1879, 2020.

[36] A. D. Lavino, L. Banetta, P. Carbone, and D. L. Marchisio. Extended Charge-On-Particle Optimized Potentials for Liquid Simulation Acetone Model: The Case of Acetone–Water Mixtures. *The Journal of Physical Chemistry B*, 122(20):5234–5241, 2018.

[37] D. Frenkel and B. Smit. Chapter 1 - Introduction. In D. Frenkel and B. Smit, editors, *Understanding Molecular Simulation*, pages 1–6. Academic Press, San Diego, USA, 2nd edition, 2002.

[38] D. Frenkel and B. Smit. *Understanding Molecular Simulation*. Academic Press, Inc., USA, 2nd edition, 2001.

[39] C. J. Cramer. *Essentials of Computational Chemistry: Theories and Models*. Wiley, New York, USA, 2nd edition, 2004.

[40] P. J. Hoogerbrugge and J. M. V. A Koelman. Simulating Microscopic Hydrodynamic Phenomena with Dissipative Particle Dynamics. *Europhysics Letters (EPL)*, 19(3):155–160, jun 1992.

[41] P. Español and P. Warren. Statistical Mechanics of Dissipative Particle Dynamics. *Europhysics Letters (EPL)*, 30(4):191–196, may 1995.

[42] R. D. Groot and P. B. Warren. Dissipative particle dynamics: Bridging the gap between atomistic and mesoscopic simulation. *The Journal of Chemical Physics*, 107(11):4423–4435, 1997.

[43] N. Lauriello, J. Kondracki, A. Buffo, G. Boccardo, M. Bouaifi, M. Lisal, and D. Marchisio. Simulation of high Schmidt number fluids with dissipative particle dynamics: Parameter identification and robust viscosity evaluation. *Physics of Fluids*, 33(7):073106, 2021.

[44] E. Dickinson and S. R. Euston. Monte Carlo simulation of colloidal systems. *Advances in Colloid and Interface Science*, 42:89–148, 1992.

[45] R. E. Anderson, V. S. Pande, and C. J. Radke. Dynamic lattice Monte Carlo simulation of a model protein at an oil/water interface. *The Journal of Chemical Physics*, 112(20):9167–9185, 2000.

[46] G. Dalkas and S. R. Euston. Molecular simulation of protein adsorption and conformation at gas-liquid, liquid–liquid and solid–liquid interfaces. *Current Opinion in Colloid & Interface Science*, 41:1–10, 2019.

[47] D. Zare, K. M. McGrath, and J. R. Allison. Deciphering β-Lactoglobulin Interactions at an Oil–Water Interface: A Molecular Dynamics Study. *Biomacromolecules*, 16(6):1855–1861, 2015.

[48] D. Zare, J. R. Allison, and K. M. McGrath. Molecular Dynamics Simulation of β-Lactoglobulin at Different Oil/Water Interfaces. *Biomacromolecules*, 17(5):1572–1581, 2016.

[49] D. L. Cheung. Adsorption and conformations of lysozyme and α-lactalbumin at a water-octane interface. *The Journal of Chemical Physics*, 147(19):195101, 2017.

[50] D. L. Cheung. Conformations of Myoglobin-Derived Peptides at the Air–Water Interface. *Langmuir*, 32(18):4405–4414, 2016.

[51] S. R. Euston. Molecular Dynamics Simulation of Protein Adsorption at Fluid Interfaces: A Comparison of All-Atom and Coarse-Grained Models. *Biomacromolecules*, 11(10):2781–2787, 2010.

[52] S. R. Euston, P. Hughes, Md. A. Naser, and R. E. Westacott. Comparison of the Adsorbed Conformation of Barley Lipid Transfer Protein at the Decane-Water and Vacuum-Water Interface: A Molecular Dynamics Simulation. *Biomacromolecules*, 9(5):1443–1453, 2008.

[53] S. R. Euston, P. Hughes, Md. A. Naser, and R. E. Westacott. Molecular Dynamics Simulation of the Cooperative Adsorption of Barley Lipid Transfer Protein and cis-Isocohumulone at the Vacuum-Water Interface. *Biomacromolecules*, 9(11):3024–3032, 2008.

[54] A. Laio and M. Parrinello. Escaping Free-Energy Minima. *Proceedings of the National Academy of Sciences of the United States of America*, 99(20):12562–12566, 2002.

[55] F. Sepehr and S. J. Paddison. Dissipative Particle Dynamics interaction parameters from *ab initio* calculations. *Chemical Physics Letters*, 645:20–26, 2016.

[56] H. Lei, B. Caswell, and G. Karniadakis. Direct construction of mesoscopic models from microscopic simulations. *Physical Review E*, 81(2):026704, Feb 2010.

[57] W. Tschöp, K. Kremer, J. Batoulis, T. Bürger, and O. Hahn. Simulation of polymer melts. I. Coarse-graining procedure for polycarbonates. *Acta Polymerica*, 49(2-3):61–74, 1998.

[58] A. Vishnyakov and A. V. Neimark. Self-Assembly in Nafion Membranes upon Hydration: Water Mobility and Adsorption Isotherms. *The Journal of Physical Chemistry B*, 118(38):11353–11364, 2014.

[59] K. Patterson, M. Lisal, and C. M. Colina. Adsorption behavior of model proteins on surfaces. *Fluid Phase Equilibria*, 302(1):48–54, 2011.

[60] A. Vishnyakov, D. S. Talaga, and A. V. Neimark. DPD Simulation of Protein Conformations: From α-Helices to β-Structures. *The Journal of Physical Chemistry Letters*, 3(21):3081–3087, 2012.

[61] K. Okuwaki, H. Doi, K. Fukuzawa, and Y. Mochizuki. Folding simulation of small proteins by dissipative particle dynamics (DPD) with non-empirical interaction parameters based on fragment molecular orbital calculations. *Applied Physics Express*, 13(1):017002, dec 2019.

[62] M. Ndao, F. Goujon, A. Ghoufi, and P. Malfreyt. Coarse-grained modeling of the oil–water–surfactant interface through the local definition of the pressure tensor and interfacial tension. *Theoretical Chemistry Accounts*, 136(1):21, 2017.

[63] A. Ghoufi, P. Malfreyt, and D. J. Tildesley. Computer modelling of the surface tension of the gas–liquid and liquid–liquid interface. *Chemical Society Reviews*, 45(5):1387–1409, 2016.

[64] A. Khedr and A. Striolo. DPD Parameters Estimation for Simultaneously Simulating Water–Oil Interfaces and Aqueous Nonionic Surfactants. *Journal of Chemical Theory and Computation*, 14(12):6460–6471, 2018.

[65] A. Maiti and S. McGrother. Bead–bead interaction parameters in dissipative particle dynamics: Relation to bead-size, solubility parameter, and surface tension. *The Journal of Chemical Physics*, 120(3):1594–1601, 2004.

[66] S. Lin, M. Xu, and Z. Yang. Dissipative particle dynamics study on the mesostructures of n-octadecane/water emulsion with alternating styrene–maleic acid copolymers as emulsifier. *Soft Matter*, 8(2):375–384, 2012.

[67] F. Alvarez, E. A. Flores, L. V. Castro, J. G. Hernández, A. López, and F. Vázquez. Dissipative Particle Dynamics (DPD) Study of Crude Oil-Water Emulsions in the Presence of a Functionalized Co-polymer. *Energy & Fuels*, 25(2):562–567, 2011.

[68] L. Rekvig, B. Hafskjold, and B. Smit. Molecular Simulations of Surface Forces and Film Rupture in Oil/Water/Surfactant Systems. *Langmuir*, 20(26):11583–11593, 2004.

[69] J. Maldonado-Valderrama, V. B. Fainerman, E. Aksenenko, M. Jose Gálvez-Ruiz, M. A. Cabrerizo-Vílchez, and R. Miller. Dynamics of protein adsorption at the oil–water interface: comparison with a theoretical model. *Colloids and Surfaces A: Physicochemical and Engineering Aspects*, 261(1):85–92, 2005.

[70] R. Miller, V. B. Fainerman, E. V. Aksenenko, M. E. Leser, and M. Michel. Dynamic Surface Tension and Adsorption Kinetics of β-Casein at the Solution/Air Interface. *Langmuir*, 20(3):771–777, 2004.

[71] V. B. Fainerman and R. Miller. Equation of State for Concentrated Protein Surface Layers at the Water/Air Interface. *Langmuir*, 15(5):1812–1816, 1999.

[72] V. B. Fainerman, E. H. Lucassen-Reynders, and R Miller. Adsorption of surfactants and proteins at fluid interfaces. *Colloids and Surfaces A: Physicochemical and Engineering Aspects*, 143(2):141–165, 1998.

[73] V. B. Fainerman, E. H. Lucassen-Reynders, and R. Miller. Description of the adsorption behaviour of proteins at water/fluid interfaces in the framework of a two-dimensional solution model. *Advances in Colloid and Interface Science*, 106(1):237–259, 2003.

[74] V. B. Fainerman, R. Miller, J. K. Ferri, H. Watzke, M. E. Leser, and M. Michel. Reversibility and irreversibility of adsorption of surfactants and proteins at liquid interfaces. *Advances in Colloid and Interface Science*, 123-126:163–171, 2006.

[75] A. Dan, R. Wüstneck, J. Krägel, E. V. Aksenenko, V. B. Fainerman, and R. Miller. Interfacial adsorption and rheological behavior of β-casein at the water/hexane interface at different pH. *Food Hydrocolloids*, 34:193–201, 2014.

[76] R. Wüstneck, V. B. Fainerman, E. V. Aksenenko, Cs. Kotsmar, V. Pradines, J. Krägel, and R. Miller. Surface dilatational behavior of β-casein at the solution/air interface at different pH values. *Colloids and Surfaces A: Physicochemical and Engineering Aspects*, 404:17–24, 2012.

[77] W. Pan, B. Caswell, and G. Karniadakis. Rheology, Microstructure and Migration in Brownian Colloidal Suspensions. *Langmuir*, 26(1):133–142, 2010.

[78] A. Panchenko, D. F. Hinz, and E. Fried. Spatial averaging of a dissipative particle dynamics model for active suspensions. *Physics of Fluids*, 30(3):033301, 2018.

[79] Q. Nie, Y. Zhong, and H. Fang. Study of a nanodroplet breakup through many-body dissipative particle dynamics. *Physics of Fluids*, 31(4):042007, 2019.

[80] Z. Li, G.-H. Hu, Z.-L. Wang, Y.-B. Ma, and Z.-W. Zhou. Three dimensional flow structures in a moving droplet on substrate: A dissipative particle dynamics study. *Physics of Fluids*, 25(7):072103, 2013.

[81] Y. Kong, C. W. Manke, W. G. Madden, and A. G. Schlijper. Effect of solvent quality on the conformation and relaxation of polymers via dissipative particle dynamics. *The Journal of Chemical Physics*, 107(2):592–602, 1997.

[82] H. Droghetti, I. Pagonabarraga, P. Carbone, P. Asinari, and D. Marchisio. Dissipative particle dynamics simulations of tri-block co-polymer and water: Phase diagram validation and microstructure identification. *The Journal of Chemical Physics*, 149(18):184903, 2018.

[83] M. Ferrari, J.-W. Handgraaf, G. Boccardo, A. Buffo, M. Vanni, and D. L. Marchisio. Molecular modeling of the interface of an egg yolk protein-based emulsion. *Physics of Fluids*, 34(2):021903, 2022.

[84] X. Wang, K. P. Santo, and A. V. Neimark. Modeling Gas–Liquid Interfaces by Dissipative Particle Dynamics: Adsorption and Surface Tension of Cetyl Trimethyl Ammonium Bromide at the Air–Water Interface. *Langmuir*, 36(48):14686–14698, 2020.

[85] V. Y. Hon, I. M. Saaid, I. C. H. Chai, N. A. A. M. Fauzi, E. Deguillard, J. van Male, and J.-W. Handgraaf. Microemulsion interface model for chemical enhanced oil recovery design. *Journal of Petroleum Science and Engineering*, 212:110279, 2022.

[86] F. Goujon, A. Dequidt, A. Ghoufi, and P. Malfreyt. How Does the Surface Tension Depend on the Surface Area with Coarse-Grained Models? *Journal of Chemical Theory and Computation*, 14(5):2644–2651, 2018.

[87] P. Español and P. B. Warren. Perspective: Dissipative particle dynamics. *The Journal of Chemical Physics*, 146(15):150901, 2017.

[88] M. Ellero and P. Español. Everything you always wanted to know about SDPD* (*but were afraid to ask). *Applied Mathematics and Mechanics*, 39(1):103–124, 2018.

[89] A. Vázquez-Quesada, M. Ellero, and P. Español. Consistent scaling of thermal fluctuations in smoothed dissipative particle dynamics. *The Journal of Chemical Physics*, 130(3):034901, 2009.

[90] J. Zhao, S. Chen, K. Zhang, and Y. Liu. A review of many-body dissipative particle dynamics (MDPD): Theoretical models and its applications. *Physics of Fluids*, 33(11):112002, 2021.

[91] Z. Li, Y.-H. Tang, H. Lei, B. Caswell, and G. Karniadakis. Energy-conserving dissipative particle dynamics with temperature-dependent properties. *Journal of Computational Physics*, 265:113–127, 2014.

[92] P. Español. Fluid particle model. *Physical Review E*, 57(3):2930–2948, 1998.

[93] R. M. Füchslin, H. Fellermann, A. Eriksson, and H.-J. Ziock. Coarse graining and scaling in dissipative particle dynamics. *The Journal of Chemical Physics*, 130(21):214102, 2009.

[94] M. Arienti, W. Pan, X. Li, and G. Karniadakis. Many-body dissipative particle dynamics simulation of liquid/vapor and liquid/solid interactions. *The Journal of Chemical Physics*, 134(20):204114, 2011.

[95] N. Mai-Duy, N. Phan-Thien, T. Y. N. Nguyen, and T. Tran-Cong. Coarse-graining, compressibility, and thermal fluctuation scaling in dissipative particle dynamics employed with pre-determined input parameters. *Physics of Fluids*, 32(5):053313, 2020.

[96] J. A. Backer, C. P. Lowe, H. C. J. Hoefsloot, and P. D. Iedema. Combined length scales in dissipative particle dynamics. *The Journal of Chemical Physics*, 123(11):114905, 2005.

[97] J. R. Spaeth, T. Dale, I. G. Kevrekidis, and A. Z. Panagiotopoulos. Coarse-Graining of Chain Models in Dissipative Particle Dynamics Simulations. *Industrial & Engineering Chemistry Research*, 50(1):69–77, 2011.

[98] T. Krüger, H. Kusumaatmaja, A. Kuzmin, O. Shardt, G. Silva, and E. M. Viggen. *The Lattice Boltzmann Method: Principles and Practice*. Springer Cham, Cham, Switzerland, 2017.

[99] F. Jansen and J. Harting. From bijels to Pickering emulsions: A lattice Boltzmann study. *Physical Review E*, 83(4):046707, 2011.

[100] Y. Shi, G. H. Tang, L. H. Cheng, and H. Q. Shuang. An improved phase-field-based lattice Boltzmann model for droplet dynamics with soluble surfactant. *Computers & Fluids*, 179:508–520, 2019.

[101] R. G. M. van der Sman and M. B. J. Meinders. Analysis of improved Lattice Boltzmann phase field method for soluble surfactants. *Computer Physics Communications*, 199:12–21, 2016.

[102] R. G. M. van der Sman and S. van der Graaf. Diffuse interface model of surfactant adsorption onto flat and droplet interfaces. *Rheologica Acta*, 46(1):3–11, 2006.

[103] A. E. Komrakova, D. Eskin, and J. J. Derksen. Lattice Boltzmann simulations of a single n-butanol drop rising in water. *Physics of Fluids*, 25(4):042102, 2013.

[104] A. E. Komrakova, O. Shardt, D. Eskin, and J. J. Derksen. Lattice Boltzmann simulations of drop deformation and breakup in shear flow. *International Journal of Multiphase Flow*, 59:24–43, 2014.

[105] H. Liu and Y. Zhang. Phase-field modeling droplet dynamics with soluble surfactants. *Journal of Computational Physics*, 229(24):9166–9187, 2010.

[106] S. Maindarkar, A. Dubbelboer, J. Meuldijk, H. Hoogland, and M. Henson. Prediction of emulsion drop size distributions in colloid mills. *Chemical Engineering Science*, 118:114–125, 2014.

[107] P. Walstra. Principles of emulsion formation. *Chemical Engineering Science*, 48:333–349, 1993.

[108] M. Icardi, E. Gavi, D. L. Marchisio, M. G. Olsen, R. O. Fox, and D. Lakehal. Validation of LES predictions for turbulent flow in a Confined Impinging Jets Reactor. *Applied Mathematical Modelling*, 35(4):1591–1602, 2011.

[109] F. Lince, D. L. Marchisio, and A. A. Barresi. A comparative study for nanoparticle production with passive mixers via solvent-displacement: Use of CFD models for optimization and design. *Chemical Engineering and Processing: Process Intensification*, 50(4):356–368, 2011.

[110] D. L. Marchisio, F. Omegna, A. A. Barresi, and P. Bowen. Effect of mixing and other operating parameters in sol-gel processes. *Industrial and Engineering Chemistry Research*, 47(19):7202–7210, 2008.

[111] J. A. Wieringa, F. Vandieren, J. J. Janssen, and W. G. Agterof. Droplet breakup mechanisms during emulsification in colloid mills at high dispersed phase volume fraction. *Chemical Engineering Research and Design*, 74:554–562, 1996.

[112] C. Almeida-Rivera and P. Bongers. Modelling and experimental validation of emulsification processes in continuous rotor–stator units. *Computers & Chemical Engineering*, 34:592–597, 2010.

[113] H. A. Barnes. Rheology of emulsions - a review. *Colloids and Surfaces A: Physicochemical and Engineering Aspects*, 91:89–95, 1994.

[114] M. Wimmer. Taylor vortices at different geometries. In C. Egbers and G. Pfister, editors, *Physics of Rotating Fluids*, pages 194–212, Berlin, Heidelberg, Germany, 2000. Springer Berlin Heidelberg.

[115] M. Wimmer and J. Zierep. Transition from Taylor vortices to cross-flow instabilities. *Acta Mechanica*, 140:17–30, 2000.

[116] X. Li, J. Zhang, and L. Xu. A numerical investigation of the flow between rotating conical cylinders of two different configurations. *Journal of Hydrodynamics*, 26:431–435, 2014.

[117] Q.-S. Li, W. Pu, and L. Xu. Transition to Taylor vortex flow between rotating conical cylinders. *Journal of Hydrodynamics, Ser. B*, 22:241–245, 2010.

[118] M. N. Noui-Mehidi, N. Ohmura, and K. Kataoka. Dynamics of the helical flow between rotating conical cylinders. *Journal of Fluids and Structures*, 20:331–344, 2005.

[119] R. C. Giordano, R. L. C. Giordano, D. M. F. Prazeres, and C. L. Cooney. Analysis of a Taylor–Poiseuille vortex flow reactor—I: Flow patterns and mass transfer characteristics. *Chemical Engineering Science*, 53:3635–3652, 1998.

[120] J. L. and D. G. Dalgleish. Variations in the binding of β-casein to oil-water interfaces detected by trypsin-catalysed hydrolysis. *Journal of Colloid and Interface Science*, 149(1):49–55, 1992.

[121] R. W. Burley and W. H. Cook. ISOLATION AND COMPOSITION OF AVIAN EGG YOLK GRANULES AND THEIR CONSTITUENT α- AND β-LIPOVITELLINS. *Canadian Journal of Biochemistry and Physiology*, 39(8):1295–1307, 1961.

[122] M. Anton and G. Gandemer. Composition, Solubility and Emulsifying Properties of Granules and Plasma of Egg Yolk. *Journal of Food Science*, 62(3):484–487, 1997.

[123] R. Xiong, G. Xie, and A. S. Edmondson. Modelling the pH of mayonnaise by the ratio of egg to vinegar. *Food Control*, 11(1):49–56, 2000.

[124] L. D. Ford, R. Borwankar, R. W. Martin, and D. N. Holcomb. Dressings and sauces. In S. Friberg and K. Larsson, editors, *Food Emulsions*, pages 361–412. Marcel Dekker, New York, USA, 3rd edition, 1997.

[125] C. M. Chang, W. D. Powrie, and O. Fennema. Electron Microscopy of Mayonnaise. *Canadian Institute of Food Science and Technology Journal*, 5(3):134–137, 1972.

[126] J. N. Dyer-Hurdon and I. A. Nnanna. Cholesterol Content and Functionality of Plasma and Granules Fractionated from Egg Yolk. *Journal of Food Science*, 58(6):1277–1281, 1993.

[127] M. Le Denmat, M. Anton, and V. Beaumal. Characterisation of emulsion properties and of interface composition in O/W emulsions prepared with hen egg yolk, plasma and granules. *Food Hydrocolloids*, 14(6):539–549, 2000.

[128] V. Martinet, V. Beaumal, M. Dalgalarrondo, and M. Anton. Emulsifying properties and adsorption behavior of egg yolk lipoproteins (LDL and HDL) in oil-in-water emulsions. In M. Anton, editor, *Food emulsions and dispersions*, page 103–116. Research Signpost, Trivandrum, 2002.

[129] W. H. Cook and W. G. Martin. Egg lipoproteins. In E. Tria and A. M. Scanu, editors, *Structural and Functional Aspects of Lipoproteins in Living Systems*, page 579–615. Academic Press, London, U.K., 1969.

[130] P. Jolivet, C. Boulard, T. Chardot, and M. Anton. New Insights into the Structure of Apolipoprotein B from Low-Density Lipoproteins and Identification of a Novel YGP-like Protein in Hen Egg Yolk. *Journal of Agricultural and Food Chemistry*, 56(14):5871–5879, 2008.

[131] R. J. Evans, D. H. Bauer, S. L. Bandemer, S. B. Vaghefi, and C. J. Flegal. Structure of egg yolk very low density lipoprotein. Polydispersity of the very low density lipoprotein and the role of lipovitellenin in the structure. *Archives of Biochemistry and Biophysics*, 154(2):493–500, 1973.

[132] S. Dauphas, V. Beaumal, A. Riaublanc, and M. Anton. Hen Egg Yolk Low-Density Lipoproteins Film Spreading at the Air-Water and Oil-Water Interfaces. *Journal of Agricultural and Food Chemistry*, 54(10):3733–3737, 2006.

[133] S. Dauphas, V. Beaumal, P. Gunning, A. Mackie, P. Wilde, V. Vié, A. Riaublanc, and M. Anton. Structures and rheological properties of hen egg yolk low density lipoprotein layers spread at the air–water interface at pH 3 and 7. *Colloids and Surfaces B: Biointerfaces*, 57(1):124–133, 2007.

[134] S. Dauphas, V. Beaumal, P. Gunning, A. Mackie, P. Wilde, V. Vié, A. Riaublanc, and M. Anton. Structure modification in hen egg yolk low density lipoproteins layers between 30 and 45mN/m observed by AFM. *Colloids and Surfaces B: Biointerfaces*, 54(2):241–248, 2007.

[135] The UniProt Consortium. Uniprot: the universal protein knowledgebase in 2021. *Nucleic Acids Research*, 49(D1):D480–D489, 11 2020.

[136] M. P. Allen and D. J. Tildesley. *Computer Simulation of Liquids*. Oxford University Press, Oxford, U.K., 2nd edition, 2017.

[137] G. A. Kaminski, R. A. Friesner, J. Tirado-Rives, and W. L. Jorgensen. Evaluation and Reparametrization of the OPLS-AA Force Field for Proteins via Comparison with Accurate Quantum Chemical Calculations on Peptides. *The Journal of Physical Chemistry B*, 105(28):6474–6487, 2001.

[138] A. D. MacKerell, D. Bashford, M. Bellott, R. L. Dunbrack, J. D. Evanseck, M. J. Field, S. Fischer, J. Gao, H. Guo, S. Ha, D. Joseph-McCarthy, L. Kuchnir, K. Kuczera, F. T. K. Lau, C. Mattos, S. Michnick, T. Ngo, D. T. Nguyen, B. Prodhom, W. E. Reiher, B. Roux, M. Schlenkrich, J. C. Smith, R. Stote, J. Straub, M. Watanabe, J. Wiórkiewicz-Kuczera, D. Yin, and M. Karplus. All-Atom Empirical Potential for Molecular Modeling and Dynamics Studies of Proteins. *The Journal of Physical Chemistry B*, 102(18):3586–3616, 1998.

[139] C. Oostenbrink, A. Villa, A. E. Mark, and W. F. Van Gunsteren. A biomolecular force field based on the free enthalpy of hydration and solvation: The GROMOS force-field parameter sets 53A5 and 53A6. *Journal of Computational Chemistry*, 25(13):1656–1676, 2004.

[140] J. Wang, P. Cieplak, and P. A. Kollman. How well does a restrained electrostatic potential (RESP) model perform in calculating conformational energies of organic and biological molecules? *Journal of Computational Chemistry*, 21(12):1049–1074, 2000.

[141] I. Levine. *Physical Chemistry*. McGraw-Hill international edition. McGraw-Hill Education, 2009.

[142] L. Verlet. Computer “Experiments" on Classical Fluids. I. Thermodynamical Properties of Lennard-Jones Molecules. *Physical Review*, 159(1):98–103, Jul 1967.

[143] D. Frenkel and B. Smit. Chapter 4 - Molecular Dynamics Simulations. In D. Frenkel and B. Smit, editors, *Understanding Molecular Simulation*, pages 63–107. Academic Press, San Diego, USA, 2nd edition, 2002.

[144] W. D. Cornell, P. Cieplak, C. I. Bayly, I. R. Gould, K. M. Merz, D. M. Ferguson, D. C. Spellmeyer, T. Fox, J. W. Caldwell, and P. A. Kollman. A Second Generation Force Field for the Simulation of Proteins, Nucleic Acids, and Organic Molecules. *Journal of the American Chemical Society*, 117(19):5179–5197, 1995.

[145] W. L. Jorgensen, J. D. Madura, and C. J. Swenson. Optimized intermolecular potential functions for liquid hydrocarbons. *Journal of the American Chemical Society*, 106(22):6638–6646, 1984.

[146] D. Frenkel and B. Smit. Chapter 3 - Monte Carlo Simulations. In D. Frenkel and B. Smit, editors, *Understanding Molecular Simulation*, pages 23–61. Academic Press, San Diego, USA, 2nd edition, 2002.

[147] A. A. Chialvo and P. G. Debenedetti. On the use of the Verlet neighbor list in molecular dynamics. *Computer Physics Communications*, 60(2):215–224, 1990.

[148] J. Kolafa and J. W. Perram. Cutoff Errors in the Ewald Summation Formulae for Point Charge Systems. *Molecular Simulation*, 9(5):351–368, 1992.

[149] E. Lindahl. Molecular Dynamics Simulations. In A. Kukol, editor, *Molecular Modeling of Proteins*, pages 3–26. Springer New York, New York, NY, 2015.

[150] M. Di Pierro, R. Elber, and B. Leimkuhler. A Stochastic Algorithm for the Isobaric–Isothermal Ensemble with Ewald Summations for All Long Range Forces. *Journal of Chemical Theory and Computation*, 11(12):5624–5637, 2015.

[151] H. Heinz and H. Ramezani-Dakhel. Simulations of inorganic–bioorganic interfaces to discover new materials: insights, comparisons to experiment, challenges, and opportunities. *Chemical Society Reviews*, 45(2):412–448, 2016.

[152] T. Hansson, C. Oostenbrink, and W. van Gunsteren. Molecular dynamics simulations. *Current Opinion in Structural Biology*, 12(2):190–196, 2002.

[153] O. Valsson, P. Tiwary, and M. Parrinello. Enhancing Important Fluctuations: Rare Events and Metadynamics from a Conceptual Viewpoint. *Annual Review of Physical Chemistry*, 67(1):159–184, 2016.

[154] T. M. Schäfer and G. Settanni. Data Reweighting in Metadynamics Simulations. *Journal of Chemical Theory and Computation*, 16(4):2042–2052, 2020.

[155] P. Tiwary and M. Parrinello. A Time-Independent Free Energy Estimator for Metadynamics. *The Journal of Physical Chemistry B*, 119(3):736–742, 2015.

[156] A. Barducci, G. Bussi, and M. Parrinello. Well-Tempered Metadynamics: A Smoothly Converging and Tunable Free-Energy Method. *Physical Review Letters*, 100(2):020603, 2008.

[157] J. F. Dama, M. Parrinello, and G. A. Voth. Well-Tempered Metadynamics Converges Asymptotically. *Physical Review Letters*, 112(24):240602, 2014.

[158] A. Laio, A. Rodriguez-Fortea, F. L. Gervasio, M. Ceccarelli, and M. Parrinello. Assessing the Accuracy of Metadynamics. *The Journal of Physical Chemistry B*, 109(14):6714–6721, 2005.

[159] M. Iannuzzi, A. Laio, and M. Parrinello. Efficient Exploration of Reactive Potential Energy Surfaces Using Car-Parrinello Molecular Dynamics. *Physical Review Letters*, 90(23):238302, 2003.

[160] W. Quapp and A. Zech. Transition state theory with Tsallis statistics. *Journal of Computational Chemistry*, 31(3):573–585, 2010.

[161] A. Zambrowicz, M. Pokora, B. Setner, A. Dąbrowska, M. Szołtysik, K. Babij, Z. Szewczuk, T. Trziszka, G. Lubec, and J. Chrzanowska. Multifunctional peptides derived from an egg yolk protein hydrolysate: Isolation and characterization. *Amino acids*, 47:369–380, 2014.

[162] J. Jumper, R. Evans, A. Pritzel, T. Green, M. Figurnov, O. Ronneberger, K. Tunyasuvunakool, R. Bates, A. Žídek, A. Potapenko, A. Bridgland, C. Meyer, S. A. A. Kohl, A. J. Ballard, A. Cowie, B. Romera-Paredes, S. Nikolov, R. Jain, J. Adler, T. Back, S. Petersen, D. Reiman, E. Clancy, M. Zielinski, M. Steinegger, M. Pacholska, T. Berghammer, S. Bodenstein, D. Silver, O. Vinyals, A. W. Senior, K. Kavukcuoglu, P. Kohli, and D. Hassabis. Highly accurate protein structure prediction with AlphaFold. *Nature*, 596(7873):583–589, 2021.

[163] M. Mirdita, K. Schütze, Y. Moriwaki, L. Heo, S. Ovchinnikov, and M. Steinegger. ColabFold: making protein folding accessible to all. *Nature Methods*, 19(6):679–682, 2022.

[164] R. Anandakrishnan, B. Aguilar, and A. Onufriev. H++ 3.0: Automating pK prediction and the preparation of biomolecular structures for atomistic molecular modeling and simulations. *Nucleic Acids Research*, 40(W1):W537–W541, 2012.

[165] J. Myers, G. Grothaus, S. Narayanan, and A. Onufriev. A simple clustering algorithm can be accurate enough for use in calculations of pKs in macromolecules. *Proteins: Structure, Function, and Bioinformatics*, 63(4):928–938, 2006.

[166] J. C. Gordon, J. B. Myers, T. Folta, V. Shoja, L. S. Heath, and A. Onufriev. H++: a server for estimating p Ka s and adding missing hydrogens to macromolecules . *Nucleic Acids Research*, 33:W368–W371, 2005.

[167] V. Mariani, M. Biasini, A. Barbato, and T. Schwede. lDDT: a local superposition-free score for comparing protein structures and models using distance difference tests. *Bioinformatics*, 29(21):2722–2728, 2013.

[168] W. L. Jorgensen and J. Tirado-Rives. Potential energy functions for atomic-level simulations of water and organic and biomolecular systems. *Proceedings of the National Academy of Sciences*, 102(19):6665–6670, 2005.

[169] L. S. Dodda, J. Z. Vilseck, J. Tirado-Rives, and W. L. Jorgensen. 1.14*CM1A-LBCC: Localized Bond-Charge Corrected CM1A Charges for Condensed-Phase Simulations. *The Journal of Physical Chemistry B*, 121(15):3864–3870, 2017.

[170] L. S. Dodda, I. Cabeza de Vaca, J. Tirado-Rives, and W. L. Jorgensen. LigParGen web server: an automatic OPLS-AA parameter generator for organic ligands. *Nucleic Acids Research*, 45(W1):W331–W336, 2017.

[171] P. Mark and L. Nilsson. Structure and Dynamics of the TIP3P, SPC, and SPC/E Water Models at 298 K. *The Journal of Physical Chemistry A*, 105(43):9954–9960, 2001.

[172] W. L. Jorgensen and C. Jenson. Temperature dependence of TIP3P, SPC, and TIP4P water from NPT Monte Carlo simulations: Seeking temperatures of maximum density. *Journal of Computational Chemistry*, 19(10):1179–1186, 1998.

[173] J. P. M. Jämbeck and A. P. Lyubartsev. An Extension and Further Validation of an All-Atomistic Force Field for Biological Membranes. *Journal of Chemical Theory and Computation*, 8(8):2938–2948, 2012.

[174] I. Ermilova and A. P. Lyubartsev. Extension of the Slipids Force Field to Polyunsaturated Lipids. *The Journal of Physical Chemistry B*, 120(50):12826–12842, 2016.

[175] M. J. Abraham, T. Murtola, R. Schulz, S. Páll, J. C. Smith, B. Hess, and E. Lindahl. GROMACS: High performance molecular simulations through multi-level parallelism from laptops to supercomputers. *SoftwareX*, 1-2:19–25, 2015.

[176] D. Van Der Spoel, E. Lindahl, B. Hess, G. Groenhof, A. E. Mark, and H. J. C. Berendsen. GROMACS: Fast, flexible, and free. *Journal of Computational Chemistry*, 26(16):1701–1718, 2005.

[177] C. Kutzner, S. Páll, M. Fechner, A. Esztermann, B. L. de Groot, and H. Grubmüller. More bang for your buck: Improved use of GPU nodes for GROMACS 2018. *Journal of Computational Chemistry*, 40(27):2418–2431, 2019.

[178] M. Bonomi, D. Branduardi, G. Bussi, C. Camilloni, D. Provasi, P. Raiteri, D. Donadio, F. Marinelli, F. Pietrucci, R. A. Broglia, and M. Parrinello. PLUMED: A portable plugin for free-energy calculations with molecular dynamics. *Computer Physics Communications*, 180(10):1961–1972, 2009.

[179] G. A. Tribello, M. Bonomi, D. Branduardi, C. Camilloni, and G. Bussi. PLUMED 2: New feathers for an old bird. *Computer Physics Communications*, 185(2):604–613, 2014.

[180] M. Parrinello and A. Rahman. Polymorphic transitions in single crystals: A new molecular dynamics method. *Journal of Applied Physics*, 52(12):7182–7190, 1981.

[181] H. J. C. Berendsen. Transport properties computed by linear response through weak coupling to a bath. In M. Meyer and V. Pontikis, editors, *Computer Simulation in Materials Science*, pages 139–155. Springer Dordrecht, Dordrecht, The Netherlands, 1991.

[182] M. Rospiccio, A. Arsiccio, G. Winter, and R. Pisano. The Role of Cyclodextrins against Interface-Induced Denaturation in Pharmaceutical Formulations: A Molecular Dynamics Approach. *Molecular Pharmaceutics*, 18(6):2322–2333, 2021.

[183] A. Hayashi, Y. Ato, A. Yamamoto, H. Yoshida, S. Yamanaka, T. Kawakami, and M. Okumura. Gibbs Energy of Hydrogen Adsorption on Pt Surface by Machine Learning Potential and Metadynamics. *Chemistry Letters*, 50(7):1329–1332, 2021.

[184] W. Norde and C. A. Haynes. Thermodynamics of Protein Adsorption. In J. L. Brash and P. W. Wojciechowski, editors, *Interfacial phenomena and bioproducts*, volume 23 of *Bioprocess technology*. Marcel Dekker, New York, USA, 1st edition, 1996.

[185] E. Moeendarbary, T. Y. Ng, and M. Zangeneh. DISSIPATIVE PARTICLE DYNAMICS: INTRODUCTION, METHODOLOGY AND COMPLEX FLUID APPLICATIONS — A REVIEW. *International Journal of Applied Mechanics*, 01(04):737–763, 2009.

[186] X. Zhou and X. Zhou. THE UNIT PROBLEM IN THE THERMODYNAMIC CALCULATION OF ADSORPTION USING THE LANGMUIR EQUATION. *Chemical Engineering Communications*, 201(11):1459–1467, 2014.

[187] D. R. Lide, ed. *CRC Handbook of Chemistry and Physics*. CRC press, Boca Raton, FL, 85 edition, 2005.

[188] W. L. Jorgensen and J. Tirado-Rives. The OPLS [optimized potentials for liquid simulations] potential functions for proteins, energy minimizations for crystals of cyclic peptides and crambin. *Journal of the American Chemical Society*, 110(6):1657–1666, 1988.

[189] W. L. Jorgensen, D. S. Maxwell, and J. Tirado-Rives. Development and Testing of the OPLS All-Atom Force Field on Conformational Energetics and Properties of Organic Liquids. *Journal of the American Chemical Society*, 118(45):11225–11236, 1996.

[190] W. L. Jorgensen, J. Chandrasekhar, J. D. Madura, R. W. Impey, and M. L. Klein. Comparison of simple potential functions for simulating liquid water. *The Journal of Chemical Physics*, 79(2):926–935, 1983.

[191] U. Essmann, L. Perera, M. L. Berkowitz, T. Darden, H. Lee, and L. G. Pedersen. A smooth particle mesh Ewald method. *The Journal of Chemical Physics*, 103(19):8577–8593, 1995.

[192] H. J. C. Berendsen, J. P. M. Postma, W. F. van Gunsteren, A. DiNola, and J. R. Haak. Molecular dynamics with coupling to an external bath. *The Journal of Chemical Physics*, 81(8):3684–3690, 1984.

[193] J. G. E. M. Fraaije, J. van Male, P. Becherer, and R. Serral Gracià. Coarse-Grained Models for Automated Fragmentation and Parametrization of Molecular Databases. *Journal of Chemical Information and Modeling*, 56(12):2361–2377, 2016.

[194] M. Diedenhofen and A. Klamt. COSMO-RS as a tool for property prediction of IL mixtures—A review. *Fluid Phase Equilibria*, 294(1):31–38, 2010.

[195] A Klamt. *COSMO-RS: From Quantum Chemistry to Fluid Phase Thermodynamics and Drug Design*. Elsevier, Amsterdam, The Netherlands, 2005.

[196] A. Jakalian, B. L. Bush, D. B. Jack, and C. I. Bayly. Fast, efficient generation of high-quality atomic charges. AM1-BCC model: I. Method. *Journal of Computational Chemistry*, 21(2):132–146, 2000.

[197] A. Jakalian, D. B. Jack, and C. I. Bayly. Fast, efficient generation of high-quality atomic charges. AM1-BCC model: II. Parameterization and validation. *Journal of Computational Chemistry*, 23(16):1623–1641, 2002.

[198] P. C. Petris, P. Becherer, and J. G. E. M. Fraaije. Alkane/Water Partition Coefficient Calculation Based on the Modified AM1 Method and Internal Hydrogen Bonding Sampling Using COSMO-RS. *Journal of Chemical Information and Modeling*, 61(7):3453–3462, 2021.

[199] A. K. Rappe and W. A. Goddard. Charge equilibration for molecular dynamics simulations. *The Journal of Physical Chemistry*, 95(8):3358–3363, 1991.

[200] P. M. Pieczywek, W. Płaziński, and A. Zdunek. Dissipative particle dynamics model of homogalacturonan based on molecular dynamics simulations. *Scientific Reports*, 10(1):14691, 2020.

[201] K. R. Hadley and C. McCabe. On the Investigation of Coarse-Grained Models for Water: Balancing Computational Efficiency and the Retention of Structural Properties. *The Journal of Physical Chemistry B*, 114(13):4590–4599, 2010.

[202] E. Zohravi, E. Shirani, and A. Pishevar. Influence of the conservative force on transport coefficients in the DPD method. *Molecular Simulation*, 44(3):254–261, 2018.

[203] A. G. Gaonkar. Effects of salt, temperature, and surfactants on the interfacial tension behavior of a vegetable oil/water system. *Journal of Colloid and Interface Science*, 149(1):256–260, 1992.

[204] D. Reith, H. Meyer, and F. Müller-Plathe. Mapping Atomistic to Coarse-Grained Polymer Models Using Automatic Simplex Optimization To Fit Structural Properties. *Macromolecules*, 34(7):2335–2345, 2001.

[205] Y. Li, B. C. Abberton, M. Kröger, and W. K. Liu. Challenges in Multiscale Modeling of Polymer Dynamics. *Polymers*, 5(2):751–832, 2013.

[206] V. Agrawal, G. Arya, and J. Oswald. Simultaneous Iterative Boltzmann Inversion for Coarse-Graining of Polyurea. *Macromolecules*, 47(10):3378–3389, 2014.

[207] J. G. E. M. Fraaije, J. van Male, P. Becherer, and R. Serral Gracià. Calculation of Diffusion Coefficients through Coarse-Grained Simulations Using the Automated-Fragmentation-Parametrization Method and the Recovery of Wilke–Chang Statistical Correlation. *Journal of Chemical Theory and Computation*, 14(2):479–485, 2018.

[208] M. E. Young, P. A. Carroad, and R. L. Bell. Estimation of diffusion coefficients of proteins. *Biotechnology and Bioengineering*, 22(5):947–955, 1980.

[209] M. T. Tyn and T. W. Gusek. Prediction of diffusion coefficients of proteins. *Biotechnology and Bioengineering*, 35(4):327–338, 1990.

[210] L. He and B. Niemeyer. A Novel Correlation for Protein Diffusion Coefficients Based on Molecular Weight and Radius of Gyration. *Biotechnology Progress*, 19(2):544–548, 2003.

[211] J. Kestin, M. Sokolov, and W. A. Wakeham. Viscosity of liquid water in the range -8°C to 150°C. *Journal of Physical and Chemical Reference Data*, 7(3):941–948, 1978.

[212] F. C. Magne and E. L. Skau. Viscosities and Densities of Solvent-Vegetable Oil Mixtures. *Industrial & Engineering Chemistry*, 37(11):1097–1101, 1945.

[213] J. H. Irving and J. G. Kirkwood. The Statistical Mechanical Theory of Transport Processes. IV. The Equations of Hydrodynamics. *The Journal of Chemical Physics*, 18(6):817–829, 1950.

[214] Culgi B.V., The Netherlands. The Chemistry Unified Language Interface (CULGI). www.culgi.com, 2020. Version 13.0.0.

[215] T. P. Hill and J. Miller. How to combine independent data sets for the same quantity. *Chaos: An Interdisciplinary Journal of Nonlinear Science*, 21(3):033102, 2011.

[216] E. K. Peter, K. Lykov, and I. V. Pivkin. A polarizable coarse-grained protein model for dissipative particle dynamics. *Physical Chemistry Chemical Physics*, 17(37):24452–24461, 2015.

[217] J. Wang and T. Hou. Application of molecular dynamics simulations in molecular property prediction II: Diffusion coefficient. *Journal of Computational Chemistry*, 32(16):3505–3519, 2011.

[218] Y. Fang and D. G. Dalgleish. Dimensions of the Adsorbed Layers in Oil-in-Water Emulsions Stabilized by Caseins. *Journal of Colloid and Interface Science*, 156(2):329–334, 1993.

[219] M. Langton, E. Jordansson, A. Altskär, C. Sørensen, and A.-M. Hermansson. Microstructure and image analysis of mayonnaises. *Food Hydrocolloids*, 13(2):113–125, 1999.

[220] K. P. Santo and A. V. Neimark. Dissipative particle dynamics simulations in colloid and Interface science: a review. *Advances in Colloid and Interface Science*, 298:102545, 2021.

[221] R. D. Groot and K. L. Rabone. Mesoscopic Simulation of Cell Membrane Damage, Morphology Change and Rupture by Nonionic Surfactants. *Biophysical Journal*, 81(2):725–736, 2001.

[222] P. Vanya, J. Sharman, and J. A. Elliott. Invariance of experimental observables with respect to coarse-graining in standard and many-body dissipative particle dynamics. *The Journal of Chemical Physics*, 150(6):064101, 2019.

[223] R. L. Anderson, D. J. Bray, A. S. Ferrante, M. G. Noro, I. P. Stott, and P. B. Warren. Dissipative particle dynamics: Systematic parametrization using water-octanol partition coefficients. *The Journal of Chemical Physics*, 147(9):094503, 2017.

[224] D. Pan, N. Phan-Thien, and B. C. Khoo. Dissipative particle dynamics simulation of droplet suspension in shear flow at low Capillary number. *Journal of Non-Newtonian Fluid Mechanics*, 212:63–72, 2014.

[225] S. Chen, N. Phan-Thien, X.-J. Fan, and B. C. Khoo. Dissipative particle dynamics simulation of polymer drops in a periodic shear flow. *Journal of Non-Newtonian Fluid Mechanics*, 118(1):65–81, 2004.

[226] Y. Zhang, J. Xu, and X. He. Effect of surfactants on the deformation of single droplet in shear flow studied by dissipative particle dynamics. *Molecular Physics*, 116(14):1851–1861, 2018.

[227] M. Laradji, H. Guo, M. Grant, and M. J. Zuckermann. The effect of surfactants on the dynamics of phase separation. *Journal of Physics: Condensed Matter*, 4:6715–6728, 1992.

[228] J. W. Cahn and J. E. Hilliard. Free Energy of a Nonuniform System. I. Interfacial Free Energy. *The Journal of Chemical Physics*, 28(2):258–267, 1958.

[229] H. Diamant and D. Andelman. Kinetics of surfactant adsorption at fluid/fluid interfaces: non-ionic surfactants. *Europhysics Letters*, 34(8):575–580, 1996.

[230] S. Engblom, M. Do-Quang, G. Amberg, and A.-K. Tornberg. On Diffuse Interface Modeling and Simulation of Surfactants in Two-Phase Fluid Flow. *Communications in Computational Physics*, 14(4):879–915, 2013.

[231] O. Theissen and G. Gompper. Lattice-Boltzmann study of spontaneous emulsification. *European Physical Journal B*, 11:91–100, 1999.

[232] V. M. Kendon, M. E. Cates, I. Pagonabarraga, J.-C. Desplat, and P. Bladon. Inertial effects in three-dimensional spinodal decomposition of a symmetric binary fluid mixture: a lattice Boltzmann study. *Journal of Fluid Mechanics*, 440:147–203, 2001.

[233] H. Diamant, G. Ariel, and D. Andelman. Kinetics of surfactant adsorption: the free energy approach. *Colloids and Surfaces A: Physicochemical and Engineering Aspects*, 183-185:259–276, 2001.

[234] A. Yun, Y. Li, and J. Kim. A new phase-field model for a water–oil-surfactant system. *Applied Mathematics and Computation*, 229:422–432, 2014.

[235] M. R. Swift, E. Orlandini, W. R. Osborn, and J. M. Yeomans. Lattice Boltzmann simulations of liquid-gas and binary fluid systems. *Physical Review E*, 54(5):5041–5052, 1996.

[236] P. L. Bhatnagar, E. P. Gross, and M. Krook. A Model for Collision Processes in Gases. I. Small Amplitude Processes in Charged and Neutral One-Component Systems. *Physical Review*, 94(3):511–525, 1954.

[237] P. V. Coveney, S. Succi, D. d'Humières, I. Ginzburg, M. Krafczyk, P. Lallemand, and L.-S. Luo. Multiple–relaxation–time lattice Boltzmann models in three dimensions. *Philosophical Transactions of the Royal Society of London. Series A: Mathematical, Physical and Engineering Sciences*, 360(1792):437–451, 2002.

[238] H. Yu, L.-S. Luo, and S. S. Girimaji. LES of turbulent square jet flow using an MRT lattice Boltzmann model. *Computers & Fluids*, 35(8):957–965, 2006.

[239] R. G. M. van der Sman. Galilean invariant lattice Boltzmann scheme for natural convection on square and rectangular lattices. *Physical Review E*, 74(2):026705, 2006.

[240] A. Onuki and R. Okamoto. Solvation and Dissociation in Weakly Ionized Polyelectrolytes. *The Journal of Physical Chemistry B*, 113(12):3988–3996, 2009.

[241] G. B. McFadden and A. A. Wheeler. On the Gibbs adsorption equation and diffuse interface models. *Proceedings of the Royal Society of London. Series A: Mathematical, Physical and Engineering Sciences*, 458(2021):1129–1149, 2002.

[242] G. I. Tóth and B. Kvamme. Analysis of Ginzburg-Landau-type models of surfactant-assisted liquid phase separation. *Physical Review E*, 91(3):032404, 2015.

[243] S. N. Maindarkar, N. B. Raikar, P. Bongers, and M. A. Henson. Incorporating emulsion drop coalescence into population balance equation models of high pressure homogenization. *Colloids and Surfaces A: Physicochemical and Engineering Aspects*, 396:63–73, 2012.

[244] R. McGraw. Description of Aerosol Dynamics by the Quadrature Method of Moments. *Aerosol Science and Technology*, 27:255–265, 1997.

[245] D. L. Marchisio, J. T. Pikturna, R. O. Fox, R. D. Vigil, and A. A. Barresi. Quadrature method of moments for population-balance equations. *AIChE Journal*, 49:1266–1276, 2003.

[246] D. L. Marchisio, R. D. Vigil, and R. O. Fox. Quadrature method of moments for aggregation–breakage processes. *Journal of Colloid and Interface Science*, 258:322–334, 2003.

[247] D. L. Marchisio and R. O. Fox. *Computational Models for Polydisperse Particulate and Multiphase Systems*. Cambridge University Press, Cambridge, U.K., 2013.

[248] J. Sierra-Pallares, D. L. Marchisio, M. T. Parra-Santos, J. García-Serna, F. Castro, and M. J. Cocero. A computational fluid dynamics study of supercritical antisolvent precipitation: Mixing effects on particle size. *AIChE Journal*, 58(2):385–398, 2012.

[249] L. Mazzei, D. L. Marchisio, and P. Lettieri. New quadrature-based moment method for the mixing of inert polydisperse fluidized powders in commercial CFD codes. *AIChE Journal*, 58(10):3054–3069, 2012.

[250] A. Buffo, M. Vanni, and D. L. Marchisio. On the implementation of moment transport equations in OpenFOAM: Boundedness and realizability. *International Journal of Multiphase Flow*, 85:223–235, 2016.

[251] A. Passalacqua, F. Laurent, E. Madadi-Kandjani, J. C. Heylmun, and R. O. Fox. An open-source quadrature-based population balance solver for OpenFOAM. *Chemical Engineering Science*, 176:306–318, 2018.

[252] R. B. Bird, W. E. Stewart, and E. N. Lightfoot. *Transport Phenomena*. John Wiley and Sons, Inc., New York, USA, 1960.

[253] T. Tosco, D. L. Marchisio, F. Lince, and R. Sethi. Extension of the Darcy-Forchheimer Law for Shear-Thinning Fluids and Validation via Pore-Scale Flow Simulations. *Transport in Porous Media*, 96(1):1–20, 2013.

[254] G. Boccardo, D. L. Marchisio, and R. Sethi. Microscale simulation of particle deposition in porous media. *Journal of Colloid and Interface Science*, 417:227–237, 2014.

[255] J. J. Cheng and I. Manas-Zloczower. Flow Field Characterization in a Banbury Mixer. *International Polymer Processing*, 5(3):178–183, 1990.

[256] D. Ramkrishna. *Population Balances: Theory and Applications to Particulate Systems in Engineering*. Academic Press, London, U.K., 2000.

[257] D. Li, Z. Gao, A. Buffo, W. Podgorska, and D. L. Marchisio. Droplet breakage and coalescence in liquid–liquid dispersions: Comparison of different kernels with EQMOM and QMOM. *AIChE Journal*, 63:2293–2311, 2017.

[258] G. Boccardo, R. Sethi, and D. L. Marchisio. Fine and ultrafine particle deposition in packed-bed catalytic reactors. *Chemical Engineering Science*, 198:290–304, 2019.

[259] B. J. Bentley and L. G. Leal. An experimental investigation of drop deformation and breakup in steady, two-dimensional linear flows. *Journal of Fluid Mechanics*, 167:241–283, 1986.

[260] H. P. Grace†. DISPERSION PHENOMENA IN HIGH VISCOSITY IMMISCIBLE FLUID SYSTEMS AND APPLICATION OF STATIC MIXERS AS DISPERSION DEVICES IN SUCH SYSTEMS. *Chemical Engineering Communications*, 14(3-6):225–277, 1982.

[261] T. Lemenand, P. Dupont, D. Della Valle, and H. Peerhossaini. Comparative efficiency of shear, elongation and turbulent droplet breakup mechanisms: Review and application. *Chemical Engineering Research and Design*, 91(12):2587–2600, 2013.

[262] R. A. Debruijn. *Deformation and breakup of drops in simple shear flows*. PhD thesis, Technische Universiteit Eindhoven, 1991.

[263] K. M. B. Jansen, W. G. M. Agterof, and J. Mellema. Droplet breakup in concentrated emulsions. *Journal of Rheology*, 45:227–236, 2001.

[264] I. M. Klink, R. J. Phillips, and S. R. Dungan. Effect of emulsion drop-size distribution upon coalescence in simple shear flow: A population balance study. *Journal of Colloid and Interface Science*, 353:467–475, 2011.

[265] A. K. Chesters. The modelling of coalescence processes in fluid-liquid dispersions: a review of current understanding. *Chemical Engineering Research and Design*, 69:259–270, 1991.

[266] M. Laakkonen, V. Alopaeus, and J. Aittamaa. Validation of bubble breakage, coalescence and mass transfer models for gas–liquid dispersion in agitated vessel. *Chemical Engineering Science*, 61:218–228, 2006.

[267] Z. Gao, D. Li, A. Buffo, W. Podgórska, and D. L. Marchisio. Simulation of droplet breakage in turbulent liquid–liquid dispersions with CFD-PBM: Comparison of breakage kernels. *Chemical Engineering Science*, 142:277–288, 2016.

[268] A. Buffo, J. De Bona, M. Vanni, and D. L. Marchisio. Simplified volume-averaged models for liquid–liquid dispersions: Correct derivation and comparison with other approaches. *Chemical Engineering Science*, 153:382–393, 2016.

[269] J. De Bona, A. Buffo, M. Vanni, and D. L. Marchisio. Limitations of simple mass transfer models in polydisperse liquid-liquid dispersions. *Chemical Engineering Journal*, 296:112–121, 2016.

[270] A. Buffo, D. L. Marchisio, M. Vanni, and P. Renze. Simulation of polydisperse multiphase systems using population balances and example application to bubbly flows. *Chemical Engineering Research and Design*, 91:1859–1875, 2013.

[271] N. Hansen. The CMA Evolution Strategy: A Comparing Review. In J. A. Lozano, P. Larrañaga, I. Inza, and E. Bengoetxea, editors, *Towards a New Evolutionary Computation: Advances in the Estimation of Distribution Algorithms*, pages 75–102. Springer Berlin Heidelberg, Berlin, Heidelberg, Germany, 2006.

[272] C. M. Pooley, H. Kusumaatmaja, and J. M. Yeomans. Contact line dynamics in binary lattice Boltzmann simulations. *Physical Review E*, 78(5):056709, 2008.

[273] C. M. Pooley and K. Furtado. Eliminating spurious velocities in the free-energy lattice Boltzmann method. *Physical Review E*, 77(4):046702, 2008.

[274] P. Lallemand and L.-S. Luo. Theory of the lattice Boltzmann method: Dispersion, dissipation, isotropy, Galilean invariance, and stability. *Physical Review E*, 61(6):6546–6562, 2000.

Appendix A

Calculation of the protein surface number density

The method used in chapter 4 to automatically determine the protein surface number density is here explained as it has been seen that a certain number of surfactants are not adsorbed at the interface. This is similar to the procedure already employed to identify the bulk concentration of solutes in interfacial systems found in the literature [223]. Figure A.1 shows an illustrative example of the method here used. From simulations of the ternary system with two symmetrical interfaces the time-averaged number density profiles of protein molecules along the normalized x-direction normal to the interface expressed as $\phi\rho'$ are extracted (a) (see Figures 4.5 and 4.6 for reference). The gradient of the number density is then computed with respect to x/L_x (b). The regions where the gradient fluctuates around zero define the bulk phases. The interface region can be identified by looking for spikes (positive and negative) in the gradient that are an order of magnitude greater than the fluctuations seen in the bulk regions. These spikes define the interface region to be included in number density calculations. Hence the standard deviation S_e of the gradient (distance between horizontal grey dashed lines) is used to identify the distinction between bulk and interface regions. The first and last intersections between the gradient curve and horizontal lines in Figure A.1(b) define the interval limits ($\hat{x}_{1,a}$ and $\hat{x}_{1,b}$) of the interface region labeled as 1 where protein molecules can be considered adsorbed at the interface. The same is done for the interface labeled as 2 (not shown). From the area (in red) subtended by the number density profile, the equilibrated surface density of protein molecules at interface c_i is then obtained as follows:

$$c_i = \frac{L_x}{2n\phi L^2} \left(\int_{\hat{x}_{1,a}}^{\hat{x}_{1,b}} \phi \rho'(x/L_x) L^2 d(x/L_x) + \int_{\hat{x}_{2,a}}^{\hat{x}_{2,b}} \phi \rho'(x/L_x) L^2 d(x/L_x) \right) , \quad \text{(A.1)}$$

where n corresponds to the number of beads representing the protein molecule, thus equal to 1 or 2 for $\phi = 3008$ or $\phi = 1504$, respectively (see Figure 4.2). Hence, c_i values are used as abscissas in Figure 4.7.

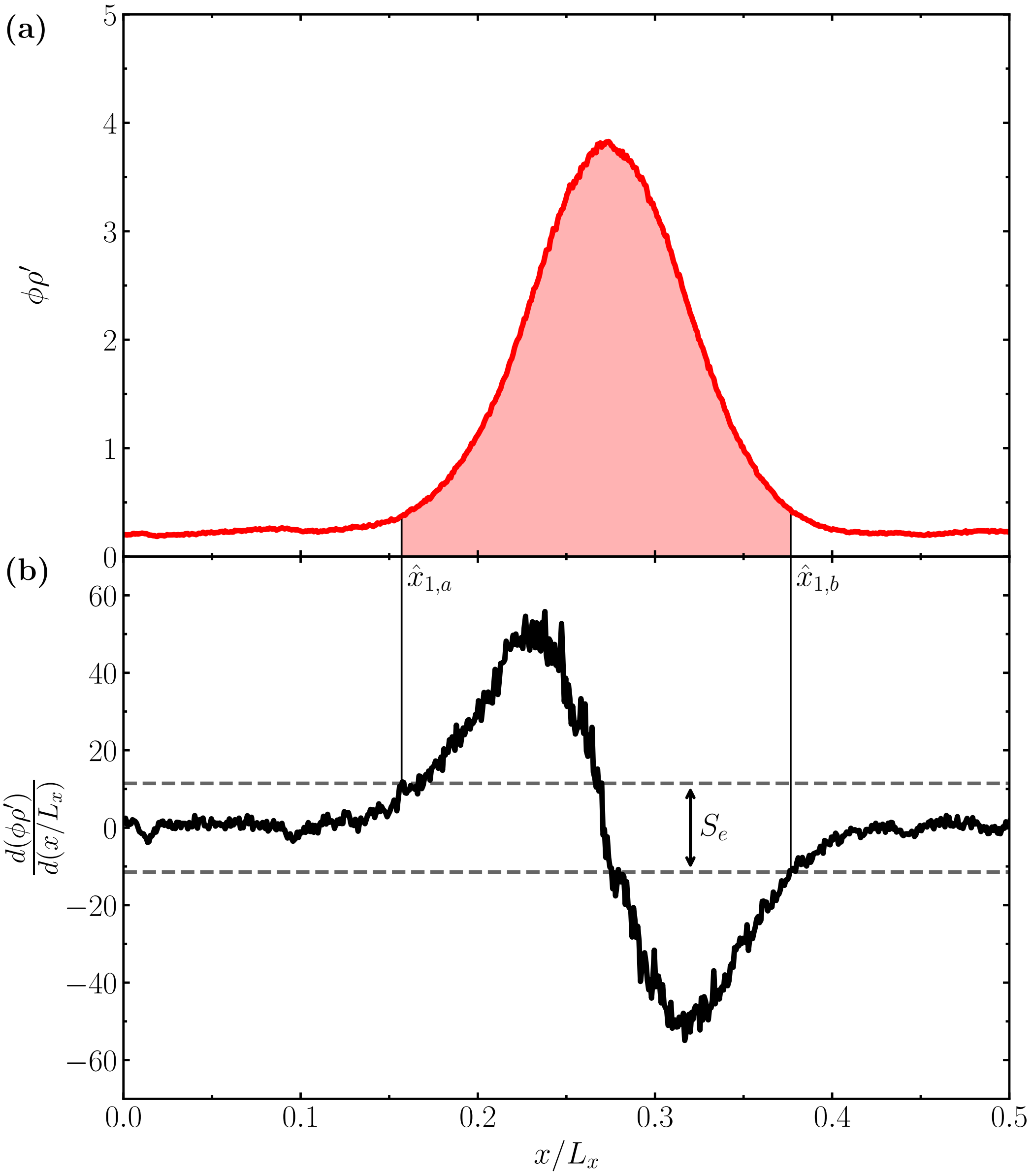

Fig. A.1 Illustrative example on how the protein surface number density is determined in this work from the number density profile of surfactants along the normalized *x*-direction normal to the interface (a) by means of evaluating its gradient curve (b). The portion of the simulation box relative to the interface labeled as 1 is only shown. Further details on the meaning of the symbol notation can be found in the text.

Appendix B

The D3Q19 set parameters

The D3Q19 set is used in the present study in chapter 5. The lattice velocity directions are split into two groups. The directions $\vec{c}_{1-6}$ point in the nearest neighbour directions:

$$\begin{bmatrix} c_{x1-6} \\ c_{y1-6} \\ c_{z1-6} \end{bmatrix} = \begin{bmatrix} 1 & -1 & 0 & 0 & 0 & 0 \\ 0 & 0 & 1 & -1 & 0 & 0 \\ 0 & 0 & 0 & 0 & 1 & -1 \end{bmatrix}, \tag{B.1}$$

and $\vec{c}_{7-18}$ point into 12 square diagonal directions:

$$\begin{bmatrix} c_{x7-18} \\ c_{y7-18} \\ c_{z7-18} \end{bmatrix} = \begin{bmatrix} 1 & -1 & 1 & -1 & 0 & 0 & 0 & 0 & 1 & -1 & 1 & -1 \\ 1 & 1 & -1 & -1 & 1 & -1 & 1 & -1 & 0 & 0 & 0 & 0 \\ 0 & 0 & 0 & 0 & 1 & 1 & -1 & -1 & 1 & 1 & -1 & -1 \end{bmatrix}. \tag{B.2}$$

The equilibrium distributions of particle populations f_q^{eq}, g_q^{eq}, and h_q^{eq} for directions $q \in 1,...,18$ are calculated as follows [272]:

$$\begin{aligned} f_q^{eq} = w_q\Bigg(p_0 - \kappa_{int}\phi(\partial_{xx}^2\phi + \partial_{yy}^2\phi + \partial_{zz}^2\phi) + c_{q\alpha}\rho u_\alpha + \frac{3}{2}\left[c_{q\alpha}c_{q\beta} - \frac{1}{3}\delta_{\alpha\beta}\right]\rho u_\alpha u_\beta \Bigg) \\ + (\kappa_{int} - D\psi)\Bigg(w_q^{xx}\partial_x\phi\partial_x\phi + w_q^{yy}\partial_y\phi\partial_y\phi + w_q^{zz}\partial_z\phi\partial_z\phi + w_q^{xy}\partial_x\phi\partial_y\phi \\ + w_q^{xz}\partial_x\phi\partial_z\phi + w_q^{yz}\partial_y\phi\partial_z\phi \Bigg) \ , \end{aligned} \tag{B.3a}$$

$$g_q^{eq} = w_q\left(\Gamma_\phi\mu_\phi + c_{q\alpha}\phi u_\alpha + \frac{3}{2}\left[c_{q\alpha}c_{q\beta} - \frac{1}{3}\delta_{\alpha\beta}\right]\phi u_\alpha u_\beta \right) \ , \tag{B.3b}$$

$$h_q^{eq} = w_q\left(\Gamma_\psi\mu_\psi + c_{q\alpha}\psi u_\alpha + \frac{3}{2}\left[c_{q\alpha}c_{q\beta} - \frac{1}{3}\delta_{\alpha\beta}\right]\psi u_\alpha u_\beta \right) \ . \tag{B.3c}$$

The populations for $q = 0$ are calculated as:

$$f_0^{eq} = \rho - \sum_{q=1}^{18} f_q^{eq} \ , \tag{B.4a}$$

$$g_0^{eq} = \phi - \sum_{q=1}^{18} g_q^{eq} \ , \tag{B.4b}$$

$$h_0^{eq} = \psi - \sum_{q=1}^{18} h_q^{eq} \ , \tag{B.4c}$$

and the bulk pressure is given by:

$$p_0 = c_s^2\rho + \frac{A}{2}\phi^2 + \frac{3B}{4}\phi^4 - k_bT[\ln(1-\psi) - \frac{C}{2}\psi^2 - E\phi\psi \ . \tag{B.5}$$

The weights read [273]:

$$\begin{aligned}
&w_{1-6} = \frac{1}{6}\,, \quad w_{7-18} = \frac{1}{12}\,,\\
&w^{xx}_{1-2} = w^{yy}_{3-4} = w^{zz}_{5-6} = \frac{5}{12}\,, \quad w^{xx}_{3-6} = w^{yy}_{1-2,5-6} = w^{zz}_{1-4} = -\frac{1}{3}\,,\\
&w^{xx}_{7-10} = w^{xx}_{15-18} = w^{yy}_{7-14} = w^{zz}_{11-18} = -\frac{1}{24}\,,\\
&w^{xx}_{11-14} = w^{yy}_{15-18} = w^{zz}_{7-10} = \frac{1}{12}\,,\\
&w^{xy}_{1-6} = w^{yz}_{1-6} = w^{zx}_{1-6} = 0\,, \quad w^{xy}_{7,10} = w^{yz}_{11,14} = w^{zx}_{15,18} = \frac{1}{4}\,,\\
&w^{xy}_{8,9} = w^{yz}_{12,13} = w^{zx}_{16,17} = -\frac{1}{4}\,, \quad w^{xy}_{11-18} = w^{yz}_{7-10} = w^{zx}_{7-14} = 0\,.
\end{aligned} \tag{B.6}$$

The stencils for the calculation of gradients and Laplacian in the pressure tensor and chemical potential are given by [273]:

$$\partial_x = \frac{1}{12}\left[\begin{pmatrix} 0 & 0 & 0\\ -1 & 0 & 1\\ 0 & 0 & 0 \end{pmatrix}, \begin{pmatrix} -1 & 0 & 1\\ -2 & 0 & 2\\ -1 & 0 & 1 \end{pmatrix}, \begin{pmatrix} 0 & 0 & 0\\ -1 & 0 & 1\\ 0 & 0 & 0 \end{pmatrix}\right], \tag{B.7a}$$

$$\nabla^2 = \frac{1}{6}\left[\begin{pmatrix} 0 & 1 & 0\\ 1 & 2 & 1\\ 0 & 1 & 0 \end{pmatrix}, \begin{pmatrix} 1 & 2 & 1\\ 2 & -24 & 2\\ 1 & 2 & 1 \end{pmatrix}, \begin{pmatrix} 0 & 1 & 0\\ 1 & 2 & 1\\ 0 & 1 & 0 \end{pmatrix}\right], \tag{B.7b}$$

where left, middle, and right matrices show slices of the stencil when $c_{zq} = 1$, 0, and -1, respectively.

Appendix C

MRT matrices

The transformation matrix **M** derived based on the work Ref. [237] reads:

$$\begin{pmatrix}
1 & 1 & 1 & 1 & 1 & 1 & 1 & 1 & 1 & 1 & 1 & 1 & 1 & 1 & 1 & 1 & 1 & 1 & 1 \\
-30 & -11 & -11 & -11 & -11 & -11 & -11 & 8 & 8 & 8 & 8 & 8 & 8 & 8 & 8 & 8 & 8 & 8 & 8 \\
12 & -4 & -4 & -4 & -4 & -4 & -4 & 1 & 1 & 1 & 1 & 1 & 1 & 1 & 1 & 1 & 1 & 1 & 1 \\
0 & 1 & 0 & -1 & 0 & 0 & 0 & 1 & -1 & -1 & 1 & 1 & -1 & -1 & 1 & 0 & 0 & 0 & 0 \\
0 & -4 & 4 & 0 & 0 & 0 & 0 & 1 & -1 & 1 & -1 & 1 & -1 & 1 & -1 & 0 & 0 & 0 & 0 \\
0 & 0 & 1 & 0 & -1 & 0 & 0 & 1 & 1 & -1 & -1 & 0 & 0 & 0 & 0 & 1 & -1 & -1 & 1 \\
0 & 0 & 0 & -4 & 4 & 0 & 0 & 1 & 1 & -1 & -1 & 0 & 0 & 0 & 0 & 1 & -1 & 1 & -1 \\
0 & 0 & 0 & 0 & 0 & 1 & -1 & 0 & 0 & 0 & 0 & 1 & 1 & -1 & -1 & 1 & 1 & -1 & -1 \\
0 & 0 & 0 & 0 & 0 & -4 & 4 & 0 & 0 & 0 & 0 & 1 & 1 & -1 & -1 & 1 & 1 & -1 & -1 \\
0 & 2 & 2 & -1 & -1 & -1 & -1 & 1 & 1 & 1 & 1 & 1 & 1 & 1 & 1 & -2 & -2 & -2 & -2 \\
0 & -4 & 2 & -4 & 2 & 2 & 2 & 1 & 1 & 1 & 1 & 1 & 1 & 1 & 1 & -2 & -2 & -2 & -2 \\
0 & 0 & 0 & 1 & 1 & -1 & -1 & 1 & 1 & 1 & 1 & -1 & -1 & -1 & -1 & 0 & 0 & 0 & 0 \\
0 & 0 & 0 & -2 & -2 & 2 & 2 & 1 & 1 & 1 & 1 & -1 & -1 & -1 & -1 & 0 & 0 & 0 & 0 \\
0 & 0 & 0 & 0 & 0 & 0 & 0 & 0 & 1 & -1 & -1 & 1 & 0 & 0 & 0 & 0 & 0 & 0 & 0 \\
0 & 0 & 0 & 0 & 0 & 0 & 0 & 0 & 0 & 0 & 0 & 0 & 0 & 0 & 0 & 1 & -1 & -1 & 1 \\
0 & 0 & 0 & 0 & 0 & 0 & 0 & 0 & 0 & 0 & 0 & 1 & -1 & -1 & 1 & 0 & 0 & 0 & 0 \\
0 & 0 & 0 & 0 & 0 & 0 & 0 & 1 & -1 & 1 & -1 & -1 & 1 & -1 & 1 & 0 & 0 & 0 & 0 \\
0 & 0 & 0 & 0 & 0 & 0 & 0 & -1 & -1 & 1 & 1 & 0 & 0 & 0 & 0 & 1 & 1 & -1 & 1 \\
0 & 0 & 0 & 0 & 0 & 0 & 0 & 0 & 0 & 0 & 0 & 1 & 1 & -1 & -1 & -1 & -1 & 1 & 1
\end{pmatrix} . \tag{C.1}$$

The relaxation matrix **S** is diagonal in the moment space:

$$S = \mathrm{diag}(0, s_e, s_\varepsilon, 0, s_q, 0, s_q, s_\nu, s_\pi, s_\nu, s_\pi, s_\nu, s_\nu, s_\nu, s_m, s_m, s_m) \ , \tag{C.2}$$

where the relaxation rates other than s_ν are chosen as follows: $s_e = 1.19$, $s_\varepsilon = s_\pi = 1.4$, $s_q = 1.2$ and $s_m = 1.98$. These values were obtained using linear analysis to achieve optimized stability of the model [274].